MULTIFRACTAL MODELLING OF LIQUID WATER CLOUDS: CLOUD SPATIAL STRUCTURE AND ITS EFFECT ON THE SOLAR RADIATION FIELD

by

Kurt S. Fienberg, B.Sc.(Hons)   (Kurt Steven)

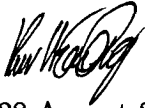Submitted in fulfilment of the
requirements for the degree of   Geog & Env.
Studies

Doctor of Philosophy

University of Tasmania (August, 2003)
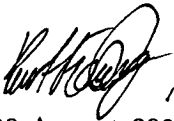
Declaration

I hereby declare that this thesis contains no material that has been accepted for the award of any other degree or diploma in any tertiary institution, and to the best of my knowledge contains no copy, paraphrase or material previously published or written by another person, except where due reference is given in the text.

28 August 2003

Authority of access

This thesis is not to be made available for loan or copy for two years following the date this statement was signed. Following that time the thesis may be made available for loan and limited copying in accordance with the *Copyright Act 1968*.

28 August 2003

Abstract

At any point in time a significant fraction of the globe is covered by liquid water clouds. Understanding the relationship between cloud and solar radiation is therefore of great importance for both climate modelling and remote sensing. Previous studies have found that cloud spatial structure has a significant effect on cloud albedo, with spatial inhomogeneities leading to less reflection of solar radiation than was predicted by the traditional homogeneous cloud model. This thesis investigates further the consequences of cloud spatial variability on atmospheric radiation, with the aim of developing methods to improve radiation modelling and remote sensing of cloud properties.

The basis of this study is the quantification of the scaling and intermittency of liquid water fields using a multifractal model. The fractionally integrated flux (FIF) model is used to both describe and numerically simulate cloud fields, with model parameters being determined from aircraft measurements made during 98 flights over northern Tasmania, Australia. The aircraft data set is divided into three broad cloud types: stratocumulus, altostratus and low level cumulus. The horizontal fluctuations in all three cloud types are shown not only to be scale invariant and non-stationary, but also to have very similar statistics with only one out of three model parameters varying significantly between cloud types.

Clouds with horizontal structure described by the FIF model but constant vertical profiles are then used in Monte Carlo radiative transfer calculations. The differences between the multifractal and homogeneous cloud results are larger than those previously reported for marine stratocumulus, due to the larger degree of inhomogeneity in the cloud types considered. The results of the Monte Carlo simulations are used to derive the "effective optical properties" of the multifractal cloud fields, defined as the optical properties of a homogeneous cloud producing the same radiative transfer results as the multifractal cloud. This allows the well-known and efficient radiative transfer techniques for homogeneous cloud to be applied to multifractal cloud. The effective optical properties were found to vary with the spatial scale under consideration, and an empirical parameterisation for the effective optical properties is presented that is a function of spatial scale, mean cloud optical depth and single-scattering albedo.

The range of conditions under which the effective optical depth approximation can be used is then examined, with vertical fluctuations in cloud liquid water, radiance changes with viewing angle, and differing single-scattering properties all considered. The approximation is found to be reasonable for most low-level cloud

conditions, with the greatest discrepancies occurring for absorbing clouds with vertical fluctuations and significant vertical extent. Finally, the effective optical depth parameterisation is tested in the satellite remote sensing of cloud liquid water path, with the results being compared to simultaneous aircraft measurements. The agreement between the data sets is significantly improved when the results are corrected for cloud inhomogeneity using the effective optical depth approximation, with the remaining errors being shown to be of the level expected due to the discrepancies in measurement scales. These (root-mean-square) errors due to the mismatch of measurement scales when comparing satellite-based and in situ measurements are estimated, using the spatial statistics of liquid water, to be approximately 27%.

Acknowledgements

I would like to thank everyone who has assisted me in this doctoral project, including:

- Hydro Tasmania for their funding and support.

- Andrew Lenton, Alex Nazarov, Christina Nebel, Graham Vertigan, and Ian Searle for the collection of the aircraft data and other aid.

- My supervisor Manuel Nunez for his consistent interest, guidance, and assistance in all aspects of the project.

- Christopher Kuchinke for many pieces of advice, but especially for his help with the work in Chapter 6.

Contents

Chapter 1

Introduction

1.1 Motivations

Low-level, mainly liquid water clouds have been estimated to cover an average of approximately one quarter of the globe [*Hartman et al.*, 1992]. This means that they have a significant impact on a wide range of fields: from hydrology and weather forecasting, to global energy balance and global circulation models, and even to the satellite remote-sensing of non-cloud atmospheric quantities (which cloudiness often impedes). In many of these applications, the study of clouds in the atmosphere requires, at various times, an understanding of atmospheric dynamics, the chemistry of cloud condensation nuclei, the statistics of droplet growth and aggregation, and other areas of knowledge. This thesis focuses on the relationship between clouds and solar radiation, an area of research relevant to both climate modelling and the remote sensing of cloud properties. The former is of interest due to the current concerns about climate change and the consequences of anthropogenic climate forcing; the latter is important because only satellite-based observations

can cover the wide spatial and temporal scales over which clouds occur in the atmosphere.

In the case of climate modelling, it has long been recognised that a significant proportion of the earth's radiation budget can be attributed to cloud radiative forcing [e.g. *Wielicki et al.*, 1995; *Mitchell*, 1989]. However, clouds influence the radiation budget in a variety of ways, both cooling the earth by increasing the albedo of the earth-atmosphere system and heating the earth by lowering the level of outgoing longwave radiation. While cirrus clouds are usually high, cold and optically-thin, and hence have a net heating effect, low level clouds have a net cooling effect because they are optically thick, reflect a relatively large amount of solar radiation, and are warm enough to have little net effect on longwave radiation [*Rossow and Lacis*, 1990]. Of these two cases, global radiation studies have found that the net radiative forcing by clouds is greatest in regions of low level cloud, and that the greatest effect is the reflection of shortwave radiation [*Harrison et al.*, 1990; *Ramanathan et al.*, 1989; *Rossow and Zhang*, 1995] . *Cahalan et al.* [1994a] estimated that a 10% change in the global average albedo of stratocumulus cloud would produce a 5°C change in the equilibrium surface temperature, equivalent to the change in surface temperature since the last ice age. From another point of view, this means that if global circulation models are incorrect in their predictions of liquid water cloud albedo then surface temperature predictions would contain significant errors. This is particularly important when considering that not only do clouds affect the climate but also changes in climate can affect cloud formation - clouds are formed by dynamic atmospheric processes affected by global warming or cooling [*Rogers and Yau*, 1989] leading to a range of possible feedback mechanisms. This makes accurate cloud modelling necessary for research into climate change.

The remote sensing of clouds has many applications beyond studying the effects

2

of cloud on the radiation budget. These include: global surveys of cloud properties to develop cloud climatologies [e.g. *Han et al.,* 1994; *Kawamoto et al.* 2001]; the estimation of rain rates and precipitation area [e.g. *Lensky and Rosenfield,* 1997]; the investigations of the effects of weather modification through cloud-seeding [e.g. *Sassen and Zhao,* 1993]; the estimation of radiation levels at the surface [e.g. *Pinker et al.,* 1995]; the validation or initiation of numerical cloud models [e.g. *Fouilloux and Iaquinta,* 1997]. Because of the vantage point they occupy, high above the earth's surface, satellite platforms are able to cover a wider range of spatial scales than ground based or aircraft measurements. This is of great advantage in measurement programs involving liquid water clouds because, as will be examined later in this thesis, their properties and structure fluctuate widely over a wide range of scales [*Davis et al.,* 1996a]. Many techniques for the remote sensing of cloud properties have been developed and they utilise many wavelengths of radiation from radar [e.g. *Bellon et al.,* 1980; *Lin et al.,* 2002], through microwave [e.g. *Simmer et al.* 1989] and thermal infrared [e.g. *Liou et al.,* 1990], to the solar spectrum [e.g. *Nakajima and King,* 1990]. However, the scope of this work is restricted to the last of these, as the bulk of global cloud data is obtained from satellite observations of reflected solar radiation.

1.2   Radiative transfer under cloudy conditions

Both climate modelling and remote sensing of cloud properties require the ability to calculate the radiation reflected and transmitted by cloud fields under various conditions. This in turn requires a cloud model to be used in these calculations. The simplest cloud model is a homogeneous distribution of liquid water bounded above and below by flat surfaces and extending indefinitely in the horizontal - this

model is known as the plane-parallel homogeneous (PPH) cloud model. However, real clouds do not conform to the PPH model, and this has consequences for radiative transfer. Clouds with inhomogeneous liquid water fields have been found to have a significantly lower average reflectance (and higher average transmittance) than a PPH cloud field with the same mean liquid water content, if the observation scale under consideration exceeds a photon mean-free-path length [*Davis et al.*,1991]. This general result has held true for all types of inhomogeneous cloud fields so far examined, including: clouds with small sinusoidal variations in water content [*Romanova*, 1998;1999]; aircraft observed cloud fields [*Los and Duynkerke*, 2001]; cloud fields generated by dynamical models [*Macke et al.*, 1999]; and fractal cloud models of various types [e.g. *Davis et al.*, 1990; *Cahalan et al.*, 1994a; *Borde and Isaka*, 1996]. Despite these consistent findings, most of the radiative transfer algorithms in climate models [e.g. *Tiedke*, 1993; *McGuffie and Henderson-Sellers*, 1997; *Gregory et al.*, 2000] and in cloud property remote sensing [e.g. *Nakajima and King*, 1990; *Kuji et al.*, 2000; *Szczodrak*, 2001] are still based on the simple PPH cloud model. Presumably this is because of the simplicity and speed of radiative transfer calculations made using the PPH assumption, because the algorithms were developed before the effects of cloud inhomogeneities became known, or because of the difficulty in completely parameterising the variability in the cloud structure. Speed of calculation is particularly important when considering the radiation flux calculations for general circulation models (GCMs) where a vast number of calculations must be made, and for multispectral remote sensing where a large number of variables is involved. There are many fast algorithms that can calculate radiative transfer for a PPH cloud, such as the delta-Eddington approximation, the doubling adding method, and discrete-ordinate radiative transfer (for summaries of various methods, see *Liou* [1990] or *Lenoble* [1985]). On the other hand, very accurate cal-

4

culation methods for radiation in inhomogeneous cloud fields - such as Monte Carlo radiative transfer [*Marchuk et al.*, 1980], the diffusion approximation approach [e.g. *Gu and Liou*, 2001], or the spherical harmonic discrete ordinate method [*Evans*, 1998] - are generally much more time consuming.

Several faster, approximate methods of radiative transfer have been developed for these applications. The first is the independent pixel approximation (IPA) [*Cahalan et al.*, 1994b], in which PPH cloud calculations are performed for pixels at a scale equal to or smaller than a photon mean-free path length, and then these results are averaged over whatever scale is being considered. The IPA avoids the effects of sub-pixel scale variability because liquid water content variability at scales smaller than the mean free path length does not have a significant effect on the radiation field [*Marshak et al.*, 1998]. The area averaging then reduces the error due to horizontal transport of radiation. If the area under consideration is small enough that horizontal transport of photons is significant, the variant known as the non-local IPA (NIPA) [*Marshak et al.*, 1996] may be used instead to take this into account. There is no particular cloud model inherent in the IPA, so some cloud model must be chosen to determine the distribution of the cloud liquid water content. Calculations performed using the IPA are much faster than Monte Carlo radiative transport code, but if the pixels or grids under consideration are at the meso-scale (or larger) the IPA calculations are still many times slower than PPH calculations, because they effectively require tens or hundreds of PPH calculations per grid point.

An alternate approach to the IPA for quick radiative transport calculations is the concept of effective optical properties. In this approach the inhomogeneous cloud is replaced in the radiative transfer calculations by a PPH cloud with the same reflectance (and/or transmittance). The optical properties of this substitute

5

PPH cloud are referred to as the "effective" optical properties of the inhomogeneous cloud. Since this approach only involves a single PPH calculation, the calculation is fast. This approach also has the important advantage of being very easy to add to existing radiation algorithms in climate models or remote sensing. However, the effective optical properties will depend on the precise distribution of the liquid water content, i.e. they will depend on the cloud model used. This concept was used by *Cahalan et al.* [1994a] in the effective thickness approximation (ETA) for cloud fields generated by the bounded cascade fractal model, and also in the 'renormalisation' scheme used by *Cairns* [2000]. In the ETA an effective optical depth is found as a function of the fractal parameter of the cloud model. The bounded cascade model was also used to formulate the equivalent homogeneous cloud approximation (EHCA) [*Szczap et al.*, 2000a;b;c], although in the EHCA the parameterisations of the effective optical properties were written in terms of generic statistics rather than model-specific parameters. The other differences between the ETA and the EHCA include the fact that the ETA only applies at the scale of the entire cloud domain and has no dependence on cloud optical depth, whereas the parameterisations in the EHCA have a direct dependence on optical depth and an indirect dependence on spatial scale. The EHCA also improves on the ETA by including absorbing clouds [*Szczap et al.*, 2000b], where an effective single-scattering albedo is used in addition to an effective optical depth.

1.3 Cloud spatial structure and the approach taken in this thesis

To implement any of these radiative transfer schemes, an accurate model of cloud structure is required. Over the last two decades the need for a realistic cloud model for radiative transfer has led various researchers to investigate cloud spatial structure and to develop inhomogeneous cloud models. This has occurred along side a general recognition that atmospheric structures and processes occur over a wide range of scales, and as part of the development of a paradigm of scale invariance and (multi)fractal analysis. *Lovejoy* [1982] first suggested that cloud spatial distributions could be modelled as a fractal structure. Various measurements since then, including *Cahalan and Joseph* [1989], *Malinowski and Zawadzki* [1993], and *Davis et al.* [1996a], have shown that cloud structure is scale invariant, and hence that a fractal model is applicable. These studies have generally concentrated on overcast marine stratocumulus cloud. Multifractal analyses to further quantify the intermittency of cloud liquid water content have been performed [*Davis et al.,* 1994; *Marshak et al.,*1997], also on marine stratocumulus. In this study an attempt is made to significantly extend this data set and begin a move toward a more complete climatology of cloud internal structure.

A range of multifractal models have been developed to describe scale invariant processes, including the lognormal model [*Kolmogorov,* 1962] and the bounded cascade model [*Cahalan,* 1989; *Cahalan et al.,*1994a]. For thorough reviews of multifractal modelling and analysis, the reader is referred to *Schertzer and Lovejoy* [1991] and *Davis et al.* [1996b]. The cloud model used in this study is the Fractionally Integrated Flux (FIF) multifractal model of *Schertzer and Lovejoy* [1987; 1991], a continuous multifractal model which has been used for cloud modeling

[e.g. *Wilson et al.*, 1991], as well as for modeling other atmospheric quantities in the "unified scaling model" of the atmosphere [*Schertzer and Lovejoy*,1985; *Chingirinskaya et al.*, 1994; *Lovejoy and Schertzer*, 1995a]. The FIF model has the advantages over other multifractal models of being able to be adjusted to a wider range of statistics [*Davis et al.*, 1994] and of being based on the symmetries of the equations governing atmospheric turbulence. While in general multifractals could require an infinite number of parameters to completely define them, this model posits that atmospheric phenomena fall into universality classes of multifractals defined by three parameters. These are stable, attractive multifractal processes. Although there has been some debate about the mathematical existence of these classes due to a possible divergence in the small scale limit, this seems to be resolved by taking alternate routes to universality - see *Schertzer and Lovejoy* [1997] for details.

Measurements have shown, for example, that turbulent velocity fields [*Chingirinskaya et al.*, 1994; *Lazarev et al.*, 1994] and rain radar reflectivities [*Tessier et al.*, 1993; *Lovejoy and Schertzer*, 1995] can be described by these universality classes. Analysis of cloudy satellite images have shown that the statistics of cloud radiances also closely fit these universal multifractals [*Lovejoy et al.*, 1993; *Tessier et al.*, 1993; *Lovejoy et al.*, 2001a]. However, the FIF model has not yet been fitted to direct in situ measurements of cloud liquid water content. This is of importance considering the non-linear relationship between liquid water content and the radiation field, and between liquid water content and precipitation. This is highlighted by the fact that when examining satellite images of cloudy atmospheres, *Tessier et al.* [1993] found different values for the FIF parameters at different wavelengths.

Therefore in this study the FIF model is compared to in situ measurements made during 98 flights over Tasmania, Australia. These measurements are used

to directly determine the FIF model parameters for three different categories of liquid water clouds. In this manner multifractal analysis is extended to cloud types other than the marine stratocumulus that have been the focus of previous analysis. Subsequently, the radiative properties of such multifractal clouds are investigated, with an eye to determining if there are differences between these clouds, described by the FIF model, and those previously examined using the bounded cascade model (with marine stratocumulus parameters). An effective properties approximation is developed for use in radiative transport calculations, in an approach similar to that taken by *Szczap et al.* [2000a;b;c] in developing the EHCA. As in the EHCA, the focus is on meso-scale pixels suitable for moderate resolution remote sensing or regional climate models. However, this approach is expanded to other liquid water clouds apart from overcast marine stratocumulus, and to include a direct dependence on pixel or grid size. The effects of such an approximation on some applications, such as the remote sensing of cloud properties or determining radiation at the surface, are also examined, as are the radiative implications of vertical variations in the liquid water field.

1.4 Thesis structure

The general goal of this work is therefore to improve the understanding of cloud spatial structure and determine how this knowledge can be used in radiative transfer applications, such as existing climate models and remote sensing algorithms. With this is mind, the structure of the thesis is given as follows:

- Chapter 2 contains a description of the models used throughout this study
  - both the FIF multifractal model used to describe the cloud fields and the

Monte Carlo radiative transfer model used to determine the radiative properties of multifractal clouds. Also presented in this chapter is a summary of multifractal statistics and analysis. In general, chapter 2 describes the major tools and methods used later in the thesis.

- Chapter 3 focuses on the analysis of the in situ measurements of cloud liquid water fields. The data is shown to fit the multifractal model and the associated multifractal parameters are empirically determined for three different cloud types. The diurnal and seasonal variation in stratocumulus spatial structure is also examined in this chapter.

- Chapter 4 is a presentation of the results of radiative transfer calculations carried out using clouds with horizontal spatial inhomogeneities described by the FIF model, but with a homogeneous vertical structure. The effective optical properties of both absorbing and non-absorbing clouds are parameterised, and the accuracy of the parameterisation under different conditions is tested. A comparison of our results with the EHCA is also made.

- Chapter 5 describes the results of radiative transfer through clouds with a multifractal structure in the vertical as well as horizontal dimensions, in order to determine the errors that result from the earlier assumption of vertical homogeneity.

- Chapter 6 investigates further the consequences of using the effective optical depth approximation by considering the radiance distributions instead of total reflectance and transmittance. A test case is considered that involves transmitted UV radiance under stratocumulus clouds. Radiance distributions calculated for multifractal clouds are compared to those of a PPH cloud with

the same total transmittance, and these results are compared to radiometric measurements.

- Chapter 7 presents a comparison of cloud properties derived from satellite remote sensing with those found from in situ measurements. The result of using the effective optical properties approximation in cloud property retrieval, instead of the PPH model alone, is examined. Also investigated is the impact of multifractal cloud structure on the comparison of data sets measured at different resolutions.

- Chapter 8 concludes this thesis and contains a summary of results, as well as recommendations for further study.

Of these chapters, the second contains no new work but is simply a summary of methods and models developed by others, while all of the subsequent chapters present original results of the doctoral research project.

Chapter 2

Cloud and Radiation Models

Many of the results that appear later in this thesis are produced in the framework of two key models: the FIF multifractal model that describes the spatial statistics of the cloud liquid water content field, and the Monte Carlo simulations that calculate the radiative properties of clouds given their spatial structure. In this chapter these two models are described, along with the analysis technique used to determine the parameters of the multifractal model from measured cloud fields, and the numerical method used to generate cloud fields.

2.1 The multifractal cloud model

Fractals are characterized by the fact that their general structures and level of detail are unaffected by changes of resolution, which is to say that they are scale invariant. Dissipative systems with non-linear dynamics, such as cloud formation and atmospheric turbulence, typically show a high degree of variability over a very wide range of scales. This makes scale invariant models such as fractals an appropriate

choice for phenomenological or statistical modelling. The original fractals used to model clouds and rain were monofractal models [e.g. *Mandelbrot* 1983] - geometric models containing 'simple' scaling which is characterized by a single (generally non-integer) fractal dimension. However, this approach has been found to be insufficient to fully describe the statistics of cloud fields [*Davis et al.* 1994; *Schertzer and Lovejoy* 1985] and multifractal models which require multiple parameters to describe their scaling behavior have been developed. For a more general review of multifractal models see *Davis et al.* [1996b] and for multifractal modelling applied to remote sensing applications see *Lovejoy et al.* [2001b].

It should also be noted that in this work all scaling is assumed to be isotropic, that is the scaling is assumed to be the same in all dimensions. This assumption is made because the primary data set examined here is one dimensional horizontal aircraft flight data, and hence the data is not available to analyse any anisotropy of scaling, or to implement the framework of generalised scale invariance developed by *Schertzer and Lovejoy* [1987;1991].

2.1.1   The cascade process

The universal FIF multifractal model [*Schertzer and Lovejoy,* 1987; 1991] which is used here, was developed out of the theory of turbulent velocity cascades. It is based on three properties of the (incompressible) Navier-Stokes equations that govern atmospheric turbulence: 1) scaling symmetry or invariance under dilations (zooms); 2) conservation of a quantity with changes of scale - the energy flux, ε, from large to small scales; 3) the fact that the dynamics are most effective between neighbouring scales i.e. energy transfer between very large and very small structures is inefficient. These properties lead to a cascade process, with large structures

being made up of substructures on a smaller scale, which are in turn made up of even smaller structures, and so on. This downwards cascade will only end when a scale is reached that is so small that frictional losses of energy dominate, which in the atmosphere is on the order of millimetres. Mathematically, this process can be represented by a multiplicative cascade, where at each step down in scale the substructures are formed by multiplying the parent structure by different (random) factors. That is, if ε_{eddy} is a variable representing a cascade structure at a large scale then the values of the substructures are given by

$$\varepsilon_{subeddy} = \varepsilon_{eddy} \cdot \mu\varepsilon, \qquad (2.1)$$

where $\mu\varepsilon$ is a (stochastic) multiplicative factor. A schematic representation of this process is shown in Figure 2.1.

In the velocity cascade process, the energy flux ε is conserved with the change of scale but the velocity fluctuations are not. In the model used here this conservation is canonical, i.e. statistical - in the average over the entire ensemble rather than in any particular realisation. Following the convention of labelling the scale under consideration, or resolution, by the ratio

$$\lambda = \frac{L_{\max}}{l}, \qquad (2.2)$$

where $L_{\max}$ is the greatest length in a data set and l is the length of grid sides at current scale, then the following scaling relation for the velocity field (v) measured at scale λ [*Kolmogorov*, 1941; *Obukhov*, 1949]:

$$\Delta v(l) \propto \varepsilon^{1/3} \cdot \lambda^{-1/3}, \qquad (2.3)$$

14

The cascade process in one dimension:

λ = 1   A completely
                         uniform field

λ = 2   After multiplication
                         by 2 random
                         factors

λ = 4   After multiplication
                         by 4 more random
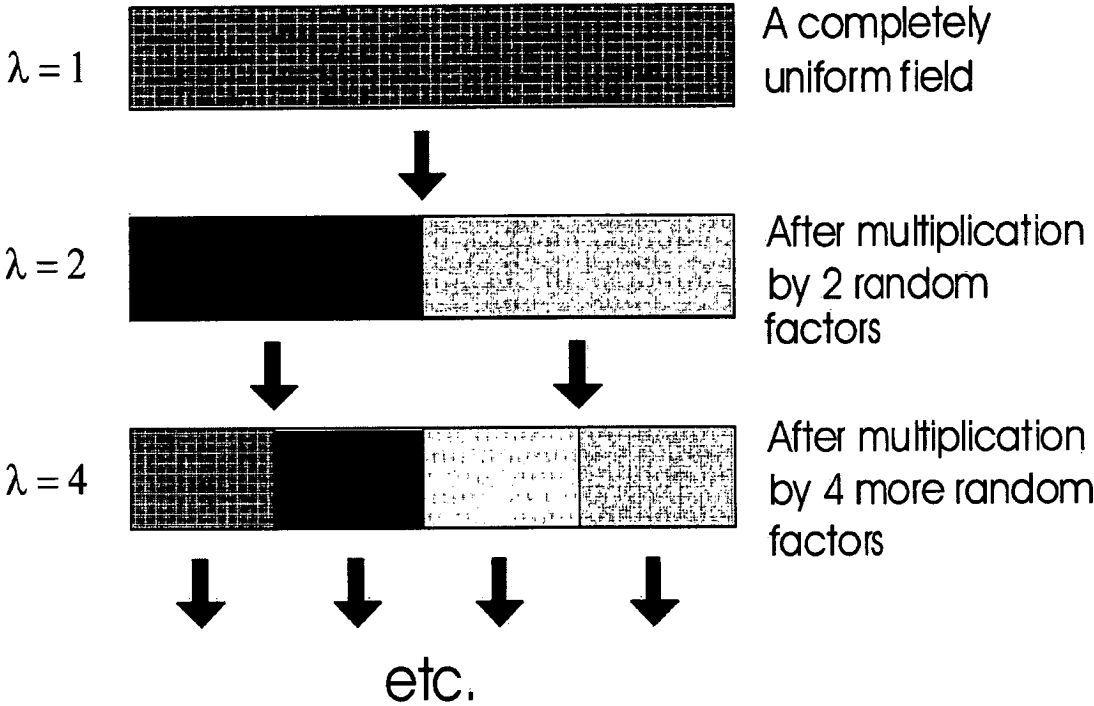   factors

etc.

Figure 2.1: A schematic representation of the cascade process in one dimension, with shading used to represent the value of the scalar field. Each structure is broken up into two substructures, transfering some or all of its value to the substructures. This is modelled mathematically by multiplicative factors being applied at each level. The scale is labelled by the ratio λ = (maximum length)/(current grid size).

15

where $\Delta v(l) = v(x + l) - v(x)$. So as the cascade process continues from large to small length scales, the velocity fluctuations decrease on average, although the ensemble-mean energy flux is constant. As each area on a larger scale is divided into smaller areas, in the cascade process, the redistribution of energy is uneven, leading at much smaller scales to some (randomly distributed) areas of extremely high values and many others with very little energy or velocity. In this way a very intermittent velocity field is formed.

This model of the spatial distribution of turbulent velocity fields can be extended to cloud fields. *Schertzer and Lovejoy* [1987], constructed the FIF model for clouds and rain, where the transport of liquid water content (ρ) by the turbulent velocity field leads to the formation of the same type of cascade for liquid water as exhibited by velocity. This cascade produces an inhomogeneous field that obeys a scaling law of a similar form to that respected by velocity [*Obukhov*, 1949]. Specifically, this is:

$$\Delta \rho(l) \propto \varphi . \lambda^{-H}, \tag{2.4}$$

where $\Delta \rho(l) = \rho(x + l) - \rho(x)$ and φ is some generic flux field of liquid water resulting from the non-linear interactions between velocity and liquid water content. This flux is a conserved field with respect to scale changes - that is, the ensemble mean $< \varphi >$ is constant with scale - and underlies the non-conserved liquid water fluctuations. The scalar parameter H is a measure of how much the non-conserved field varies from the conserved one. The exact form of φ and the value of H are dependent on the precise form of the equations governing the transport of liquid water by the velocity field. *Schertzer and Lovejoy* [1987] show that if liquid water field is transported by passive advection then $H = \frac{1}{3}$, but passive advection is not assumed *a priori* in this study because the assumption that (2.4) holds is more

16

general, and the field φ and the parameter H can be calculated from the aircraft liquid water data. For a positive value of H the observed field ρ is non-stationary, while the field φ is always stationary. This means that is often easier to deal with the flux field than use the density field directly.

The flux of liquid water φ can be calculated from the observable ρ by using a power-law filter, multiplying in Fourier space by $|\mathbf{k}|^{H}$ [*Schertzer and Lovejoy*, 1991], where **k** is the wavenumber. Alternatively, the field ρ can be produced from a known flux φ by filtering by $|\mathbf{k}|^{-H}$, also known as fractional integration [*Wilson et al.*, 1991], and this gives the model its name. This is further outlined in section 2.1.6.

2.1.2 Multifractal Statistics

The statistics of a multifractal field can be described by the formalism of the codimension [*Schertzer and Lovejoy*, 1992; *Mandelbrot*, 1991]. The codimension is used to define the statistics of the multifractal field in a scale independent manner. For any (normalised) multifractal field x_λ measured at the scale λ the codimension, $c(\gamma)$, is defined by the following relationship, in terms of the probability distribution:

$$\Pr(x_\lambda \geq \lambda^\gamma) \approx \lambda^{-c(\gamma)}, \qquad (2.5)$$

where γ can be any real number. Here the "$\approx$" symbol indicates equality up to a prefactor which is a function of γ. So $c(\gamma)$ is independent of scale and can be used to find the probability of obtaining x_λ greater than a threshold value. The codimension $c(\gamma)$ will vary depending on the exact multifractal dynamics that produce the field. However the universal FIF multifractal model that is used in this study argues that all multifractals fall into certain universality classes, whose codimension functions

17

are described in section 2.1.3. If the codimension $c(\gamma)$ is known then we have a statistical description of the multifractal.

Another useful statistic for a scale invariant field x_λ is the universal scaling exponent, $K(q)$, which is defined in terms of the scaling properties of the qth order statistical moment:

$$< x_\lambda^q >= \lambda^{K(q)}, \tag{2.6}$$

where the brackets $< . >$ indicate ensemble averaging. Note that the multifractal field x_λ must be normalised so that $< x_\lambda >= 1$. Like $c(\gamma)$ the function $K(q)$ is independent of scale. Also like $c(\gamma)$, the function $K(q)$ could theoretically be of almost any form, but the $K(q)$ of the universality classes of the FIF model is described in section 2.1.3. Thus there are two statistical functions describing the multifractal, one related to the scaling of the probability distribution, the other to the statistical moments. However the description using codimensions and the description using the universal scaling exponent are interchangeable because the functions $c(\gamma)$ and $K(q)$ are related by the Legendre transform [*Parisi and Frisch,* 1985]:

$$K(q) = \max_\gamma(q\gamma - c(\gamma)), \tag{2.7}$$

$$c(\gamma) = \max_q(q\gamma - K(q)). \tag{2.8}$$

The only restriction on the $c(\gamma)$ and $K(q)$ functions for multifractals is that they be convex functions (positive second derivative). Thus either one of these functions is sufficient to describe the fractal properties of a field, because one can be derived from the other.

Returning to the FIF model specifically, if a conserved flux φ is related to liquid water content ρ by (2.4), then it is possible to show [*Schertzer and Lovejoy,* 1991]

18

that their codimensions, $c_\varphi(\gamma_\varphi)$ and $c_\rho(\gamma_\rho)$, are identical, that is

$$c_\rho(\gamma_\rho) = c_\varphi(\gamma_\varphi).$$
(2.9)

The fluctuations in the observed field, $\Delta\rho$, also have the same codimension function but the related scaling exponent function $K_{\Delta\rho}(q)$ is modified by the parameter H according to equation (2.4) to give:

$$K_{\Delta\rho}(q) = K_\varphi(q) - qH.$$
(2.10)

Thus the statistical properties of the observed field are directly and relatively simply related to the those of the underlying flux. And because the flux field is stationary, it is often easier to work with than the non-stationary field ρ.

2.1.3   Universality classes

The functions $c(\gamma)$ and $K(q)$ would be sufficient to define the multifractal structure of cloud liquid water fields. However, the codimension and universal scaling exponent are continuous functions and hence could require an infinite number of parameters to describe accurately. Fortunately, *Schertzer and Lovejoy* [1987] demonstrate that stable, attractive multifractal processes exist and that the mixing of different multifractal processes (or the densification of a multifractal process) leads to these universality classes. As a result, according to the universal FIF model, all multifractal fields have conserved flux φ with the following codimension function and

universal exponents [*Schertzer and Lovejoy*, 1991]:

$$c(\gamma) = \begin{cases} C_1 \left(\frac{\gamma}{C_1 \alpha'} + \frac{1}{\alpha} \right)^{\alpha'} & \alpha \neq 1 \\ C_1 \exp \left(\frac{\gamma}{c_1} - 1 \right) & \alpha = 1 \end{cases} \qquad (2.11)$$

$$K(q) = \begin{cases} \frac{C_1}{\alpha - 1} \left(q^\alpha - q \right) & \alpha \neq 1 \\ C_1 q \ln q & \alpha = 1 \end{cases} \qquad (2.12)$$

with $\frac{1}{\alpha'} + \frac{1}{\alpha} = 1$. The two parameters in equations (2.11) and (2.12), C_1 and α, therefore fully define the statistics of the conserved flux in universal multifractal processes. The statistics of the field with non-conserved fluctuations can then be found using equations (2.9), (2.10) and the non-conservation parameter H. Hence there are three basic universal parameters required to describe any field in this scheme:

- C_1 is a measure of the mean inhomogeneity or intermittency, as it is the codimension of the mean field value. In the case of the conserved flux, it is the fixed point of $c(\gamma)$. A totally homogeneous field has $C_1 = 0$.

- α is a measure of the degree of multifracticality. This means that it determines the magnitude of the departures from the mean, and the radius of curvature of the codimension function. While C_1 is a measure of the sparseness of the mean process, α is a measure of how much the sparseness varies as you move away from the mean. A geometric fractal, or monofractal, has $\alpha = 0$.

- H is a measure of the departure from conservation of the fluctuations of the field, as described in the previous section. It also describes the degree of non-stationarity of the field. A stationary field has $H = 0$.

20

By varying these three independent parameters the FIF multifractal model can be used to describe or simulate a wide range of statistical behaviour. Examples of the functions $c(\gamma)$ and $K(q)$ for several different parameter values are shown in Figure 2.2a and Figure 2.2b respectively. The parameter values appropriate for cloud fields are determined from aircraft measurements of cloud liquid water in Chapter 3.

2.1.4 'Bare' and 'dressed' quantities and multifractal phase transitions

It must now be noted that the relationships for $c(\gamma)$ and $K(q)$, described by (2.11) and (2.12) respectively, are only seen to hold in observed data up to some critical value of γ or q, above which the behaviour of these functions becomes linear [e.g. *Tessier et al.*, 1993; *Chigirinskaya*, 1994]. This behaviour at extreme γ and q is known as Self Organised Criticality (SOC) and is described further in *Schertzer and Lovejoy* [1992] and *Bak et al.* [1987].

To explain the reason for this behaviour it is necessary to consider the consequences of how measurements of multifractal quantities are made, and to draw the distinction between "bare" and "dressed" quantities [*Schertzer and Lovejoy*, 1987]. The bare quantities are those that have been discussed so far - they are the result of a cascade process from large scales all the way down to the homogeneity scale. However, experimentally measured quantities generally have a resolution that is much coarser than the homogeneity scale of the atmosphere. Dressed multifractal quantities are defined as those quantities obtained by integrating, or averaging, over a completed cascade to produce a value at a lower resolution, corresponding to the way that experimental measurements are made. Both types of quantities have the
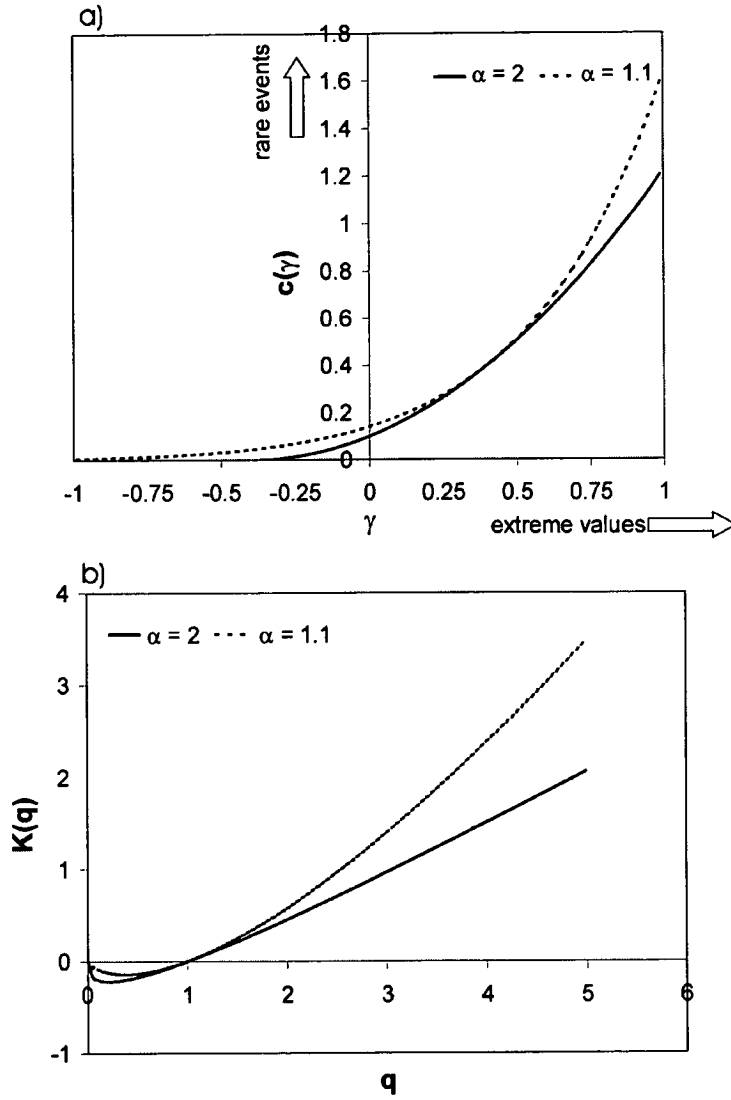
Figure 2.2: Examples of the functions: a) $c(\gamma)$ and b) $K(q)$, for two values of α and for $C_1 = 0.4$. Note that $K(q)$ must pass through the origin and $(1,0)$, and that $c(\gamma)$ has the fixed point (C_1, C_1).

22

same spatial statistics for low values of the exponents q (or γ), and for the universality classes of the FIF model, these are described by (2.11) and (2.12). But while the bare quantities follow these relationships for all values of q (or γ), the dressed quantities have a critical-order moment q_D (and corresponding $\gamma_D = \frac{dK}{dq}(q_D)$) above which the functions $K(q)$ are not well defined because the statistical moments diverge [*Schertzer et al.*, 1993]. For dressed quantities of dimension D, the critical value q_D is given by:

$$K(q_D) = (q_D - 1)D. \qquad (2.13)$$

However, for any particular measurement with a finite number of sampled points, the maximum value of q (or γ) for which $K(q)$ (or $c(\gamma)$) is well defined may be less than q_D and is determined by the number of samples as well as the dimension [*Schertzer and Lovejoy*, 1992]. In this case the critical order q_s below which the structure functions show the behaviour predicted by the FIF model (equation 2.12) is predicted to be [*Tessier et al.*, 1993]:

$$q_s = \left(\frac{D + D_s}{C_1}\right)^{1/\alpha},$$

where the sampling dimension D_s is given by $D_s = \log N_s / \log \lambda_s$. Here λ_s is the maximum scale ratio in the measurements (i.e. maximum length divided by length of smallest resolution) and N_s is the number of realisations measured. For example, if the data set were 5 aircraft flights measuring cloud properties at resolution of 100m for a total path of 100km per flight, then N_s would be 5, λ_s would be 1000 (=100km/100m) giving $D_s = 0.23$.

The maximum q below which measured values of the universal exponent $K(q)$ are well defined is therefore the smaller of q_D and q_s. The value of q_D represents a firm limit that is determined solely by the number of dimensions of the quantity,

while q_s is determined by the number of realisations sampled - this indicates that once the value of q_s exceeds q_D then any further increase in the number of samples studied will not enlarge the range of exponents for which information can be obtained.

So for dressed quantities such as integrated measurements, the function $K(q)$ (and $c(\gamma)$) does not conform to equation (2.12) when $q \geq \min(q_D, q_s)$, but is instead linear in q. This change in the behaviour of the statistics of a measured multifractal field at a critical exponent is labelled a "multifractal phase transition" [*Schertzer et al.*, 1993]. Examples will be seen in the statistics of in situ measurements of liquid water content that are examined in Chapter 3.

2.1.5   Double trace moment analysis

The method used in this work to determine the multifractal behaviour of cloud liquid water content is the Double Trace Moment (DTM) technique of *Lavallée et al.*[1993]. This method is summarised below for a one dimensional data series, such as the liquid water content measured from aircraft-mounted instruments. It can be used to test scaling and universality, and determines the parameters of the FIF model.

First consider the stationary flux field, φ. The flux can be determined from the measured liquid water content by power law filtering by k^H, i.e. fractional differentiation of order H. Although the dimensional analysis and passive scalar model [*Schertzer and Lovejoy*, 1987] predicts a value of $H = \frac{1}{3}$, as in (2.4), a value of H is not assumed here. Fortunately, *Lavallée et al.*[1991] demonstrated that a power-law filter of any order greater than H would produce the same results in the DTM technique. Therefore the procedure of *Tessier et al.*[1993] is followed

and differences are taken between the adjacent points in the data series, since this approximates the effect of multiplying by the wavenumber k in Fourier space. This will produce the correct results as long as H is less than 1. If the resolution of the sensor is at scale λ', then the "pseudo-flux", $\varphi_{\lambda'}$, at point x is given by

$$\varphi_{\lambda'}(x) = |\rho(x + \Delta x_{\lambda'}) - \rho(x)| \tag{2.14}$$

where $\Delta x_{\lambda'}$ is the distance between adjacent points at resolution λ' ($\Delta x_{\lambda'} = L_{\max}/\lambda'$). The flux is then raised to a exponent, η, and integrated to give a field at a lower resolution λ. This field is labelled the "η-flux" $\Pi_\lambda^{(\eta)}$ and is given by:

$$\Pi_\lambda^{(\eta)}(x_i) = \int_{x_i}^{x_i + \Delta x_\lambda} [\varphi_{\lambda'}(x')]^\eta dx', \tag{2.15}$$

with $x_{i+1} = x_i + \Delta x_\lambda$, $i = 1, 2, ..., \lambda$, and Δx_λ is the distance between adjacent points at resolution λ ($\Delta x_\lambda = L_{\max}/\lambda$). The double trace moment of the field at the scale λ is then found by raising $\Pi_\lambda^{(\eta)}(x)$ to a second exponent (q), summing over the entire range (i.e. summing over all x_i) and then taking the ensemble average, i.e.

$$Tr_\lambda(\varphi_{\lambda'}^\eta)^q = \left\langle \sum_i^\lambda [\Pi_\lambda^{(\eta)}(x_i)]^q \right\rangle \tag{2.16}$$

with an independent second exponent, q, being used. This process is repeated for various values of exponents η and q, and for a range of scales λ (all lower resolutions than λ'). If the process modelled is scale invariant then [*Tessier et al.*, 1993]:

$$Tr_\lambda(\varphi_{\lambda'}^\eta)^q \propto \lambda^{K(q,\eta)-(q-1)}, \tag{2.17}$$

where the double exponent $K(q,\eta)$ has been introduced. When $\eta = 1$ the usual scaling exponent is retrieved i.e. $K(q,1) = K(q)$. When this process is applied to

a universal (FIF) multifractal the following holds [*Lavallée et al.,* 1993]:

$$K(q, \eta) = \eta^{\alpha} K(q).$$

<div align="right">(2.18)</div>

Therefore a graph of $\log K(q, \eta)$ versus $\log \eta$ for a range of values of η should produce a linear relationship, the slope of which is α. The intercept of the line is $\log K(q)$ and hence, with a known α, the parameter C_1 can be found using equation (2.12). This can be done for various values of q to improve the accuracy of the parameter derivation.

It should be noted here that when considering dressed multifractal fields, such as measurements with resolution above the homogeneity scale, the double exponent $K(q, \eta)$ is affected by undersampling problems at high values of q or η. This means that like $K(q)$, the double exponent has critical order values above which it is not well defined and observations will not follow the relation (2.18). This problem should occur when the value of $\max(q\eta, \eta)$ is greater than $\min(q_s, q_D)$, where q_s and q_D are the critical exponents defined in the previous section. As long as only values of η lower than this are considered, then the relation (2.18) holds and can be used to find the parameters α and C_1.

With α and C_1 estimated, the parameter H can then be found from the energy spectrum, $E(k)$, defined by

$$E(k) = \frac{1}{2} \left\langle |\tilde{\rho}(k)|^2 + |\tilde{\rho}(-k)|^2 \right\rangle,$$

<div align="right">(2.19)</div>

where k is the wavenumber and $\tilde{\rho}(k)$ is the Fourier transform of the liquid water content, ρ. If the energy spectrum follows a power law with $E(k) \propto k^{-\beta}$, then the scaling exponent β is obtained from the slope of a log-log graph. The scaling

exponent, β, is related to the parameter H by [*Lovejoy and Schertzer*, 1995b]:

$$\beta = 1 - K(2) + 2H,$$

and hence substituting from equation (2.12) for $K(2)$ and rearranging, the following expression for H is obtained:

$$H = \frac{\beta - 1}{2} + \frac{C_1(2^\alpha - 2)}{2(\alpha - 1)}. \tag{2.20}$$

In this manner all three of the parameters of the FIF model can be estimated using this technique.

2.1.6 Numerical simulation of multifractal fields

In order to use multifractal clouds in radiative transfer calculations, a method of numerically generating FIF multifractal fields is required. The generation technique used here is the "continuous cascade" method developed by *Pecknold et al.* [1993], and it is summarised below. In this method the Fourier space techniques are used to generate a multifractal field at any scale.

As described in section 2.1.1, a multifractal cloud liquid water field ρ_λ at scale λ can be generated from the stationary (multifractal) flux field φ_λ using Fourier filtering. The question is then how to generate a stationary multifractal field such as φ_λ. To determine the stochastic generation process, first we consider the properties of the multifractal field φ_λ and then find a random generation process that produces fields with these properties.

The basic properties of the stationary multifractal field are: the statistics given by the codimension $(c(\gamma))$ and universal exponent function $(K(q))$ described in

section 2.1.2; scale invariance; the multiplicative nature of the cascade process, as was described by equation (2.1) and shown in Figure 2.1. Scale invariance and the multiplicative nature of the cascade combine to give the following relationship between the field values at the same point but at two different scales:

$$\varphi_{\lambda\lambda'} = \varphi_\lambda \varphi_{\lambda'} \tag{2.21}$$

where λ and λ' are two spatial scales, so that $\lambda\lambda'$ is a third scale at higher resolution than either of the two. Equation (2.21) is a result of scale invariance - it is saying that zooming in from scale λ to scale $\lambda\lambda'$ is the same as going from the top scale ($\lambda = 1$) to λ'.

Since it is often easier to deal with additive properties than multiplicative ones, it is convenient to introduce the generators Γ_λ of the multifractal field φ_λ such that at each point

$$\varphi_\lambda = \exp(\Gamma_\lambda). \tag{2.22}$$

Determining the generators Γ_λ is then sufficient to find the field φ_λ - so the goal is now to find generators Γ_λ that satisfy all the known properties of the multifractal field. The multiplicative property of the field, (2.21), becomes an additive property of the generators so that

$$\Gamma_{\lambda\lambda'} = \Gamma_{\lambda'} + \Gamma_\lambda \tag{2.23}$$

If the field is normalised so that $< \varphi_\lambda >= 1$ then the definition of the universal exponent function $K(q)$, given by equation (2.6), gives

$$\langle \exp(q\Gamma_\lambda) \rangle = \langle \varphi_\lambda^q \rangle = \lambda^{K(q)}. \tag{2.24}$$

If a new function $K_\lambda(q)$ is defined by $K_\lambda(q) = K(q)\ln(\lambda)$, then equation (2.24)

gives

$$\exp(K_\lambda(q)) = \lambda^{K(q)} = < \exp(q\Gamma_\lambda) > . \tag{2.25}$$

This means that the function $K_\lambda(q)$ describes how the statistical moments vary with λ and is the 2nd Laplace characteristic function of the generator Γ_λ i.e. the logarithm of the Laplace transform of the probability density [*Schertzer and Lovejoy, 1991*]. From this it is possible to determine all the properties required for the generators Γ_λ and these are [*Pecknold et al., 1993*]:

1. The set of generators must be stable under addition so that equation (2.23) always holds, i.e. the random number distribution must be such that the addition of numbers drawn from the distribution produces the same distribution.

2. In order to be certain that the structure functions are finite (and $K(q)$ is well defined) the probability distribution of the generator must fall off faster than exponentially for positive Γ_λ, as can be shown from (2.24) [*Schertzer and Lovejoy, 1991*].

3. From equation (2.25), the Fourier spectrum of Γ_λ must fall off as the inverse of the wavenumber k in order to obtain a $K_\lambda(q)$ that scales as $\ln \lambda$, and hence to produce a $K(q)$ independent of λ [*Pecknold et al., 1993*].

4. If Λ is the highest resolution then the generator field Γ_Λ must be band limited to between $[1, \Lambda]$, since there should be no variations in the field at resolutions higher than Λ.

5. The field should be normalised so that $K(1) = 0$ to maintain conservation of the field i.e. so that $< \varphi_\lambda > = 1$ for all λ.

So to determine the generators Γ, the problem is then: what type of random number distribution will fit these 5 criteria? Lévy distributions are the only stable, attractive classes of random variables under addition [*Feller*, 1971], and hence the only set of distributions that satisfy the first criterion. Lévy variables are defined as the limits of the normalised sum of independent random vectors, i.e. a Lévy variable S is

$$S = \lim_{n \to \infty} \frac{x_1 + x_2 + \ldots. + x_n}{n^{1/\alpha}} \qquad (2.26)$$

where x_i are independent random variables in $\Re$, and α is the Lévy parameter $(0 \le \alpha \le 2)$. To satisfy the second condition listed above we must choose only an extremal asymmetric Lévy distribution for the generators, that is one that has significantly more large negative values than large positive values, so that $\langle \varphi_\lambda^q \rangle$ is finite for all q after exponentiation of the generators. A random value from an extremal Lévy distribution can be calculated using the following expression [*Chambers et al.*, 1976]:

$$S(\alpha) = \begin{cases} \frac{\sin \alpha.(\Phi - \Phi_0)}{(\cos \Phi)^{1/\alpha}} \left(\frac{\cos(\Phi - \alpha(\Phi - \Phi_0))}{W} \right)^{(1-\alpha)/\alpha} & \alpha \ne 1 \\ \frac{2}{\pi} \left(\left(\frac{\pi}{2} - \Phi \right) \tan \Phi + \ln \left(\frac{\pi W \cos \Phi}{\pi - 2\Phi} \right) \right) & \alpha = 1 \end{cases} \qquad (2.27)$$

where $\Phi_0 = \frac{\pi}{2}(1 - |1 - \alpha|)/\alpha$, Φ is a random value drawn from a uniform distribution on $(-\frac{\pi}{2}, \frac{\pi}{2})$, and W is a random value drawn from an exponential distribution $(\Pr(W) = e^{-W})$. The random deviates Φ and W are mutually independent.

So to satisfy the first two criteria the asymmetric Lévy variables are used. Using the relation (2.27) a single independent value $S(\alpha)$ is randomly generated from the Lévy distribution for each point in the field at the finest scale Λ. To obtain the correct statistics for the multifractal field, as given by (2.11) and (2.12), each of the variables $S(\alpha, x)$ is multiplied by $\left(\frac{C_1}{\alpha - 1} \right)^{1/\alpha}$ [*Wilson et al.*, 1991]. The conditions 3 and 4 are then satisfied by Fourier filtering. The first step in doing this numerically

30

is to apply a fast Fourier transform (FFT) to the field of random Lévy variables. The k^{-1} behaviour of the Fourier spectrum demanded by condition 3 is achieved by multiplying the resulting Fourier spectrum by $|\mathbf{k}|^{-\frac{d}{\alpha'}}$ [*Pecknold et al.*, 1993], where d is the number of dimensions of the field being generated. The fourth condition is satisfied by filtering out any of the spectrum outside of the desired range of $[1, \Lambda]$, i.e. multiply by the function $f(\mathbf{k}, \Lambda)$ which is 1 for $|\mathbf{k}| \leq \Lambda$ and decays exponentially for $|\mathbf{k}| > \Lambda$. The exponential decay is used instead of a sharp cutoff to zero because sharp cutoffs cause sinusoidal 'ringing' effects when transformed back to real space. Finally the difference between the FFT and the continuous Fourier transform is taken into account by multiplying by the following factor [*Pecknold et al.*, 1993]

$$\kappa_d(\Lambda) = \frac{\int_1^\Lambda k^{-d} d\mathbf{k}}{\sum_1^\Lambda \frac{1}{k^d}}. \tag{2.28}$$

This gives a final expression for the field of generators of

$$\Gamma_\Lambda = \mathcal{F}^{-1}\left(\left(\frac{C_1}{\alpha-1}\right)^{1/\alpha} \tilde{S}(\alpha, k) |\mathbf{k}|^{-\frac{d}{\alpha'}} f(\mathbf{k}, \Lambda)\kappa_d(\Lambda)\right), \tag{2.29}$$

where $\tilde{S}(\alpha, k)$ is the Fourier transform of the field of random Lévy variables, and $\mathcal{F}^{-1}$ is the inverse Fourier transform function. The multifractal field, φ_Λ, is then found by taking the exponential of the generators Γ_Λ, according to (2.22). The fifth and final criterion is then satisfied by dividing this field by the expectation value $\Lambda^{C_1/(\alpha-1)}$ to normalise φ_Λ. Some examples of simulated fields φ_Λ generated in this manner are shown in Figure 2.3. Part a) of the figure shows three versions of φ_Λ, generated using different values of α but leaving C_1 constant, with the same seed used in the random number generator to show the effect of varying α. Figure 2.3b on the other hand shows three curves generated with the same α but different values of the parameter C_1. Note that the Levy parameter α used in the simulation of

31
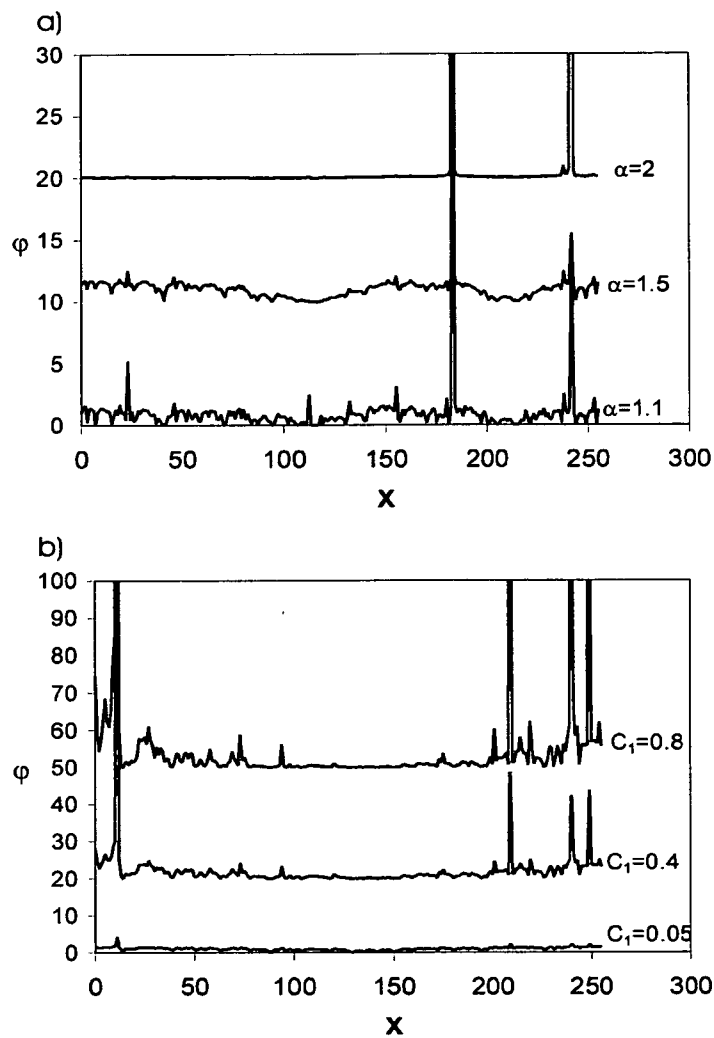
Figure 2.3: Randomly generated 1D flux fields φ_Λ at a scale of $\Lambda = 256$. a) shows the effect of changing the value of α. C_1 is held constant at 0.1 b) shows the effect of changing C_1 when $\alpha = 1.5$. In both plots the 3 fields are linearly offset for ease of viewing, and the same seed is used in the random number generator for all 3.

32

the field and the multifractal parameter α are the same quantity, i.e. multifractals generated using this method have a multifracticality parameter α equal to the Lévy parameter used in their generation.

Generating the non-stationary field
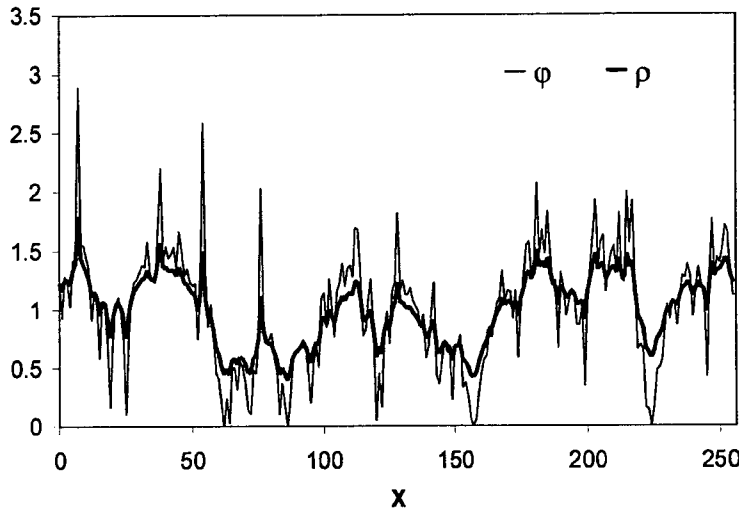
Figure 2.4: A numerically generated flux φ_Λ in one-dimension, and the field ρ_Λ that results from fractionally integrating the flux with $H = 0.3$. Both fields are normalised so that the mean is one. Parameters are $\alpha = 1.5$, $C_1 = 0.1$ and $\Lambda = 256$.

The non-stationary liquid water content field ρ is related to the stationary flux field φ by equation (2.4). This relationship shows that if the non-stationarity parameter H were equal to 1, then ρ could be found by integrating the field φ. But since H could be any real number, ρ must be found by a process known as fractional integration of the flux field φ. This process involves taking the Fourier transform of φ, multiplying the field by the factor $|k|^{-H}$, where k is the wavenumber, and
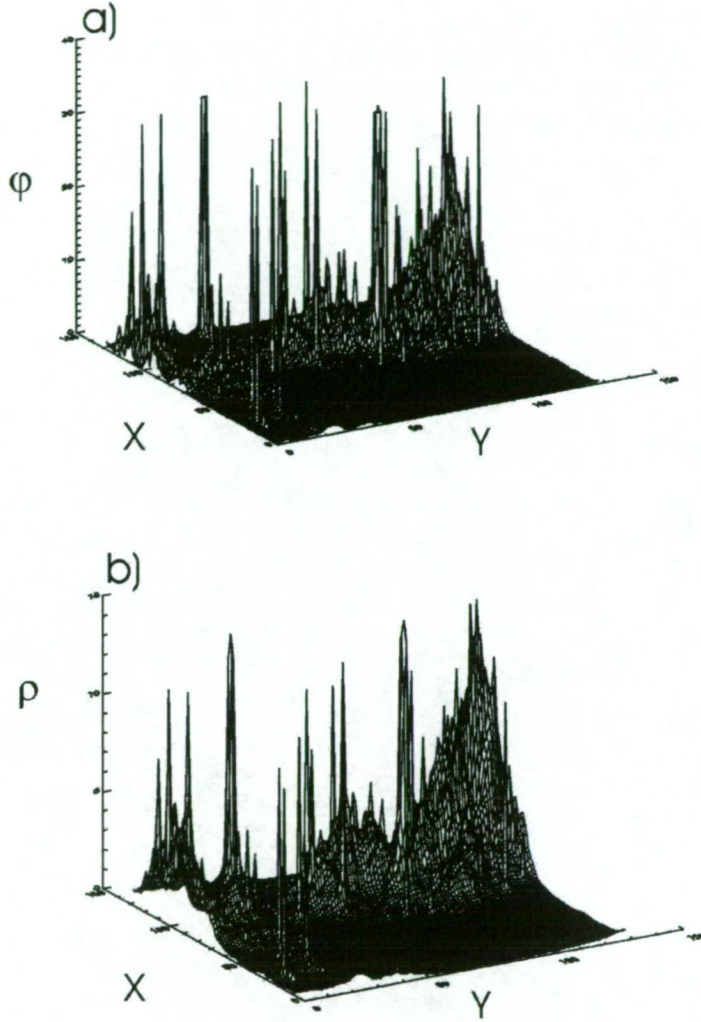
Figure 2.5: Examples of 2d multifractal generation with scale $\Lambda = 128$, $\alpha = 1.5$, $C_1 = 0.1$. a) shows the flux field φ and b) shows the fractionally integrated field ρ. Both are normalised so that the mean is 1. The coordinates are specified as grid-point number, absolute length is not yet specified.

34

then taking the inverse transform, that is

$$\rho = \mathcal{F}^{-1}\left(\tilde{\varphi}(\mathbf{k})\,|\mathbf{k}|^{-H}\right),\qquad(2.30)$$

where $\tilde{\varphi}(\mathbf{k})$ is the Fourier transform of the field of random Lévy variables, and $\mathcal{F}^{-1}$ is the inverse Fourier transform function. This is known as fractional integration because if H is a positive integer then the result is the same as integrating the field H times. This process allows the liquid water content field to be simulated at any scale Λ by fractionally integrating the flux field, φ_Λ, numerically generated as described above. The final step in generating the liquid water content field is to multiply ρ by the desired mean of the entire field (since the mean of the field generated by the process so far is one). An example of the one dimensional simulated field φ_Λ and the resulting ρ_Λ are shown in Figure 2.4 for $\Lambda = 256$ and $H = 0.3$. Note that the general effect of the fractional integration from φ_Λ to ρ_Λ is a smoothing of the field. Figure 2.5 shows the same results for an example value of a two dimensional flux field φ_Λ and the resulting ρ_Λ with $\Lambda = 256$ and $H = 0.3$. It will be seen in section 3.2 that these simulated fields closely reflect the statistics of cloud liquid water.

A summary of all the steps taken in generating the multifractal liquid water content field is shown in flow diagram form in Figure 2.6.

2.2 Monte Carlo Radiative Transfer

The Monte Carlo radiative transfer technique is probably the most straightforward method to find the radiative properties of inhomogeneous media such as cloud fields. It involves the direct simulation of the process of radiation propagation

Generate S(x,α)

This stage generates a random Levy variable at each point in the field at the highest resolution Λ, using equation 2.27. The variable x is the position, and α is the fractal parameter chosen for the field.

Fourier transform
$$\tilde{S}(k,\alpha) = F(S(x,\alpha))$$

This stage takes a Fast FourierTransform F(), of the field S(x,α). The result is the field $\tilde{S}(k,\alpha)$, where k is the wavenumber

$$\tilde{\Gamma}_\Lambda(k) = \left(\frac{C_1}{\alpha-1}\right)^{1/\alpha} \tilde{S}(k,\alpha)|k|^{-\frac{d}{\alpha}}$$

The Fourier transform of the generators Γ_Λ is found by applying the power law factor $|k|^{-d/\alpha}$, where d is the no. of dimensions of the field, and the normalisation factor $\left(\frac{C_1}{\alpha-1}\right)^{1/\alpha}$

Inverse transform
$$\Gamma_\Lambda(x) = F^{-1}(\tilde{\Gamma}_\Lambda(k).\kappa_d(\Lambda))$$

The inverse Fourier Transform F^{-1} is then applied to the field, with the factor κ_d being a correction for the use of a FFT rather than a continuous Fourier transform, as given by equation 2.28

$$\varphi_\Lambda(x) = \exp(\Gamma_\Lambda(x))$$

The stationary multifractal field φ_Λ is then found by taking the exponent of the generator field Γ_Λ

Fourier filter
$$\rho_\Lambda(x) = F^{-1}\left(|k|^{-H} F(\varphi_\Lambda)\kappa_d\right)$$

A non-stationary multifractal field is then found using a Fourier Filter of $|k|^{-H}$ on the stationary field φ_Λ, where H is the chosen non-stationarity parameter.

Figure 2.6: Flow chart summarising numerical generation of multifractals.

- a large number of photons are traced through the media in question as they are scattered or absorbed. The main drawback of the Monte Carlo method is the relatively large amount of computer time necessary to trace a statistically significant number of photons through the system in order to get reasonably accurate results. A thorough description of the Monte Carlo method in radiative transfer and its various applications can be found in *Marchuk et al.* [1980]. In this section the basic technique used throughout this study to determine cloud radiative properties is outlined.

In this work the forward simulation method is used. This means that the photons are traced from the time they enter the system until they leave or are absorbed, as opposed to a backwards Monte Carlo method where photons are traced in reverse out from a fixed detector until they reach a light source. In this case the system in question is either a column of the atmosphere containing a cloudy layer, or simply the cloudy region alone. Both will be used later in this thesis, when the exact geometries used for different applications will be specified.

2.2.1 Photon tracing

The photons are defined by a position within the system, described by the position vector $\mathbf{x} = \{x, y, z\}$, and direction of propagation, specified by the vector $\Omega = \{a, b, c\}$ which is normalised so that its modulus equals one. In order to simulate the possibility of absorption, each photon is also given a weight W that represents the probability that it has not been absorbed during its motions through the system. The photons enter at the top surface of the system at a (uniformly distributed) random position in a direction determined by the position of the sun. Obviously $W = 1$ when the photon enters the system. The following steps are then

used to trace each photon through the system:

1. The free path length l that the photon travels before the next collision is determined (see section 2.2.2).

2. The possibility of the photon leaving the system is considered. If the photon encounters the top or bottom of the system before travelling a distance l, the current weight W is added to the total of the photons leaving the system, and the simulation of this photon is finished. Exiting photons are binned by exit position, exit direction, total path length travelled and number of scattering events before leaving. The horizontal boundaries are considered periodic, so that if they are encountered the photon reappears at the opposite side of the system at the same height.

3. If the photon has not escaped, the position of the next collision are calculated using the transforms $x \rightarrow x + al$, $y \rightarrow y + bl$, $z \rightarrow z + cl$.

4. The chance of absorption is taken into account. The probability that the photon is scattered at a collision event is the single-scattering albedo, ω, of the medium, so the chance of absorption rather than scattering is $(1 - \omega)$. The weighting, W, of the photon is reduced to $W\omega$, and the remainder of the weight, $W(1 - \omega)$, is added to the total absorption in the medium.

5. The direction of the photon after the collision is determined from the phase function of the scattering medium. The phase function, $P(\theta)$, is the probability density of having a scattering angle θ between the incoming direction and outgoing direction of the photon at the collision. The cumulative probability

PP of a photon being scattered between 0 and θ is then

$$PP(\theta) = \int_0^\theta P(\theta')d\theta' \tag{2.31}$$

A uniform random number is chosen on $[0,1]$ and $PP(\theta)$ is set to this number. Equation (2.31) is then solved numerically to give the upper limit θ, the scattering angle. The azimuth angle, ϕ, of the scattering is then randomly chosen from a uniform distribution on $[0, 2\pi]$. If $\mu = \cos\theta$ then the direction of the photon after the collision is found using the transforms:

$$a \rightarrow a\mu - (b\sin\phi + ac\cos\phi)\left[(1 - \mu^2) \div (1 - c^2)\right]^{1/2} \tag{2.32}$$

$$b \rightarrow a\mu - (a\sin\phi + bc\cos\phi)\left[(1 - \mu^2) \div (1 - c^2)\right]^{1/2} \tag{2.33}$$

$$c \rightarrow c\mu - (1 - c^2)\cos\phi\left[(1 - \mu^2) \div (1 - c^2)\right]^{1/2} \tag{2.34}$$

6. With the new direction, position and weight, return to step 1.

This process is repeated for all of the photons considered. After all the photons have been traced until they exit the system, the sum of weights that have been binned as passing out the top of the system, passing out the bottom of the system, or being absorbed, are used to calculate the reflectance, transmittance or absorptance of the system respectively. Radiance distributions can also be found for the transmitted or reflected radiation from the binned photons exiting the system. These quantities are calculated for the whole system but also for separate grid-squares within the system so that the radiative properties at different spatial scales can be examined.

2.2.2 Maximal Cross-section method for finding free-path length

The only step not fully detailed in the previous section was the method of determining the path length l of the photon before a collision occurs. If the radiance of a beam of radiation in a particular direction is initially I_0, then after a distance l the radiance in the beam is

$$I = I_0 \exp(- \int_0^l \beta_{ext}(\mathbf{x}) dx). \qquad (2.35)$$

where $\beta_{ext}(x)$ is the volume extinction coefficient in the medium at the position $\mathbf{x}$ and is defined as the rate of extinction of a beam of radiation per unit length (with units of m^{-1}). The exponent in (2.35) is the optical depth τ along this particular path, that is

$$\tau = \int_0^l \beta_{ext}(\mathbf{x}) dx = - \ln \frac{I}{I_0} \qquad (2.36)$$

The optical depth is therefore dimensionless. The probability of a photon having a collision in distance l is then $PR = \frac{I}{I_0}$. The simplest way to randomly generate a free path length l for a particular photon is therefore to generate a random PR using a uniform distribution on $(0, 1)$. This is then used to give a random value of τ using the expression $\tau = - \ln PR$. The equation (2.36) is then solved for the free path length l. However this method can be difficult, or at least very time consuming, if the function β_{ext} is complicated, such as a multifractal field on a high spatial resolution grid. Even though the field β_{ext} is known, to solve (2.36) for l in a multifractal field it is generally necessary to accumulate optical depth grid-square by grid-square, and then linearly interpolate in the last grid-square.

Therefore in this study we use the maximal cross-section method used by *Mar-*

40

shak et al. [1995] and *Marchuk et al.* [1980]. This method involves transforming the integral radiative transfer equation [*Marshak et al., 1995*]

$$\mathbf{\Omega} \cdot \nabla I + \beta_{ext}(\mathbf{x})I(\mathbf{x}, \mathbf{\Omega}) = \omega\beta_{ext} \int I(\mathbf{x}, \mathbf{\Omega}')P(\mathbf{\Omega} \cdot \mathbf{\Omega}')d\mathbf{\Omega}' \qquad (2.37)$$

where $\mathbf{I}(\mathbf{x}, \mathbf{\Omega})$ is the radiance at position $\mathbf{x}$ and in direction $\mathbf{\Omega}$, and P is the phase function. The first term on the left of equation (2.37) is the gradient of the intensity field, the second term represents the extinction of the intensity already travelling in the direction $\mathbf{\Omega}$, and the term on the right of equation (2.37) is the scattering source function. Equation (2.37) can be manipulated to give

$$\mathbf{\Omega} \cdot \nabla I + \beta_{\max}I(\mathbf{x}, \mathbf{\Omega}) = \beta_{\max} \int \left[\frac{\beta_{ext}(\mathbf{x})}{\beta_{\max}}\omega P(\mathbf{\Omega} \cdot \mathbf{\Omega}') + \left(1 - \frac{\beta_{ext}(\mathbf{x})}{\beta_{\max}}\right) \delta(\mathbf{\Omega} - \mathbf{\Omega}')\right] I(\mathbf{x}, \mathbf{\Omega}')d\mathbf{\Omega}',$$
$$(2.38)$$

where $\beta_{\max} = \max_{\mathbf{x}} \beta_{ext}(\mathbf{x})$. Equation (2.38) can be interpreted as the radiative transfer equation for a fictitious medium in which $\beta_{\max}$ is the constant extinction coefficient throughout the medium, and the phase function at any point is a combination of:

- $\omega P(\mathbf{\Omega} \cdot \mathbf{\Omega}')$, which occurs with a probability of $\frac{\beta_{ext}(\mathbf{x})}{\beta_{\max}}$ (physical scattering)

- $\delta(\mathbf{\Omega} - \mathbf{\Omega}')$, which occurs with a probability of $1 - \frac{\beta_{ext}(\mathbf{x})}{\beta_{\max}}$. ("mathematical scattering")

The first part of this modified phase function represents the physical scattering. The second part is purely a mathematical construct since the photon always goes in the same direction after it "scatters", because the delta function, $\delta(\mathbf{\Omega} - \mathbf{\Omega}')$, is only non-zero when $\mathbf{\Omega} = \mathbf{\Omega}'$. The true path length l in the real medium is then found by tracing the photon through this fictitious medium (using the simple method

of solving (2.36) for the path length since the extinction coefficient is constant) until a collision occurs in which there is physical scattering rather than "mathematical scattering". Which type of collision occurs is randomly determined by the probability $\frac{\beta_{ext}(\mathbf{x})}{\beta_{\max}}$ of physical scattering.

In summary, the following steps are followed to find the path length l in the (real) medium:

1. Calculate the optical depth covered in the fictitious medium before scattering using $\tau = -\ln PR$, where PR is a random number from a uniform distribution on (0,1).

2. The distance travelled is $l' = \tau \div \beta_{\max}$, since the fictitious medium has constant volume extinction coefficient $\beta_{\max}$.

3. Determine whether scattering at this point is physical or mathematical, using a uniform random number R between 0 and 1. If $R \leq \frac{\beta_{ext}(\mathbf{x})}{\beta_{\max}}$ then the scattering is physical, if $R > \frac{\beta_{ext}(\mathbf{x})}{\beta_{\max}}$ then the scattering is purely mathematical and the photon continues straight ahead.

4. If the scattering is purely mathematical then return to step 1 and repeat the process, if the scattering is physical then the process stops and the path length in the real medium l is the sum of the values of l' since the last physical scattering.

This value of l is then used in the Monte Carlo algorithm described in the previous section (i.e. section 2.2.1). The advantage of this method of calculating l is that it makes the calculation time almost insensitive to the size of cloud grid used or the variability of the cloud field [*Marshak et al.*, 1995]. It is of no advantage for

calculations in homogeneous cloud fields, but it is much faster for radiative transfer in multifractal clouds at small grid sizes.

2.2.3 Cloud properties

While the cloud properties used in the Monte Carlo simulations throughout this study will vary, it is possible to make some general comments about them here. Throughout this work the inhomogeneity in clouds is assumed to be solely due to variations in the number density of cloud droplets, not in the size of cloud droplets. Therefore the liquid water content varies but the droplet size distribution is constant throughout the cloud. In terms of optical properties this means that the scattering phase function and single-scattering albedo are constant throughout the cloud but the volume extinction coefficient β_{ext} varies in space. Although in some cases completely homogeneous clouds will be used in calculations for the sake of comparison, more often the focus will be on clouds whose liquid water content is multifractal and generated as was described section 2.1.6. The exact geometry and dimensions of the clouds will be specified later as they vary with the different applications. The resolution of the multifractal cloud is generally 25 m, meaning that the cloud is generated in a grid of cubes that are 25 m x 25 m x 25 m. The scale parameter λ will then be given by

$$\lambda = \frac{L_{\max}}{25m},$$
(2.39)

where $L_{\max}$ is the total side length of the cloud field. Within the grid-cubes the clouds are assumed to be homogeneous. Although this assumption of small scale homogeneity is unrealistic, it has been shown that variations at or below the scale of the photon mean free-path have very little effect on the radiative properties of

clouds [*Marshak et al.*, 1998; *Cahalan*, 1989]. This mean free-path length in liquid water clouds varies with the cloud properties but is on the order of 50 m [*Marshak et al.*, 1998].

If the cloud liquid water content allocated to grid-cube by the multifractal generation method is ρ, then it can be related to the optical properties in the following manner. The cloud liquid water content (in units of gm^{-3}) at any point is related to the droplet size distribution by

$$\rho = DN \int_0^\infty \frac{4}{3}\pi r^3 n(r).dr, \qquad (2.40)$$

where D is the density of water (in gm^{-3}), N is the total droplet number concentration (units of m^{-3}) and $n(r)$ is the (normalised) probability of the droplet radius being between r and $r + \Delta r$, for infinitesimal Δr. On the other hand, the volume extinction coefficient is given by

$$\beta_{ext} = N \int_0^\infty Q_{ext} n(r).\pi r^2 dr \qquad (2.41)$$

where the extinction efficiency factor Q_{ext} is defined as the ratio between the extinction cross-section of a particle and its geometric cross-section and is given by the Mie scattering formula for spherical droplets [*e.g. Goody and Yung*, 1989]. Combining the two relationships (2.40) and (2.41), it can be shown that

$$\beta_{ext} = \frac{3\bar{Q}\rho}{4D r_{eff}} \qquad (2.42)$$

where $\bar{Q}$ is the mean extinction efficiency factor, given by $\bar{Q} = \int_0^\infty Q_{ext}n(r)r^2 dr \div$

44

$\int_0^\infty n(r)r^2 dr$, and r_{eff} is the effective cloud droplet radius defined by:

$$r_{eff} = \frac{\int_0^\infty n(r)r^3 dr}{\int_0^\infty n(r)r^2 dr}. \tag{2.43}$$

For the UV and visible wavelengths where the droplet radius tends to be significantly larger than the wavelength, Q_{ext} and therefore $\bar{Q}$ is very close to 2 [*Stephens*, 1976]. For other wavelengths, the Mie scattering formulae can be used to find $\bar{Q}$ for the droplet radius distribution in question, as well as the other single-scattering properties such as the phase function and single-scattering albedo. However *Hu and Stamnes* [1993] demonstrated that the single scattering properties of clouds varied with changing effective radius but did not vary much between different shaped radius distributions with the same r_{eff}. In the same work, parameterisations of some of these single scattering properties were developed as functions of r_{eff} and wavelength, and these are used here to find $\bar{Q}$ and other single scattering properties. Therefore if r_{eff} is chosen, the multifractal liquid water content field can be used in (2.42) to give β_{ext} for each grid-cube. Generally a value of approximately 10 μm will be taken, since this is typical for low level liquid water content clouds [*Han et al.*, 1994], but this is varied in some cases.

Apart from β_{ext}, the other properties required for the Monte Carlo model are the single-scattering albedo ω and the phase function $P(\theta)$. The parameterisation of *Hu and Stamnes* [1993] give the ω and the asymmetry factor g for each r_{eff} (at each wavelength). The asymmetry factor is defined in terms of the phase function:

$$g = \int_0^\pi P(\theta) \cos\theta d\theta, \tag{2.44}$$

and determines the relative ratios of forward to backward scattering of radiation from the droplets: $g = 1$ represents forward scattering only, $g = -1$ backwards

only and $g = 0$ represents perfectly isotropic scattering. For visible wavelengths and typical r_{eff} values the asymmetry factor of liquid water clouds is approximately 0.85, indicating strong forward scattering. With the known asymmetry factor, the Henyey-Greenstein phase function $P_{HG}(\theta, g)$ is used in the Monte Carlo radiative transfer - it is given by

$$P_{HG}(\theta, g) = \frac{1 - g^2}{(1 + g^2 - 2g\cos\theta)^{3/2}}.$$ (2.45)

This phase function, as opposed to a phase function constructed from the Mie scattering theory and typical droplet size distribution, was chosen in order to allow the phase function to be easily varied to test the effect of changing scattering properties on cloud radiative transfer.

Therefore a known liquid water field ρ and a chosen r_{eff} can be used to calculate all the optical properties required for the Monte Carlo radiative transfer simulations. In this manner the multifractal model of cloud liquid water content and the Monte Carlo radiative transfer model are combined to determine the solar radiation field in clouds.

2.2.4 Whole atmosphere calculations

If we are performing radiation calculations for the whole atmosphere rather than just the cloud, as is done in section 6.2, the scattering properties need to be adjusted for non-cloud attenuation, such as Rayleigh scattering, aerosol or molecular absorption (see *Goody and Young* [1989], *Paltridge and Platt* [1976], or *Chandrasekhar* [1950] for more details on these types of extinction). The model is modified by replacing the cloud volume extinction coefficient in each grid square by the sum of the individual volume extinction coefficients for all attenuating species. The phase

function in each grid square is then the weighted average of the phase functions, with the weighting for each species being given by the value of β_{ext} for that species. Similarly, the single-scattering albedo for each grid-square is the weighted average over all the species, with each value of ω being weighted by the value of β_{ext} for that species. Finally, surface reflectance can be taken into account by including the chance of the photons being reflected from the lower surface of the system (instead of passing out of the system), with the probability of reflection being given by the ground albedo at that wavelength.

Chapter 3

Analysis of in situ measurements of liquid water content

3.1 Introduction

In this chapter the spatial distribution of cloud liquid water content is examined, using the framework of the FIF multifractal model to analyse aircraft measurements. As outlined in Chapter 1, fitting the FIF multifractal model to in situ data forms the basis of this thesis, since it is this knowledge of the spatial statistics of low- and mid-level liquid water clouds that allows the analysis of radiative properties that follows in subsequent chapters. One question of interest here is how the in situ data compares with the remote sensing studies of cloud fields [e.g. *Lovejoy et al.*, 2001b; *Tessier et al.*, 1993] that have found different FIF parameters. Apart from finding the parameters of the FIF model for use in radiative studies, the other goals of this chapter include extending multifractal analysis of in situ data from the marine stratocumulus type concentrated on in previous studies [e.g. *Marshak*

48

et al, 1997; *Davis et al.*, 1994] to two other types of low-level liquid water clouds - altostratus and low-level cumulus clouds. In this case there are two key questions: are they also scale invariant over a range of scales, and if so how do their fractal parameters compare to stratocumulus. In the case of stratocumulus cloud, not only are a significant number of flights added here to increase the data set analysed (over land in this case rather than in purely marine conditions) but an attempt is made to investigate the variability of the multifractal properties over time - both the diurnal and seasonal variations are considered.

To achieve these objectives, this chapter is structured in the following way. Initially, some of the statistics of the liquid water field are presented for all three cloud types (stratocumulus, altostratus and cumulus) and the cloud fields are shown to be scale invariant. Subsequently, the data is compared to the FIF universal multifractal model and the associated multifractal parameters are empirically determined. The diurnal and seasonal variation in stratocumulus spatial structure is then investigated. In addition, once the spatial distribution of the cloud fields has been parameterised, a relationship is found between mean liquid water content and the percentage of the horizontal layer filled with cloud.

3.2 Measured multifractal statistics of liquid water content

3.2.1 The data set

Liquid water content was measured in cloud fields over northern Tasmania, Australia, with an aircraft-mounted King hot-wire probe [*King et al.*, 1978]. Flights

were made over the course of three years: 1999, 2000 and 2001. Data collection was spread over the months between April and November, inclusive, because the aircraft was not available during summer. A variety of cloud conditions were investigated. Three broad categories of cloud type were examined: stratocumulus, altostratus and cumulus. Cloud type was determined by visual observation from the aircraft while above the cloud field that was measured, with the height of the cloud bank (determined when descending through the cloud) also taken into account. Approximate cloud cover was also determined visually from above the cloud field. The minimum cloud cover for which data was collected was 0.25, but there is some selection bias toward higher cloud cover because flights were not made unless satellite images seemed to indicate "cloudy" conditions. On occasions when multiple cloud layers were present the cloud type and approximate cover recorded are those of the layer in which liquid water content was measured.

An example data series taken in stratocumulus cloud on October 31, 2000 is shown in figure 3.1. It shows strong intermittency - the majority of values are small but there are a few extreme values that are much greater than mean.

On each flight the liquid water content was recorded on horizontal runs, at a frequency of 1Hz. Aircraft speed was used to convert this time series into a spatial series. This gives a resolution of approximately $100m$. For analysis purposes each data series was considered to begin once the aircraft levelled off at the determined measurement height, and to end when the aircraft deviated significantly from horizontal flight.
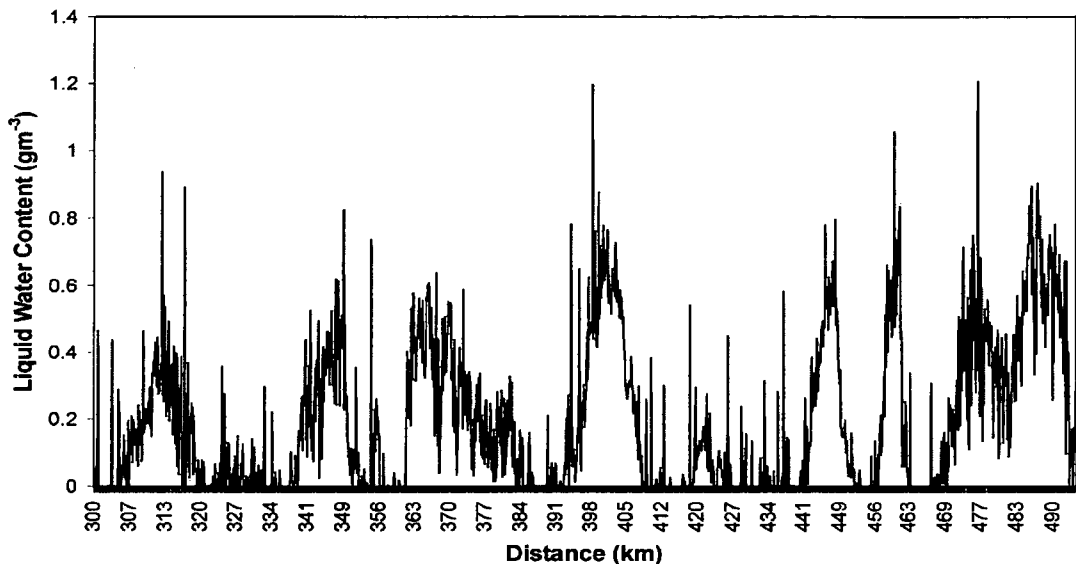
Figure 3.1: The liquid water content measured by a King hot-wire probe during a flight through stratocumulus cloud on the 31 Oct 2000, as a function of flight distance.

3.2.2 Energy Spectra

In the multifractal analysis of these liquid water content series, the first thing considered is the energy spectrum $E(k)$ of the liquid water content field, ρ, as given by equation (2.19). When comparing a range of liquid water content probes, *Davis et al.* [1996a] found that King probe to be reliable at measuring energy spectra down to scales on the order of $10m$.

Fourier transforms were carried out using a numerical Fast Fourier Transform (FFT) algorithm. To remove the noise present in individual spectra, the method of "octave averaging" has been used, as suggested by *Davis et al.* [1996a], following their comparison of noise reduction techniques. This involves averaging $E(k)$ into

bins of increasing size, E_m:

$$E_m = \frac{1}{2^m} \sum_{i=2^m}^{2^{m+1}-1} E(k_i), \qquad (3.1)$$

The energy spectra for four individual stratocumulus cloud flights are shown in figure 3.2, plotted on logarithmic scales. As the results of interest are the linear behaviour and slope of these data sets, the spectra have been offset vertically for ease of viewing. The lines shown are least squares fitted to data for scales less than 25km. These spectra all seem to demonstrate scaling behaviour for the majority of the scales covered, as can be seen by their linear behaviour. This implies that the same processes are at work over all these scales. The scaling exponent, β, of the energy spectra vary, with the average value for stratocumulus being $\beta = 1.43$, and a standard deviation of 0.11. Note that this is lower than the value of $\frac{5}{3}$ calculated for turbulent velocity fields using dimensional analysis [*Kolmogorov*, 1941].This is significant becasue the 5/3 value for the spectral slope has often been assumed a priori in statistical models of clouds [e.g. *Cahalan et al.*, 1994; *Baker*, 1993; *Marshak et al.*, 1995]. The lower spectral slope observed here means that although the cloud fields are non-stationary, they are relatively hgher degree of variation at smaller spatial scales then predicted by these models.

Some flights, such as that on 03/10/01 shown in Figure 3.2, seem to show a scale break at 20-40km, with the spectrum flattening out in this range. Similar scale breaks have been noted by other researchers [e.g. *Davis et al.*, 1996a]. However, as can be seen with the flight on 06/06/01 in figure 3.2, other flights extending out to the same scale range do not show any obvious break in scaling. Since the spectral exponents of intermittent quantities are often difficult to estimate reliably, and require large data sets, ensemble averages are considered to resolve this issue
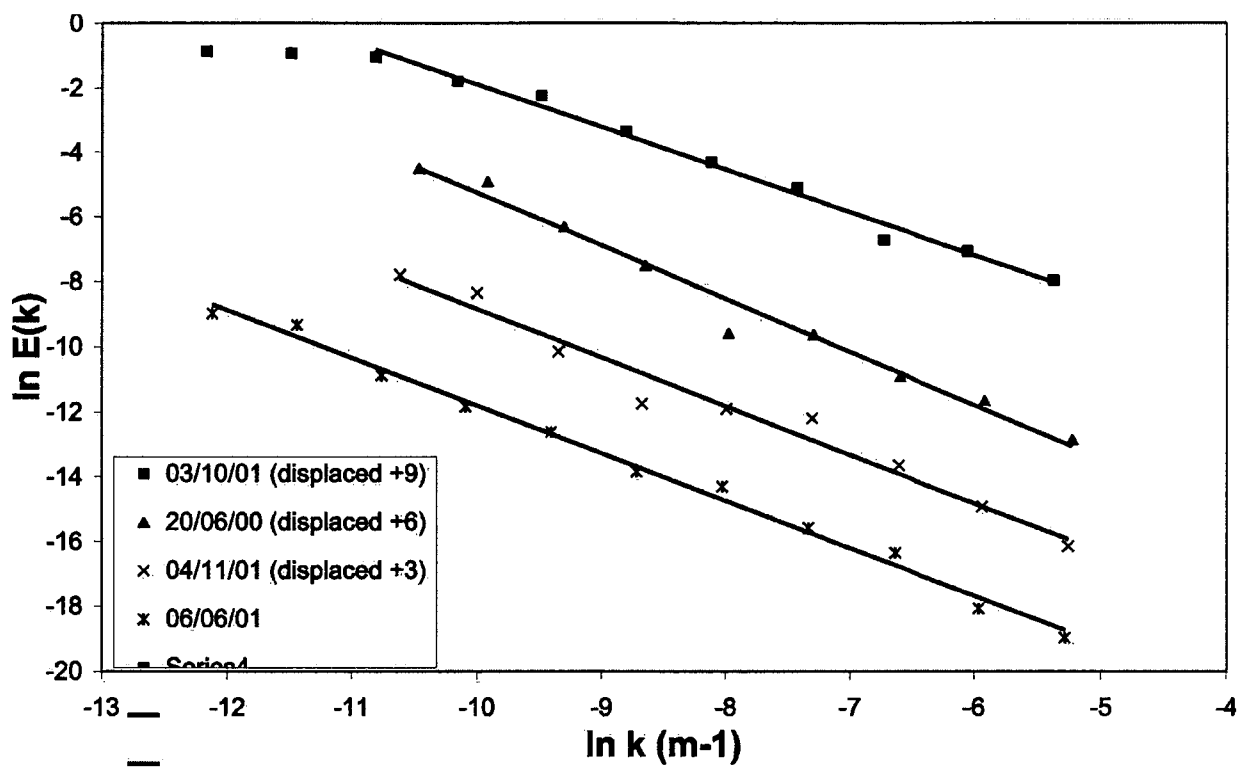
Figure 3.2: The energy spectrum of liquid water content, plotted on logarithmic scales. For four individual flights, with octave averaging to reduce noise in the spectra.

of the scale breaks.

When the stratocumulus data was considered as a whole ensemble, no scale break was apparent at low frequencies for stratocumulus. This can be seen in Figure 3.3, where the energy spectrum is plotted for all the stratocumulus data considered a single ensemble. Figure 3.3 also contains the energy spectra of the other two cloud types, again with the spectra of all flights of each type averaged to give an ensemble spectrum (as directed by the definition (2.19)). Again all three cloud types exhibit a power law behaviour, which is linear on the log-log plots, over the majority of the scales shown. This implies that the processes of cloud formation and transport are the same over these scales. Since we are interested in testing linear behaviour on this graph and finding the slope of the line, but not the intercept, the data sets in figure 3.3 have been vertically offset for ease of viewing. Note that although the plots in Figure 3.3 cover a range of scales up to 160km, the only cloud type that shows signs of a scale break (or change of slope in the plot) at low frequencies (large spatial scales) is the altostratus, which seems to begin to level out at around 25-50km. The stratocumulus and cumulus spectra maintain their power law behaviour up to the lowest frequency (largest scales) measured. At the highest frequencies however all three plots seem to flatten out slightly. This flattening of the spectrum at high frequencies has been traced to noise in the electronics which was observed even in clear sky flights. These data points were therefore excluded from the linear fits shown in Figure 3.3. Because of this noise, no attempt was made to ascertain the high frequency limit of the scaling regime.

The slopes of all three spectra are slightly, but significantly, lower than the value of $\frac{5}{3}$ calculated for turbulent velocity fields using dimensional analysis. Also note that with ensemble averaging, the level of noise is a lot lower so octave averaging is not necessary. The value of the power law exponent, β, that is found from the slope

54
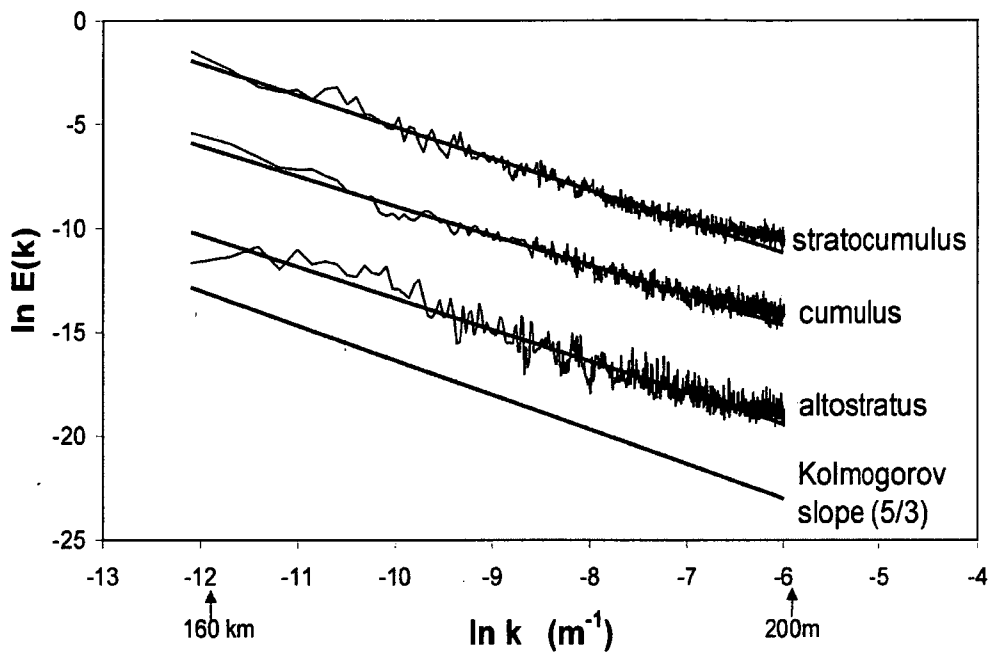
Figure 3.3: The energy spectra, $E(k)$, of the liquid water content of three different cloud types (altostratus, stratocumulus and cumulus), derived from in-situ measurements of cloud liquid water content. Each spectrum is an ensemble average over all flights of each cloud type. A line with a 5/3 Kolmogorov slope is included for comparison.

of the energy spectrum is shown in Table 3.1 for each cloud type, together with the number of flights for each category of cloud. Given the statistical errors involved (also listed in the table), these spectral exponents are close enough to be considered the same. Thus, except for the scale break that appears to occur in altostratus at ~25km, the energy spectrum of horizontal variations in cloud liquid water content appears to be roughly constant across the three cloud types considered.

Table 3.1: The fractal parameters calculated from aircraft measurements of cloud liquid water content, divided into cloud types. For each cloud type the table lists: the number of flights made; the exponent of the energy spectra, β; the three fractal parameters of the FIF multifractal model, α, C_1 and H. The mean values for all flights considered together are also shown.

Cloud type	No. of flights	β	α	C_1	H
Stratocumulus	47	1.43 ± 0.02	1.47 ± 0.03	0.108 ± 0.002	0.30 ± 0.02
Altostratus	33	1.44 ± 0.04	1.54 ± 0.06	0.082 ± 0.001	0.29 ± 0.03
Cumulus	28	1.48 ± 0.03	1.42 ± 0.08	0.126 ± 0.003	0.34 ± 0.03
All	98	1.44	1.48	0.106	0.31

3.2.3 The universality parameters
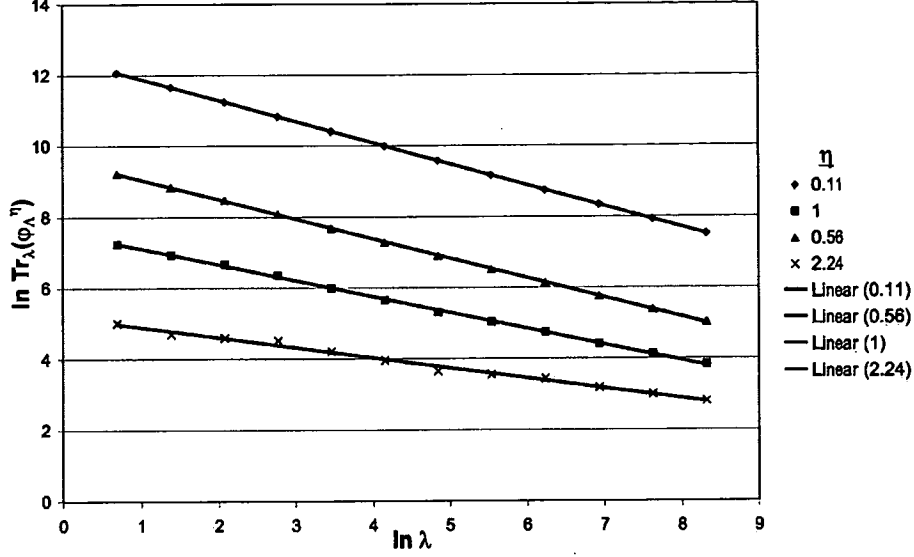
Figure 3.4: The double trace moment $Tr_\lambda(\varphi_{\lambda'}^\eta)^q$ as a function of scale, λ, plotted on a log-log graph for q=2 and a range of η values. For a flight in stratocumulus cloud on the 6th of June 2001.

Using the DTM technique described in section 2.1.5, the data was analysed both as individual realisations and as ensemble averages of the three cloud types. Figure 3.4 shows the logarithm of the double trace, $\ln[Tr_\lambda(\varphi_{\lambda'}^\eta)^q]$, versus $\ln \lambda$ from an example of the individual flight data, from 06/06/01. The same plot for when the double trace of all the flights is averaged to give ensemble values in each of the three cloud categories is shown in figure 3.5. The fact that these plots are nearly linear confirms that these fields are scale invariant over the range covered, as spectral analysis has already shown. The slopes of these lines were computed to yield the double exponent $K(q, \eta)$, as described in (2.17). A plot of $\log K(q, \eta)$ against $\log \eta$ for the example flight is then shown in figure 3.6, with an identical plot for the ensemble averaged quantities shown in Figure 3.7. All of these plots show
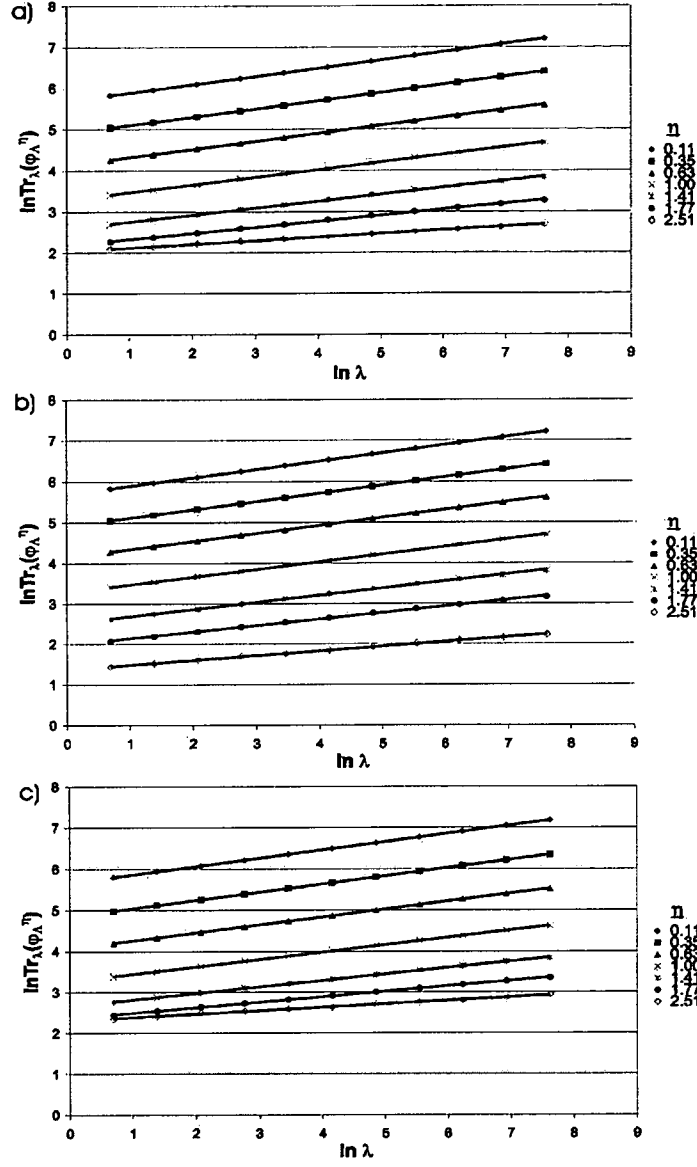
Figure 3.5: The ensemble averaged double trace moment, $Tr_\lambda(\varphi_{\lambda'}^\eta)^q$, as a function of scale, λ, plotted on logarithmic axes for cloud types: a) stratocumulus, b) cumulus and c) altostratus. For $q = 0.8$ and a range of η values.

near straight line relationships up until a critical moment, after which point the value of $K(q, \eta)$ starts to become almost independent of η (due to under-sampling). This is the consequence of examining "dressed" multifractals with a finite number of samples, as was identified by *Tessier et al.* [1993] when presenting the DTM method. As noted in sections 2.1.4 and 2.1.5, the multifractal parameters can be found if only values of η lower than the critical value are considered, since below that point the plots in Figure 3.7 should be linear with slope α. Testing this, if only points where $\log \eta \leq 0$ are considered then the correlation coefficient r^2 for the linear relationships shown in Figure 3.7 is above 0.92 in every case, while the p values of the fit is always less than 0.01. This linear behaviour indicates that the horizontal liquid water content series are behaving as predicted by the universal FIF model. The universal parameters, α and C_1, were derived from the slope and intercept of these plots, as was described in section 2.1.5. The parameter values calculated for the ensemble averages are shown in Table 3.1.

As with the spectral exponent, β , the values for α in table 3.1 are close enough that the parameter can be considered constant across cloud types. However the ensemble averaged values of C_1 show more significant (relative) deviation, although the values are still not vastly different. With $C_1 = 0.126$, the cumulus cloud fields have a higher mean intermittency than the stratocumulus, with $C_1 = 0.108$, which in turn is slightly more intermittent then the altostratus ($C_1 = 0.082$). The low values of C_1 implies that the conserved multifractal flux is not extremely sparse in comparison to other multifractal fields (for example, *Chigirinskaya et al.* [1994] found $C_1 \simeq 0.3$ for horizontal measurements of the turbulent velocity field). The relatively large α indicates that a monofractal description would not fit the data well, as it is far from the monofractal value of $\alpha = 0$.

It may be seen from equation (2.18) that the scaling exponent $K(q)$ should be
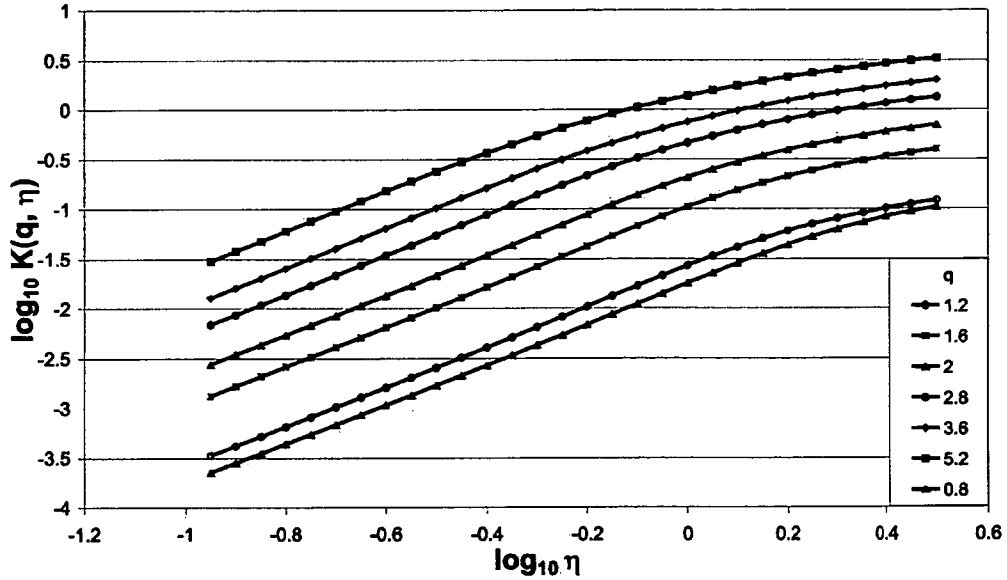
Figure 3.6: The double exponent $K(q, \eta)$ as a function of η on a log-log plot. The data was taken during a flight through startocumulus cloud on 6/6/2001.

retrieved from the double exponent $K(q, \eta)$ when $\eta = 1$ i.e. $K(q) = K(q, 1)$. To confirm that the spatial statistics of the liquid water content can be described by the FIF model, the scaling exponents $K(q)$ for the three cloud types are plotted in figure 3.8 along with the theoretical values calculated using the universal parameters in table 3.1 and equation (2.12). In each of the three cases there is a close fit to the universal model until a critical exponent, at which point there is a multifractal phase transition followed by a linear relationship. These changes in behaviour at high q appear to be the first order multifractal phase transitions described in *Schertzer and Lovejoy* [1992], which are due to the divergence of moments in "dressed" multifractal quantities, combined with the effect of finite sample size as discussed in section 2.1.4. For the stratocumulus the critical exponent is $\simeq 6.2$, for the altostratus it is also $\simeq 6.2$, and for the cumulus cloud the critical ex-
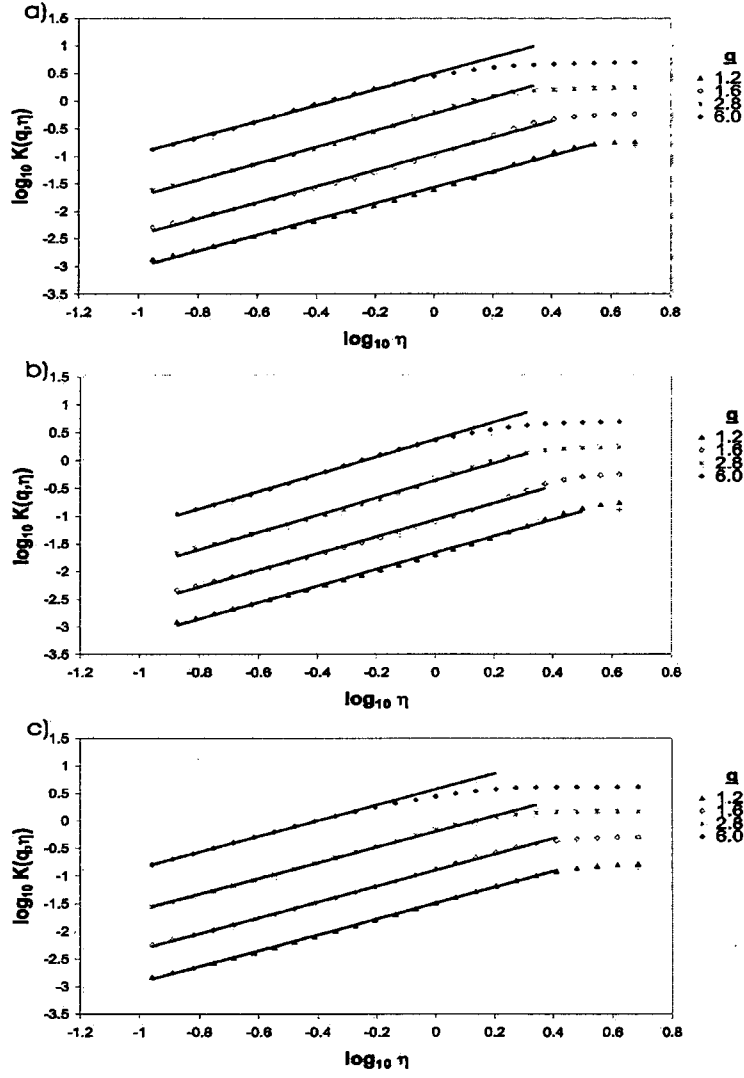
Figure 3.7: The logarithm of the double exponent $K(q,\eta)$ as a function of $\log \eta$, calculated from the ensemble averaged trace moments for the three cloud types: a) stratocumulus, b) cumulus, c)altostratus. The plots are shown for various values of q. They all show linear behaviour with equal slope (α) up to some critical value of η, at which point they become constant with η.

61
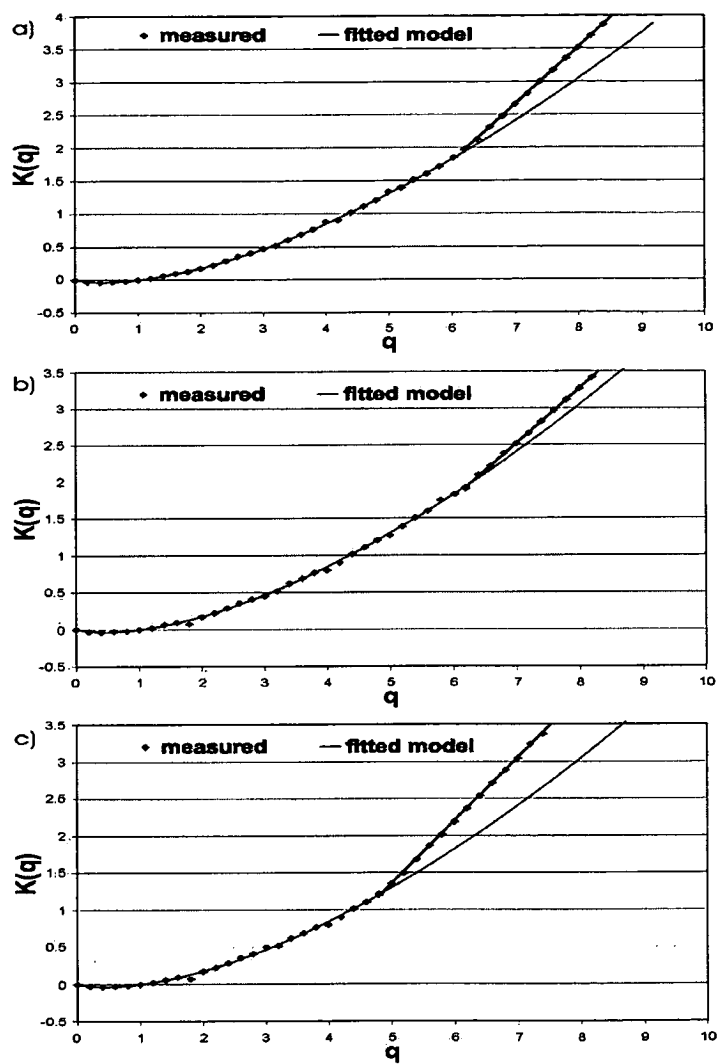
Figure 3.8: The scaling exponent $K(q)$ for a)stratocumulus cloud, b) cumulus and c)altostratus.

ponent is approximately 4.8. Compare this to the critical exponents q_s predicted by the multifractal parameters in Table 3.1 using the relations in section 2.1.4, which are $\sim$ 6.4 for stratocumulus,$\cdot \sim$ 6.5 for altostratus and $\sim$ 5.2 for cumulus cloud. The differences between cloud type are caused by the differing value of C_1 and the different number of flights for each type. The measurements therefore show critical exponents slightly lower than predicted.

Finally, the value of the non-conservation parameter H was determined using equation(2.20), and is also listed in the table 3.1. The values are again very similar across the cloud type groupings. They are also very close to the value of $\frac{1}{3}$ that is predicted by the passive advection transport model of *Schertzer and Lovejoy* [1987]. In general this value of H between zero and one indicates that the cloud is non-stationary, i.e. the statistical properties are not invariant under translations, but has stationary increments [*Davis et al.*, 1996b].

The properties found for stratocumulus clouds in Table 3.1 agree well with the multifractal analyses of liquid water content from ten flights in marine stratocumulus in *Marshak et al.* [1997]. That study found ensemble averaged values of $C_1 = 0.10$ and $H = 0.28$ (they did not calculate α). The universal parameters calculated using satellite-measured cloud radiances by *Tessier et al.* [1993] are also in general agreement for values of C_1 (0.07-0.10 for different satellite channels) and H (0.3-0.5), although the α values of 1.1-1.35, are generally lower. On the other hand, *Lovejoy et al.* [2001a] found $\alpha = 1.87$ and 1.90 for visual and infrared satellite images respectively, while again finding similar C_1 values. Of course, due to the non-linear relationship between cloud liquid water content and the reflected radiation field, it is not clear that there is any reason to expect their fractal parameters to be same.

3.2.4 Diurnal cycle of stratocumulus clouds

Using lidar measurements, *Cahalan et al.*[1994], found a diurnal cycle of stratocumulus spatial structure in the framework of the bounded cascade model. This indicated that the stratocumulus structure was altered by the well-known daily cycle of the atmospheric boundary layer. To investigate this with in-situ flight data and the FIF model, the data series was divided according to which hour of the day the run occurred. Each hour of the day was then considered to be a separate ensemble. Note that data from any particular flight may fall into several different hours. The DTM analysis was then performed for each of these hour-ensembles. To reduce the effect of any annual or seasonal cycle (as will be examined in section 3.2.5), the data in each hourly bin was weighted so that each month made an equal contribution to the ensemble. This was done by multiplying the data from each flight in a month by the inverse of the number of flights in that month. The resulting universal fractal parameters are shown in Figure 3.9, plotted as a function of time of day. Only stratocumulus data was used here. The number of flights in each hour bin is listed in Table 3.2.

Table 3.2: The number of flights in each hour-based bin.

hour (AEST)	1	2	3	4	5	6	7	8	9	10	11	12
# flights	2	2	1	2	2	3	4	2	2	3	4	5
hour (AEST)	13	14	15	16	17	18	19	20	21	22	23	24
# flights	6	2	2	5	4	4	1	2	2	0	1	2

Cahalan et al.[1994] used a "bounded cascade" model, with their fractal parameter f measuring inhomogeneity. Although there is no direct relationship, this parameter is most equivalent to the parameter C_1 used here, as both are measures of mean inhomogeneity. The results found in that study are qualitatively similar to the cycle of C_1 seen in Figure 3.9a, with the inhomogeneity decreasing in the

64
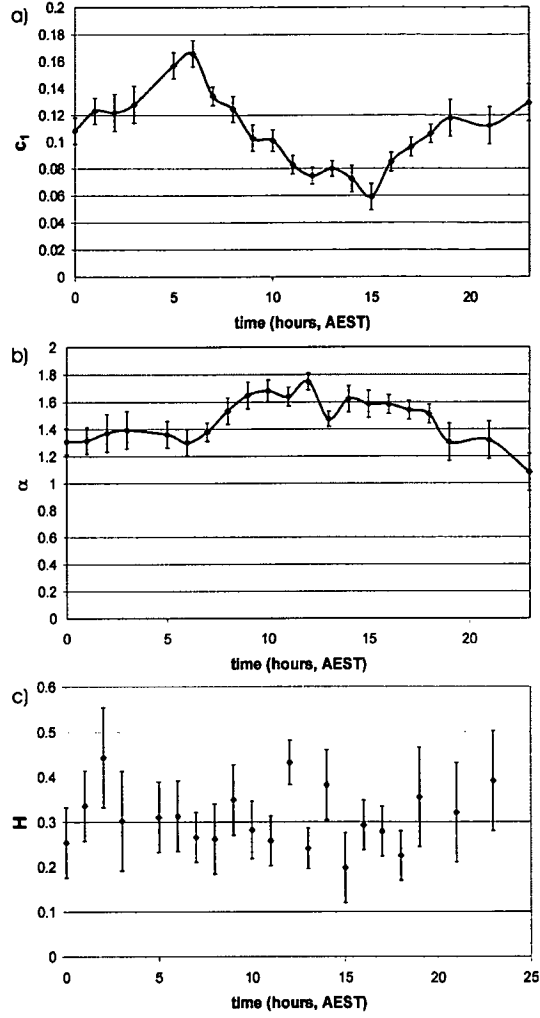
Figure 3.9: The diurnal cycle in the multifractal parameters of stratocumulus cloud. While a) C_1, and b) α, show signs of a diurnal pattern, c), H, does not. Time is in Australian Eastern standard time (AEST).

afternoon and increasing over the evening. There also appears to be a cycle in α over the day shown in Figure 3.9b, with higher values during the day. There is no discernible pattern with time of day for the nonstationarity parameter H (Figure 3.9c). It must be pointed out however that due to the low number of data series associated with some of these times of the day, the parameters calculated here are not as robust as those for all series of each cloud type as shown by the error bars in the figure (which show standard deviation in the data set for the hour).

Although not shown here, there were no clear patterns to be seen in the parameters of the other two cloud types. This may be a result of the smaller number of flights in those to cloud types, which not only increased the standard error at each point but left gaps in the daily record.

3.2.5   Annual/Seasonal cycle of stratocumulus clouds

If the spatial structure of stratocumulus clouds changes with the diurnal cycle of the atmospheric boundary layer, it is not unreasonable to expect that it will also show signs of the annual or seasonal cycle that exists in the boundary layer. To investigate this the 48 flights in stratocumulus cloud were regrouped according to which month of they were conducted in. Flights were only conducted in the 9 months between April and November (inclusive) so the complete annual span cannot be observed, but the variation in cloud spatial structure over the seasons of autumn, winter and spring can be examined. All the flights conducted in each month were then considered a single ensemble for the purpose of applying the DTM analysis method. To remove the diurnal cycle seen in section 3.2.4, the data in each monthly bin was weighted so that each hour of the day made an equal contribution to the monthly-ensemble. This was done by multiplying the data from each flight in

66

an hour of the day by the inverse of the number of flights in that hour. The results of the multifractal analysis are plotted in Figure 3.10 as a function of the month. The number of flights in each month is listed in Table 3.3 Again there is some

Table 3.3: The number of flights in each month-based bin.

month	1	2	3	4	5	6	7	8	9	10	11	12
# flights	0	0	0	9	3	8	4	8	3	7	5	0

evidence of a cycle in the parameters C_1 and α, but not for the non-stationarity parameter H. The variation in the mean-intermittency parameter, C_1, is such that it increases over autumn, is largest in the winter months of June, July and August, and decreases during spring until November. As in the diurnal case the change in the multifracticality parameter α is roughly opposite to that of C_1, with decreases over autumn, the lowest values in the winter months and a steady increase over spring.

3.3 The probability distribution and cloudy fraction

The cloud cover fraction of a cloud field is clearly related to the spatial distribution of the liquid water content. In this section the Probability Distribution - Multiple Scaling (PDMS) method of *Lavallée et al.* [1991] is used to independently calculate the codimension function and confirm the universal parameters found in the previous section. In doing this the probability distribution is also calculated, which allows us to deduce the probable fraction of the horizontal flight layer taken up by cloud.

The PDMS method is discussed in more detail in *Lavallée et al.* [1991] and

67
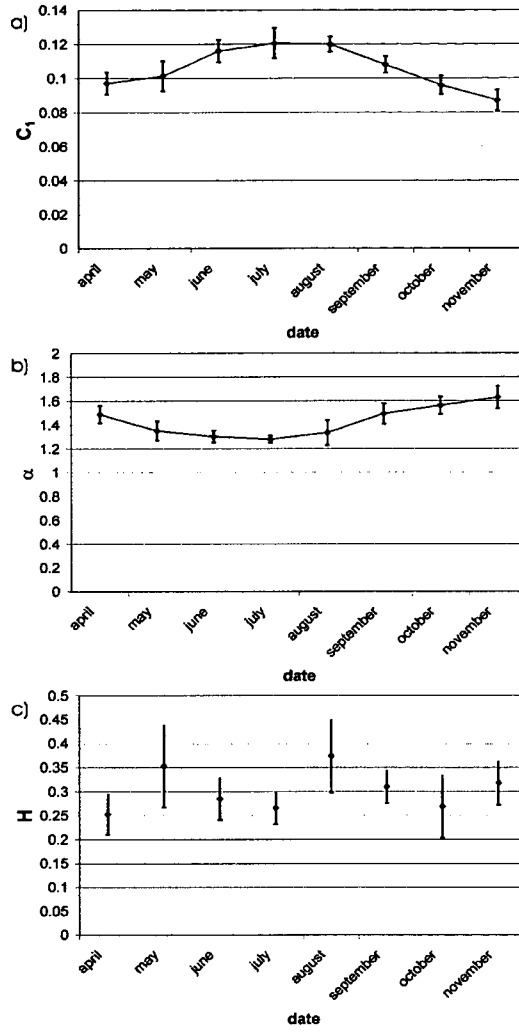
Figure 3.10: The annual cycle in the multifractal parameters of stratocumulus cloud. While a) C_1, and b) α, show signs of a annual pattern, c), H, does not.

Schertzer and Lovejoy [1995b]. Given the similar values of the universal parameters found in section 3.2.3, all three cloud types are considered a single ensemble in this section. By using a larger ensemble it is hoped to produce a more accurate estimation of the fractal statistics.

The liquid water content, ρ, was first normalised by the ensemble average to give a dimensionless quantity $\bar{\rho} = \frac{\rho}{<\rho>}$. From the definition of the codimension, (2.5), if $\bar{\rho}$ is a scale invariant then its probability distribution is given by

$$\Pr(\bar{\rho} > \lambda^{\gamma}) = B\lambda^{-c(\gamma)} \tag{3.2}$$

where B is a function of γ,. Plots of $\log \Pr(\bar{\rho} > \lambda^{\gamma})$ as a function of $\log \lambda$ for various values of γ, are shown in figure 3.11. Regression analysis of all fitted lines shown gave a Pearsons correlation coefficient R^2 greater than 0.9 and p values less than 0.01. The linear behaviour confirms, once more, that the data set is scale invariant. The lines shown are least squares fits. The slopes of these lines estimate the codimensions, $c(\gamma)$, while the (fitted) intercepts give the logarithm of the prefactor B. The $c(\gamma)$ thus derived are shown in figure 3.12, plotted as a function of γ. Also shown in figure 3.12 are the theoretical values of $c(\gamma)$ that were calculated using equation (2.11) for a universal multifractal process with parameters $\alpha = 1.5$, $C_1 = 0.1$. The close agreement between these two again confirms that the liquid water content can be described by the universal FIF multifractal model with these parameters. This agreement continues up until the critical singularity, γ $\simeq 0.45$, where there is again a multifractal phase transition and the onset of self organised criticality due to the fact that the measurements are dressed rather than bare quantities. The logarithm of the prefactors B, determined from the intercept of the lines fitted in figure 3.11, are plotted as a function of γ in figure 3.13. These
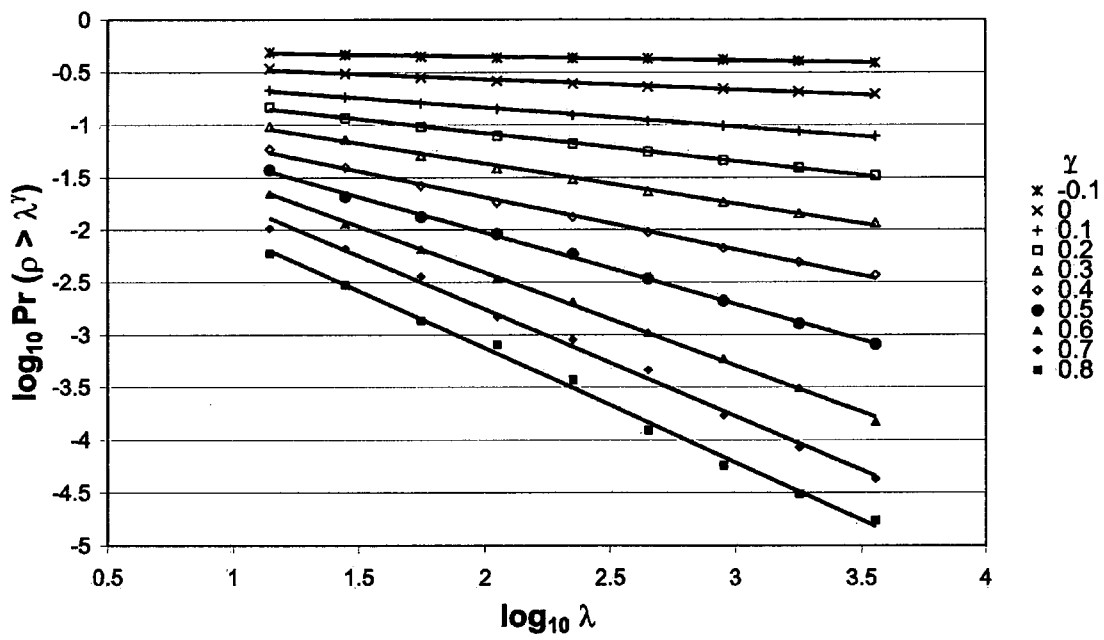
Figure 3.11: The probability of the (normalised) liquid water content exceeding λ^γ for a range of γ values. Plotted on a log-log graph. The least squares fit line is also shown for each γ.
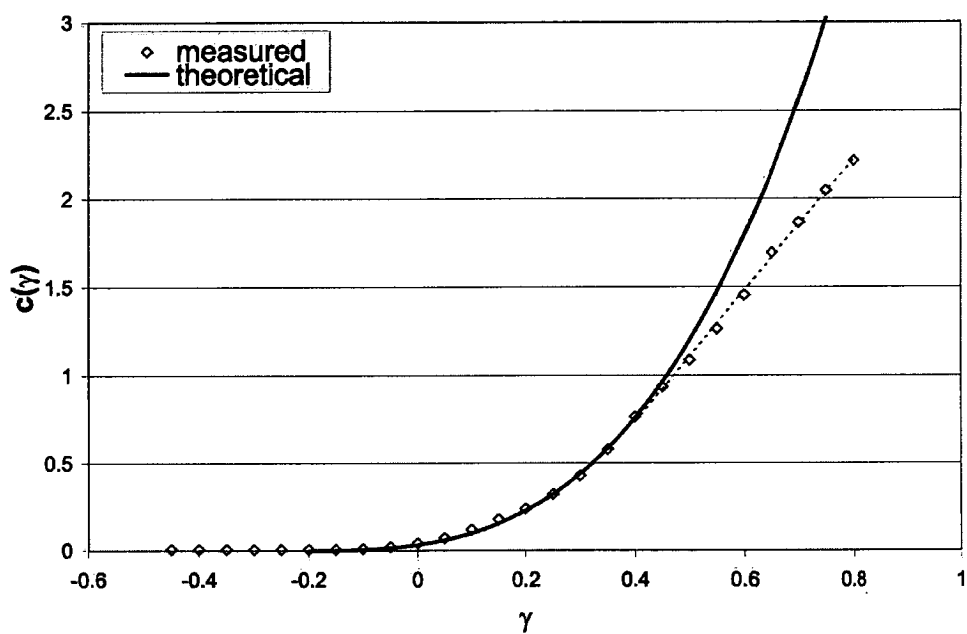
Figure 3.12: The codimension function $c(\gamma)$ calculated from the scaling behaviour of the liquid water content of all flights. The solid line is the modelled values for $\alpha = 1.48$, $C_1 = 0.106$.
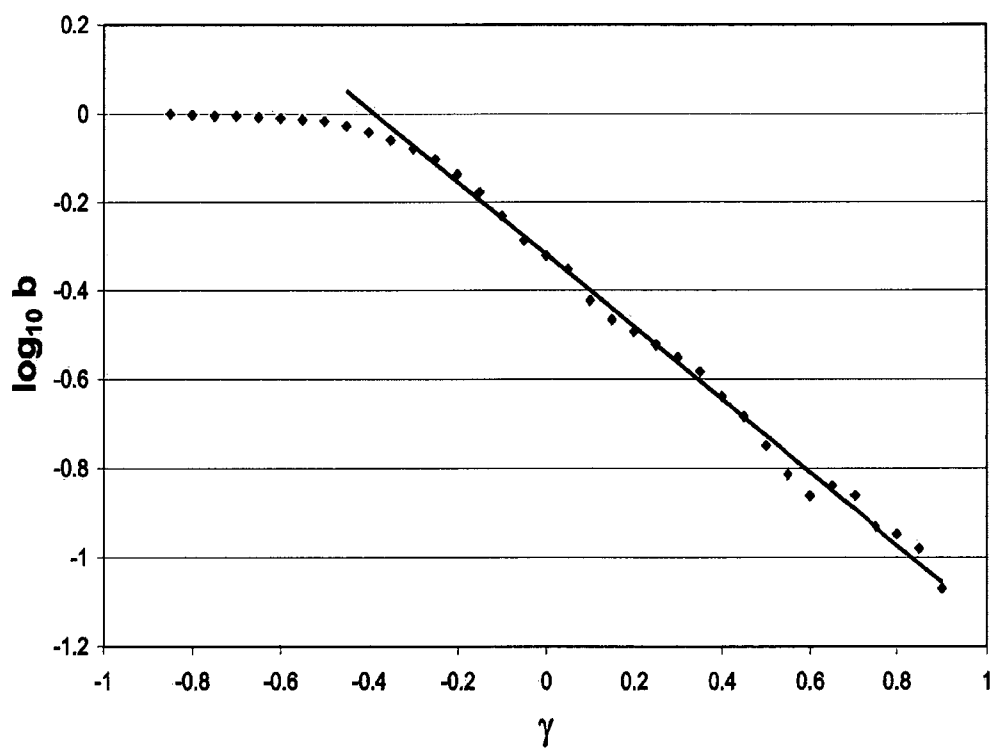
Figure 3.13: The logarithm of the prefactors, $b(\gamma)$, of the probability function.

appear to be fairly linear with γ, except for the very small singularities ($\leq$-0.4). In determining the probability distribution for cloud fraction calculations, below, the linear relation shown in figure 3.13 is used. This parameterisation is

$$\log_{10} B(\gamma) = \begin{cases} -0.820\gamma + 0.318 & \gamma \leq -0.388 \\ 0 & \gamma \leq -0.388 \end{cases} \tag{3.3}$$

This should approximate the probability distribution well except for the singularities much less than the mean.

The resolution of liquid water content measurements is $\sim 100m$. Under the multifractal model there is always some positive level of liquid water in each 'pixel', but it can be arbitrarily small. Therefore in order to use the flight data to model the fraction of the horizontal flight level covered by cloud, a cut off level must be chosen - below what average liquid water content in the 100m segment do we call the segment clear? This cut off level can be above zero for two reasons: noise in the liquid water content signal and small amounts of liquid water in a mainly clear 100m. However, exactly what this cut off level, ρ_{min}, should be is not clear. Observation of the instrument signal in known clear sky conditions indicates that this level should be $\sim 0.01 - 0.02\ gm^{-3}$. Clear sky conditions were identified by visual observation that no cloud was nearby. In the remainder of this section, this cut off is set to $0.01\ gm^{-3}$. However, the following method could be used with any choice for ρ_{min}.

The problem of cloud fraction in certain horizontal layer, given a certain mean liquid water content for a Flight, is effectively "downscaling" or "zooming in" from a coarse resolution to a finer one. Downscaling is described further in *Lovejoy et al.* [2001b]. The objective is to estimate the fraction of data points with a liquid water content greater than ρ_{min}, at a resolution of 100m, given a mean liquid water

73

content for a particular flight. If the liquid water content field were constant in the vertical this would be effectively estimating cloud cover at a resolution of 100m, but in reality it only estimates the fraction of cloud in the particular height layer of the flight. This assumes that the liquid water *statistics* are isotropic in the horizontal i.e. that the probability of a point being cloudy is the same in the rest of the layer as it is on the flight track.

The scale ratio for the flight, λ_1, is given by

$$\lambda_1 = \frac{\text{total length of flight}}{100m}, \tag{3.4}$$

and the mean liquid water for the particular flight is ρ_{mean}. The scale invariance of the field means that the statistical relation (3.2) holds at this scale as well, giving the following equation for the probability of a segment being cloudy:

$$\Pr(\text{``cloudy''}) = \Pr(\frac{\rho}{\rho_{mean}} > \frac{\rho_{\min}}{\rho_{mean}} = \lambda_1^{\gamma_{\min}}) = B(\gamma_{\min}).\lambda_1^{-c(\gamma_{\min})}, \tag{3.5}$$

where $\gamma_{\min} = \log_{\lambda_1}(\rho_{\min}/\rho_{mean})$. Using (3.5) with the codimension function given by (2.11) for a universal multifractal with the mean fractal parameters for all cloud types, $\alpha = 1.48, C_1 = 0.106$, the predicted cloud fraction in the layer was calculated as a function of mean liquid water content for the flight. The prefactor $B(\gamma)$ was calculated using the relationship shown in Figure 3.13. The total flight length was assumed to be 100km and the $\rho_{\min}$ to be 0.01 gm^{-3}. This function is shown in Figure 3.14. The sharp cut off when the cloud fraction reaches unity is due to the linear approximation of $\log_{10} B(\gamma)$. To test this function, it was compared to the sixty three flights that extended for more than 100km. For each flight two cloud cover values are plotted: one derived from the King hot wire probe data and the other dathered by visual information. The King probe data series were severed to

74
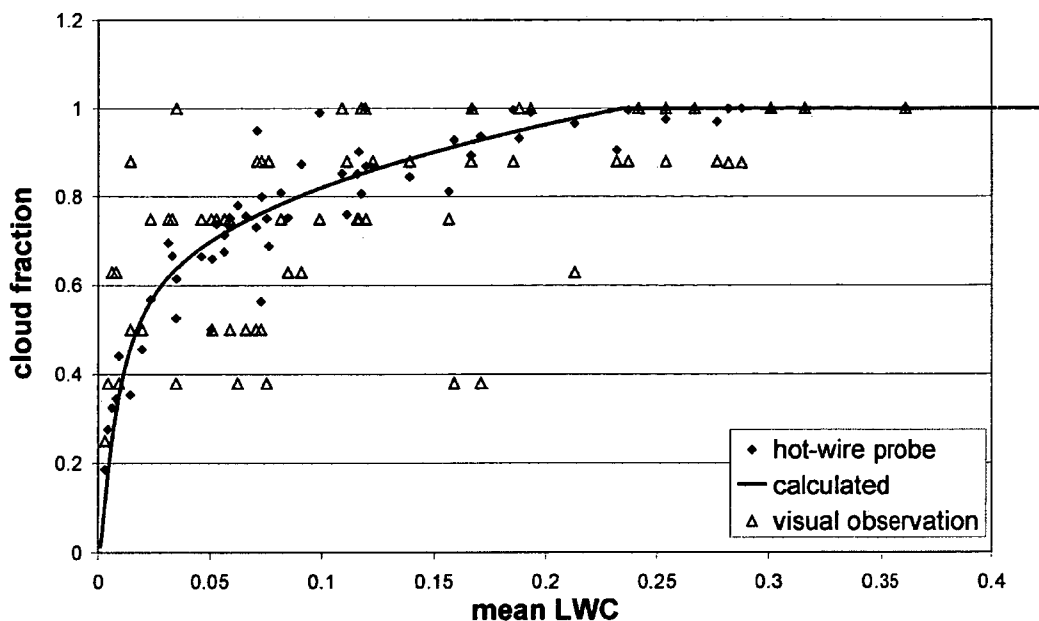
Figure 3.14: The cloud cover as a function of the mean liquid water content measured by the King hot-wire probe. The solid line is the modelled relationship value, while the triangles are the visually estimated cloud cover and the solid diamonds are the cloud cover deduced from the King hot-wire probe measurements. The King probe values are determined by finding the fraction of the series above 0.01g/m3.

be 100km in length; then fraction of these data series above 0.01 gm^{-3} was taken to indicate the cloud fraction on the flight track, and plotted on the Figure 3.14 as a function of the mean liquid water content for the flight (as measured by the King probe). Finally the visual estimations of cloud cover in the flight layer were also added to this figure, again plotted as a function of the measured mean liquid water content. Although there is a lot of scatter in figure 3.14, this is not surprising given the statistical nature of the relationships involved and the difference in definition between visual cloud cover and liquid water content estimated cloud fraction - the visual estimation was made from above the cloud before the data collection began

so may not be relevant to the horizontal run, most of which is separated from the visual observation in both time and space. It also takes into account the cloud at range of heights, not just the specific height of the horizontal run. The hot-wire probe and the modelled values show a much better correlation than the visual estimation and the model. The figure indicates that there is a relationship between mean liquid water content and cloud fraction at that height as estimated by the hot-wire probe, and that equation (3.5) can be used to estimate this relationship. To quantify the accuracy of the cloud cover prediction consider the relative bias, defined as

$$\text{relative bias} = \frac{\text{cloud fraction (predicted) - cloud fraction (King probe)}}{\text{cloud fraction (King probe)}}. \quad (3.6)$$

The mean relative bias is +2.1% and the standard deviation of the relative bias is 12.5%, showing a reasonable mean prediction of cloud cover but significant scatter.

Note that the approach to cloud cover used here can also be applied to radiative modelling of broken cloud fields - in the model used here "clear" pixels are not required to have no liquid water content, but simply small enough values that extinction due to cloud droplets becomes insignificant compared to other atmospheric extinction. This can represent a generally clear pixel with a very small fraction of cloud in it or simply such a low number of liquid water drops spread across the pixel that they have no visible effect. A randomly generated multifractal liquid water field can then be used to simulate broken cloud conditions, so long as the mean liquid water content of the field is low enough to give the desired cloud percentage using equation (3.5).

3.4 Summary of Chapter 3

In this chapter in-situ liquid water content data was analysed with a focus on multifractal properties. All flights from three different cloud types were shown by their energy spectra to be scale invariant for a range of scales up to 25km, as expected from previous studies. Although some flights seemed to indicate a scale break between 25km and 50km, others seemed to show the same power-law extending up to the limit of the data, $\sim$ 160km. When considering ensemble averaged data however, only the altostratus ensemble indicated a scale break at the meso-scale. This implies that the scaling regime in the (horizontal) spatial structure of the low-level water clouds extends to the range of this data set - to the hundreds of kilometers, if not further. The altostratus data set was the smallest of the three cloud types considered, with only 22 flights examined, but if the scale-break is genuine the smaller scaling regime may be due to the higher clouds being above the boundary layer where different dynamic processes apply.

The statistics of the horizontal cloud distribution were further analysed using the double trace moment analysis, with a focus on testing the universal FIF model. The multifractal statistics of all three cloud type ensembles were found to be well described by the universality classes predicted by this model. Furthermore, the universal parameters of all three cloud types were very similar. All three cloud types were found to be non-stationary and multifractal. The only parameter found to differ between cloud types by more than a standard error in the estimate was C_1, the mean intermittency parameter. Even C_1 did not vary greatly between cloud types, with all cloud types having a relatively low sparseness in the mean underlying flux. This implies that the horizontal variations in all cloud types are created by the same processes.

The diurnal cycle of stratocumulus multifractal parameters was also investigated, with a cycle being observed despite the smaller ensembles considered when the data was divided into hourly blocks. In this cycle the mean inhomogeneity decreased in the afternoon and increased in the evening, with a peak at 6am, while the degree of multifracticality varied in the opposite manner. Similarly, a pattern of changes with the seasons were seen in the fractal parameters of stratocumulus cloud when monthly means were considered: in this case C_1 was highest in the (southern-hemisphere) winter, while α was at its highest values at this time. These variations mirror the cycles of the atmospheric boundary layer, in which the solar forcing produces diurnal and annual cycles in boundary layer height, temperature, and degrees of turbulence [Stull, 1988].

Finally, the fit to the universal model and the universal parameters were confirmed using the scaling properties of the probability distribution of the data. This probability distribution information was then used to determine a relationship between cloud fraction at the flight height and the mean liquid water content. This highlights the fact that this cloud model can be applied, not only to overcast skies and internal cloud variations, but to broken cloud fields as well. In the remainder of this study the cloud model and parameters found here are used to investigate the radiative properties of inhomogeneous cloud fields.

Chapter 4

Radiative properties of horizontally multifractal clouds

4.1 Introduction

In this chapter the multifractal cloud model is used to examine the radiative properties of cloud fields that are horizontally inhomogeneous but constant in the vertical direction. The goal is to first understand the effects of the multifractal cloud structure on the cloud radiative properties, and then to develop an effective optical properties approximation so that multifractal cloud fields can be replaced with a homogeneous cloud in radiative transfer algorithms. Both of these objectives have already been achieved for overcast marine stratocumulus cloud using the bounded cascade model [e.g. *Cahalan et al.*, 1994; *Szczap et al.*, 2000a], but in this study a different cloud model is examined, with parameters that are based on a wider range of clouds and cloud covers. This is of interest because these different conditions may produce differences in the radiative properties.

To begin the chapter, the exact geometry and parameters used in the numerical generation of inhomogeneous cloud fields and the radiative transfer code are outlined. The results of the radiative transfer calculations and the parameterisation of the effective optical depth of non-absorbing clouds are then presented in section 4.3. This is followed in section 4.4 by a similar analysis of the radiative properties of absorbing clouds. Section 4.5 then examines the accuracy of the parameterisation of the effective optical depth under different conditions, including varying the asymmetry factor and considering the reflected radiance distribution instead of total reflectance. For the majority of this chapter only clouds with the mean fractal parameter values found in chapter 3 are used, but in section 4.5.2 the consequences of varying the FIF parameters are presented and the difference in radiative properties between the cloud types are shown. Finally, a comparison of the parameterisation developed here with the EHCA of *Szczap et al.* [2000a;b;c] is included in section 4.6.

4.2 The Cloud and Radiation Models

4.2.1 Numerical generation of multifractal cloud fields

In the first part of this study stratocumulus clouds, altostratus clouds, and cumulus clouds all demonstrated very similar fractal model parameters. Therefore for the majority of this chapter the parameters used are $\alpha = 1.48$, $C_1 = 0.106$, $H = 0.3$, which are the mean parameter values for all cloud fields considered in chapter 3. The effects of varying these parameters will be considered in section 4.5. These parameters only apply to the horizontal spatial structure of these cloud types, since the aircraft measurements from which they were derived were taken on horizontal

flight tracks. Therefore, in this chapter the multifractal model is used to simulate only the horizontal variations in the cloud liquid water fields. Liquid water content is kept constant in the vertical. Although these clouds may be referred to in this work as "2-dimensional" multifractal clouds, the cloud fields modeled are three dimensional - the label refers to the fact that the multifractal structure only applies to the two horizontal dimensions. This simple assumption of vertical homogeneity should be reasonable for clouds with relatively low optical depth such as typical stratiform cloud and low level cumulus [*Romanova*, 1998], but errors will increase with optical depth as the total height of the cloud becomes greater than the photon mean free path length. The effect of vertical variations is further investigated in chapter 5.

With the mean parameters derived from aircraft measurements, the continuous cascade simulation method in section 2.1.6 was used to generate multifractal liquid water fields whose (horizontal) statistics match those of real clouds as closely as possible. The multifractal liquid water fields were generated to be 6.4km×6.4km squares in the horizontal with the minimum grid size being 25m in length. The liquid water field is homogeneous within each 25 m grid squares but varies from square to square. Therefore the maximum scale ratio of the multifractal liquid water field, ρ, is $\lambda = \frac{6400}{25} = 256$. Although the measurements analysed in the previous chapter only had a resolution of 100m it is assumed that the scaling regime extends down to 25m, as was seen for marine stratocumulus by *Davis et al.* [1996a] and also by *Gerber et al.* [1994]. The height of the cloud field, h, was set to 500m, since this is approximately the mean global height for low level stratiform cloud [*Kawamoto et al.*, 2001]. The effective droplet radius r_{eff}, was assumed to be constant throughout the cloud. Therefore the volume extinction coefficient β_{ext} was proportional to the liquid water content ρ, and was given be equation (2.42). The vertical optical depth

for any of the 25m grid squares was then $\tau = \beta_{ext}h$, and the mean optical depth (τ_{mean}) for any area simply the arithmetic mean over the grid squares within the area. After the numerical generation of the multifractal liquid water field, the field was scaled by a constant factor to give a chosen value of τ_{mean}.

4.2.2 Monte Carlo radiative transfer calculations

The Monte Carlo radiative transfer described in section 2.2 was used to estimate the radiative properties of the cloud fields. Since the droplet radius distribution was assumed to be constant throughout the cloud, so was the scattering phase function. The baseline case of this study was a cloud with effective radius $r_{eff} = 10\mu m$ at a wavelength of $0.55\mu m$. Using the parameterisation of *Hu and Stamnes* [1993], these properties give an assymetry factor of $g = 0.85$ and a single scattering albedo (ω) very close to 1. Clouds with these parameters were used initially, and then the effect of varying the single scattering albedo was investigated by varying the single-scattering albedo through the values of $\omega = 1.0, 0.999, 0.99, 0.98, 0.95, 0.92,$ 0.9. The sensitivity to variations in the assymetry fractor, g, were also considered and will be discussed in section 4.5.

Note that although these studies are essentially considering changes in a combination of different varaibles, i.e. different wavelength, different particle size and different liquid water content, they provide information on the sensitivity to each of the optical parameters separately. This allows the study to determine the range of application of the resultant parameterisation. For instance, the different single scattering albedo would be applicable for results in the near infra-red wavelengths. As a specific example, of $r_{eff} = 15$ and a wavelength of $2.247\mu m$ gives $\omega = 0.95$ and $g = 0.87$, but so does $r_{eff} = 36$ and a wavelength of $1.855\mu m$. The results

82

found here for $\omega = 0.95$ would apply to both cases.

This Monte Carlo radiative transfer code was used with both plane-parallel homogeneous clouds and multifractal clouds. Both PPH cloud and multifractal cloud had the same geometry: a square prism of 6.4km×6.4km in the horizontal and 500m in height. For multifractal clouds, mean optical depth over the entire cloud domain was set to $\tau_{mean} = 2, 4, 8, 16, 32, 64, 100$. Since the generation of multifractal fields is a stochastic process, five different cloud fields were generated for each optical depth.

The radiation simulations for each cloud field was done using 20 million photons. The model was run with photons entering the top surface of the model with incident zenith angle, θ_0, of 0°, 20°, 40°, 60° and 80°, in order to simulate the clouds being illuminated from different solar zenith angles. The transmittance, reflectance and absorptance were recorded for each 25m×25m grid square at bottom and top surface of the cloud. The area averaged transmittance, reflectance and absorptance were calculated for squares with sides of 0.8km, 1.6km and 3.2km, as well as 6.4km, in order to simulate the effect of spatial variations on pixels of different sizes.

4.3   Conservative Scattering Results

In this section the results of the radiation modelling are reviewed for the case where the single-scattering albedo is set to one, i.e. the case in which there is no absorption within the cloud.. The reflectance and transmittance calculated at the 6.4km scale for both the multifractal and homogeneous clouds, are shown on figure 4.1 as a function of the mean optical depth, τ_{mean}.   These results are for a solar zenith angle of 40°. The error bars shown in the graph for the multifractal cloud are the standard errors resulting from the variations between the five cloud fields at each
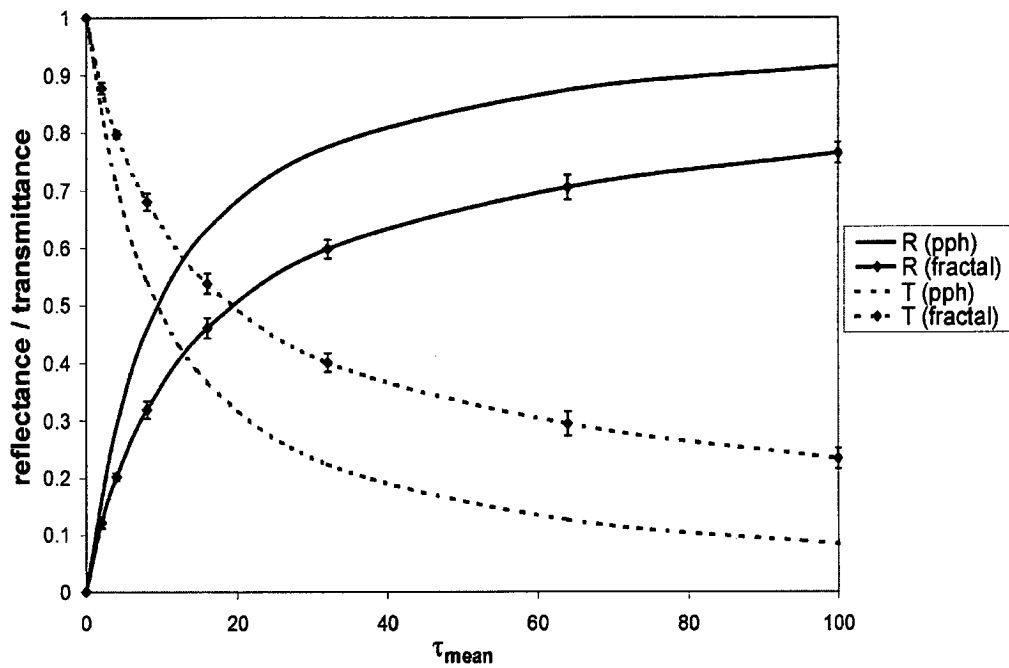
Figure 4.1: The transmittance and reflectance of cloud fields at a solar zenith angle of 40 degrees. Diamonds indicate the points for multifractal clouds at a spatial averaging scale of 6.4 km, with the error bars showing the variation due to the random generation of cloud fields. The lines without individual data points represent homogeneous clouds. Dashed lines indicate transmittance and solid lines indicate reflectance.

optical depth - the point plotted is the mean value of the five cloud fields. It can be seen that, as previous studies have shown, the inhomogeneities in the multifractal cloud fields reduce the reflectance, and increase the transmittance, in comparison with homogenous cloud. Note that the (absolute) difference between the two cloud types is smallest when the mean optical depths are very low, and this difference increases with optical depth until around $\tau_{mean} = 20$. From optical depths of 20 to 100, the difference remains roughly constant at approximately 0.15, which is close to 30% at $\tau_{mean} = 20$ and just below 20% at $\tau_{mean} = 100$. This is somewhat larger than the absolute bias of 0.09 in the same range found by *Cahalan et al.* [1994a] for bounded cascade clouds with the parameters of marine stratocumulus, probably due to the more inhomogeneous nature of the clouds examined here.

4.3.1 Definition of the effective optical depth approximation

The aim is now to find, for a multifractal cloud at a particular averaging scale, the optical depth of a PPH cloud with the same radiative properties. Denote the optical depth of a homogeneous cloud with the same transmittance as the multifractal cloud by τ_{eff}^{T} , and the optical depth of a homogeneous cloud with the same reflectance as τ_{eff}^{R}. Both τ_{eff}^{R} and τ_{eff}^{T} were found by matching the multifractal cloud properties with those of the homogeneous cloud, using cubic spline interpolation. At the maximum pixel size of 6.4 km the periodic boundary conditions of the radiative transfer model ensures that $\tau_{eff}^{R} = \tau_{eff}^{T}$, but at smaller averaging scales this no longer holds because of horizontal transport between pixels. Hence if the effective optical depth is defined based on the reflectance, there is some error in transmittance, and vice versa. Figure 4.2 shows τ_{eff}^{T} plotted against τ_{eff}^{R} for clouds

illuminated at solar zenith angle, θ_0, of 20° and 80° at averaging scales of 3.2 km and 1.6 km. At $\theta_0 = 20°$ there is little difference between τ_{eff}^T and τ_{eff}^R. But when $\theta_0 = 80°$ the horizontal transport of photons is increased and there is a much lower correlation between the two. Following *Szczap et al.*[2000a], the relative differences can be quantified using the root-mean-square dispersion, defined in general between two series A_i and B_i to be:

$$D_{disp}(A_i, B_i) = \left\{ \frac{2}{N} \sum_{i=1}^{N} \frac{[A_i - B_i]^2}{[A_i + B_i]^2} \right\}^{1/2}, \qquad (4.1)$$

where N is the total number of data points. As discussed in *Szczap et al.* [2000a], the root-mean-square (RMS) dispersion is a measure of the mean divergence from the 1:1 line (where A_i equals B_i). Although defined in terms of the relative diference between data series (in equation 4.1), the RMS dispersion can also be thought of as $D_{disp} = 2\sqrt{\sin^2 \alpha}$ where α is the angle between the 1:1 line, and the line between the origin and point (A_i, B_i). In the case of effective optical depths, $D_{disp}(\tau_{eff}^T, \tau_{eff}^R)$ is approximately proportional to the relative error in transmission and reflection for moderate values of the optical depth i.e. between 10 and 40 [*Szczap et al.*, 2000a]. At low optical depth $D_{disp}(\tau_{eff}^T, \tau_{eff}^R)$ underestimates the relative error in transmission or reflection, while at high optical depths in overestimates them. However, the RMS dispersion is used to evaluate the relative error in the model because it allows a summary of the relative errors in reflection and transmission (and later absorption) in a single value.

The values of $D_{disp}(\tau_{eff}^T, \tau_{eff}^R)$ for averaging scales of 3.2, 1.6 and 0.8 kilometers are shown in Figure 4.3 as function of the solar zenith angle. This shows that the difference between τ_{eff}^T and τ_{eff}^R increases with increasing solar zenith angle and with decreasing pixel size, due to the fact that both increase the effect of horizontal
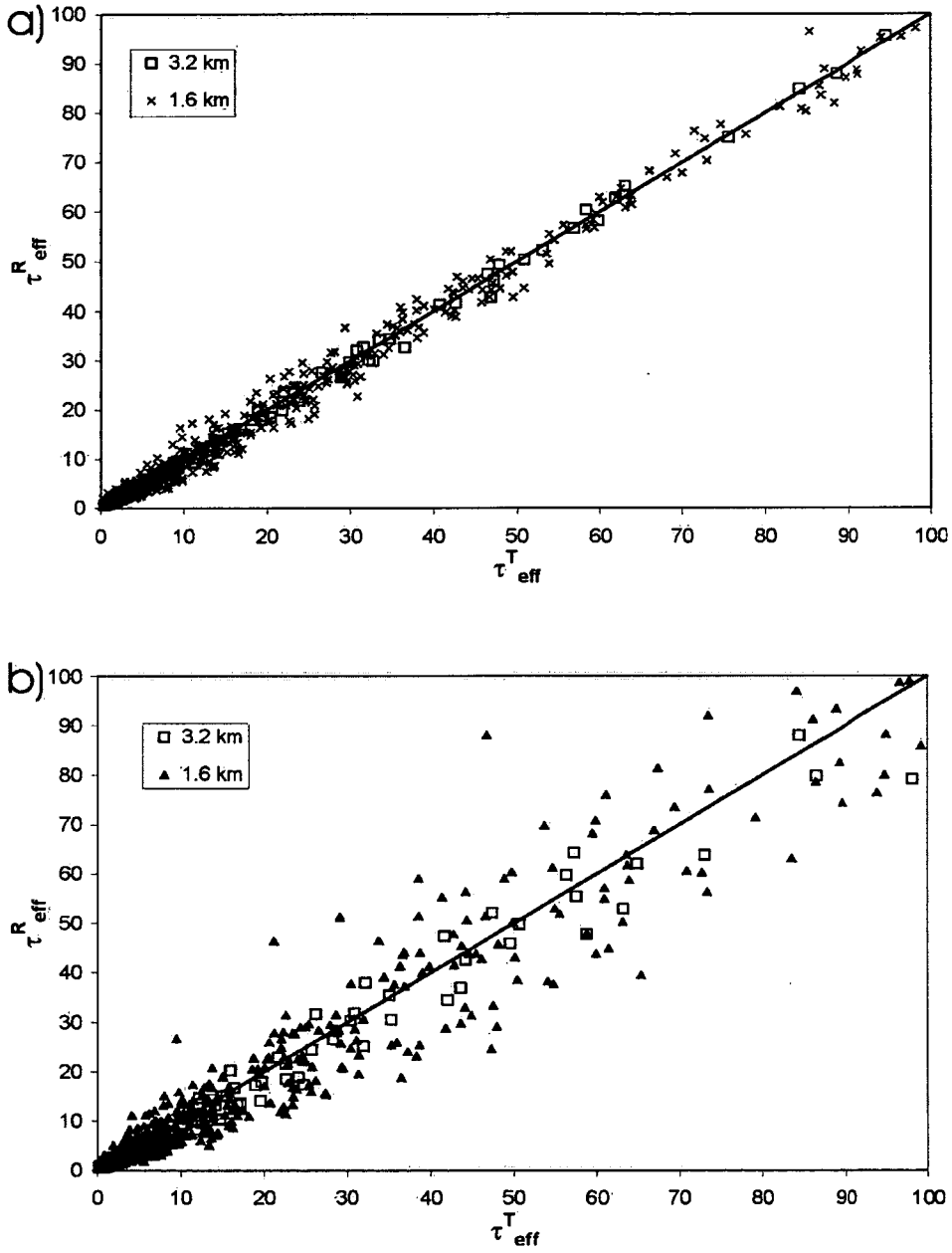
Figure 4.2: Comparisons of the effective optical depth based on reflectance and that based on transmittance. The solar zenith angle is a) 20 degrees and b) 80 degrees. Both show points for multifractal cloud in pixel sizes of 3.2 km and 1.6 km. The solid lines shown are 1:1 reference lines.

transport of radiation between pixels. If a homogeneous cloud with optical depth τ_{eff}^R is used in radiative transfer calculations of both reflectance and transmittance, Figure 4.3 gives the size of the errors that can be expected in calculating transmittance. So if 5% is chosen as a reasonable level of error, then Figure 4.3 shows that
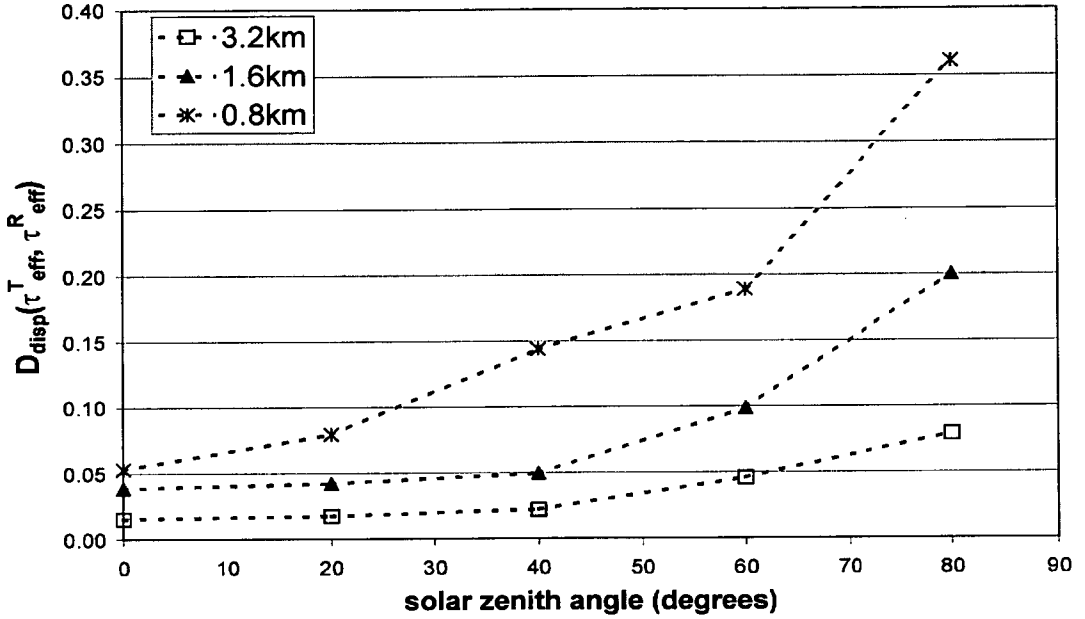
Figure 4.3: The root-mean square dispersion between τ_{eff}^R and τ_{eff}^T - $D_{disp}(\tau_{eff}^T, \tau_{eff}^R)$ - as a function of solar zenith angle. Shown for three different spatial averaging scales. This function quantifies the error involved in using a single effective optical depth when estimating both reflectance and transmittance.

τ_{eff}^R can be used in transmittance calculations when the solar zenith angle is 60° or less for a pixel size of 3.2 km, or when the solar zenith angle is 40° or less for a pixel size of 1.6 km, but never for a pixel size of 0.8 km. Larger averaging scales would increase the acceptable solar zenith angle range further. The reflective case (τ_{eff}^R) was chosen here because of its application to moderate-resolution satellite remote

sensing, and due to the fact that most climate models have sufficiently large grid sizes that the error in transmittance would be small. Similar analysis could be performed for τ_{eff}^T if desired however.

Now consider the solar zenith angle dependence of τ_{eff}^R. Figure 4.4 shows the relative dispersion between τ_{eff}^R calculated at $\theta_0 = 0$ and τ_{eff}^R calculated at the other solar zenith angles. Again there is an increase in differences with in-
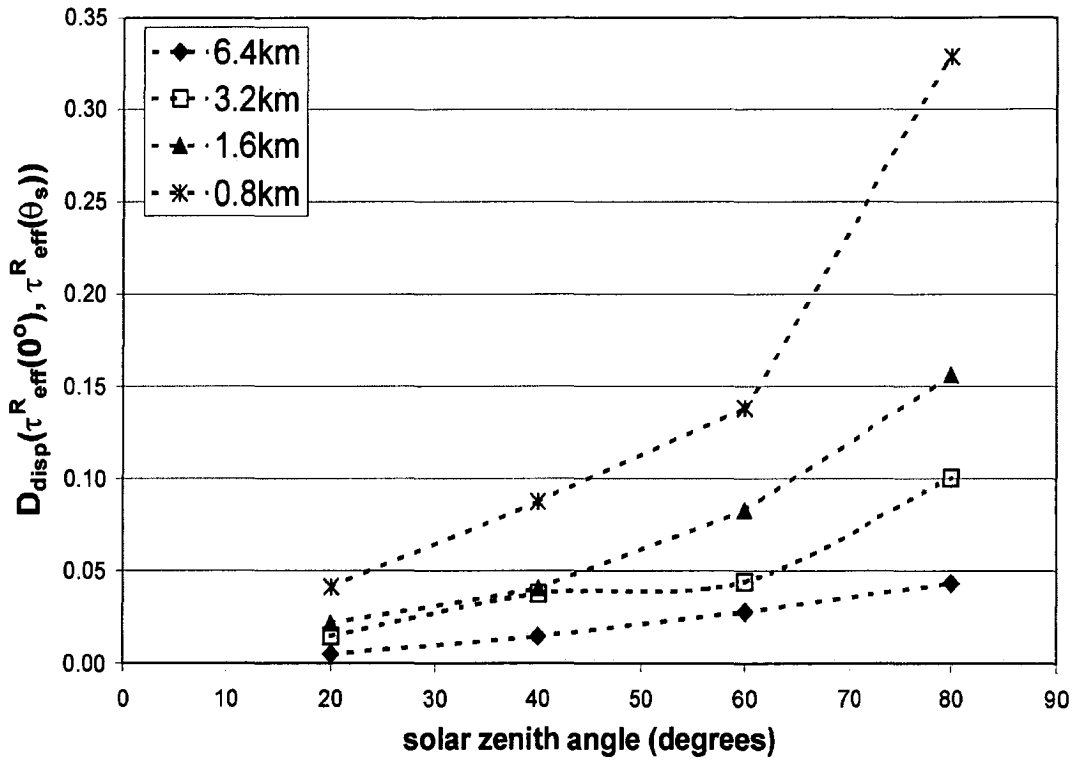
Figure 4.4: This graph quantifies the variation of the effective optical depth with different solar zenith angle. Each data point is the relative dispersion, between the effective optical depth at a solar zenith of zero degrees and the effective optical depth at the solar zenith angle shown. Results are shown for a range of spatial-averaging scales.

creasing solar zenith angle and with decreasing pixel sizes. Since the values of $D_{disp}(\tau_{eff}^R(0^\circ), \tau_{eff}^R(\theta_0))$ are less than 5% in the ranges indicated above, i.e. for $\theta_0 \leq 40^\circ$ at a resolution of 1.6 km, for $\theta_0 \leq 60^\circ$ at 3.2 km and for all zenith angles considered at 6.4 km, a single effective optical depth can be used within these ranges with a minimum of error in the approximation.

Having defined when a PPH cloud with optical depth τ_{eff}^R can be substituted for an multifractal cloud in radiative transport calculations, now consider the effect of pixel size on the effective optical depth. Figure 4.5 shows τ_{eff}^R for two different averaging scales as a function of the mean optical depth, τ_{mean}, of the multifractal cloud. The dotted 1:1 line in the figure is where a homogeneous clouds would fall. It can be seen in Figure 4.5 that τ_{eff}^R is smaller, i.e. further from the homogeneous case, for the larger pixel size. Figure 4.5 also shows that τ_{eff}^R is closest to τ_{mean}, and therefore behaving most like a homogeneous cloud, when τ_{mean} is small. Alternatively, when τ_{mean} is large τ_{eff}^R seems to approach a straight line, with a lower slope at the larger pixel size.

4.3.2 Parameterization of the effective optical depth

Noting the behavior observed for τ_{eff}^R as pixel size and τ_{mean} varied, an empirical relation for the effective optical depth was determined by fitting the data for all pixel sizes and zenith angles to the following function of τ_{mean} and pixel scale:

$$\tau_{eff}^{calc} = \left(A(1 - D\lambda^{-k}) \left(\frac{1 + B\tau_{mean}}{1 + C\tau_{mean}} \right) + D\lambda^{-k}\tau_{mean} \right) \cdot \left(1 - \exp\left(\frac{-\tau_{mean}}{A(1 - D\lambda^{-k})} \right) \right),$$
$$(4.2)$$

where A, B, C, D and k are constants and λ is the scale ratio, i.e. the ratio between the pixel size under consideration and the minimum grid size used in our
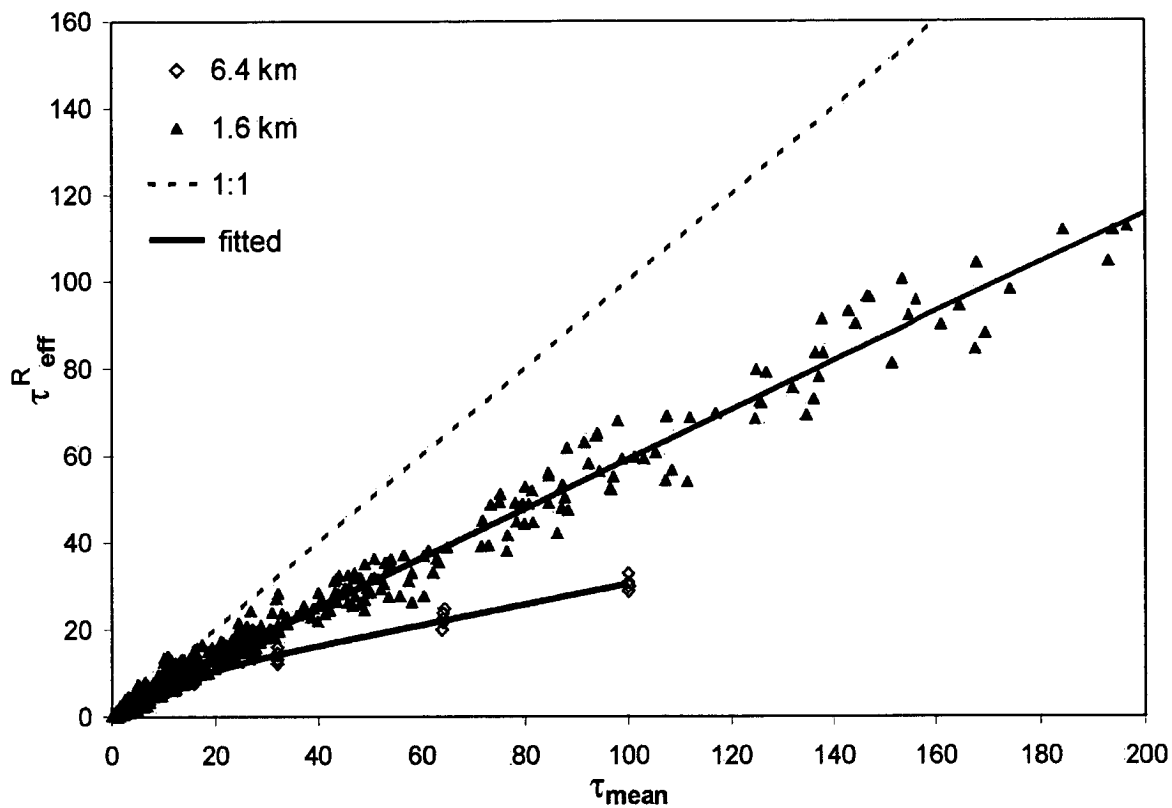
Figure 4.5: The effective optical depth based on reflectance, τ_{eff}^R, plotted as a function of the mean optical depth, τ_{mean}. For a solar zenith angle of 40 degrees and pixel sizes of 6.4 km and 1.6 km. Solid lines are the empirical parameterizations for the two pixel sizes. The dashed line is the one-to-one reference line that represents the homogenous cloud case.

calculations: $\lambda = \frac{\text{current spatial scale}}{25m}$. The function (4.2) is of the same form as that developed for lognormal multifractal clouds by *Borde and Isaka* [1996] and for bounded cascade clouds by *Szczap et al.* [2000a], but here an explicit dependence on pixel size has been introduced in order to generalize the parameterization to different resolutions. The pixel size is used as a substitute for a measure of the inhomogeneity - since according to the multifractal model the average degree of fluctuation should be function of scale ratio λ. For example, the structure functions of the variations in the optical depth of the FIF multifractal cloud are [*Schertzer and Lovejoy,* 1991]

$$\langle (\Delta \tau)^q \rangle \propto \lambda^{K(q) - Hq}, \qquad (4.3)$$

where $\Delta \tau$ are the fluctuations in optical depth at scale λ, q is any positive exponent and $K(q)$ is a function that is characteristic to the multifractal. The degree of departure from the PPH case should be related to fluctuations of τ in some way, but without knowing the exact relationship involved the very simple form λ^{-k} is assumed to quantify the degree of homogeneity.

The constants in (4.2) were determined using a Levenberg-Marquardt non-linear least squares fit to the τ_{eff}^R values for all pixel sizes from 0.8 to 6.4 kilometers and for all solar zenith angles. Since there were many more data points at the smaller spatial scales, the points were weighted by the inverse of the number of points at that pixel size, in order to assign each scale equal importance. The parameter values that were determined in this manner are: $A = 11.26$, $B = 8.02$, $C = 10.1$, $D = 6.72$, $k = 0.607$. The solid lines that are shown in figure 4.5 are the values calculated using equation (4.2) with these parameters, at the spatial scales of 1.6 km and 6.4 km.

To further illustrate the effect of spatial resolution, Figure 4.6 shows the values

calculated using (4.2) at 4 different pixel sizes. At small pixel sizes and small values of τ_{mean}, τ_{eff} approaches τ_{mean}. As pixel size increases, the deviation from PPH behavior (where $\tau_{eff} = \tau_{mean}$) also increases. Note that equation (4.2) is not meant to be used for pixel sizes less than 0.8 km due to the errors between τ_{eff}^R and τ_{eff}^T, and between τ_{eff}^R at different solar zenith angles. Nevertheless, it is interesting to note that the asymptotic slope $D\lambda^{-k}$ would achieve a PPH value of 1 for a spatial scale of close to 575m ($\lambda \sim 23$). This would imply that at this scale the horizontal photon transport completely smooths over any inhomogeneity effects (see also *Marshak et al.*[1995] for radiative smoothing).

To investigate the accuracy of the parameterization, equation (4.2) is compared with the τ_{eff}^R determined from the Monte Carlo radiative transfer results. The root-mean-square dispersion between the two series, $D_{disp}(\tau_{eff}^{calc}, \tau_{eff}^R)$, is presented in Figure 4.7 as a function of solar zenith angle for the pixel sizes 1.6 km, 3.2 km and 6.4 km. Again, the errors in the parameterization increase with zenith angle and decrease with spatial averaging size. For comparison, the root-mean-square dispersion that results from the traditional approach of using a PPH cloud with the *same* mean optical depth as the multifractal one, $D_{disp}(\tau_{mean}, \tau_{eff}^R)$, is also shown in Figure 4.7. Typically the errors when using the effective optical depth parameterization are 2 to 4 times smaller than when using the PPH assumption alone. Furthermore, the error when using the PPH assumption alone increases with pixel size, as previously noted in section 4.3.1 and shown in figure 4.5. This means that the larger the spatial scale, the greater the improvement in using the effective optical depth approximation.

To show how these values of $D_{disp}(\tau_{eff}^{calc}, \tau_{eff}^R)$ translate to transmittance errors, Figure 4.8 shows the absolute errors in transittance that would result from using t_{eff}^{calc} in PPH calculations instead of a true multifractal cloud calculation. For com-
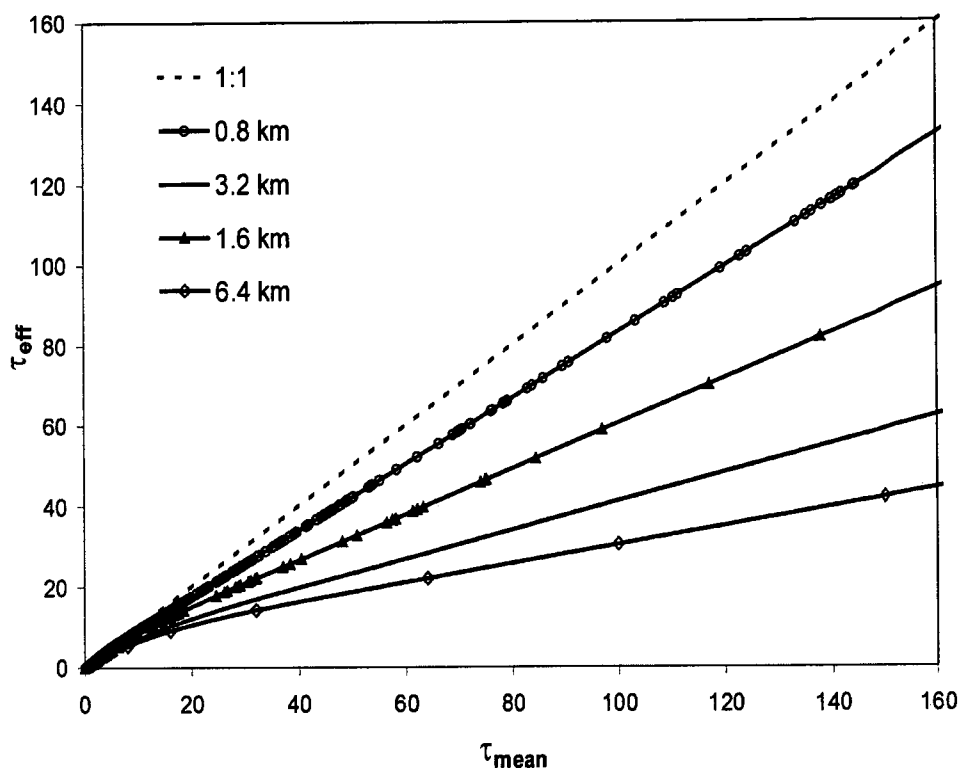
Figure 4.6: The parameterization of the effective optical depth, τ_{eff}^{calc}, as a function the mean optical depth and pixel size. Plotted to show the effect of pixel size. No true values are shown, only the parameterized values from function . The dotted line is a one-to-one reference line that shows the position of PPH cloud in the graph.
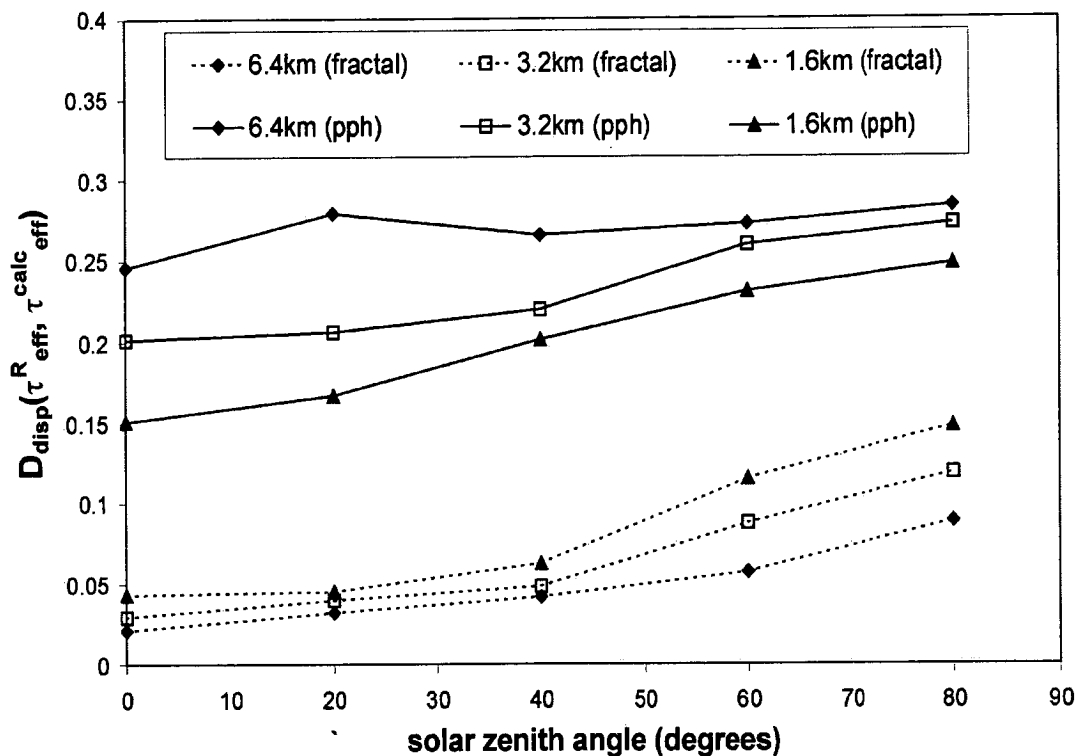
Figure 4.7: The root-mean-square dispersion, $D_{disp}(\tau_{eff}^R, \tau_{eff}^{calc})$, between the calculated effective optical depth and the true effective optical depth (derived from the monte carlo calculations). The points linked by the dotted lines (labelled fractal) show the errors when using the parameterisation, while the points linked by solid lines show the errors that would result from using the common assumption of a PPH cloud with optical depth equal to the mean optical depth of the cloud.
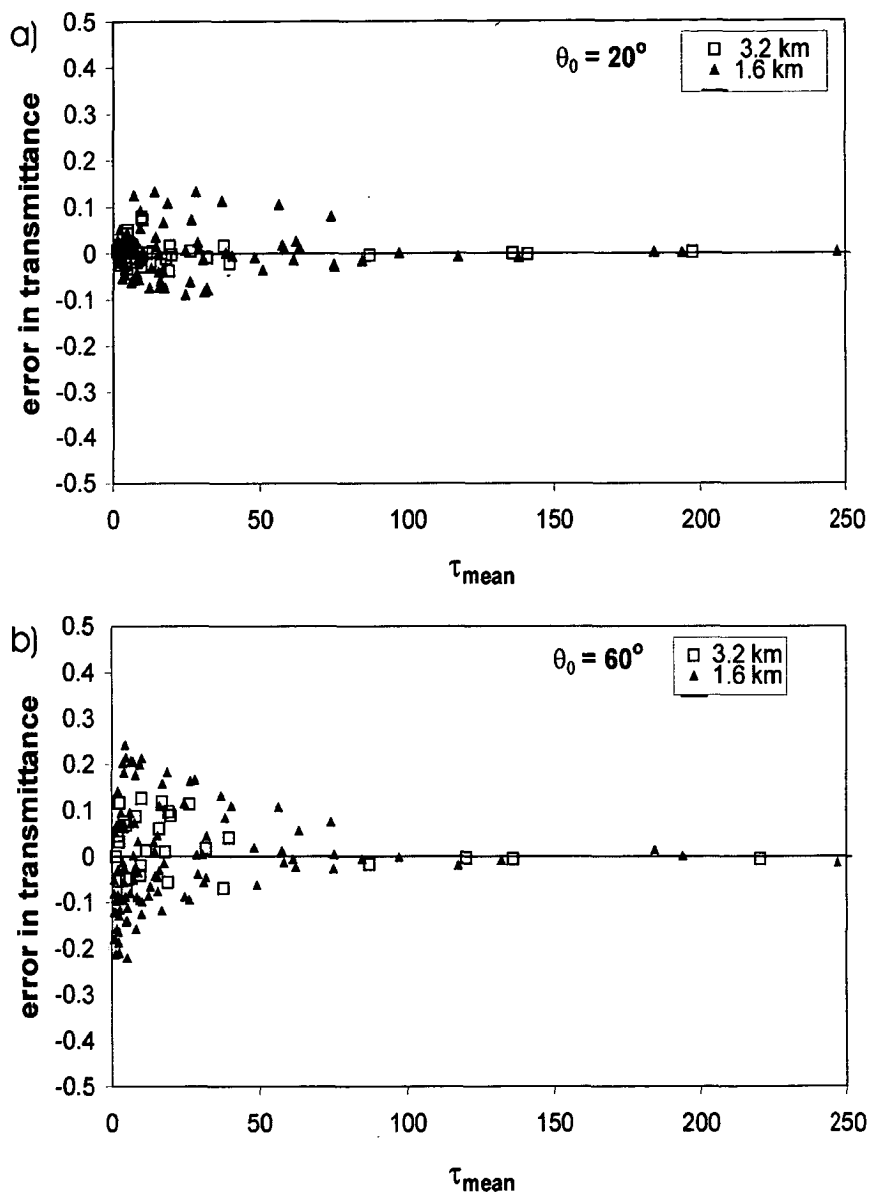
Figure 4.8: The absolute errors in transmission when using the effective optical depth approximation with τ_{eff}^{calc}, instead of a monte carlo radiative model with multifractal cloud. For solar zenith angles of a) 20 and b) 60 degrees

parison Figure 4.9 shows the absolute errors in transmittance that results from the traditional approach of using a PPH cloud with the *same* mean optical depth as the multifractal one. It can be seen that while significant errors remain when using the effective optical depth approximation with τ_{eff}^{calc}, they are significantly lower than the traditional method and the mean bias has been removed so that the errors are distributed around zero.

4.4 Non-Conservative Scattering Results

In this section the effective optical properties of absorbing cloud fields are considered. Figure 4.10 shows the transmittance (T), reflectance (R) and absorptance (A) for homogeneous and multifractal clouds, both with single-scattering albedo ω of 0.99. The spatial scale of these results is 6.4 km and the solar zenith angle used is 40°. The error bars shown are again due to the difference between the five different realizations of the multifractal field. As in the case of non-absorbing clouds, the transmittance is consistently higher, and the reflectance lower, for multifractal clouds than for homogeneous clouds. The absorptance too is lower in multifractal clouds. The absolute differences in radiative parameters (R, T, A) between the cloud model types are in general slightly less than those of the purely scattering clouds shown in figure 4.1, but are still significant. Moving to the case of $\omega = 0.95$, shown in figure 4.11, it can be seen that with absorption increased even more the differences between the PPH cloud and the multifractal cloud are further reduced. This general trend of decreased differences with decreased ω is presumably because the increase in absorption reduces the average distance travelled by photons in the cloud and hence reduces the importance of cloud spatial structure. Note that the radiative properties dependence on optical depth are decreased for the lower values

97
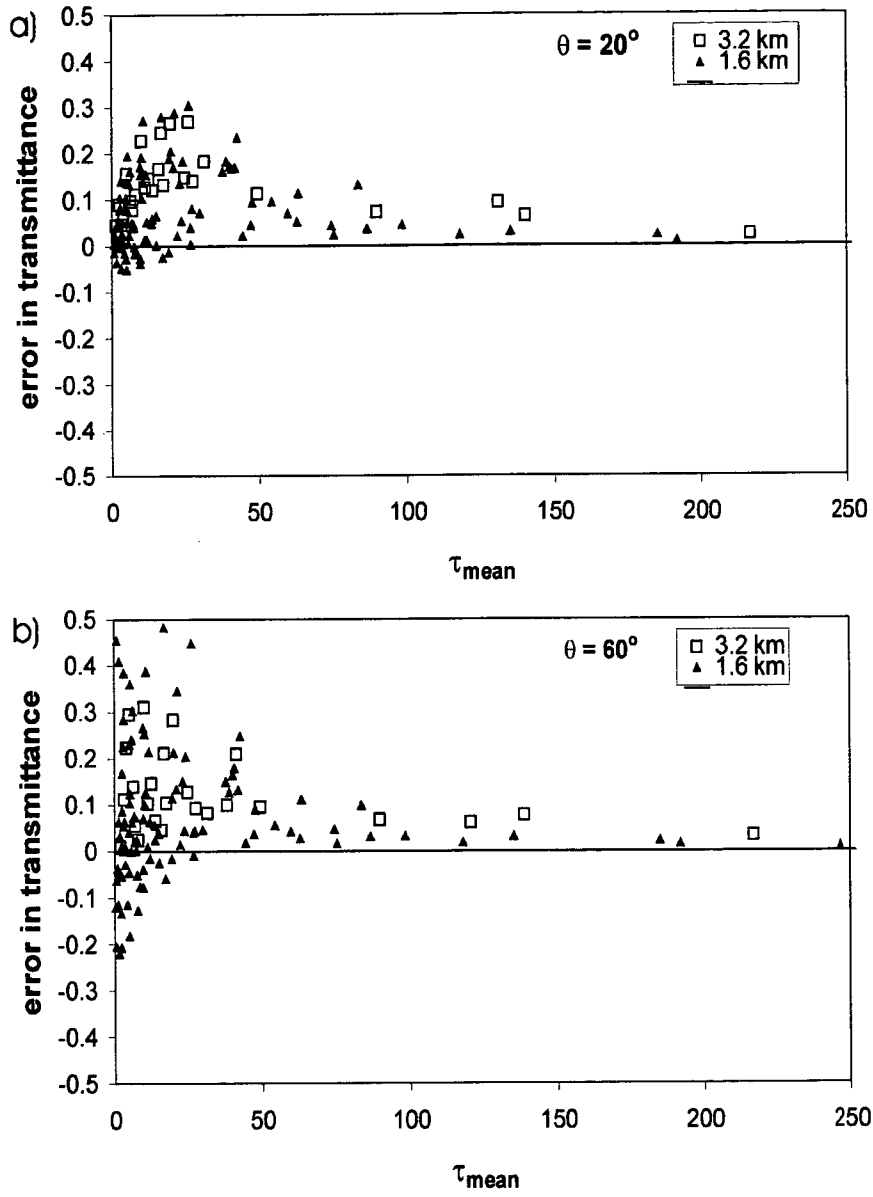
Figure 4.9: The absolute errors in transmission when using PPH assumption, instead of a monte carlo radiative model with multifractal cloud. For solar zenith angles of a) 20 and b)60 degrees

98
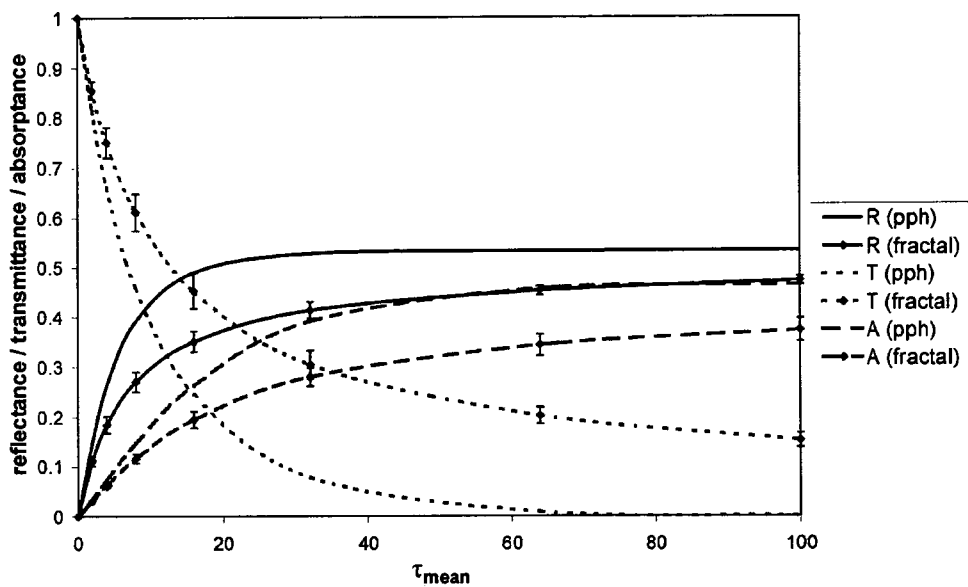
Figure 4.10: The reflectance, transmittance and absorptance for clouds with single-scattering albedo of 0.99. Multifractal points are for 6.4 km pixels. Both PPH and multifractal cloud values are for a solar zenith angle of 40 degrees.
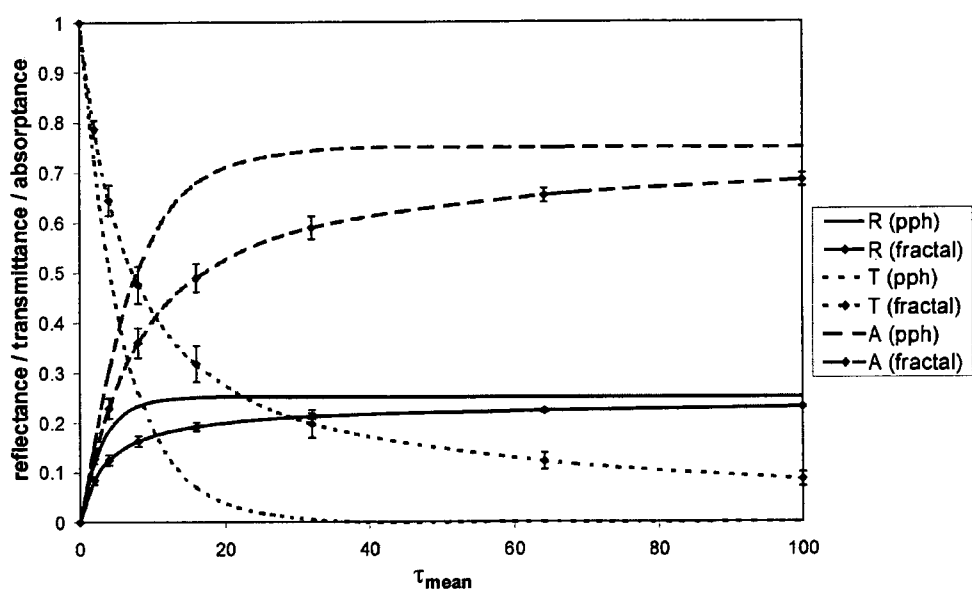
Figure 4.11: The reflectance, transmittance and absorptance for clouds with single-scattering albedo of 0.95. Multifractal points are for 6.4 km pixels. Both PPH and multifractal cloud values are for a solar zenith angle of 40 degrees.

of τ.

As in the case of the non-absorbing clouds, the goal is to find a PPH cloud that can replace the multifractal cloud in radiative transfer calculations. However there are now three radiative values to keep constant between the multifractal cloud model and the equivalent PPH cloud: T, R and A. Even using the approximation that in large enough cloud fields

$$T + R + A \simeq 1, \tag{4.4}$$

this still demands two independent properties to define the equivalent PPH cloud. Again following *Szczap et al.* [2000b], an effective single-scattering albedo is therefore added to the effective optical depth used in section 4.3. Specifically, the effective single-scattering albedo is defined as the single scattering albedo of the PPH cloud with the same radiative properties as the multifractal cloud field under consideration.

4.4.1 Consistency of the approximations for absorbing clouds

For cloud fields of sufficiently large horizontal extent (which makes horizontal transport of photons negligible), the condition (4.4) holds and the effective optical properties may be calculated using any two of the three radiative outputs (T, R, or A). However, for smaller pixels horizontal transport may be significant, so that instead of equation (4.4) we have

$$T + R + A + H = 1, \tag{4.5}$$

101

where H is the horizontal flux. Now we have 3 free parameters instead of 2. That is, even if a PPH cloud has the same T and R as the multifractal cloud field it will not have the same absorptance if the net horizontal transport is not the same. Denote the effective optical depth and effective single-scattering albedo based on transmittance and reflectance by τ_{eff}^{RT} and ω_{eff}^{RT} respectively. Similarly, the optical properties of a PPH cloud with the same transmittance and absorptance as the multifractal cloud field are τ_{eff}^{TA} and ω_{eff}^{TA}, while those of a PPH cloud with the same R and A values are τ_{eff}^{RA} and ω_{eff}^{RA}. All these effective optical properties were calculated by comparing the Monte Carlo radiative transfer values of T, R, or A for the multifractal cloud fields to those values for the PPH cloud, using (2D) spline interpolation to fill the gaps between calculated values.

Effective optical depth

To quantify the differences between the three different definitions of the effective optical depth the root-mean-square dispersion, as defined in equation (4.1), is again used. The values of $D_{disp}(\tau_{eff}^{RT}, \tau_{eff}^{TA})$ are shown in Table 4.1. These values were calculated for all single-scattering albedos considered three different single scattering albedos: $\omega = 0.90, 0.95, 0.99$. As in the non-absorbing case, it can be seen that the discrepancy between different effective optical depth definitions is greater at the higher solar zenith angles and smaller pixel sizes. If the acceptable level of discrepancy is taken to be 5%, Table 4.1 shows that the 3.2 km pixels meet this criterium for $\theta_0 \leq 60°$, and that the 1.6 km pixels are within this range for $\theta_0 \leq 40°$, but the 0.8 km pixels generate errors of less than the acceptable range only when $\theta_0 = 0°$. Very similar results are seen for $D_{disp}(\tau_{eff}^{RT}, \tau_{eff}^{RA})$.

102

Table 4.1: Presents the root-mean-square dispersion, $D_{disp}(\tau_{eff}^{RT}, \tau_{eff}^{TA})$, between two definitions of the effective optical depth of multifractal cloud, τ_{eff}^{RT} and τ_{eff}^{TA}. Also shown is the root-mean-square dispersion between two defintions of the effective single-scattering albedo, $D_{disp}(\omega_{eff}^{RT}, \omega_{eff}^{TA})$. Both calculated at 5 solar zenith angles (θ_0) and three spatial averaging sizes, for absorbing clouds with single scattering albedos $\omega = 0.9, 0.95, 0.99$.

ω	θ_0	$D_{disp}(\tau_{eff}^{RT}, \tau_{eff}^{TA})$			$D_{disp}(\omega_{eff}^{RT}, \omega_{eff}^{TA})$		
		3.2 km	1.6 km	0.8 km	3.2 km	1.6 km	0.8 km
	0°	0.014	0.019	0.036	0.007	0.009	0.102
	20°	0.020	0.023	0.081	0.016	0.037	0.144
0.9	40°	0.029	0.034	0.141	0.021	0.028	0.206
	60°	0.038	0.084	0.260	0.033	0.044	0.211
	80°	0.151	0.147	0.305	0.053	0.058	0.315
	0°	0.023	0.027	0.049	0.012	0.017	0.119
	20°	0.031	0.032	0.093	0.021	0.044	0.154
0.95	40°	0.038	0.044	0.174	0.030	0.036	0.247
	60°	0.049	0.098	0.285	0.041	0.051	0.258
	80°	0.169	0.182	0.327	0.063	0.065	0.373
	0°	0.030	0.034	0.053	0.021	0.022	0.125
	20°	0.042	0.041	0.109	0.031	0.053	0.163
0.99	40°	0.047	0.044	0.185	0.044	0.049	0.259
	60°	0.050	0.110	0.295	0.053	0.068	0.269
	80°	0.179	0.222	0.379	0.077	0.079	0.320

Effective single-scattering albedo

Table 4.1 also shows the root-mean-square dispersion between ω_{eff}^{RT} and ω_{eff}^{TA}, $D_{disp}(\omega_{eff}^{RT}, \omega_{eff}^{TA})$. This shows the same general trends of discrepancies increasing with solar zenith angle and decreasing with increasing pixel size. Using the same criteria of 5% error, both 3.2 km and 1.6 km pixels are acceptable for solar zenith angles of 60° or less, but the 0.8 km pixels are never within this acceptable range. Combining these results with those for the effective optical depth, it can be seen that 3.2 km pixels are acceptable for $\theta_0 \leq 60°$, 1.6 km pixels are acceptable when $\theta_0 \leq 40°$, and 0.8 km pixels are never acceptable. Pixels larger than 3.2 km would increase the acceptable solar zenith angle range even further. Note that this acceptable range for the absorbing cloud is the same as that for the non-absorbing cloud found in section 4.3.1.

For the remainder of this analysis it was chosen, fairly arbitrarily, to work with τ_{eff}^{RT} and ω_{eff}^{RT}. Using a PPH cloud with these optical properties would produce the same reflectance and transmittance as the multifractal cloud field - there would be some error in absorptance as detailed above, but as long as the pixel size and solar zenith angles were within our acceptable range, this error would be small.

4.4.2   Empirical parameterization

Effective optical depth

The parameterization of effective optical depth of non-absorbing clouds found in section 4.3.2 is now generalised to include clouds with single scattering albedo less than 1. Figure 4.12 shows τ_{eff}^{RT} as a function of τ_{mean} for four different single-scattering albedos, at a pixel size of 6.4 km. The general trend is for the effective
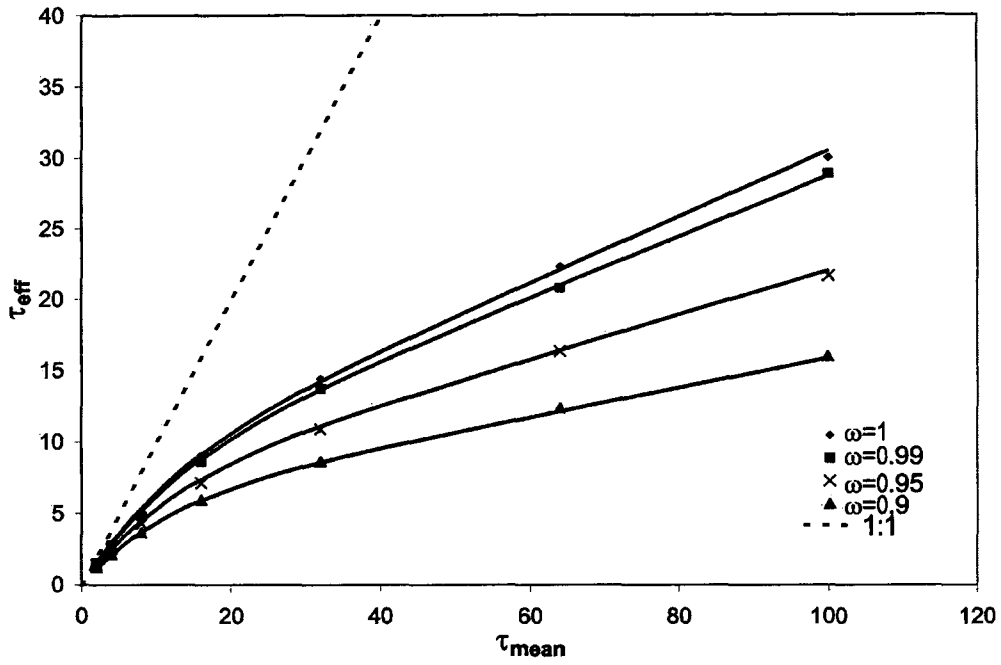
Figure 4.12: The effective optical depth τ_{eff}^{RT} as a function of the mean optical depth, for clouds with a range different single-scattering albedos. All values are for pixels of 6.4km x 6.4 km. Points are the average values of τ_{eff}^{RT} over 5 multifractal realizations. The dashed line is the one-to-one reference line, and the solid lines are the values given by the empirical parameterization.

optical depth to be lower for lower single scattering albedos, i.e. for the effective optical depths to decrease with increased absorption. The asymptotic slope (that the effective optical depth approaches at high τ_{mean}) is also lower for lower ω.

The values of τ_{eff}^{RT} for absorbing cloud with different values of single scattering albedo were fitted to the function (4.2) that was used for non-absorbing clouds in section 4.3.2. The parameters B and D in (4.2) were adjusted for absorbing clouds, with the other parameters held to the same values as for non-absorbing clouds. These two parameters were allowed to vary becasue visual observation of the data indicated that changing single scattering albedos changed the slope and intercept of the assymptotic line (which τ_{eff}^{RT} aproachs at high τ_{mean}). This fit was performed using a non-linear least squares fit for all pixel sizes calculated between 0.8 and 6.4 kilometers and all solar zeniths angles considered. Figure 4.13 shows the values of the parameters B and D as a function of $(1 - \omega)$, which is a measure of the degree of absorption per scattering event. The parameter B is roughly linear in $(1 - \omega)$ and fits the line $8.02 - 20.19(1 - \omega)$. The parameter D on the other hand appears to be exponentially decreasing with $(1 - \omega)$ and can be estimated by the relation $6.7 \exp(-8.26(1 - \omega))$. This gives a final set of parameters for equation (4.2) to estimate the effective optical depth: $A = 11.26$, $B = 8.02 - 20.19(1 - \omega)$, $C = 10.1$, $D = 6.7 \exp(-8.26(1 - \omega))$, $k = 0.607$. The solid lines shown in figure 4.12 are the values calculated using the parameterization (4.2) with these parameters at pixel size 6.4 km.

Effective single-scattering albedo

Figure 4.14 shows the ratio ω_{eff}^{RT}/ω as a function of the mean optical depth of the multifractal cloud field for a pixel size of 3.2 km and three different single-scattering albedos. This ratio is usually less than one, i.e. the effective single-scattering albedo

106
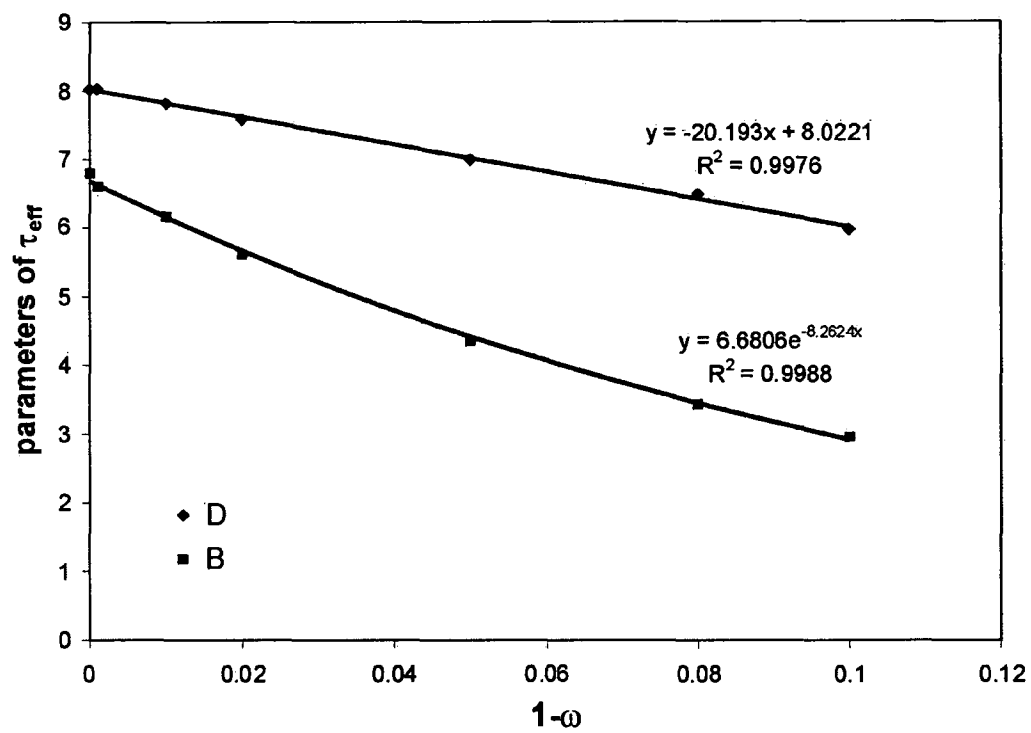
Figure 4.13: The parameters of the empirical fit that were varied with single scattering co-albedo $(1-\omega)$.

is less than the actual single-scattering albedo in the multifractal cloud.   The
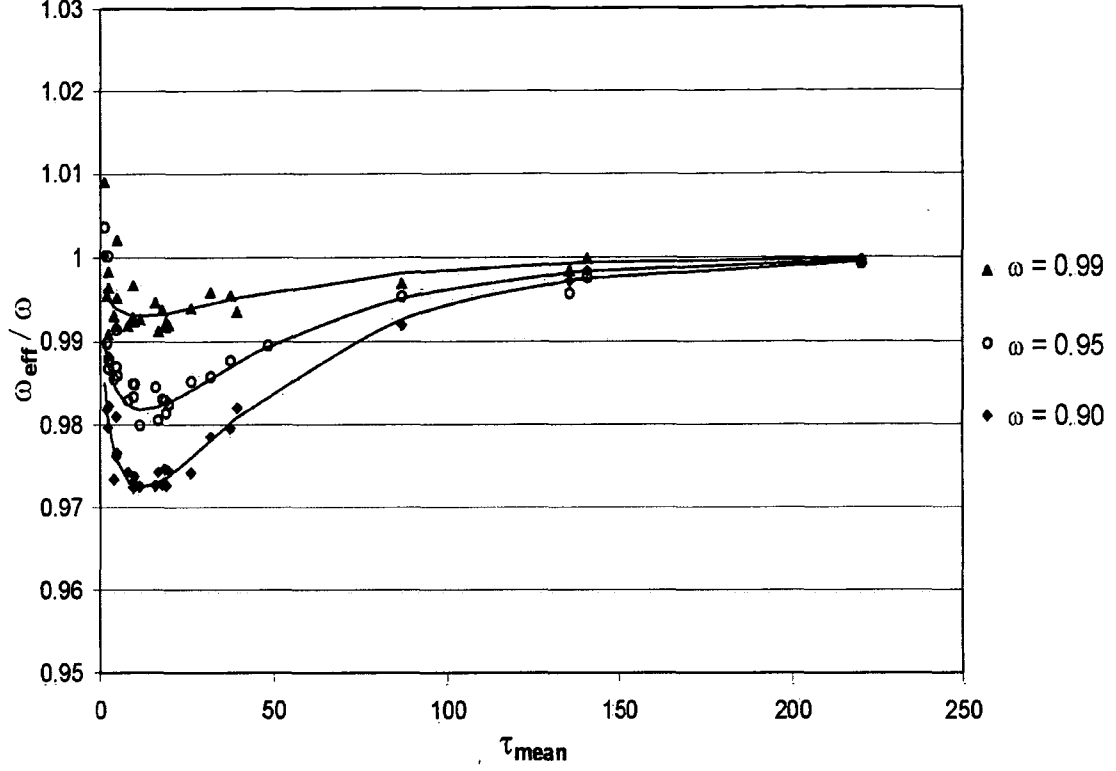
Figure 4.14: The ratio of the effective single-scattering albedo to the true value in multifractal cloud, ω^{RT}_{eff}/ω, as a function of the mean optical depth. For three values of the single scattering albedo, at a pixel size of 3.2 km. The solid lines represent the empirical parameterization.

general trend with τ_{mean} is a rapid decrease in ω^{RT}_{eff}/ω to a minimum, followed by a slow asymptotic return to unity. This indicates that the increased absorption is most significant at low to moderate cloud optical depths. Also, the ratio ω^{RT}_{eff}/ω is in general lower for lower ω. Finally, the effect of spatial averaging scale is shown in figure 4.15, for a single-scattering albedo of 0.90. Again the difference between the multifractal cloud and PPH cloud increases with averaging scale, demonstrated

108

by the decrease in ω_{eff}^{RT}/ω.
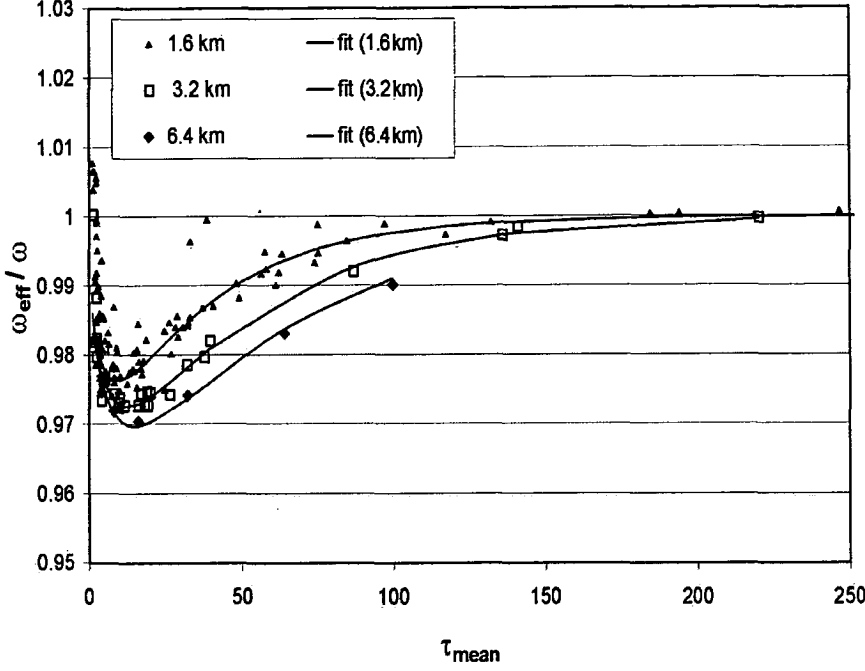
Figure 4.15: The ratio between the effective single-scattering albedo to the actual single-scattering albedo in the multifractal cloud, ω_{eff}^{RT}/ω, as a function of mean optical depth when $\omega = 0.90$. For three different pixel sizes. The solid lines are the values for the empirical parameterization.

Having observed these trends in the values of the effective single-scattering albedo, an empirical fit to the data was made using the following function:

$$\omega_{eff}^{calc} = \omega \left\{ 1 - E(1-\omega)^l \tau_{mean}^m \exp\left(\frac{-\tau_{mean}^n}{F(1 - G\lambda^{-p})} \right) \right\}, \qquad (4.6)$$

where E, F, G, l, m, n, and p are constants. The function (4.6) has the general form of that used by Szczap et al. [2000b], but once more their inhomogeneity parameter has been replaced in (4.6) by an explicit dependence on the spatial scale

109

λ. Another non-linear least squares fit was performed to find the values of the constants in the function (4.6), using all data points of spatial scale 0.8, 1.6, 3.2 and 6.4km and all solar zenith angles. The values of the constants were thus found to be $E = 0.061$, $F = 17.37$, $G = 6.59$, $l = 0.603$, $m = 0.489$, $n = 0.784$, and $p = 0.613$. The solid lines shown in figure 4.14 and figure 4.15 were found using these parameter values in the function (4.6).

4.4.3 Error analysis

The errors in the effective optical depth parameterization for absorbing clouds, in the form of $D_{disp}(\tau_{eff}^{RT}, \tau_{eff}^{calc})$, are shown in Table 4.2, for all solar zenith angles and for spatial scales of 1.6 km, 3.2 km and 6.4 km. This error is approximately 5% for the 6.4 km pixels, and 10% for the 1.6 km pixels, with the 3.2 km pixels falling between the two. There is less of an increase in dispersion with solar zenith angle in Table 4.2 then there was for the non-absorbing case, shown in Figure 4.7, presumably because absorption decreases horizontal transport of photons and hence the effect of solar zenith angle. The errors for the parameterisation are significantly less then those for the PPH assumption alone, $D_{disp}(\tau_{eff}^{RT}, \tau_{mean})$,shown in Table 4.3 to be on the order of 20-30%.

Table 4.2 also presents the error in the parameterization of the effective single-scattering albedo, $D_{disp}(\omega_{eff}^{RT}, \omega_{eff}^{calc})$. For both the 6.4 km and 3.2 km pixels, errors are less than 5% with little variation with solar zenith angle, but errors for the 1.6km pixels vary between 5 and 15 percent as solar zenith angle increases. At the smaller pixel size the dependence on solar zenith angle is larger because the horizontal transport becomes more significant. At all three pixel sizes the parameterization of the effective single-scattering albedo gives a significant improvement on the errors

Table 4.2: Contains the root-mean-square dispersion, $D_{disp}(\tau_{eff}^{RT}, \tau_{eff}^{calc})$, between the parameterised effective optical depth. and the effective optical depth of the multifractal cloud found using the radiative transport results. Also shows the root-mean-square dispersion, $D_{disp}(\omega_{eff}^{RT}, \omega_{eff}^{calc})$, between the effective single-scattering albedo that was derived from the Monte Carlo radiative transfer results and that predicted by the parameterisation. These were found for absorbing clouds at 5 solar zenith angles (θ_0) and three spatial averaging sizes.

θ_0	$D_{disp}(\tau_{eff}^{RT}, \tau_{eff}^{calc})$			$D_{disp}(\omega_{eff}^{RT}, \omega_{eff}^{calc})$		
	6.4 km	3.2 km	1.6 km	6.4 km	3.2 km	1.6 km
0°	0.032	0.045	0.097	0.006	0.013	0.048
20°	0.035	0.052	0.106	0.008	0.013	0.044
40°	0.044	0.055	0.111	0.008	0.014	0.065
60°	0.057	0.085	0.109	0.010	0.030	0.093
80°	0.051	0.096	0.133	0.019	0.044	0.144

Table 4.3: The relative dispersion, $D_{disp}(\tau_{eff}^{RT}, \tau_{mean})$, that would result from using the common assumption of a PPH cloud with optical depth equal to the mean optical depth of the (multifractal) cloud. Also presents $D_{disp}(\omega_{eff}^{RT}, \omega)$ - the error that results from using a PPH cloud with the same single-scattering albedo as the multifractal cloud (rather than the effective). Found for absorbing clouds at 5 solar zenith angles (θ_0) and three spatial averaging sizes.

θ_0	$D_{disp}(\tau_{eff}^{RT}, \tau_{mean})$			$D_{disp}(\omega_{eff}^{RT}, \omega)$		
	6.4 km	3.2 km	1.6 km	6.4 km	3.2 km	1.6 km
0°	0.306	0.240	0.177	0.047	0.053	0.087
20°	0.310	0.246	0.198	0.047	0.052	0.103
40°	0.321	0.252	0.187	0.046	0.053	0.117
60°	0.334	0.273	0.185	0.045	0.057	0.224
80°	0.328	0.268	0.196	0.046	0.096	0.265

that results from using the PPH assumption when the cloud is multifractal in nature, $D_{disp}(\omega_{eff}^{RT}, \omega)$, which are shown in Table 4.3.

To further explore the absolute errors when using the effective optical properties approximation, Figure 4.16 plots the absolute error in transmittance when using the effective optical properties parameterisation instead of a monte carlo simulation with multifractal cloud. Results are shown for three different single-scattering albedos, with errors decreasing as ω decreases.

4.5 Accuracy of the approximation under different conditions

In this section the focus is on the accuracy of the empirical optical properties approximation and our parameterization of it, when the scattering phase function or the cloud fractal parameters vary. The case where a reflected radiance value is required, instead of the total reflectance, is also considered.

4.5.1 Varying the asymmetry parameter

Thus far in the analysis the single-scattering albedo has been varied, but the scattering phase function has not. This is clearly not realistic since the scattering phase function will vary with cloud droplet size distribution and the wavelength of light under consideration. In order to test the effect of different phase functions on the parameterisation of the effective optical properties, the Henyey-Greenstein phase function was kept but the asymmetry parameter g was varied. Figure 4.17 shows the variation in g with cloud effective droplet radius for four wavelengths between

112
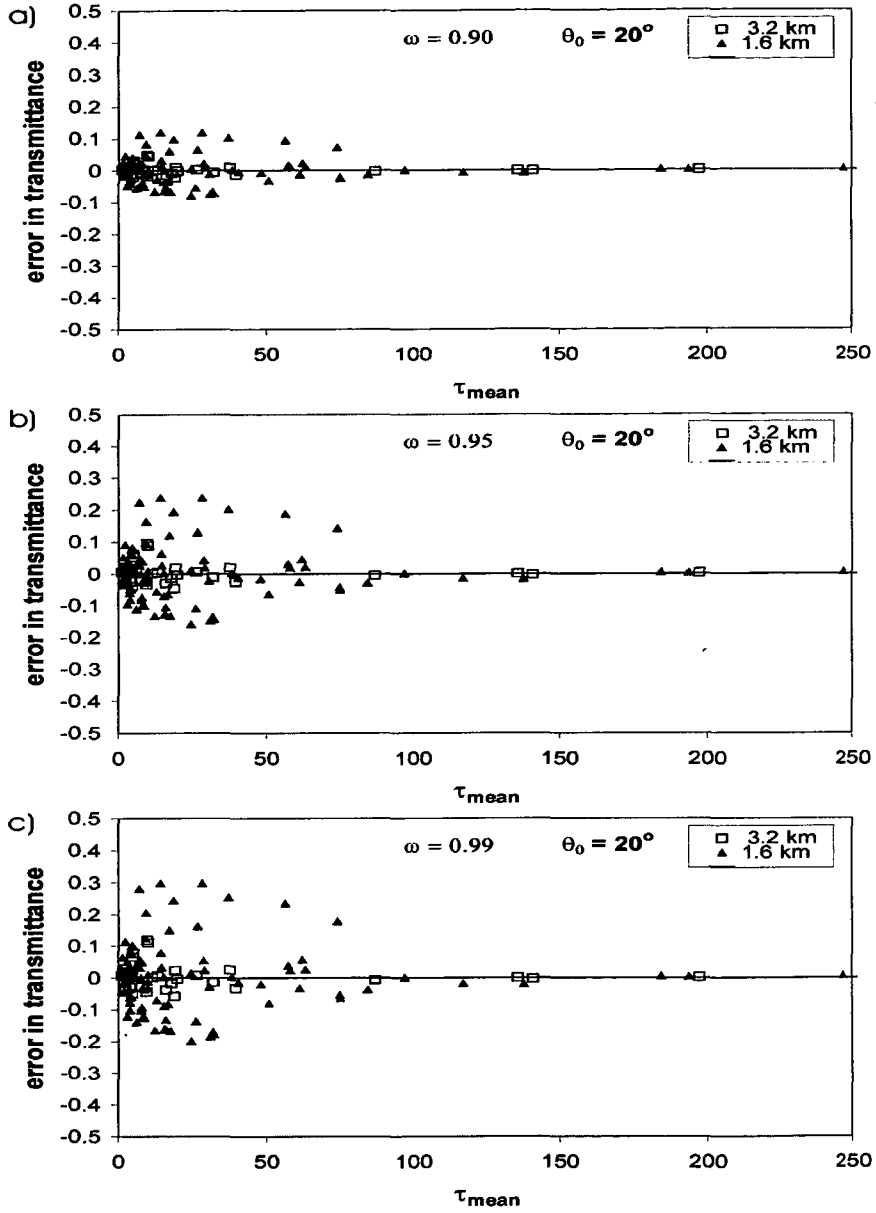
Figure 4.16: The absolute errors in transmission when using the effective optical properties parameterisation instead of a monte carlo radiative model with multi-fractal cloud. For 3 single scattering albedos.

113
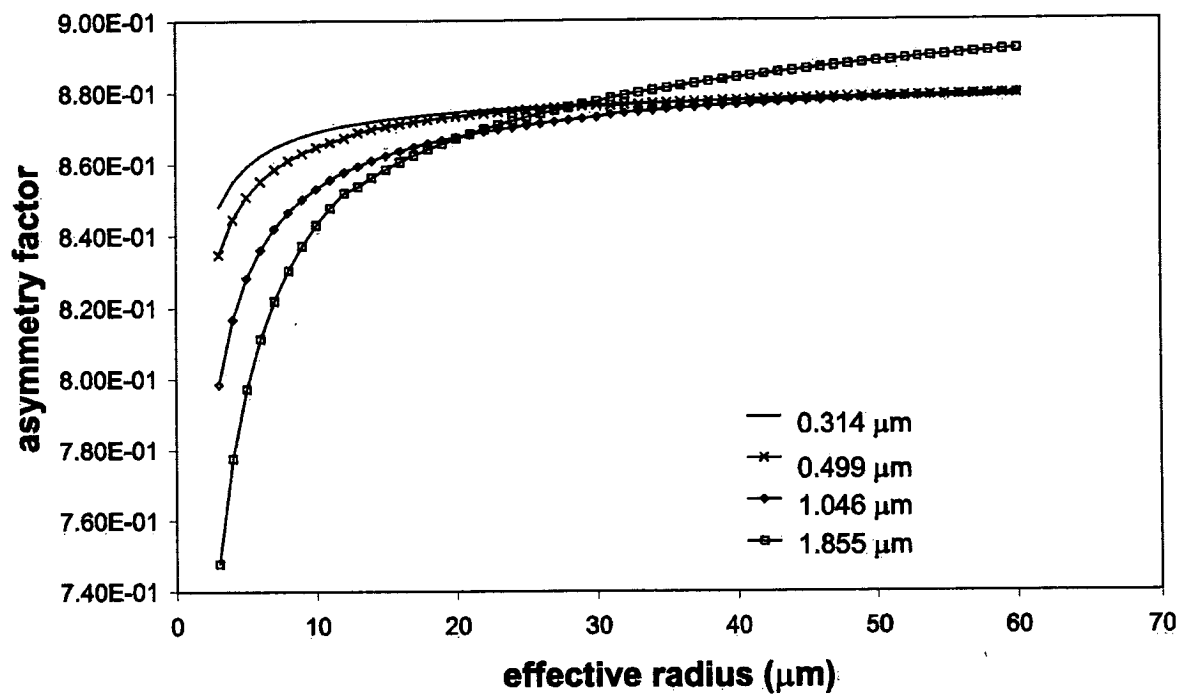
Figure 4.17: The asymetry factor, g, as a function of the effective cloud droplet radius for several wavelengths across the solar spectrum.

114

0.314 μm and 1.855 μm. These were calculated using the parameterisation of *Hu and Stamnes* [1993]. From figure 4.17 it can be seen that for much of the solar spectrum and for typical droplet radius values, the asymmetry parameter is between 0.8 and 0.9. Therefore the Monte Carlo radiative transfer calculations described in sections 2.2 and 4.2.2 were performed for both multifractal and PPH cloud fields with $g = 0.8$ and $g = 0.9$. Only the non-absorbing case is considered here.

The effective optical depths were found from the radiative transport results as described in section 4.3.1, using PPH cloud with the same asymmetry parameter as the multifractal cloud. The τ_{eff}^R found for multifractal cloud fields of spatial size 6.4 km and 1.6 km, with $g = 0.8$ and $g = 0.9$ are plotted in Figure 4.18. Also in the figure are solid lines that represent the parameterization described in section 4.3, which were derived uisng $g = 0.85$. These results indicate that there is only a small variation in τ_{eff}^R with the change in the asymmetry factor between 0.8 and 0.9. To further quantify the parameterization errors Table 4.4 shows $D_{disp}(\tau_{eff}^{calc}, \tau_{eff}^R)$ for $g = 0.8$ and $g = 0.9$. Although there is an increase over the dispersion found in Figure 4.7 (where $g = 0.85$), it is relatively small, especially when considering that these are relatively extreme values of g within the solar spectrum. Of course this increase in error could be reduced by recalculating the constants in (4.2) at the new asymmetry factor.

The absolute errors in transmission when using the effective optical properties approximation with clouds with different values of g are can be seen in Figure 4.19.
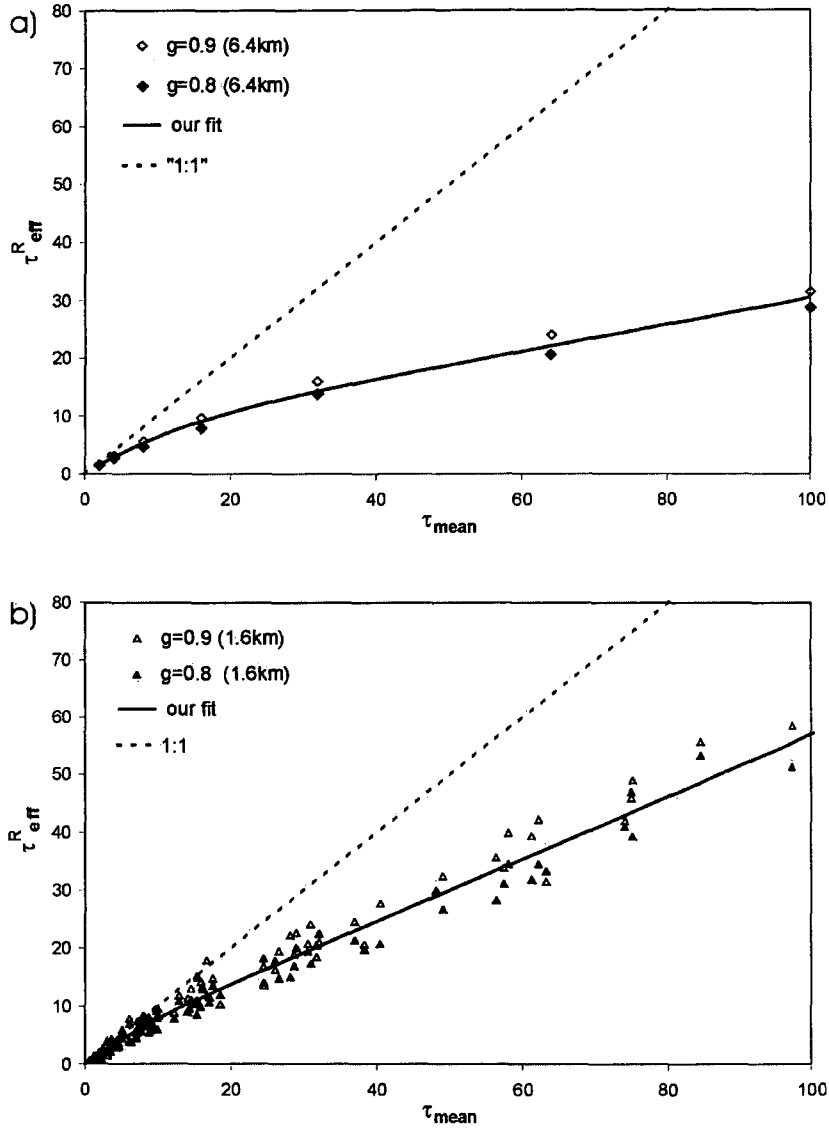
Figure 4.18: The effective optical depth for clouds with two different values of the asymmetry parameter, g=0.8 and g=0.9. The spatial averaging size is a)6.4 km and b)1.6 km. In both cases the parameterized values (derived using g=0.85) are also plotted as a solid line, and the 1:1 reference line is also shown.

116
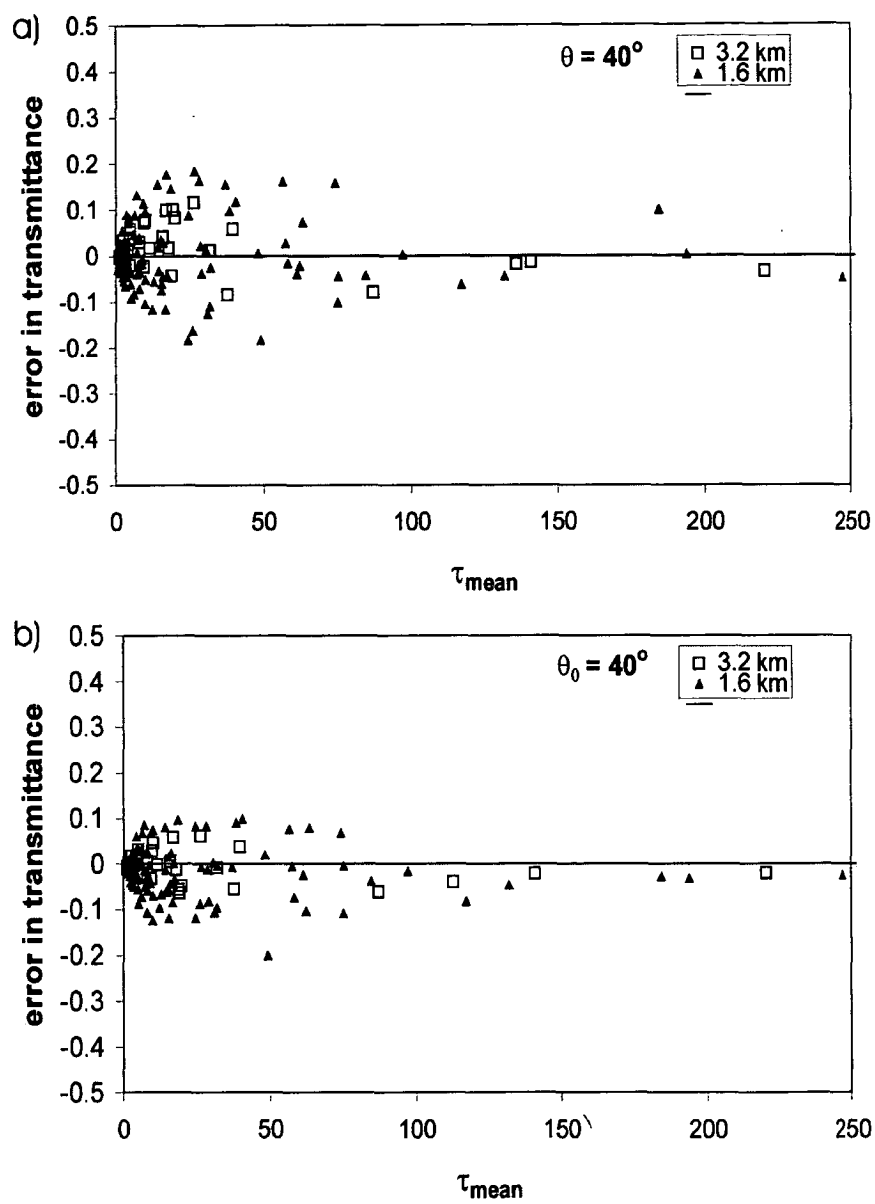
Figure 4.19: The absolute errors in transmission when using the effective optical properties approximation with varying assymetry parameter. For a) g=0.8 and b) g=0.9

117

Table 4.4: The errors involved in using the parameterisation developed here, if the asymmetry parameter is $g = 0.8$ and $g = 0.9$. Found for non-absorbing clouds at 5 solar zenith angles (θ_0) and three spatial averaging sizes.

θ_0	$D_{disp}(\tau_{eff}^R, \tau_{eff}^{calc})$, $g = 0.8$			$D_{disp}(\tau_{eff}^R, \tau_{eff}^{calc})$, $g = 0.9$		
	6.4 km	3.2 km	1.6 km	6.4 km	3.2 km	1.6 km
0°	0.074	0.075	0.081	0.053	0.063	0.075
20°	0.077	0.083	0.103	0.054	0.072	0.100
40°	0.088	0.101	0.110	0.057	0.091	0.106
60°	0.107	0.131	0.147	0.081	0.124	0.145
80°	0.123	0.158	0.212	0.101	0.135	0.206

4.5.2 Varying the fractal model parameters

The fractal model parameters used thus far were found, in chapter 3, by considering the liquid water content data from 98 flights considered as a single ensemble. However within these flights there was some small variation between cloud types and even an indication of diurnal variability for stratocumulus clouds. The fractal model parameters, α, C_1 and H, were calculated for each flight separately, solely to get some indication of how widely the fractal parameters may vary. This was done using the double trace moment analysis, described in section 2.1.5. These parameters approximated a normal distribution about the ensemble values. Cloud fields were generated using parameters at approximately one and two standard deviations above and below the mean values, as well as at the mean values, to give $3^3 = 27$ cases. The parameter values used were $\alpha = 1.2, 1.48, 1.7$; $C_1 = 0.05, 0.106, 0.15$; $H = 0.2, 0.3, 0.4$.

Radiative transfer calculations were performed for all of the multifractal cloud fields, assuming no absorption. Some reflectance results are graphed in Figure 4.20. Each part of figure 4.20 plots the three cases for one fractal parameter varying while the others are held at the mean value. The reflectance for PPH cloud is presented
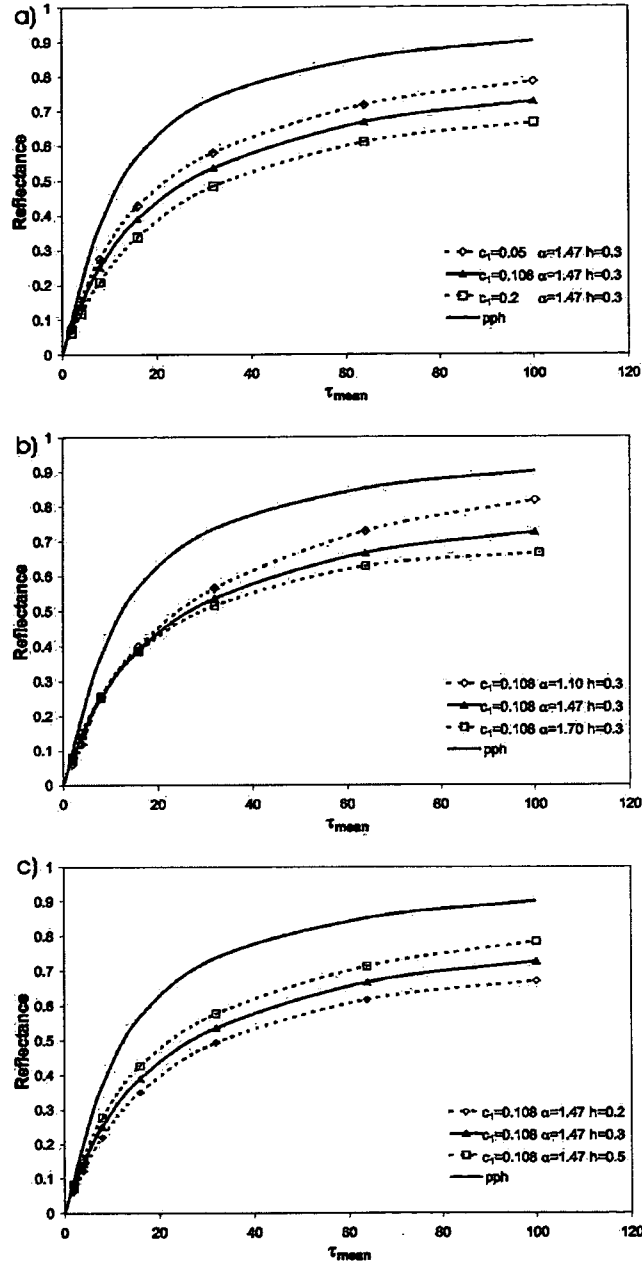
Figure 4.20: The reflectance values for multifractal cloud fields with different fractal parameters. The figures show the effect of changing the parameter: a) C_1 b) α c) H. Also shown in each figure are the reflectance curves for a multifractal field with the mean parameters, and the curve for the PPH cloud. Solar zenith angle is 40 degrees.

119

for comparison. Figure 4.20a) shows that as the inhomogeneity parameter, C_1, increases, the reflectance values decrease, as the cloud moves further from the homogeneous case. Similarly as α increases and the more extreme values appear in the field, the reflectance values decrease as seen in figure 4.20b) . However, figure 4.20c) reveals that a higher value of the non-conservation parameter H yields a higher reflectance curve that is closer to the homogeneous case, as increasing H has a smoothing effect on the field.

To analyze the accuracy of the effective optical depth parameterization, the two most extreme of these cases are considered: case A, where the cloud radiative properties are furthest from the homogeneous case, with $\alpha = 1.7$, $C_1 = 0.15$, and $H = 0.2$; case B, in which the radiative properties are closest to the homogeneous case with $\alpha = 1.2$, $C_1 = 0.05$, $H = 0.4$. For these two extreme cases the effective optical depth τ_{eff}^R was found from the radiative transfer results and the degree of error in the effective optical depth parameterization was estimated using $D_{disp}(\tau_{eff}^{calc}, \tau_{eff}^R)$, where τ_{eff}^{calc} is that given by the function (4.2). The results are presented in Table 4.5. Comparing these to the original ensemble-mean case (see Figure 4.7), it can be seen that the error is larger in both case A and case B, with the values of the root-mean-square dispersion at low solar zenith angles increasing from below 5% in the ensemble-mean case to around 10% for extreme cases. At High solar zenith angles the increase is not as great, but the errors were already large in the mean case. Note that in case B the usual pattern of greater errors at smaller spatial average size is reversed at low zenith angles. This is because the pixel size dependency in the parameterization moves it closer to the case B results as the pixel size decreases.

The absolute errors in transmission when using the effective optical properties approximation in case A and case B are shown in Figure 4.21.
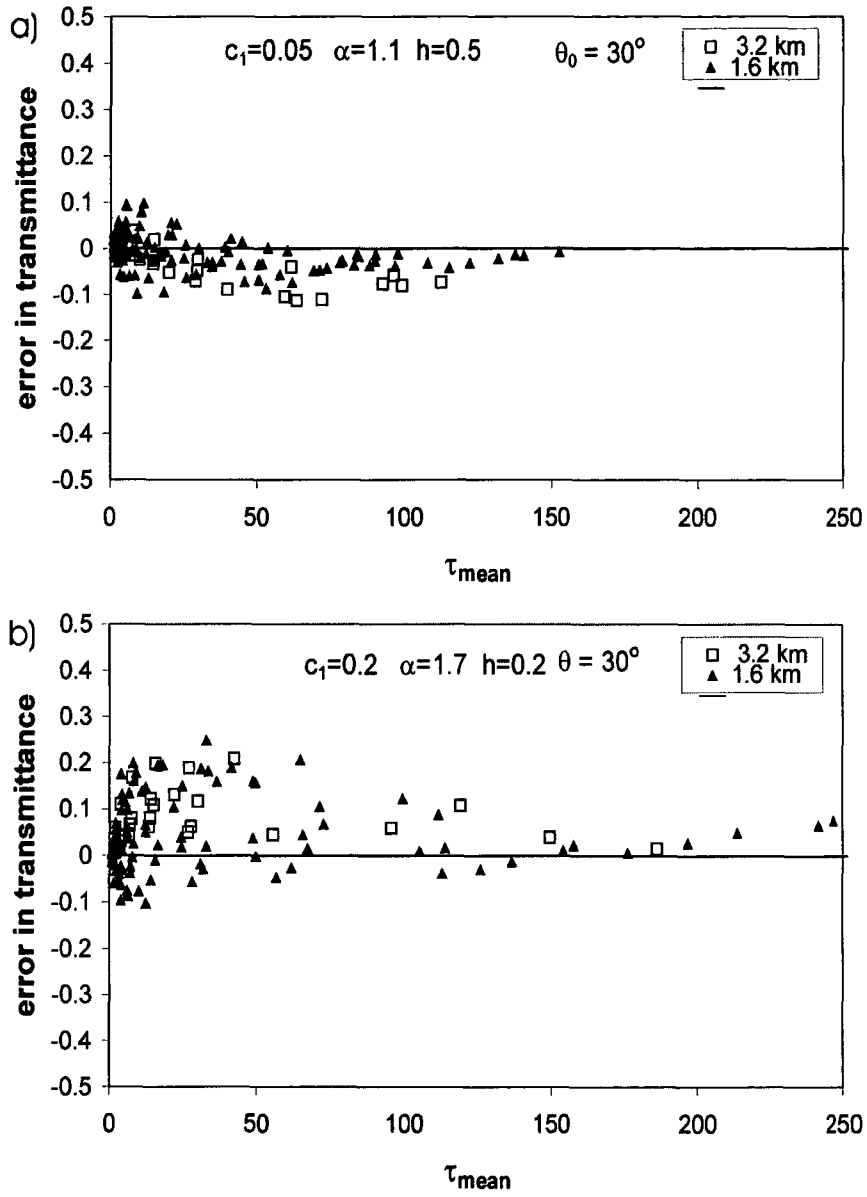
Figure 4.21: The absolute errors in transmission when using the effective optical properties approximation with varying fractal parameters. For two extreme cases (case A and B).

121

Table 4.5: The errors resulting from using our parameterisation if the cloud has different fractal parameters. Two extreme fractal parameter cases are considered: case A, where $\alpha = 1.7$, $C_1 = 0.15$, and $H = 0.2$, and case B, where $\alpha = 1.2$, $C_1 = 0.05$, $H = 0.4$. Calculated for non-absorbing clouds at 5 solar zenith angles (θ_0) and three spatial averaging sizes.

θ_0	$D_{disp}(\tau_{eff}^R, \tau_{eff}^{calc})$, case A			$D_{disp}(\tau_{eff}^R, \tau_{eff}^{calc})$, case B		
	6.4 km	3.2 km	1.6 km	6.4 km	3.2 km	1.6 km
0°	0.073	0.094	0.105	0.116	0.096	0.066
20°	0.081	0.095	0.103	0.126	0.098	0.078
40°	0.092	0.108	0.131	0.129	0.102	0.105
60°	0.130	0.134	0.161	0.132	0.112	0.136
80°	0.149	0.179	0.207	0.164	0.152	0.174

It should be noted that the two extreme cases considered are indeed quite extreme. Since each extreme fractal parameter was chosen to be at 2 standard deviations from the mean values, the probability of all three parameters being as far from the mean as case A or B would be of the order of 0.05% if the variations in the fractal parameters are independent. However, the analysis in sections 3.2.4 and 3.2.5 show that in both the diurnal and seasonal cycles C_1 and α vary roughly in opposition, so are they are not independent. These opposed cycles will tend to keep the radiative properties of the clouds close to the mean values. Therefore the extreme cases considered here are even less probable then 0.05%. Thus these values are taken to be the upper limits on the error in the parameterization.

Variations between cloud types

As well as these extreme cases defined by the variation in fractal parameters among individual flights, it is also possible to consider the difference in radiative properties between the three cloud types whose statistics were described in Chapter 3. The Monte Carlo radiation simulations were performed for multifractal cloud fields

generated using the mean parameters for altostratus, stratocumulus and cumulus clouds that were presented in Table 3.1. Once again only conservative scattering was used. The resulting reflectance values for each cloud type in 6.4 km pixels are shown in Figure 4.22. Also shown for comparison is the reflectance of a PPH
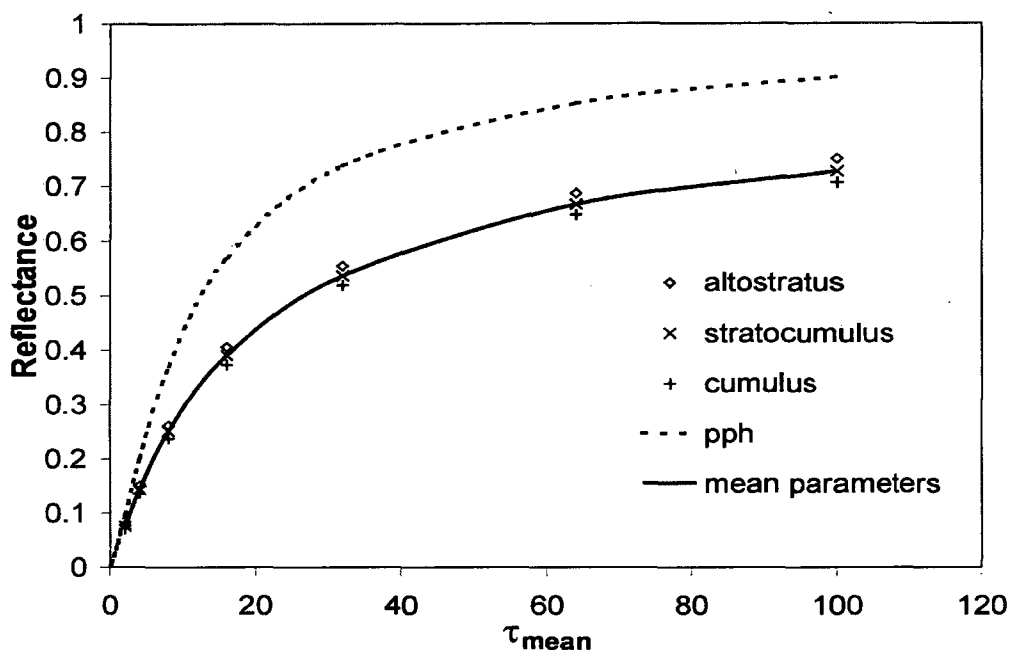
Figure 4.22: The reflectance of multifractal clouds generated using the measured parameters of the three cloud types considered in chapter 2: altostratus, stratocumulus and cumulus. The reflectance of PPH cloud and multifractal cloud with the mean parameter values are also shown for comparison.

cloud and that of a multifractal cloud with the mean parameter values. As noted in Chapter 3, the only parameter that differed significantly between these three cloud types was the intermittency parameter C_1. It was seen above that increasing the parameter C_1 caused the fractal cloud to be further from the PPH case, and thus we would expect cumulus cloud, with the highest C_1, to be the furthest from

123

the PPH case and altostratus to be the closest. This is reflected by the results in Figure 4.22, which shows the cumulus cloud to have lower reflectance than the mean parameter case, stratocumulus to be very close to the mean parameter case, and altostratus to have a slightly higher reflectance at all τ_{mean}. The difference between the mean case and the altostratus, and between the mean case and the cumulus, is approximately 3% for τ_{mean} between 32 and 100.

4.5.3 Reflected radiance distributions

For satellite remote sensing calculations it is not only the entire reflectance that is important but the radiance in a particular direction. Thus it is not sufficient for remote sensing calculations to have a PPH cloud with the same reflectance as the multifractal cloud, it must also have the same reflected radiance distribution. This hypothesis was tested using the radiance distributions output from the radiative transport calculations, which were recorded at a resolution of 5 degrees in the zenith and 10 degrees in the azimuth. Figure 4.23a) shows reflected radiance distribution for a multifractal cloud with mean optical depth of 32 and figure 4.23b) shows reflected radiance distribution for a PPH cloud with the same total reflectance i.e. a PPH cloud with optical depth τ_{eff}^R. These plots are for a single multifractal realisation. Both are for a solar zenith angle of 60° and are the average values over 6.4 km. The radiance distributions have been normalized so that $\iint I(\theta, \phi) \sin\theta \cos\theta d\theta d\phi = 1$, where $I(\theta, \phi)$ is the radiance reflected from the top of the cloud in the direction with zenith angle θ and azimuth angle ϕ. Azimuth angle here is defined such that the sun (or light source) is at $\phi = 180$, so forward-scattered light proceeds in the direction $\phi = 0$. Figure 4.23 shows the two distributions to be quite similar.

124

a)

$\phi=180^{\circ}$
(backwards)

$\phi=0^{\circ}$
(forwards)

```
90      60      30       0      30      60      90
```
Zenith angle (degrees)

b)

$\phi=180^{\circ}$
(backwards)

$\phi=0^{\circ}$
(forwards)

```
90      60      30       0      30      60      90
```
Zenith angle (degrees)
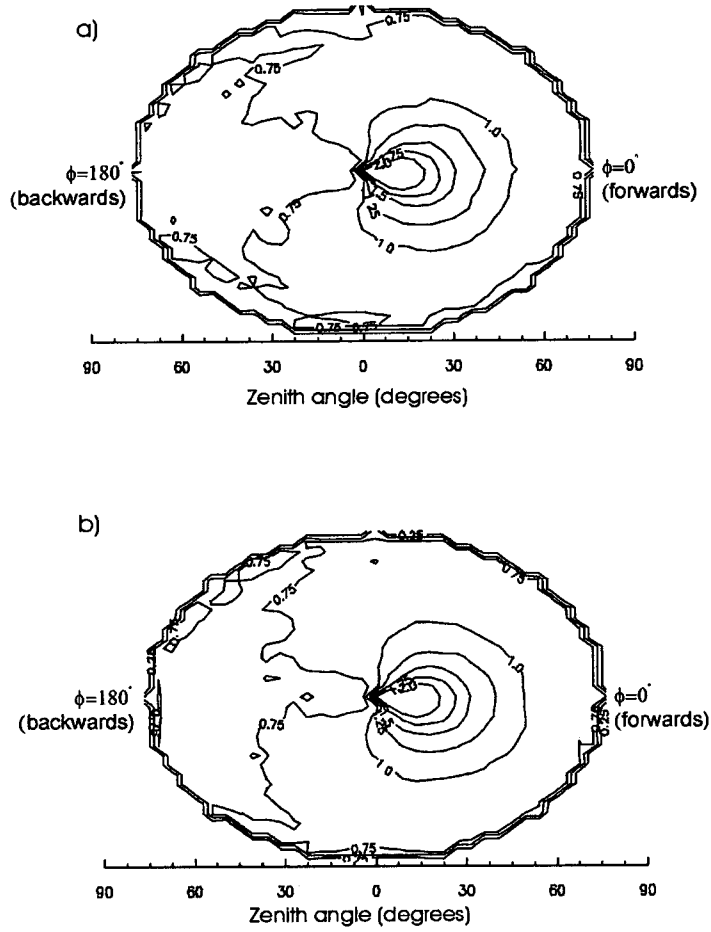
Figure 4.23: A contour plot of the distribution of the reflected radiance for: a) a multifractal cloud with a mean optical depth of 32, b) a PPH cloud with the same total reflectance as the multifractal cloud ($\tau = 14.5$). Both plots are for solar zenith angle of 60 degrees and a pixel size of 6.4 km.

125

To quantify the difference between the PPH and fractal cloud radiance distributions, the relative error in the reflected radiance was considered; if $I(\theta, \phi)$ is the radiance reflected from the multifractal cloud and $I_{PPH}(\theta, \phi)$ is the radiance reflected in the same direction from the PPH cloud of optical depth τ_{eff}^{R}, the relative error is

$$\text{relative error in } I = \frac{I_{PPH}(\theta, \phi) - I(\theta, \phi)}{I(\theta, \phi)}. \tag{4.7}$$

The mean of the relative error across the distribution is zero because the total reflectance in the PPH cloud is equal to the fractal cloud. The standard deviation of the relative error, as the azimuth and the multifractal reaslisation was varied, is shown in a contour plot in Figure 4.24 as a function of τ_{mean} and viewing zenith angle. This relative error was found, when all realisations were considered, to be approximately normally distributed about with change in the azimuth, so that the standard deviation apeears and approximate measure of the spread in the error. The figure shows the results for 4 different zenith angles. The general trend seems to be an increase in spread of the error with both solar zenith and viewing zenith angles, and a decrease with increasing optical depth. This shows that the differences involved are relatively small, with the standard deviation exceeding 0.05 only when the viewing zenith angles or solar zenith angle is very high (above 70 degrees). Thus the reflected radiance distribution of the fractal cloud is quite similar to that of the PPH cloud with the same total reflectance. This implies that the effective optical properties approximation considered here can be used in satellite remote sensing applications, at least in the case of conservative scattering with large pixels. The error in radiance distribution does increase slightly with decreasing pixel size, as can be seen in Figure 4.25 for 3.2 km pixels and Figure 4.26 for 1.6 km pixels.

But even in the case of 1.6 km pixel the error only exceeds 10% at high viewing and solar zenith angles and for low optical depths.

126
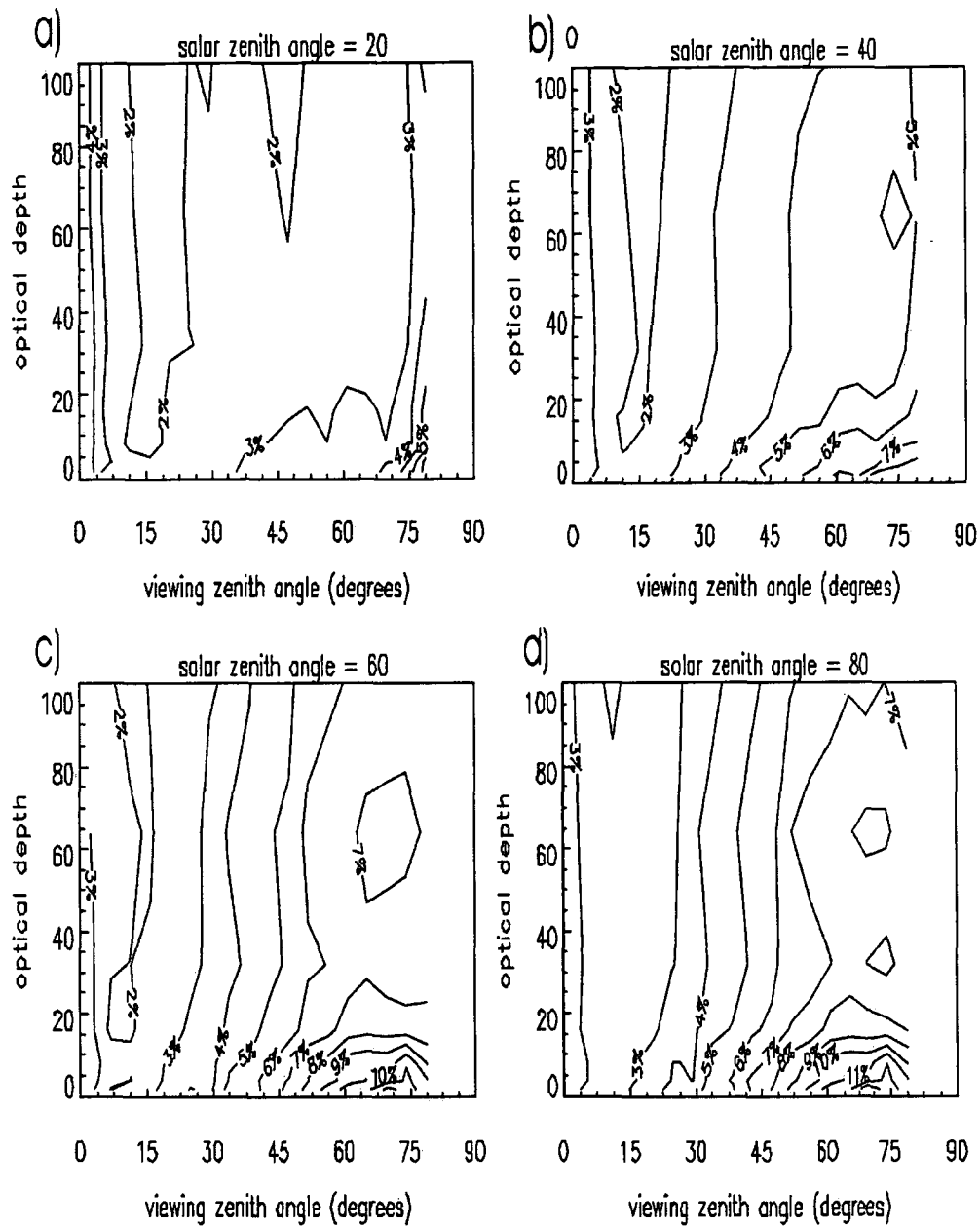
Figure 4.24: The standard deviation in the relative error between the upwelling radiance given by a multifractal cloud and a PPH with the same reflectance. Shown as a contour plot as a function of viewing zenith angle and optical depth. For a spatial size of 6.4 km and for 4 different solar zenith angles.
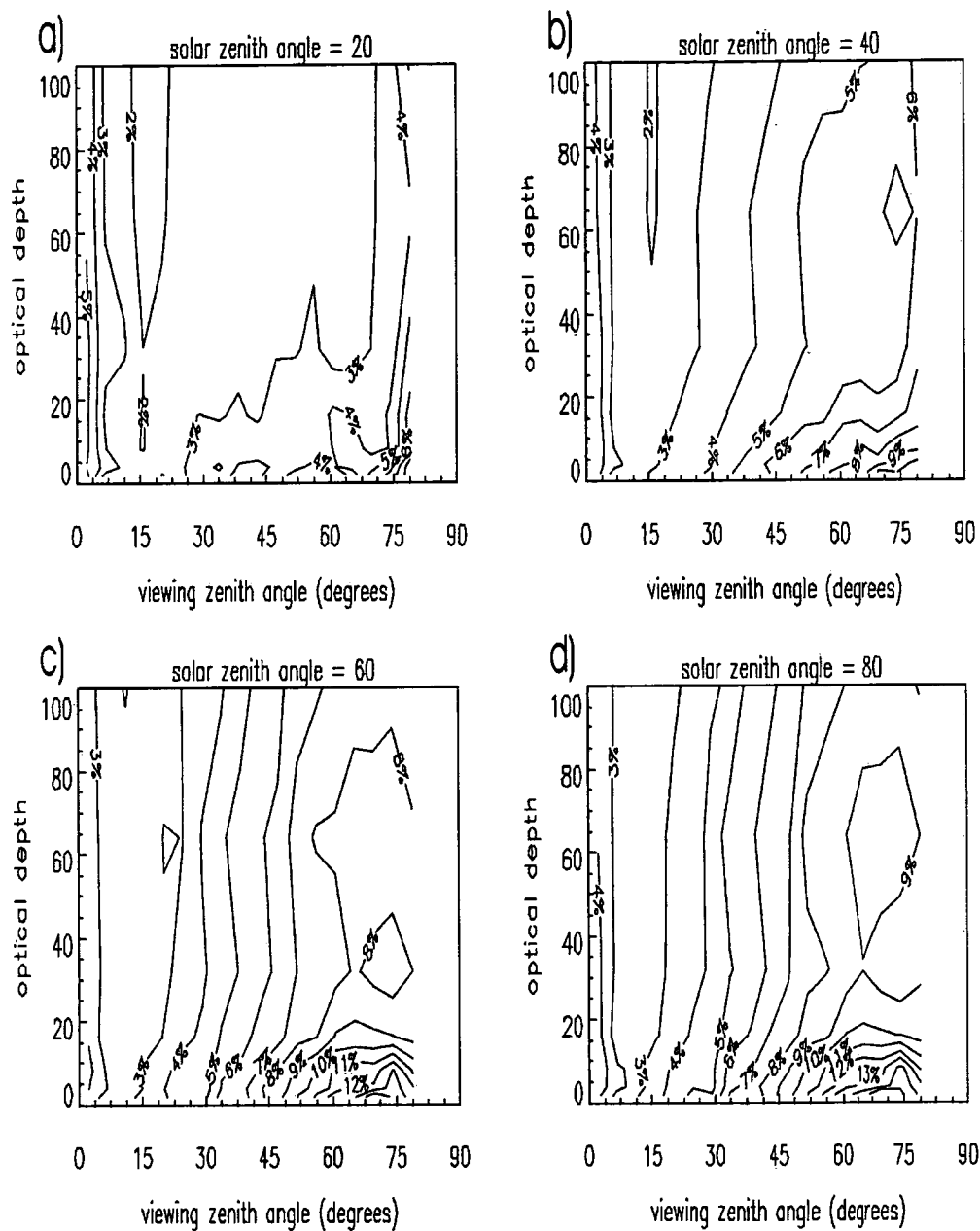
Figure 4.25: The standard deviation in the relative error between the upwelling radiance given by a multifractal cloud and a PPH with the same reflectance. Shown as a contour plot as a function of viewing zenith angle and optical depth. For a spatial size of 3.2 km and for 4 different solar zenith angles.

128
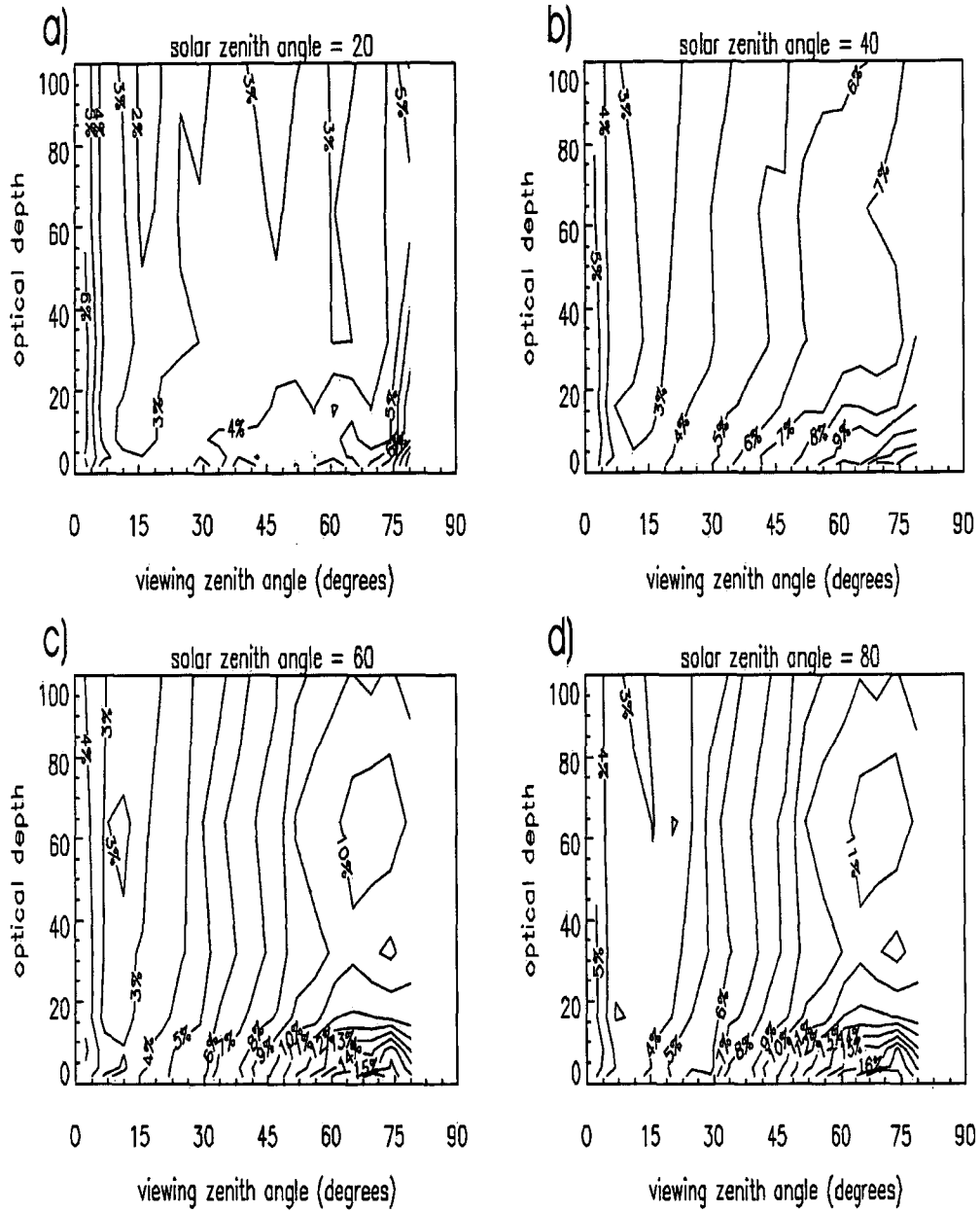
Figure 4.26: The standard deviation in the relative error between the upwelling radiance given by a multifractal cloud and a PPH with the same reflectance. Shown as a contour plot as a function of viewing zenith angle and optical depth. For a spatial size of 1.6 km and for 4 different solar zenith angles.

129

4.6 Comparison with the EHCA

As noted in chapter 1, the approach taken in this study is based on that developed by *Szczap et al.*[2000a; b; c], in the EHCA. In both cases the goal is to replace an inhomogeneous cloud with a PPH cloud with the effective optical properties. In this sense the approximation developed here could be considered a version of the EHCA with different parameterization of the effective optical properties. One reason that the parameterisations differ is that they are based upon different fractal cloud models. The EHCA was developed using the bounded cascade model [*Cahalan et al.*, 1994]. The parameterization for the effective optical properties in the EHCA uses the "relative inhomogeneity parameter", ρ_τ, defined by $\rho_\tau = \sigma(\tau)/\tau_{mean}$ where $\sigma(\tau)$ is the standard deviation of the optical depth within the averaging area. For example the effective optical depth for non-absorbing clouds is parameterised by [*Szczap et al.*, 2000a]:

$$\tau_{eff}^{calc} = \left[A \frac{1 + B\tau_{mean}}{1 + C\tau_{mean}} (1 - \exp(D\rho_\tau)) + \tau_{mean} \left\{ 1 + E \left(1 - \exp(F\rho_\tau)\right)\right\}\right] \quad (4.8)$$
$$\cdot \left[1 - \exp\left(-\frac{\tau_{mean}}{A(1 - \exp(D\rho_\tau))}\right)\right]$$

where the constants are $A = -4.53 \times 10^{-2}$, $B = 1.57 \times 10^{-2}$, $C = 2.64 \times 10^{-1}$, $D = 12.6$, $E = 5.68 \times 10^{-2}$, $F = 3.78$. Although this does not contain any explicit reference to the parameters of the bounded cascade model, the constants in the parameterization were derived using this model with the typical parameters for marine stratocumulus clouds. On the other hand, in this study the FIF model was used to generate cloud fields with the mean parameters derived from measurements of an ensemble of stratocumulus, altostratus and cumulus cloud with cloud covers ranging from 0.25 to 1.0. As a result the clouds used here in radiative transport

calculations are more variable than those used in creating the EHCA.

The parameter ρ_τ was calculated for the FIF multifractal clouds considered in section 4.3, and this was used to find the effective optical depth that would be predicted by the EHCA using equation (4.8). The effective optical depths predicted by the EHCA at a spatial scale of 6.4 km are plotted in Figure 4.27 against τ_{eff}^R the effective optical depth determined from the radiative transfer calculations. The
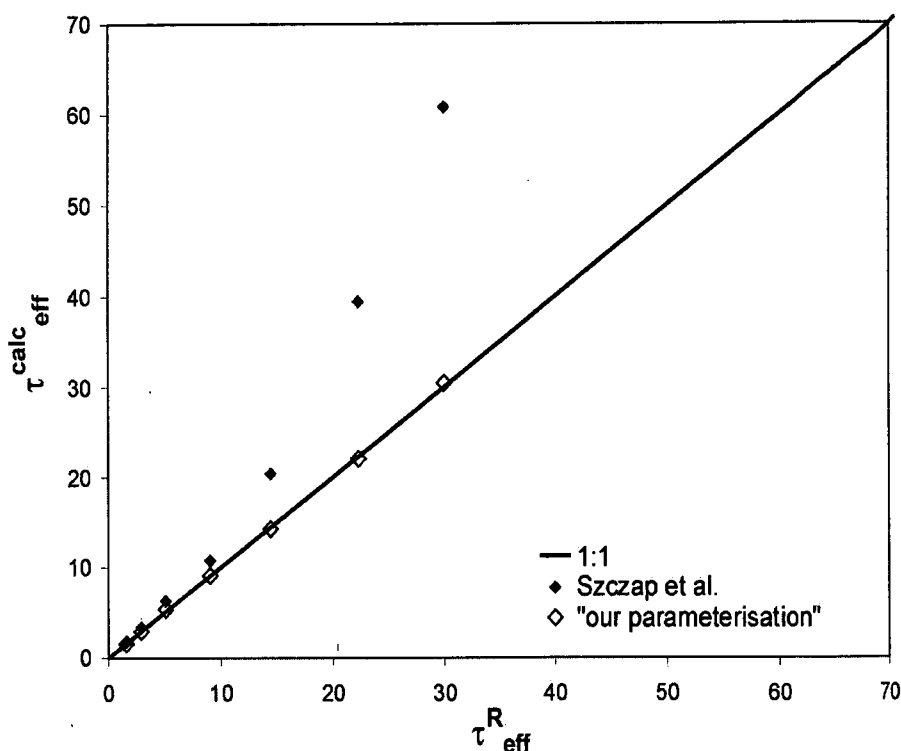
Figure 4.27: A plot of estimated effective optical depth against the effective optical depth determined from Monte Carlo radiative transfer calculations. Points estimated using the parameterisation of Szczap et al. [2000a] are shown, as well as those estimated using the parameterisation developed here. Values shown are for multifractal cloud generated by the FIF model, and a spatial averaging size of 6.4 km.

effective optical depth predicted by the parameterization developed here, (4.2), is also plotted for comparison. This comparison shows that the EHCA parameterization consistently overestimates the effective optical depth, especially at higher values. This should not be surprising since in their analysis of the applicable range of the EHCA *Szczap et al.* [2000c] found that their parameterization did not fit well clouds with a very high degree of inhomogeneity. Specifically they found that their parameterization could be applied to clouds with $\rho_\tau < 1.5$, and the average value for the FIF cloud fields used here is $\rho_\tau = 1.63$ at 6.4 km. Therefore the EHCA parameterization is not applicable to the cloud model used here.

Not only is the cloud model used here more inhomogeneous, the nature of the parameterization used here is also different from the EHCA. Equations (4.2) and (4.6) express the effective optical properties as functions of the pixel size and mean optical depth, and make no mention of a local measure of the inhomogeneity such as ρ_τ. The degree of inhomogeneity is instead indirectly included as a function of pixel size. This means that these functions are specific to this cloud model. Although a new parameterization could be fitted using a local measure of sub-pixel inhomogeneity such as ρ_τ, using the local properties in this way is of little advantage in practice because in most applications, such as remote sensing or climate models, the sub-pixel variations are not known for each case and some average model value would have to be assumed anyway. Thus our method subsumes this average inhomogeneity value into the parameterization. This also has the added advantage of making the dependence on pixel size explicit - and pixel size is a factor that does vary across applications.

4.7 Summary of chapter 4

In this section the radiative properties of multifractal cloud fields were investigated using Monte Carlo radiative transfer. The general results of cloud inhomogeneity that other researchers have found were confirmed - specifically that inhomogeneous clouds have higher transmittance but lower reflectance and absorptance than PPH clouds of the same mean optical depth. However, clouds considered here varied more from the PPH case than was shown for marine stratocumulus in other studies (with the bounded cascade models). Furthermore, the multifractal cloud fields were found to vary more from the homogeneous case as spatial averaging size increased above 0.8 km. In order to provide a framework for simple radiative transfer using PPH cloud models, the effective optical properties of the multifractal cloud fields were then examined. The conditions under which the effective optical properties approximation could be used to derive all radiative outputs were found in terms of solar zenith angle and spatial averaging size. Under these conditions the parameterizations that were found for effective optical depth and, in the case of absorbing clouds, effective single-scattering albedo, can be used to easily generate a homogenous cloud to replace the multifractal one in radiative transfer calculations. The errors involved in using this parameterisation, which depends explicitly on the pixel size and implicitly on the cloud model, were seen to be significantly less than those that would result from using the simple PPH assumption alone. Varying the scattering phase function and asymmetry factor, within the typical range seen for the solar spectrum and for most values of the cloud effective droplet radius, was found to have minimal effect on the effective optical properties. In addition, little difference was found between the reflected radiance distributions of the multifractal and PPH clouds with the same total reflectance, allowing the effective optical

properties approximation to be of use in satellite remote sensing calculations.

The effect of varying the fractal parameters of the model were also considered. It was found that increasing C_1 or α increased the difference from the PPH case (lowering reflectance and raising transmittance) while the smoothing effect of increasing H had the opposite effect. The errors in effective optical depth parameterisation when varying the multifractal parameters was also examined.

Chapter 5

Radiative properties of 3-dimensionally multifractal clouds

In the previous chapter, the focus was on clouds with horizontal inhomogeneity but with constant liquid water profiles in the vertical direction. However, vertical inhomogeneity can also influence the degree of solar radiation reflected and transmitted by cloud, and hence affect cloud properties retrieved from satellite data as well as radiation levels at the ground. Therefore in this chapter the consequences of vertical variability for cloud radiative properties are examined. Previous studies [*Romanova*, 1998; *Stephens et al.*, 1991; *Marshak et al.*, 1998] have found that vertical inhomogeneities have relatively little effect in clouds of low vertical extent. However these same studies have also demonstrated that the differences between the radiative properties of vertically homogeneous and vertically inhomogeneous clouds increases with increasing vertical optical depth. The magnitude of these dif-

ferences and at which optical depth they become significant depends on the amount of inhomogeneity of the cloud liquid water content. This of course is determined by the cloud model used. Therefore the effect of vertical variations based on the FIF cloud model are examined here.

Unfortunately, unlike the case for horizontal liquid water data, little in situ data was available to provide information on vertical cloud structure. Given this limitation, an isotropic cloud model is used in this chapter - the horizontal variations measured in chapter 3 are assumed to also apply to the vertical structure of the cloud and the spatial statistics are therefore assumed to be the same in all dimensions. This is not necessarily realistic, since there are different structures and processes in the vertical dimension, but it is the simplest inhomogeneous model that incorporates vertical variations in a multifractal structure. However, there is some evidence for such an assumption: in the case of radar reflectivities of rain clouds *Tessier et al.* [1993] found that horizontal and vertical structure were both multifractal in nature and that both fit the FIF model with parameters that were very similar (horizontal $\alpha = 1.4$, $C_1 = 0.12$, $\beta = 1.45$; vertical $\alpha = 1.35$, $C_1 = 0.10$, $\beta = 1.4$).

The main objective of this investigation of 3-dimensionally multifractal clouds is to determine the effects on the radiation field caused by the addition of vertical variations and test the accuracy of the (2D multifractal cloud-based) results found in chapter 4 under these conditions. The possibility of developing an effective optical properties approximation for the 3-dimensionally multifractal clouds is also examined. Little previous work has been done on 3D fractal cloud properties; although *Borde and Isaka* [1996] found the effective optical properties of lognormal multifractal clouds with both vertical and horizontal variations, the calculations were done in only two dimensions (1 vertical and 1 horizontal), and before this

136

thesis the effective optical properties of fully 3-dimensionally multifractal clouds have not been considered.

The structure of this chapter is very similar to that followed in chapter 4 for vertically homogeneous clouds. First the results of the Monte Carlo simulations for non-absorbing clouds are examined and used to find the effective optical depths. The errors in the parameterisation of the effective optical depth when there are vertical variations are then presented. Following this the same steps are then followed for absorbing clouds.

5.1   The modelling

This numerical process described in section 2.1.6 was used to generate the 3-dimensional multifractal liquid water content fields for the Monte Carlo radiation modeling. Again, the mean parameters of all clouds considered in Chapter 3 were used for the FIF model: $\alpha = 1.48$, $C_1 = 0.106$, $H = 0.3$. The multifractal cloud fields were generated to be cubes of side length $3.2\,km$. Within these cubes was a grid, with grid cubes being $25\,m$ on each side. This gives a highest resolution with a scale ratio of $\lambda = 128$. As in the previous modelling, the liquid water content, ρ, is constant within each 25m grid cell - but now the value of ρ varies with both the vertical and horizontal position of the grid cell. The continuous cascade generation method as described in section 2.1.6 was used to give the value of ρ at each point in the grid. The droplet radius distribution (and hence the droplet effective radius) is again held constant throughout the cloud, thus allowing the volume extinction coefficient β_{ext} in each grid cell to be proportional to the liquid water content in the cell, as given by equation (2.42). Since the vertical profile is no longer constant, the vertical optical depth at any point is now $\tau = \int_0^{3200m} \beta_{ext}dz$, where z is the ver-

137

tical displacement. The mean optical depth τ_{mean} of the multifractal cloud is still the arithmetic mean over the cloud area of the vertical optical depths. After each random generation, the liquid water content, ρ, (and therefore β_{ext}) were scaled to give the desired value of τ_{mean} for the cloud field. The mean optical depths chosen for the multifractal clouds were: $\tau_{mean} = 2, 4, 8, 16, 32, 64, 100$. The Monte Carlo radiative transfer method presented in section 2.2 was then used to find the radiative properties of these cloud fields. Twenty fields were randomly generated at each optical depth and the radiative results averaged. Like in chapter 4, for the majority of the calculations the asymmetry factor was taken to be $g = 0.85$, calculated using the parameterisation of *Hu and Stamnes* [1994] with a wavelength of $0.55\mu m$ and effective radius of $10\mu m$. But as was discussed in section 4.5, the asymmetry factor does not vary much over most of the solar spectrum. Also as in chapter 4, the single-scattering albedo, ω, was varied through the values of $\omega = 1.0, 0.999, 0.99, 0.98, 0.95, 0.92, 0.9$.

This Monte Carlo radiative transfer code was used with homogeneous clouds (homogeneous in 3 dimensions), as well as the multifractal clouds. The simulations for each cloud field was done using 50 million photons. The model was run with photons entering the top surface of the model with zenith angle, θ_0, of 0°, 20°, 40°, 60° and 80°, in order to simulate the clouds being illuminated from different solar zenith angles. The transmittance, reflectance and absorptance were recorded for each horizontal 25m×25m grid square in the model. The area averaged transmittance, reflectance and absorptance were calculated for square areas with sides of 0.8km and 1.6km, as well as 3.2km, in order to simulate the effect of spatial variations on pixels of different sizes.
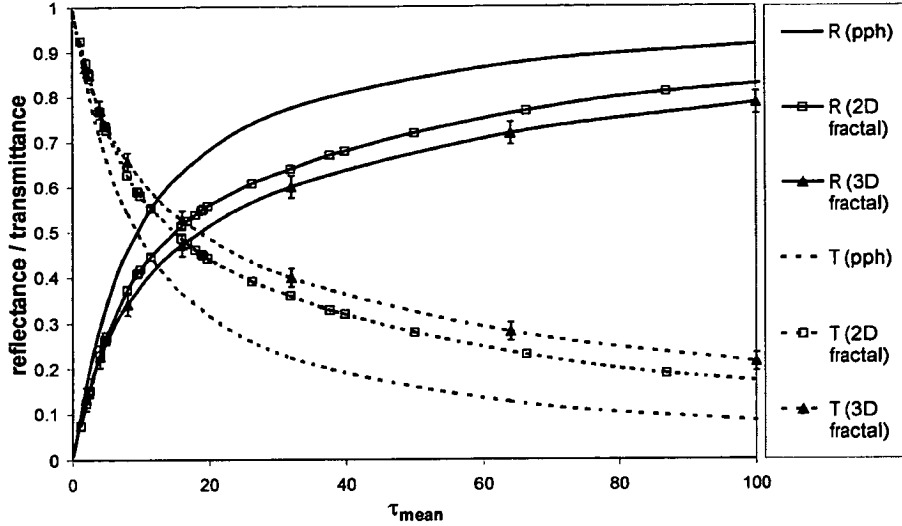
Figure 5.1: The reflectance and transmittance calculated from the Monte Carlo radiation code for homogeneous clouds, 2D multifractal clouds (horizontally inhomogeneous, vertically constant) and 3D multifractal clouds. Calculated for an averaging scale of 3.2km. The error bars shown are the standard error due to averaging over the 5 realisations of the multifractal cloud field.

5.2 Conservative scattering results

The reflectance and transmittance calculated when $\omega = 1$ for the homogeneous and 3D multifractal clouds at the 3.2km scale, are displayed in Figure 5.1 as a function of τ_{mean}. Points are the mean values over the 5 realisations at each optical depth. Also shown in figure 5.1 are the reflectance and transmittance that are calculated using the effective optical depth approximation, (4.2), developed for 2D multifractal clouds in section 4.3 - the 2D curves in the figure are found by finding the parameterised value of the effective optical depth and then finding the radiative properties of a PPH cloud with that optical depth. The cloud fields with variations in all three dimensions vary further from the homogeneous case than the cloud with

139

only horizontal variations. This difference increases with τ_{mean}, with the reflectance bias going from less than 1% for $\tau_{mean} \leq 10$ to ~5 − 7% for optical depths between 20 and 100. These differences decrease with decreasing pixel size. Therefore it is confirmed that for clouds with low optical depths the error caused by using a cloud that has constant liquid water content in the vertical is quite small. However, once the optical depth reaches 15 or 20, the bias becomes more significant. To put these optical depths in context, the typical for stratocumulus value is ~13 [*Cahalan et al.*, 1994a]. It will depend on the application whether thick clouds must be considered and whether a 5-7% bias is important. If this is significant, it is possible to alter the effective optical depth parameterisation to more correctly model 3D multifractal clouds.

The effective optical depths based on the cloud transmittance (τ_{eff}^T), and those based on cloud reflectance (τ_{eff}^R), can be determined by comparing the Monte Carlo model outputs for the 3D multifractal cloud with the PPH cloud, as in section 4.3.1. Cubic spline interpolation was used to find the optical depth of the PPH cloud with the same transmittance (or reflectance) as the multifractal cloud. As shown in Figures 5.2 and Figure 5.3, the two types of effective optical depths for the 3D multifractal cloud are quite similar for low solar zenith angles, with the differences between them following similar patterns as those of the 2D multifractal clouds in chapter 4. The notable difference here is that while the discrepancies between τ_{eff}^R and τ_{eff}^T in Figure 5.3 are less than or equal to those in the 2-dimensionally multifractal case (for the same pixel size) at solar zenith angles ≤ 40, they are greater than in the 2D case at solar zenith angles of 60 and 80 degrees (see Figure 4.3 for the 2D case). Similarly the 3D multifractals follow the same trends as the vertically homogeneous cloud in the area of solar zenith dependence of the effective optical depths, but there is again a higher increase of dispersion at higher zenith

140
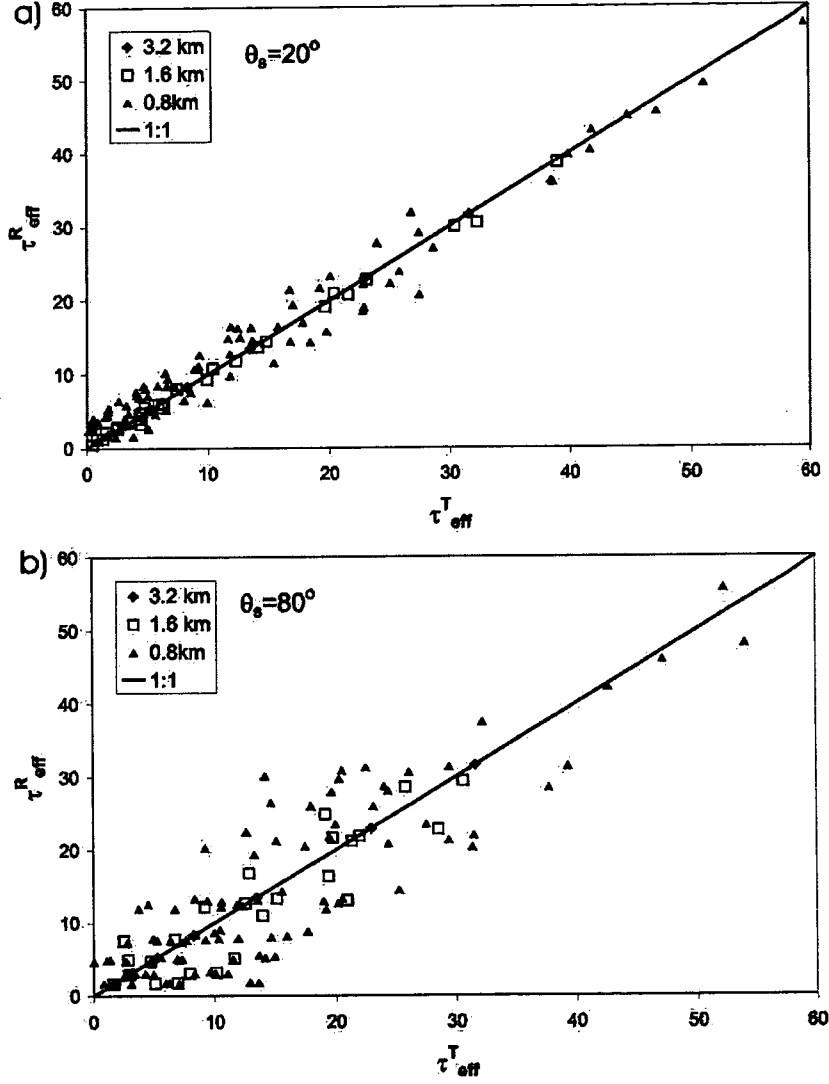
Figure 5.2: A comparison of the effective optical depths obtained from the reflectance and transmittance of 3D multifractal clouds. Horizontal averaging scales used are 1.6km and 0.8 km, and the incident zenith angle is: a)twenty degrees and b) eighty degrees.
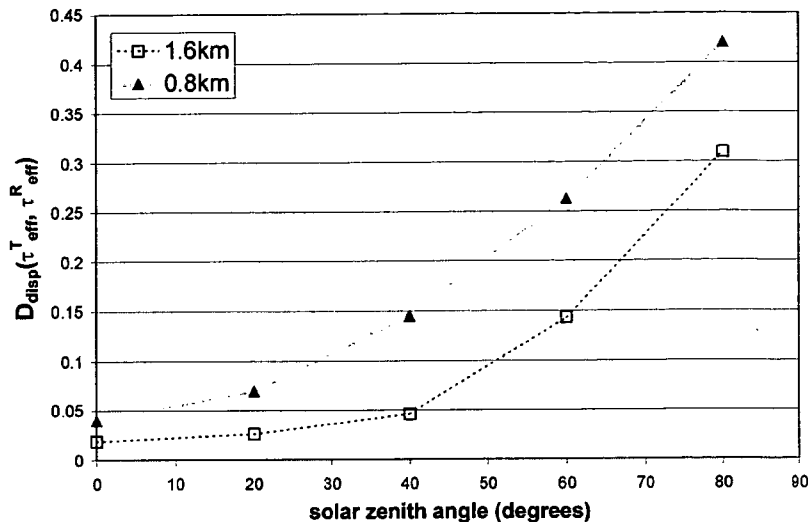
Figure 5.3: The relative dispersion between τ_{eff}^{R} and τ_{eff}^{T} as a function of incident zenith angle for averaging scales of 1.6km and 0.8km.

angles. This last point is shown for τ_{eff}^{R} in Figure 5.4, which plots the relative dispersion $D_{disp}\left(\tau_{eff}^{R}(0°), \tau_{eff}^{R}(\theta_0)\right)$ (as defined by equation (4.1)) as a function of θ_0. Despite this increased dependency on solar zenith angle, the root-mean-square dispersion was still less than 5% for solar zenith angle less than 45 degrees for a pixel size of 1.6km, indicating that the effective optical depth approximation could still be used to calculate both T and R for low solar zenith with minimum error. The increased dependence on solar zenith angle could well be a result of the geometry changes in this case, with the higher cloud height allowing greater horizontal transport of photons before exiting the cloud when the solar zenith angles are higher.

Next consider the pixel size dependence of the effective optical depth. Figure 5.5 shows τ_{eff}^{R}, for different averaging scales, as a function of the mean optical depth, τ_{mean}, of the multifractal cloud. These values are for an incident zenith angle

142
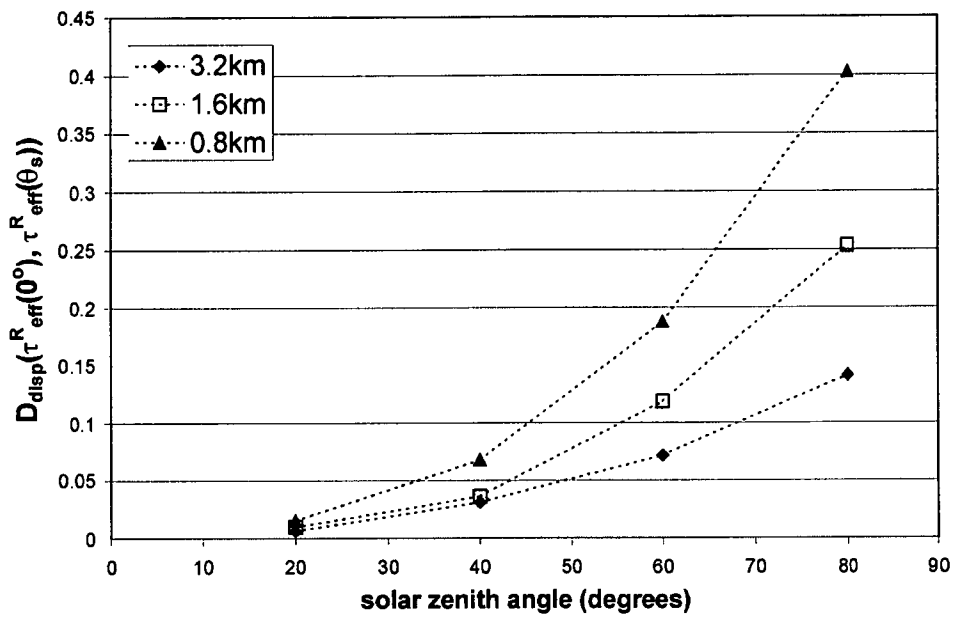
Figure 5.4: The root-mean-square dispersion between the effective optical depth at a solar zenith angle of 0 and the effective optical depth at solar zenith angle θ_s. For 3-dimensionally multifractal clouds.
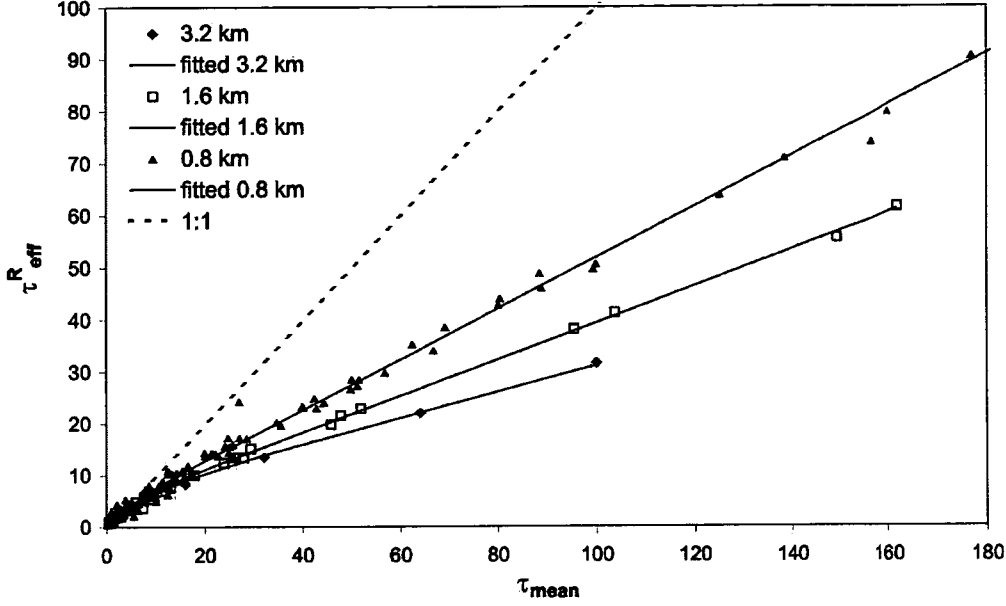
Figure 5.5: The effective optical depth as a funtion of mean optical depth of the multifractal cloud segment. Calculated for pixel sizes of 0.8km, 1.6km, and 3.2km, with an incident angle of zero. The lines shown are those calculated by the empirical fit found specifically for the 3D multifractal clouds.

of $0°$, and the dotted 1:1 line in the figure is where homogeneous clouds would fall. This figure shows behaviour qualitatively the same as for 2D multifractal clouds, with τ_{eff}^R decreasing, moving further from the homogeneous case, as the averaging scale increases. Figure 5.5 also shows, for all pixel sizes, that τ_{eff}^R is close to τ_{mean} and therefore behaving like a homogeneous cloud, when τ_{mean} is small. Alternatively, when τ_{mean} is large τ_{eff}^R seems to approach a straight line. All of this is the same as for cloud with only horizontal variations. However, when the τ_{eff}^R for the 3D multifractal cloud were fitted to the function (4.2), which was used to parameterise effective optical depth in chapter 4, some differences are revealed. The non-linear least squares fit to the function yielded the following parameter values

144
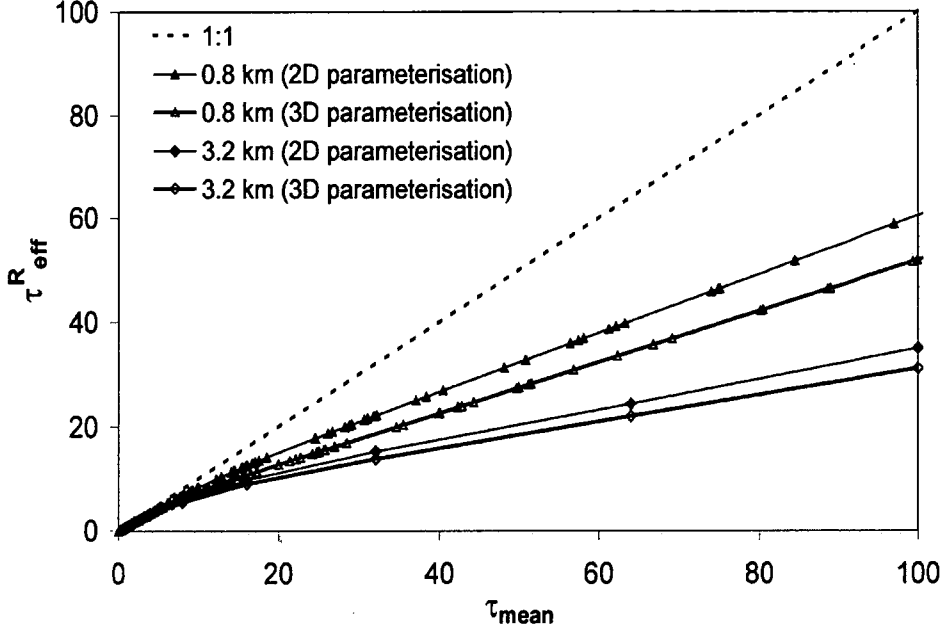
Figure 5.6: A comparison between the effective optical depth parameterisations for 3-dimensionally and 2-dimensionally (vertically homogeneous) multifractal clouds. Shown for 0.8 and 3.2 km pixels.

for the relationship: $A = 8.448$, $B = 7.56$, $C = 8.49$, $D = 2.54$, $k = 0.475$. The solid lines in Figure 5.5 are the parameterised values produced by using these new parameters in the function 4.2. The noteworthy difference here is the lower value of the exponent k, compared to the value of 6.72 found for 2D multifractal cloud. The lower value of k indicates a lesser degree of dependence on the spatial averaging size. This is illustrated in Figure 5.6, which compares the values of τ_{eff} calculated using the parameters found here for 3D fractal clouds and those found using for 2D fractal clouds in chapter 4. Both cases are shown for 0.8 km and 3.2 km pixels. This shows that while effective optical depths at 3.2 km are relatively similar, at the 0.8 km scale the 2D multifractal clouds are much closer to homogenous case.

This means that the values of the effective optical depth of the 3-dimensionally multifractal clouds do not approach the homogeneous case as rapidly as the pixel size decreases.

Figure 5.7 shows the errors in the effective optical depth of 3D multifractal cloud estimated by this parameterisation, in the form of $D_{disp}\left(\tau_{eff}^R, \tau_{eff}^{calc}\right)$ where τ_{eff}^{calc} is the parameterised value. Values are also shown for pixel sizes of 3.2 km and 1.6 km. Also shown in the figure is the error that results from using the parameterisation with the parameter values found for 2D multifractal clouds in chapter 4, and the error resulting from the traditional assumption of using a PPH cloud with an optical depth equal to τ_{mean} of the multifractal cloud. This figure shows that both parameterisations are significant improvements over the PPH model alone, as hoped. It is also possible to see that the original 2D parameterisation produces an error of 0.02 to 0.03 above that of the approximation developed especially for the 3D clouds. This is largely due to the differences at relatively high optical depth. If the root-mean-square dispersion, $D_{disp}\left(\tau_{eff}^R, \tau_{eff}^{calc}\right)$, is calculated only for optical depths ≤ 20, than the use of the 2D parameterisation produces a value approximately 0.01 higher than the specifically created 3D parameterisation. In both cases the relatively small increase in error indicates that the parameterisation developed for vertically homogeneous clouds is reasonable, even when clouds are vertically variable.

The absolute errors in transmittance that occur when using the effective optical properties approximation for 3D multifractal clouds are shown in Figure 5.8.Compare this to errors in transmittance that result from using the traditional method of PPH calculations with same mean optical depth an the multifractal cloud, which are shown in Figure 5.9.Note that, as in the 2D case, using the effective optical depth approximation, instead of the traditional PPH assumption,

146
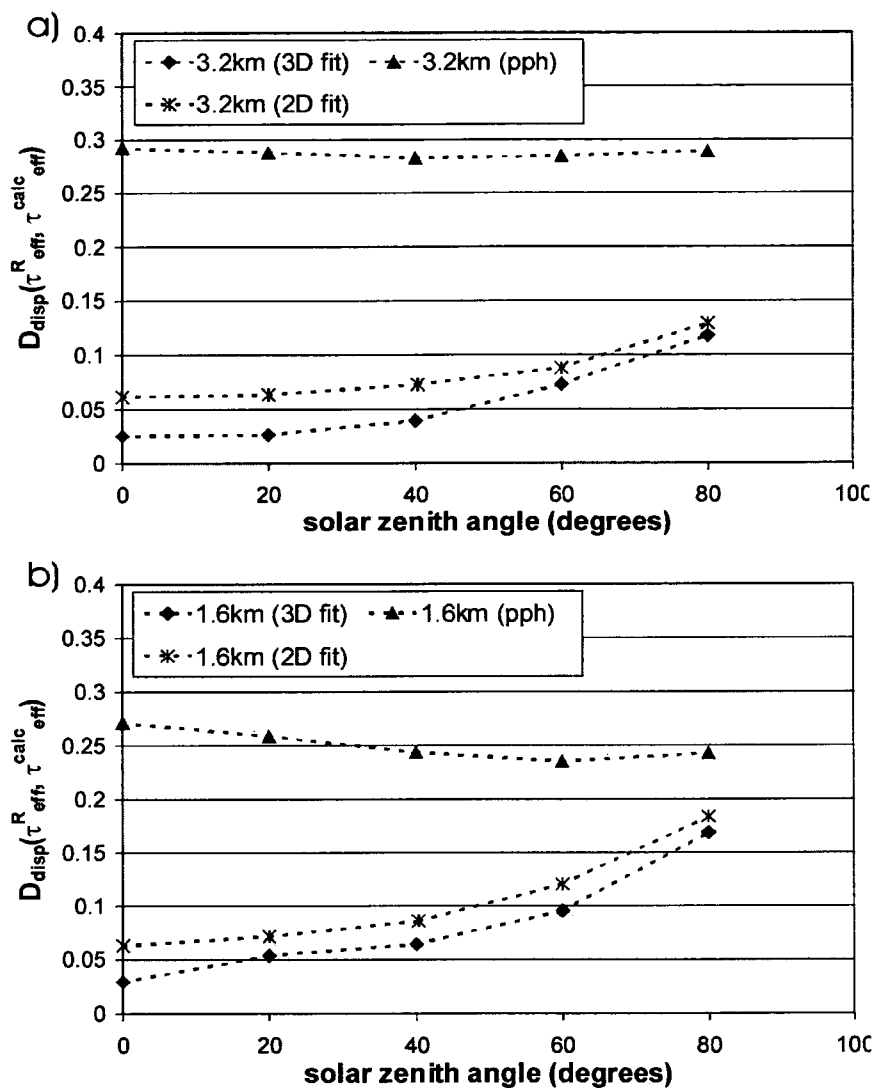
Figure 5.7: The root-mean-square dispersion between the effective optical depth found using the Monte Carlo results and that found using the empirical parameterisation. Plotted for a) 3.2 km and b) 1.6 km pixels. Values are shown for the original parameterisation (2D) as well as for parameters determined for 3D multifractal cloud. The errors when using the simple PPH assumption alone are also shown.
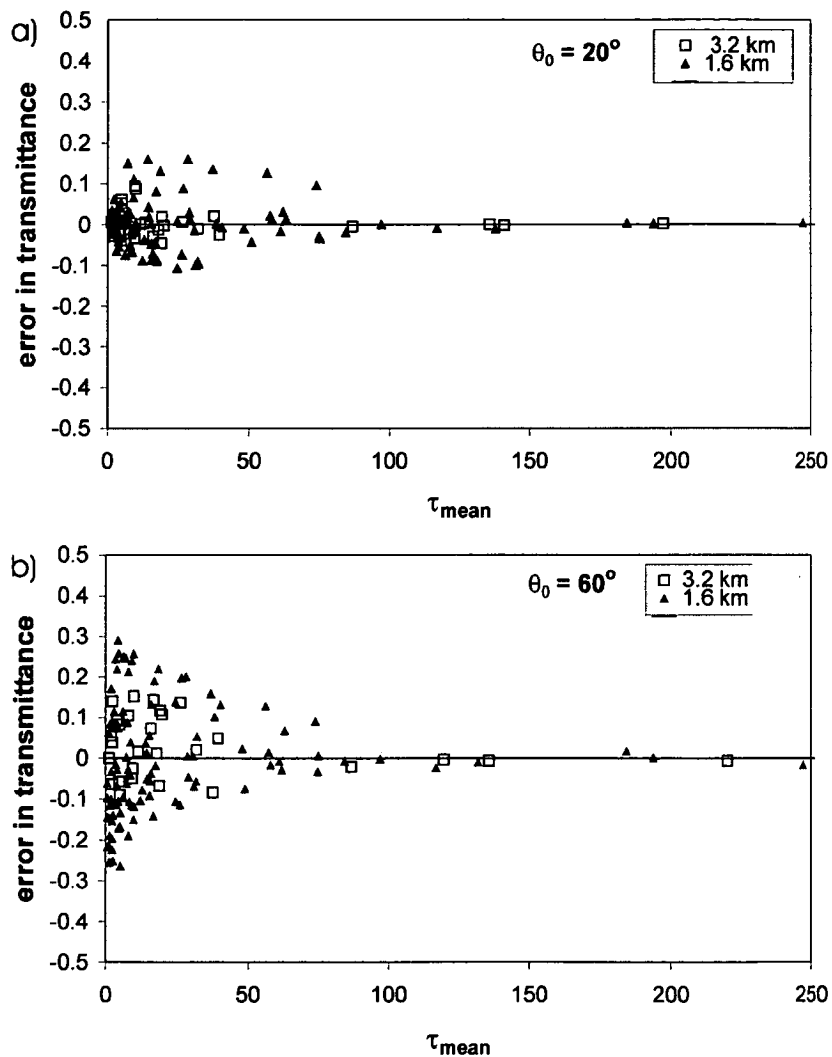
Figure 5.8: The absolute errors in transmittance that occur when the effective optical depth approximation is used instead of a monte carlo radiative transport code with 3D multifractal cloud. For solar zenith angles of a) 20 and b) 60 degrees.
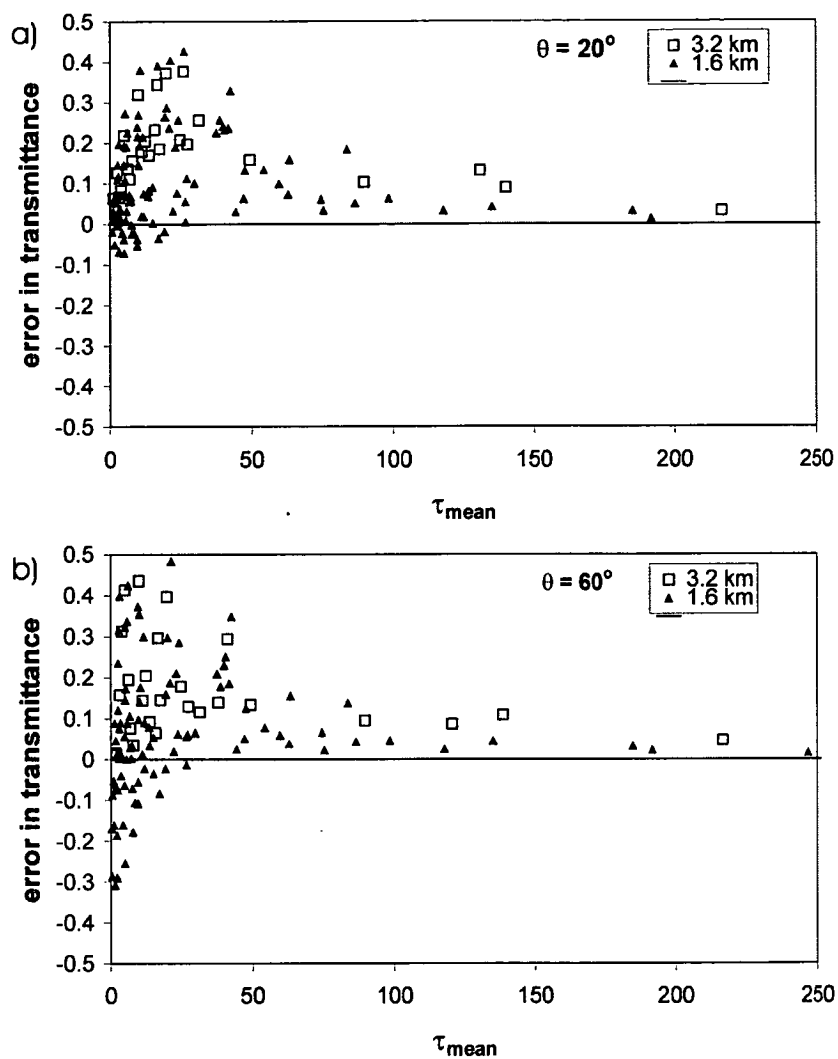
Figure 5.9: The absolute errors in transmittance that occur when PPH assumption alone is used instead of a monte carlo radiative transport code with 3D multifractal cloud. For solar zenith angles of a) 20 and b) 60 degrees.

149

eliminates the mean bias in the data and reduces the absolute errors.

5.3 Non-conservative scattering results

The results of the Monte Carlo simulations for absorbing clouds with single-scattering albedo of 0.99 are plotted in Figure 5.10. Part a of the figure shows the reflectance and transmittance at a spatial size of 3.2km, while part b shows the absorptance. The figure also shows the radiative properties of PPH cloud and those that are calculated using the effective optical properties parameterisation developed for 2D multifractal absorbing clouds in section 4.4. Unlike the conservative scattering case, the 3D multifractal cloud with $\omega = 0.99$ behaves quite differently from the vertically homogeneous version. The reflectance of the cloud demonstrates much the same trends as in the non-absorbing case, i.e. diverging from the 2D multifractal case as τ_{mean} increases above 10 and generally being further from the PPH curve. However, the transmittance and absorptance both behave differently - they are very close to the 2D multifractal curve for low values of τ_{mean} but when they diverge they actually move closer to the PPH curve rather than away. In fact, the absorptance of the 3D multifractal cloud is almost identical to that of the PPH cloud at $\tau_{mean} = 100$. These differences between the 3D multifractal and vertically-homogeneous multifractal cases become quite large, reaching an absolute value of ~ 0.1 at $\tau_{mean} = 100$, which is $\sim$50% of the transmittance and $\sim$25% of the absorptance at that optical depth. Therefore the parameterisation developed for the 2D multifractal cloud is clearly not suitable for absorbing clouds with large optical depths. On the other hand, smaller optical depths (below 15-20) the parameterisation appears to produce more reasonable results.

Some further light is shed on this phenomenon by some other statistics of the

150
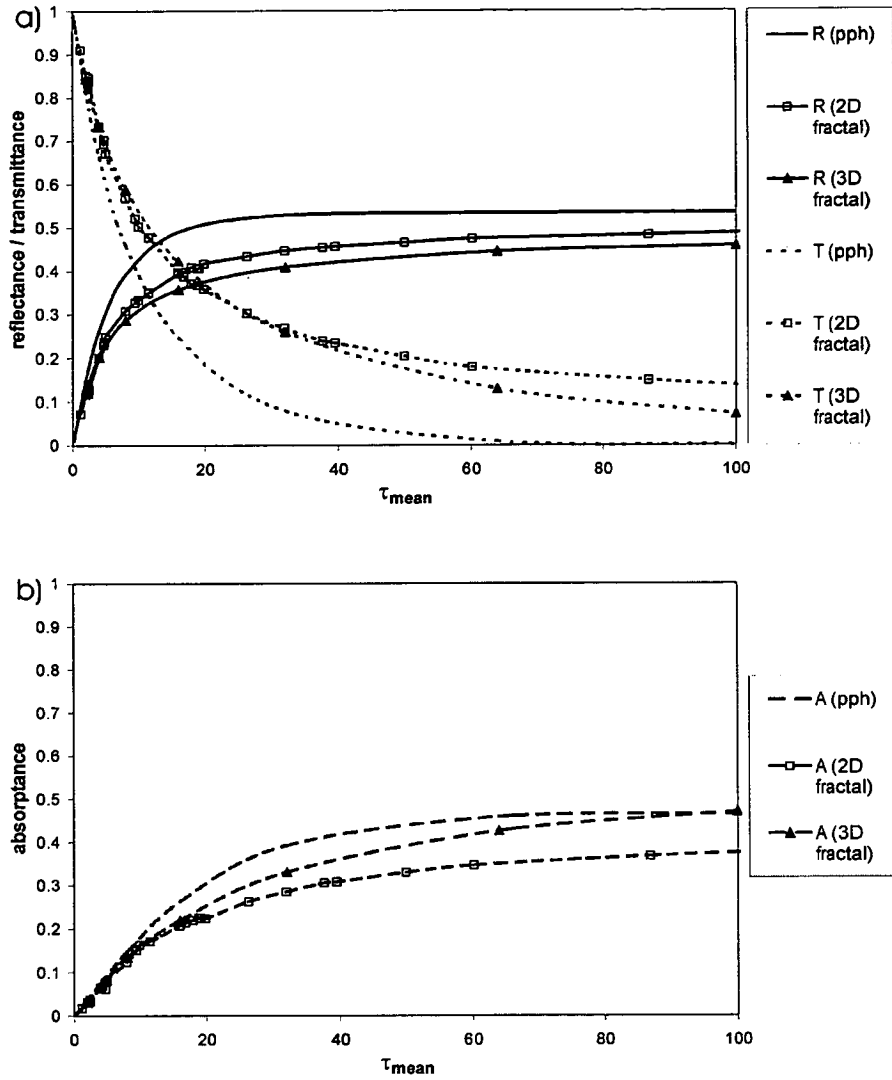
Figure 5.10: a) the reflectance and transmittance of 3D multifractal cloud with single scattering albedo 0.99, spatial scale 3.2 km. b) shows absorptance for the same conditions. Results for 2D multifractal and PPH cloud are also shown for comparsion. All for a solar zenith angle of 40 degrees.

Monte Carlo modeling - the mean free-path length and average number of scattering events of photons in the cloud. Table 5.1 contains the mean free-path length and average number of scattering events per photon, for 2D multifractal and 3D multifractal clouds. For the purposes of this comparison the 2D multifractal case

Table 5.1: The mean free-path length (mfp)and average number of scattering events (# *scat. events*) in the cloud, for 3-dimensionally multifractal clouds and clouds with horizontal fractal structure and vertically costant profiled (labelled 2D multifractal clouds here). For a range of mean cloud optical depths, τ_{mean}.

τ_{mean}	3D multifractal cloud		2D multifractal cloud	
	mfp (m)	# *scat. events*	mfp (m)	# *scat. events*
2	829	6.37	796	6.86
4	421	13.5	393	15.2
8	214	28.6	196	31.0
16	109	60.2	99.5	62.9
32	50.9	135	38.4	106
64	25.8	255	19.8	187
100	19.6	326	12.9	242

listed here is from a simulation of vertically homogeneous, horizontally multifractal clouds with the same geometry (3.2 km cubes). The single scattering albedo is 0.99 in each case. For 3D multifractal clouds with large optical depths ($\tau_{mean} \geq 36$), the mean free-path length is greater than for 2D multifractal clouds with the same τ_{mean}, but so is the number of scattering events. This means that although the photons are travelling further between collisions, they are not passing out of the cloud. This would suggest that the photons almost become "trapped" in low liquid water areas of the cloud field, bouncing between "walls" (regions of higher extinction) - travelling a long distance between collisions but not being able to escape the cloud field. The higher number of average scattering events leads to the higher level of absorption. On the other hand, at optical depths of 16 or less the number of scattering events are similar for the two cases.

152

To determine if an effective optical properties approximation can be found for absorbing clouds, the relative differences between the effective optical properties determined using reflectance with transmittance, and those found using reflectance and absorptance were again considered. Figure 5.11 displays $D_{disp}(\tau_{eff}^{RT}, \tau_{eff}^{RA})$ and $D_{disp}(\omega_{eff}^{RT}, \omega_{eff}^{RA})$. This shows the differences between the different definitions of the effective single scattering albedo to be very large in comparison with 2D multifractal clouds. The errors of above 8% in all cases indicates that the effective optical properties approximation cannot be applied without quite large errors in at least one of T, R or A. This is due to the larger total photon path length in cloud and hence larger horizontal transport of photons.

It is possible of course to only consider, for example, the effective optical properties based on R and T and ignore the errors in A. Of course this is not useful for studies of the radiation budget but may be sufficient for remote sensing studies - space (ground) based remote sensing only requires he calculation of reflectance (transmittance). Similar calculations could of course be done for any combination of 2 of the 3 radiative properties. The effective optical depths defined in terms of a PPH cloud with the same reflectance and transmittance, τ_{eff}^{RT}, are graphed in Figure 5.12 as functions of τ_{mean}, for the spatial averaging size of 3.2 km. For comparison the effective optical depth for 2D multifractal clouds at the same pixel size is also shown in the figure. Although the same general trends seen for the 2D multifractal clouds are also observed again here, with τ_{eff}^{RT} decreasing with decreasing single-scattering albedo, the values for different values of ω are much closer to each other at low values of τ_{mean}. Also the values of τ_{eff}^{RT} at high optical depth are also significantly lower (up to 25% lower at $\tau_{mean} = 100$) than those in the 2D multifractal case at the same spatial scale. However the values of τ_{eff}^{RT} do appear to have the correct shape to be fitted to an empirical function of the same form as

153
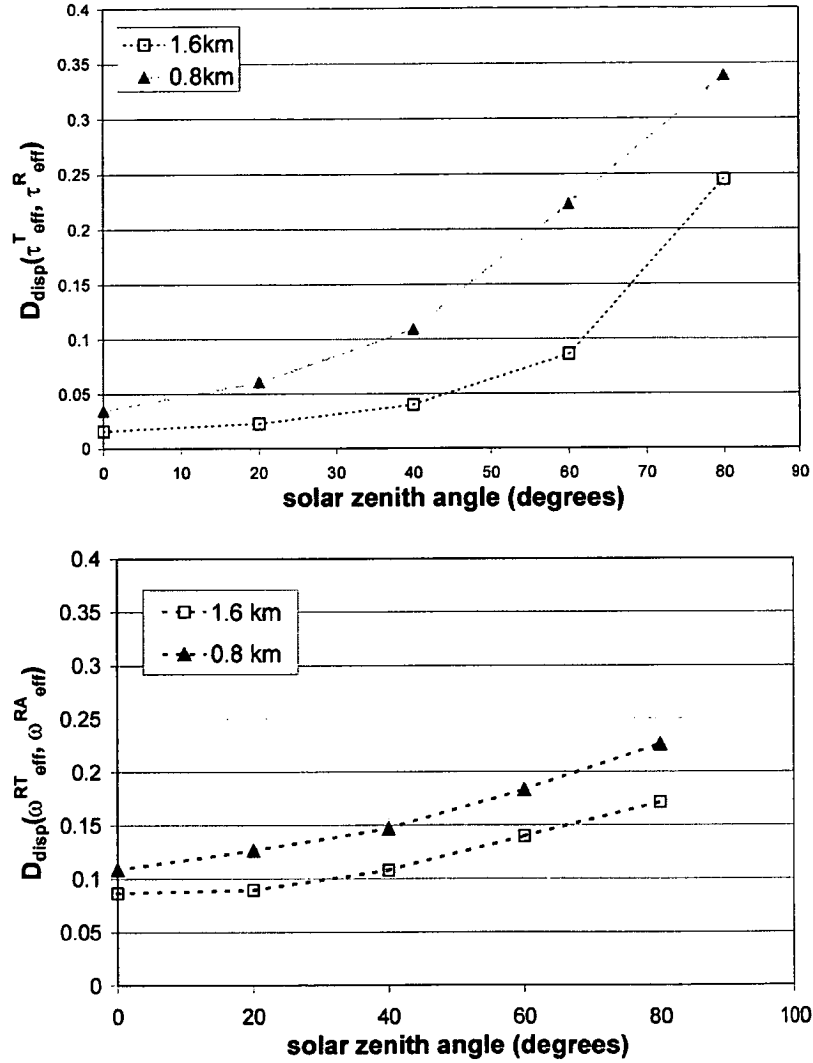
Figure 5.11: The root-mean-square dispersion between the effective optical properties of 3D multifractal cloud calculated using reflectance and transmittance (RT) and that found from reflectance and absorptance (RA). a) shows for effective optical depth and b) effective single scattering albedo. Both for 1.6 and 0.8 km pixels
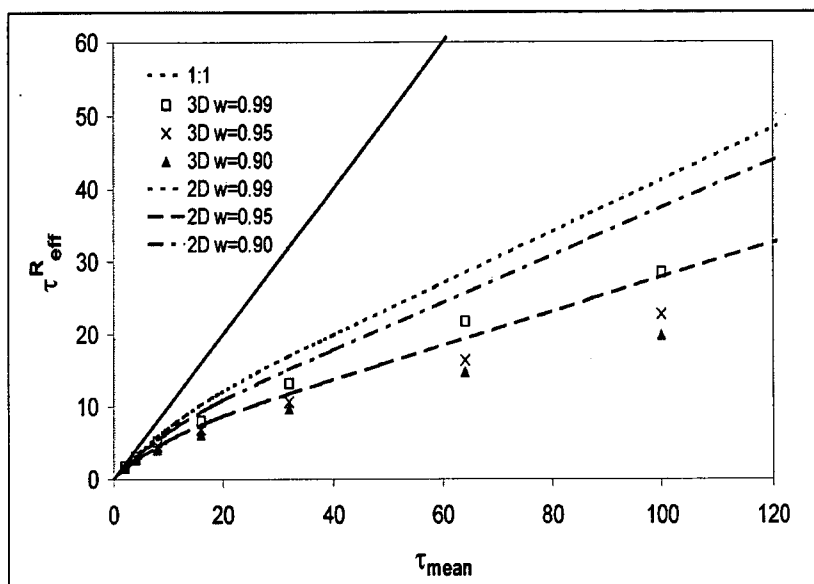
Figure 5.12: The effective optical depth τ_{eff}^{RT} plotted as a function of the mean optical depth of the 3D multifractal cloud field. For a pixel size of 3.2 km and a range of single scattering albedos ω. The effective optical depth for 2D multifractal clouds at the same pixel size and single scattering albedo is shown for comparison.

that used the effective optical depths of the 2D multifractal cloud (equation (4.2))

Now consider the effective single-scattering albedos defined by the PPH cloud with the same reflectance and transmittance, ω_{eff}^{RT}. Figure 5.13 displays the ratio, ω_{eff}^{RT}/ω, of the effective single-scattering albedo divided by the actual droplet single-scattering albedo, plotted against τ_{mean}. Figure 5.13a shows the ratio ω_{eff}^{RT}/ω for three different values ω at the spatial scale of 3.2 km. On the other hand, Figure 5.13b shows ω_{eff}^{RT}/ω for three different spatial scales with $\omega = 0.90$. These graphs show two clear differences from the effective single scattering albedos that were developed for vertically-homogeneous clouds. The first of these is shown most clearly in Figure 5.13a where the values of ω_{eff}^{RT}/ω can be seen not to return quickly to 1 at high values of τ_{mean} as was seen for 2D multifractal clouds. This is a result of the high absorptance at high τ_{mean} - the effective single scattering albedo must remain lower than ω to produce the higher absorptance while maintaining a lower reflectance. The other departure from the patterns seen for 2D multifractal clouds is that in Figure 5.13b there is no clear increase in ω_{eff}^{RT}/ω with decreasing pixel size - in fact there is no clear pixel size dependence. This seems to indicate that the degree of vertical inhomogeneity is important in determining ω_{eff}^{RT}, since it is not affected by changing the horizontal pixel size. Because of these differences the form of the equation (4.6), used to parameterise the effective optical depth for 2D multifractal clouds, is not suitable for 3D clouds if large values of τ_{mean} are included. Therefore it is not possible to correct for vertical variations by simply changing the parameter values in the approximation for absorbing clouds, in the way that was done for 3D non-absorbing clouds.

The errors in the effective optical properties of absorbing clouds that result from using the parameterisation determined for 2D multifractal clouds were determined using the functions $D_{disp}(\tau_{eff}^{RT}, \tau_{eff}^{calc})$ and $D_{disp}(\omega_{eff}^{RT}, \omega_{eff}^{calc})$, where the superscript
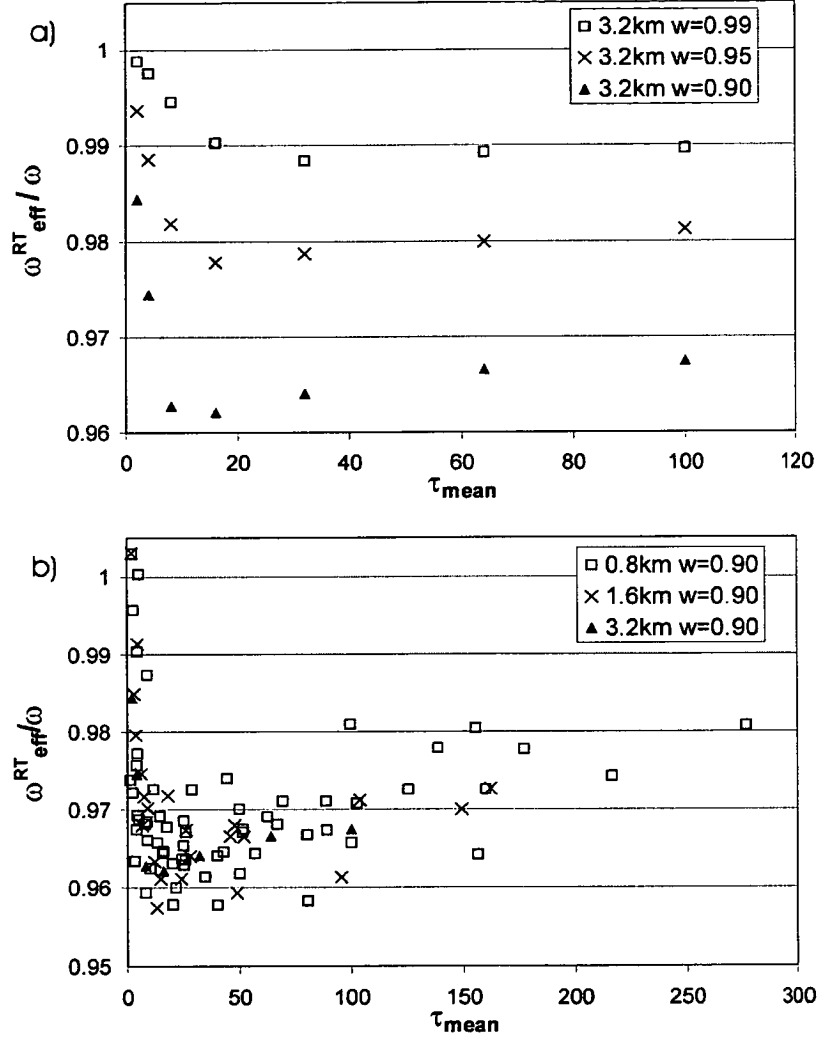
Figure 5.13: The ratio of effective single scattering albedo ω_{eff}^{RT} to the droplet single scattering albedo ω, for 3D multifractal cloud. a) plots the data for different values of ω, while b) varies the pixel size for $\omega = 0.90$.

calc indicates the values given by the parameterisation found in section 4.4. The root-mean-square dispersion of the effective optical depth is found in Figure 5.14 and that of the effective single-scattering albedo in Figure 5.15. Part a in both figures shows the errors at a spatial scale of 3.2 km while part b shows the errors for pixels of 1.6 km. In addition to the discrepancies in the parameterisation for 2D multifractal clouds if 3D multifractals are present, these figures also show the errors that result from this parameterisation if only clouds with $\tau_{mean} \leq 20$ are considered. Finally, the errors resulting from using the PPH assumption alone, $D_{disp}(\tau_{eff}^{RT}, \tau_{mean})$ and $D_{disp}(\omega_{eff}^{RT}, \omega)$, are also shown for comparison. It is apparent that the 2D parameterisation for absorbing clouds is not suitable when clouds have vertical variations - indeed for 1.6 km pixels the parameterisation is little better than the PPH assumption. However, these figures also demonstrate that the error in the parameterisation is much smaller when only clouds with relatively small mean optical depths are considered.

5.4 Summary of Chapter 5

In the case of non-conservative scattering, the radiative properties of the 3D multifractal clouds were found to be quite similar to those of clouds which are horizontally multifractal but vertically homogeneous. The non-absorbing 3D multifractal clouds simply had properties which were slightly further from the PPH case than the 2D multifractal clouds. As previous studies had found, the difference caused by introducing vertical variations increased with mean cloud optical depth. An alternative set of parameters was found for the empirical function for the effective optical depth of 3D multifractal cloud, but using the original parameters found for 2D cloud only increased the root-mean-square dispersion by at most 0.03, or 0.01
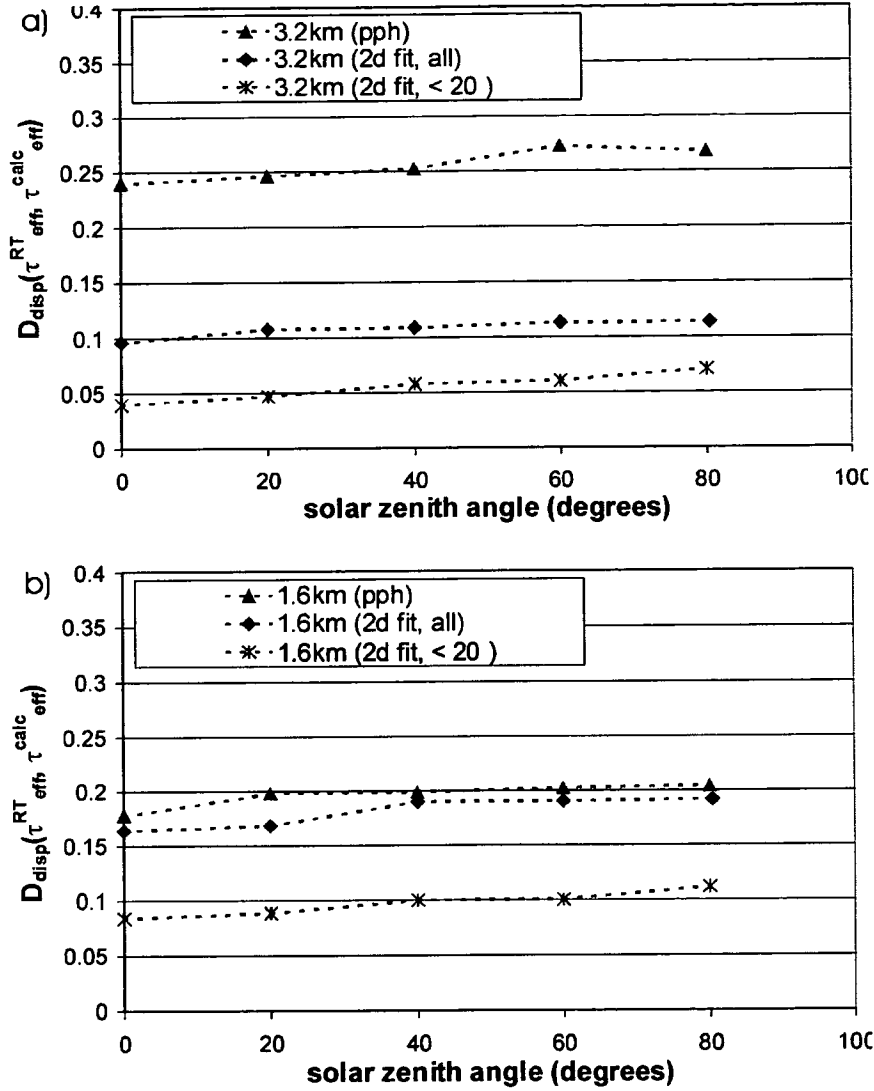
Figure 5.14: The root-mean-square dispersion between the effective optical depth of 3D multifractal cloud calculated from the Monte Carlo results, τ_{eff}^{RT}, and the parameterisation estimate τ_{eff}^{calc} done for the parameterisation developed for vertically homogeneous clouds. Values are also shown for the errors in the parameterisation if only cloud with $\tau_{mean} \leq 20$ are considered, and for the errors produced if the PPH assumption is made and the effective optical depth is set to τ_{mean}. Part a is for 3.2 km pixels and part b for 1.6 km pixels.

159
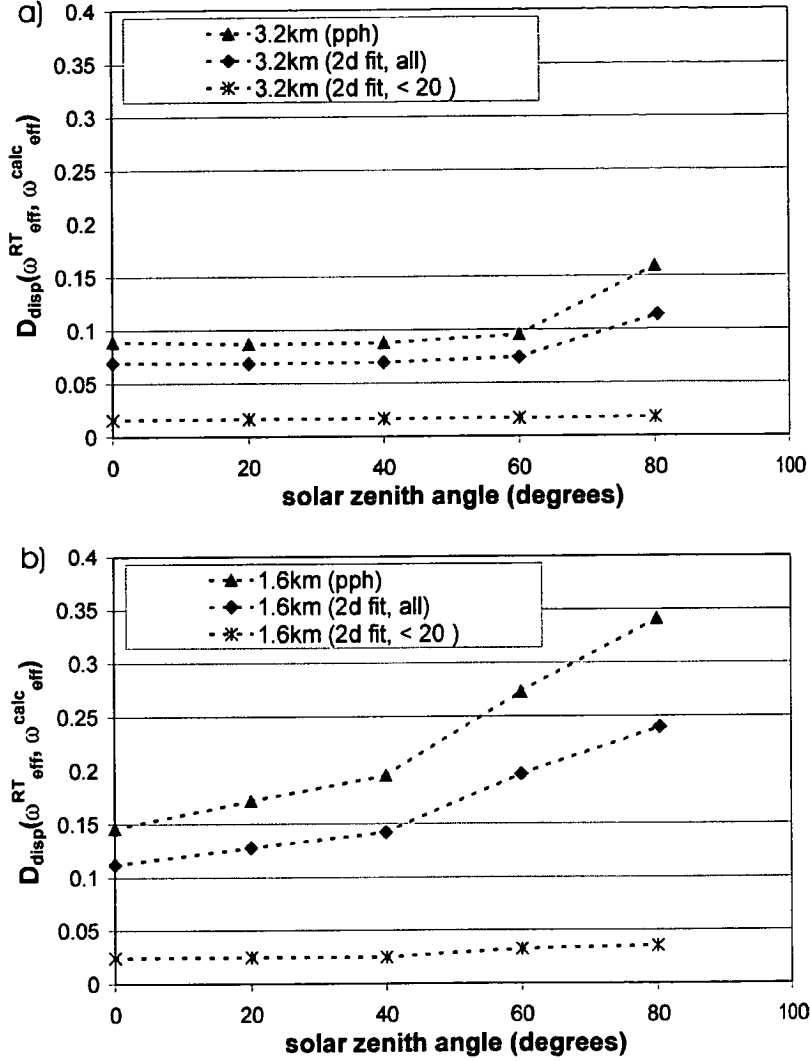
Figure 5.15: The root-mean-square dispersion between the effective single-scattering of 3D multifractal cloud calculated from the Monte Carlo results, ω_{eff}^{RT}, and the parameterisation estimate ω_{eff}^{calc}. Done for the parametersation developed for vertically homogeneous clouds. Values are also shown for the errors in the parameterisation if only cloud with $\tau_{mean} \leq 20$ are considered, and for the errors produced if the PPH assumption is made and the effective optical depth is set to τ_{mean}. Part a is for 3.2 km pixels and part b for 1.6 km pixels.

if only optical depths less than 20 were considered. Therefore the original parameterisation can probably be used with confidence in most cases where there is no absorption. Furthermore, if a more accurate model of the vertical statistics were derived, the consistent trends in the effective optical depth of non–absorbing clouds indicates that a new parameterisation could be found by simply recalculating the parameters of the approximation. There was an increase in the error between τ_{eff}^R and τ_{eff}^T at high solar zenith angles in this case, compared to the 2D case.

Absorbing clouds by contrast displayed qualitatively different behaviour when vertical inhomogeneity was introduced, specifically for large τ_{mean}. Although multifractal clouds with vertical variations reflect less radiation than those with constant vertical profiles, they absorb more and transmit less when the mean optical depths are large. That is, they do not simply move further from the PPH case as might have been expected and was seen for the elastic scattering in 3D clouds. As a result the effective optical properties could not be estimated using the parameterisation developed for multifractal clouds with no vertical variations, except where the mean optical depth was small (≤ 20). In fact, not only the particular parameterisation but the whole concept of an effective optical properties approximation could not be applied to absorbing clouds due to the difference between ω_{eff}^{RT} and ω_{eff}^{RA}, which indicates that there is no single PPH cloud that can accurately be substituted for an absorbing 3D multifractal cloud. This casts doubts on the validity of other studies that have found parameterisations for absorbing clouds by considering only 2-dimensionally variable clouds [e.g. *Szczap et al.*, 2000b] - although these parameterisations may be valid for determining a single radiative parameter (eg reflectance), it does not seem likely that they can accurately produce all three of T, R and A for realistic clouds.

To put these results in context, note that for an effective droplet radius of

$r_{eff} = 10$, $\omega \leq 0.99$ for wavelengths greater than $1.4\mu m$, while in the range of 0.3-0.7 μm the single scattering albedo is ~ 0.99999. Therefore the elastic scattering results are applicable in the UV and visible wavelength ranges, but not in the infrared region. So the effective optical depth approximation may be applicable to the shorter wavelengths, but not to the infrared. That is, for calculations in the infrared it does not seem possible to simply correct current PPH algorithms for 3-dimensional variations in clouds with large vertical dimension. This means another approach will need to be developed for these cases, probably involving radiation calculations performed directly on 3D clouds.

Chapter 6

Transmitted radiation under cloudy skies[1]

In the Chapter 4 it was shown that a homogeneous cloud with a reduced optical depth could be used to replace a multifractal cloud in radiation calculations and the error in the reflected radiance distribution would be very small. Although this is sufficient for satellite remote sensing, other applications such as climate models and ground based remote sensing are dependent on the transmitted radiation. In this chapter the distribution of transmitted radiance is considered and it is shown that even if a multifractal cloud and a PPH cloud have the same total transmittance the distribution of the radiance varies.

To demonstrate the effects of the spatial structure of clouds on the sky-radiance distribution, the ultraviolet (UV) section of the solar spectrum is used as an ex-

---

[1]The majority of this chapter can be found in the paper "A comparison of cloudy-sky UV-B radiance distribution measurements and radiative transfer calculations using a fractal cloud model" by K. Kuchinke, K. Fienberg and M. Nunez, submitted to *J. Appl. Meteorol.* Although the copyright is held by the American Meteorological Society, permission has been granted for publication in this thesis.

ample. This allows the comparison of the modelled results with measurements of the UV sky-radiance distribution made in Hobart, Tasmania. As discussed in section 4.5, there is relatively little difference between the optical properties of cloud droplets in the UV and the visible parts of the spectrum, so the results should be easily generalisable. The transmitted UV radiance under cloudy conditions is also of interest for its own sake, since many biological processes are dose-dependent, reacting to intense UV radiation events at short time scales [*Lesser et al.*, 1994; *Cullen and Lesser*, 1991] so that the spatial and temporal distribution of the radiation is as important as the total average transmittance. Various studies have been undertaken in an attempt to replicate the UV sky radiance distribution under cloudy skies [e.g. *Harrison and Coombes*, 1988; *Rosen and Hooper*, 1989; *Grant and Heisler*, 1997]. However, actual cloudy-sky analytical sky radiance distribution functions are limited, with *Grant et al.* [1997] finding a best fit for UV radiance measurements to an empirical distribution function [*Coombes and Harrison*, 1988].

Measurement of sky radiance can also be difficult because it is hampered by an inability to encapsulate rapid variations in the sky hemisphere. This shortfall is of particular concern in cloudy sky conditions where short-term variability of solar radiation is more likely. Most scanning systems take a relatively long time to cover the sky compared to the speed with which clouds move overhead and hence alter the radiation field. Under these conditions, any radiometric interpolation to correct for the mismatched temporal scans results in a possible loss of valuable cloud/sky information that could be retrieved. Although various attempts have been made to overcome this deficiency [eg. *Weihs et al.*, 2000], instantaneous measurement of the complete sky radiance field is not yet possible.

In this chapter a sky radiance measurement and modelling scheme is developed for some common cloud conditions. Emphasis is on encapsulation of the real spatial

and temporal radiance variability that exists. For high quality measurements of sky radiance distribution, the instrument utilised is the Variable Sky Platform (VSP) first documented in *Kuchinke* [2002] and *Kuchinke and Nunez* [2003]. This device allows for retrieval of 2-min azimuthally-averaged sky radiance information as a function of zenith angle. In effect it facilitates rapid scans of the sky by sacrificing knowledge of the azimuthal dependency. These measurements are compared to the results of the Monte Carlo radiative transfer simulations for UV radiation under stratiform cloud conditions, using both PPH clouds and the 2D verison of the FIF multifractal cloud model. Some parameterisations are then suggested so that PPH calculations can be corrected to accurately model the radiance distribution under variable cloud.

6.1 VSP radiance measurements

6.1.1 VSP Description

The VSP instrument is fully described by *Kuchinke* [2002] and *Kuchinke and Nunez* [2003]. Only a brief outline of the functioning of the instrument is given here. The basic concept involved is the hydraulic movement of a specially modified Solar Light Company 501-A UV biometer (SLC) within a vertically-mounted shading cylinder. A schematic representation of the VSP is shown in Figure 6.1. The internal wall of the cylinder is specially coated to minimize reflection and emphasis during its design was on timing accuracy. The erythemal filter of the SLC is thus exposed to varying degrees of sky view factor over very short time intervals. As a result of this it was necessary to correct all signal output from the sensor due to the effect of the 0.14-sec instrument time constant. A comparison of measurements just before

and after the sun is exposed to any and all of the SLC phosphor filter respectively (positions (1) and (2) in Figure 6.1a) will give us the following

$$I(2) - I(1) = I_d \cos \theta_0 + D_{\theta 2} - D_{\theta 1} = I_d \cos \theta_0 + \Delta D, \qquad (6.1)$$

that is the difference between the measured irradiance at the two points, $I(1)$ and $I(2)$, is equal to the direct beam irradiance, $I_d \cos \theta_0$ (where I_d is the intensity and θ_0 is the solar zenith angle) plus a residual diffuse quantity $\Delta D = D_{\theta 2} - D_{\theta 1}$. This residual value is the quantity of radiation that exists in the portion of sky $\Delta \theta$ subtended by the filter as it moves vertically between the described before and after-sun positions. Extrapolation across this relatively small $\Delta \theta$ allows us to easily determine ΔD. Once the direct irradiance is obtained, it can be subtracted from all readings corresponding to all cylinder positions above where the sun strikes the sensor. Subsequent comparison of any two positions of the sensor in the cylinder - positions (4) and (3) in Figure 6.1b - allow for derivation of ΔD for all zenith angles θ using

$$I(4) - I(3) = (I_d \cos \theta_0 + D_{\theta 4}) - (I_d \cos \theta_0 + D_{\theta 3}) = D_{\theta 4} - D_{\theta 3} = \Delta D_{(4-3)}, \quad (6.2)$$

where $I(3)$ and $I(4)$ are the measured irradiance at points 3 and 4 respectively, and ΔD is related to the uncorrected azimuthally averaged sky radiance $I'(\theta)$ by

$$\Delta D = 2\pi I'(\theta) \sin \theta \cos \theta \Delta \theta. \qquad (6.3)$$

This represents the radiation in a thin annulus of sky centred directly above the instrument. In this study, the steradian interval for VSP averaging is approximately 0.1 steradians. Thus, the radiance value $I'(\theta)$ is the azimuthally-averaged value for
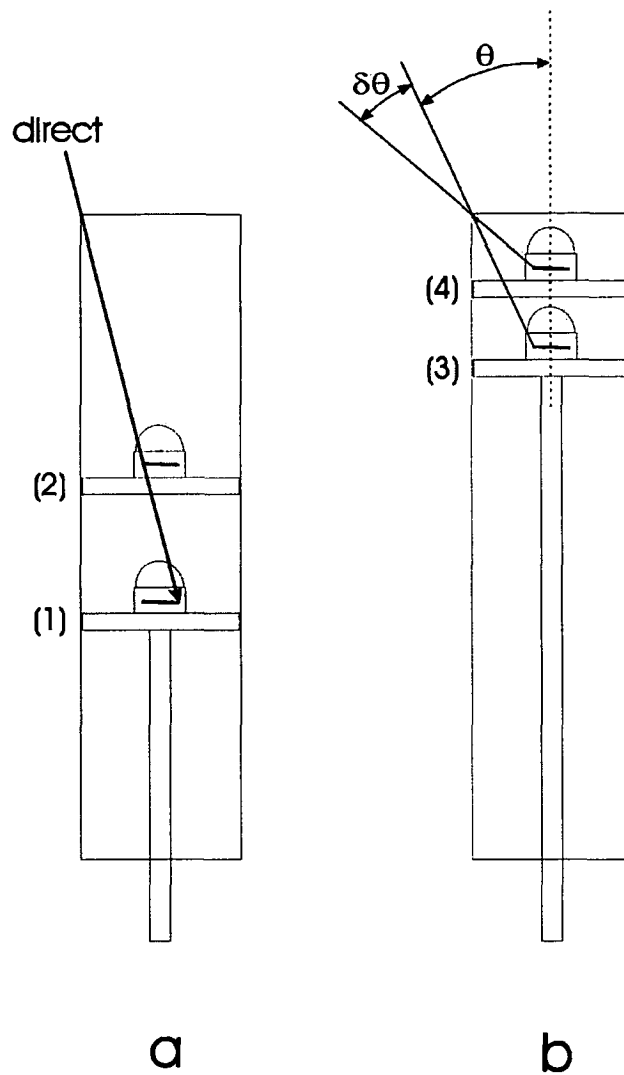
Figure 6.1: Figures 1a and b: schematic of VSP cylinder with SLC. Successive vertical positions of the sensor allows the radiance from an increment of sky $\delta\theta$ to be sampled

a small zenith angle interval. Based on the given steradian interval, this equates to a zenith angle interval of two to three degrees at low zenith angles and one degree at high angles, centred at the zenith angle in question. The final VSP-measured radiance $I'(\theta)$ is equivalent to the real radiance $I(\theta)$ multiplied by instrument cosine response $C(\theta)$ [*Kuchinke and Nunez*, 2001]. In this manner the azimuthal average radiance $I(\theta)$ may be obtained for any zenith angle θ.

Similarly, the cosine corrected total diffuse irradiance (D_{VSP}) for any two-minute interval is obtained by application of the relationship:

$$D_{VSP} = 2\pi \int_0^{2\pi} \frac{I'(\theta)}{C(\theta)} \sin\theta \cos\theta d\theta, \qquad (6.4)$$

Note that in this method the cosine response is accurately weighted with regards to the real sky distribution, and it avoids the temporal interpolation errors and sky radiance homogeneity assumptions that are implicit to shadow-band arrangements. Division of each $I(\theta)$ by D_{VSP} gives a normalized sky radiance measurement $f(\theta)$ to be used in this paper. Here, $f(\theta)$ is proportional to $I(\theta)$ in any direction and the implication is that the difference across any zenith curve is now largely due to cloud distribution. Under normal operating conditions, it takes 120 seconds for the SLC instrument to move from its uppermost position, offering an uninterrupted view of the sky, to its lowest position 459.0-mm from the top of the cylinder. At this bottommost position the zenith angle sky view of the sensor is 10.5, accomplished at a platform speed of $3.82\,mm\,s^{-1}$ and a sampling rate of 0.75 seconds. At this sampling rate, much slower than the instrument time constant, the coarsest zenith angle resolution ($\delta\theta$ in Figure 6.1b) for a sensor approaching the top of the cylinder is 1.35. A five second pause in hydraulic movement is then performed once the instrument actually reaches the top of the cylinder. This facilitates VSP

168

measurements of global irradiance, G_{VSP}.

6.1.2 Measurement Acquisition

The VSP is mounted on the roof of the Geography Department climate station platform at the University of Tasmania, Hobart, Australia (42.90S; 147.33E). The site rests 38-metres above mean sea level and is situated 3-km south of the Hobart city centre. The observing site affords maximum exposure from the northeast through east to the southeast. Exposure from northwest through west to south is affected by Mt. Wellington and the surrounding foothills by up to 8.0. At no time are instruments subject to shading from nearby obstacles. The SLC instrument inside the VSP was calibrated as described *Kuchinke and Nunez* [2001].

The accurate VSP-determination of the direct beam intensity, I_d in equation (6.1), relies on a relatively static cloud field during any two minute VSP run. Cloud disruption of the direct beam during this time makes it difficult to separate the direct and diffuse components and hence retrieve a sky radiance profile. To ensure reliable radiance data in this study, the VSP algorithm in section 6.1.2 was only applied to 2 *min* runs characterized by an unchanged global irradiance signal during the same time interval. For this purpose, a SLC instrument similar to that deployed in the VSP operates in tandem five metres from the VSP. The standard deviation of the global signal from this instrument was calculated for every two minutes (at a sampling rate of 0.75 s). If the standard deviation was greater than 2.0 mWm^{-2}, the cloud field was considered non-static and the VSP run was rejected from the scheme. VSP measurements were retrieved for the morning of 7 January 2001 and the afternoon of 5 January 2002. The selected morning was characterized by 8 *octas* total cloud cover. This was further subclassified as 5 *octas* of low level 1 stratus

169

nebulosus cloud and 7 *octas* of low level 2 stratus nebulosus cloud. The selected afternoon was characterized by 6 *octas* total cloud cover. This was broken down into 3 *octas* of low level 1 stratus nebulosus cloud and 3 *octas* of stratocumulus cloud (with no stratocumulus cumulogenitus). Cloud measurements were undertaken every three hours by the Hobart Bureau of Meteorology in accordance with WMO cloud types and levels. The total cloud cover during each period was constant whereas the instances of the low level 1 and 2 clouds varied by ± 1 *octas*. At no time were other clouds present. Both days were also characterized by similar ozone and visibility conditions, a requisite for modelling cloud optical depth to be discussed ahead in section 6.2.1. For the morning period, two sets of eight consecutive 2 *min* VSP radiance runs were selected corresponding to solar zenith angles (at the mid-point of each run) of 29.8 to 32.6 and 48.5 to 51.9. For the afternoon period, five runs from 29.29 to 33.15 and eight runs from 48.10 to 51.66 were selected. All of the runs within each solar zenith angle set were then averaged across zenith angle to give one azimuthally averaged sky radiance curve approximately centred at solar zenith angle of 30 and 50, and corresponding to the average over around 18 mins in duration. Note here that three 2 *min* runs are missing at $\theta_0 = 30$ on the 5 January 2002. This is because on partial-cloudy days significant cloud disruption of the direct beam during any 2 *min* run is more likely. Hence, the data set was rejected using the standard deviation criterion based on the in situ global measurements described earlier.

6.2 Radiance modelling

Monte Carlo radiative transfer calculations (described in section 2.2) were performed using clouds generated by the FIF multifractal model described in section

2.1. The fractal parameters used were $\alpha = 1.48$, $C_1 = 0.106$, $H = 0.3$, which are the mean parameter values for all cloud fields considered in chapter 3. The cloud fields were taken to be 6.4 x 6.4-km in horizontal dimensions, 0.5-km thick and with a base 1.0-km above the ground. Unlike in the previous chapters where only the radiative transfer through the cloud field was considered to compare cloud models, in this part of the study an entire column of the atmosphere is considered and the radiation at the ground (rather than at the cloud base and top) is the quantity of interest. For non-cloud attenuating species the atmosphere was assumed to have a typical mid-latitude summer profile, as used in the MODTRAN radiative code [*Berk et al.* 1989, *Berk and Anderson*, 1995]. Each cloud liquid water field had a constant profile in the vertical and a multifractal horizontal structure generated according to the guidelines in section 2.1.6. A wavelength of 0.3086 μm was used, since this is the nominal wavelength of the VSP-mounted SLC instrument based on its response curve. A constant effective radius of $r_{eff} = 10\,\mu m$ was assumed throughout the cloud field. This is acceptable since at this wavelength g is relatively insensitive to changes in droplet radius distribution. This wavelength and droplet radius implied an asymmetry factor g of 0.869, which was calculated using the parameterization of Hu and Stamnes [1992]. The parameterization of single-scattering albedo in the same work yielded a value of 0.99994, or almost no absorption. Model input for UV ground albedo was 0.08, based on spectral measurements conducted at the VSP site utilizing a Macam SR9910 spectroradiometer. Each simulation was undertaken using 50 million photons and the model was initially run with solar zenith angles (θ_0) of 0°, 20°, 30°, 40°, 50°, 60° and 80°. Mean cloud optical depths τ_{mean} of 2, 4, 8, 16, 32, 64 and 100 were used as input at each solar zenith angle. In addition to clouds generated with liquid water content varying according to the 2-dimensional version of the FIF multifractal model, calculations for the traditional plane paral-

171

lel homogeneous (PPH) clouds were also made for comparison purposes. For each simulation the irradiance at the ground in each 25m ground pixel was recorded, as was the incoming radiance distribution averaged in bins of 5 degrees in the zenith and 10 degrees in the azimuth. Model data was then averaged over all pixels in the 6.4-km grid. The modelled direct beam was then subtracted from all global radiance distributions to give diffuse sky radiance distributions. Modelled radiance data was then azimuthally integrated and divided by the total diffuse irradiance in order match the VSP measurements described earlier in section 6.1.

6.2.1 Cloud optical depth retrieval

For determination of cloud optical depth, a clear sky calculation was generated using the Monte Carlo model described above. The global irradiance at the ground calculated for each of the cloudy cases (G_{cloud}) was then compared to that under clear sky conditions (G_{clear}) to give a ground-based "cloud transmittance", $T_g = G_{cloud}/G_{clear}$, at each of the solar zenith angles used in the cloud simulation. Shown in Figure 6.2 is a plot of T_g as a function of the mean cloud optical depth (τ_{mean}) for both the multifractal and PPH cloud models. Example results here are for $\theta_0 = 30°$ and show once again that the multifractal cloud has a consistently higher transmittance than the PPH cloud due to the inhomogeneity of the cloud. Note the similarity to the cloud transmittance for visible wavelengths that was seen in Figure 4.1 in the previous chapter. The optical depth of the cloud under which the VSP measurements were made was determined by comparing the real cloud transmittance at that time to those calculated for the two cloud models in Figure 6.2. The cloud transmittance (rather than irradiance at the ground) was used to reduce the influence of other atmospheric conditions. Its real value was estimated by dividing the cloudy-sky VSP-measured global irradiance by the same quantity

Modelled cloud transmission
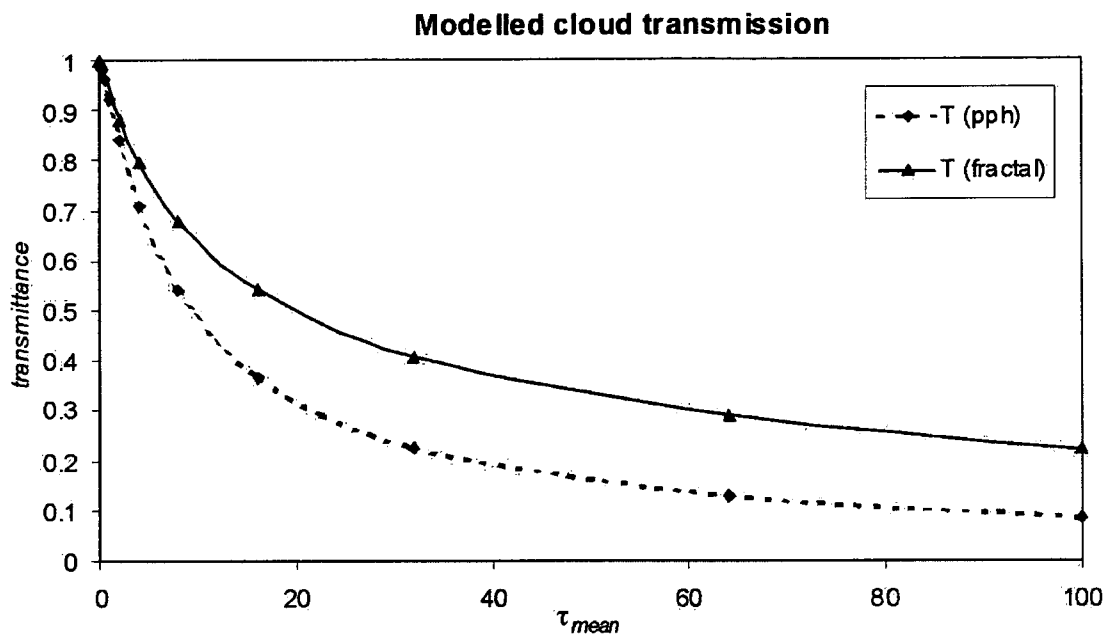
Figure 6.2: The modelled values of the ground-based "cloud transmittance" (G_{cloud}/G_{clear}) versus mean cloud optical depth. For a solar zenith angle of 30 degrees.

measured using the VSP on a clear day with the same ozone and similar visibility. For the cloudy case, the global irradiance was found using the 2 minute VSP global irradiance measurements in situ to the radiance data described in section 6.1. The mean of each set of 2-min global irradiance data gave the desired cloud-sky global irradiance quantity centred about the solar zenith angle in question. VSP clear-sky data was obtained in the same manner and temporally aligned for comparison purposes. Table 6.1 gives the selected clear sky and two cloud days used for the analysis as well as TOMS derived ozone. Visibility is also given and derived from Hobart Bureau of Meteorology observations. Cubic spline interpolation was then used to find the optical depths of the multifractal and PPH cloud with the same transmittance as measured by the VSP, and these optical depths are also shown in Table 6.1. Note that the optical depth found for the PPH cloud is, by definition, the value of the effective optical depth for the multifractal cloud field.

After determining these optical depths, the Monte Carlo radiation code was then executed with both multifractal and PPH cloud corresponding to the exact optical depths derived from the VSP measurement conditions. A single realisation of the multifractal cloud was generated for each analysis. The resultant radiance distributions are given in the following section.

Table 6.1: The measured mean of the ground-based cloud transmittance and corresponding cloud optical depths (for fractal and plane parallel scenarios), as well as other statistics for each day.

Date	Ozone (DU)	Visibility (km)	Cloud Cover (octas)	$\theta_0 = 30$ degrees			$\theta_0 = 50$ degrees		
				T_g	$\tau_{fractal}$	τ_{PPH}	T_g	$\tau_{fractal}$	τ_{PPH}
14 Dec 99	298	30	0	1	0	0	1	0	0
05 Jan 02	294	20-25	6	0.638	10.06	5.5	0.573	12.64	6.63
07 Jan 01	296	30	8	0.301	56.30	19.16	0.368	38.48	15.98

6.3 Comparison of VSP radiance measurements with model output

In this section the transmitted radiance modeled under multifractal clouds is compared with VSP sky radiance measurements. The normalised diffuse radiance function $f(\theta)$ is also considered for homogenous cloud with the same total transmittance as the multifractal cloud (therefore with a lower optical depth). Figures 6.3 and 6.4 give the $f(\theta)$ results for overcast and 6-octas (from herein referred to as broken) stratiform clouds respectively. Within each figure are two graphs representing θ_0 of 30 and 50 (a and b respectively). Recall that the modelled radiance distributions are an ensemble average across a $6.4\,km$ grid at a $25\,m$ resolution, while the measured distributions are averaged over approximately 20 minutes. In addition, all radiance values are azimuthally integrated, spanning 0 to $\frac{\pi}{2}$ zenith angle range at a resolution of five degrees for model data and one to two degrees for measured data. This small zenith angle interval is denoted zenith-discrete-angle. For a purely isotropic sky field the normalised radiance parameter $f(\theta)$ would be constant and equal to $\frac{1}{\pi}$. In reality, this is seldom the case. Contributing to the anisotropy is the aerosol forward scattering of the direct beam above the cloud field, namely the diffuse circumsolar component as argued for clear skies by *Morris and Lawrence* [1971]. It is recognized that optically thick cloud in this region of the sky is likely to diffuse this component due to the accompanying increase in multiple scattering events. For example, the PPH model assumes a uniformly distributed mean cloud field with no inhomogeneities. For realistic liquid water content and transmission values, the circumsolar effect is completely smoothed out, resulting in a smoothly decreasing PPH curve in all the figures. In contrast, the inhomogeneity in the multifractal cloud field results in regions of low liquid water content where the

175
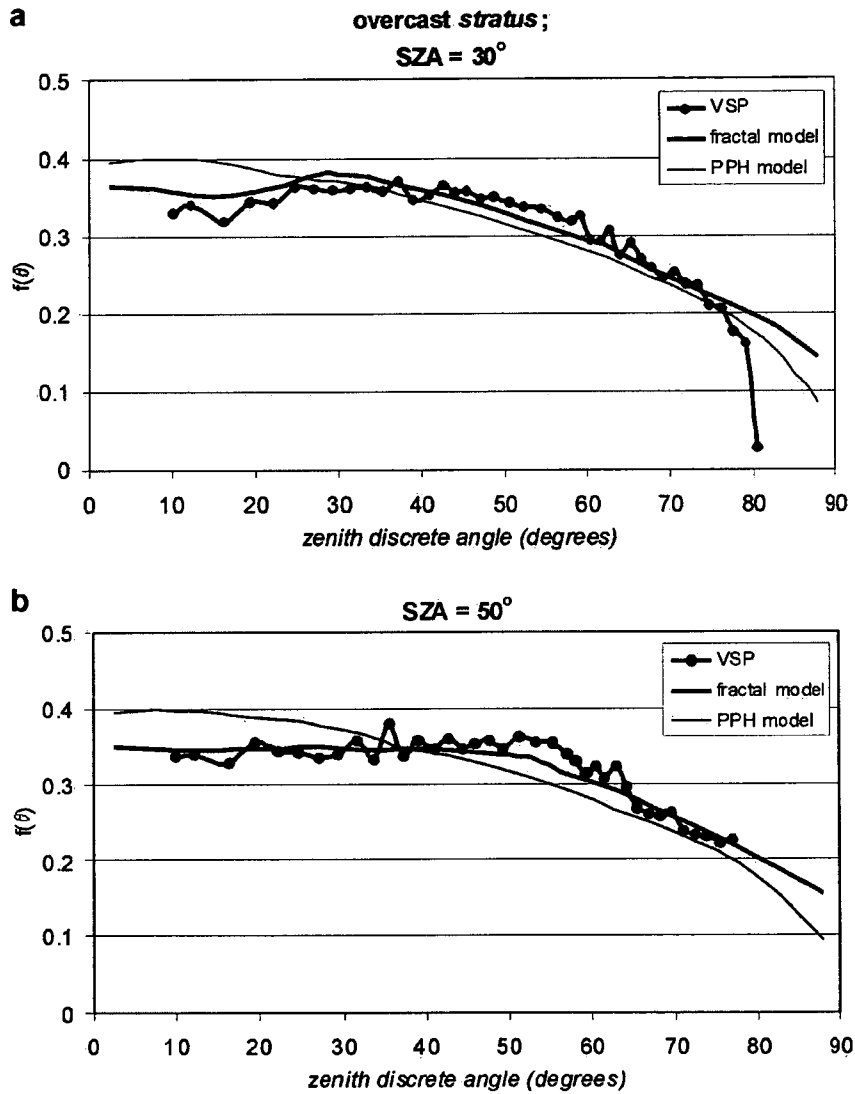
Figure 6.3: Comparison of VSP measured sky radiance with the modelled results using multifractal and PPH cloud models. For overcast stratiform cloud conditions and solar zenith angles of a) 30° and b)50°. The function f, plotted as the ordinate, is the normalised and azimuthally-averaged radiance.
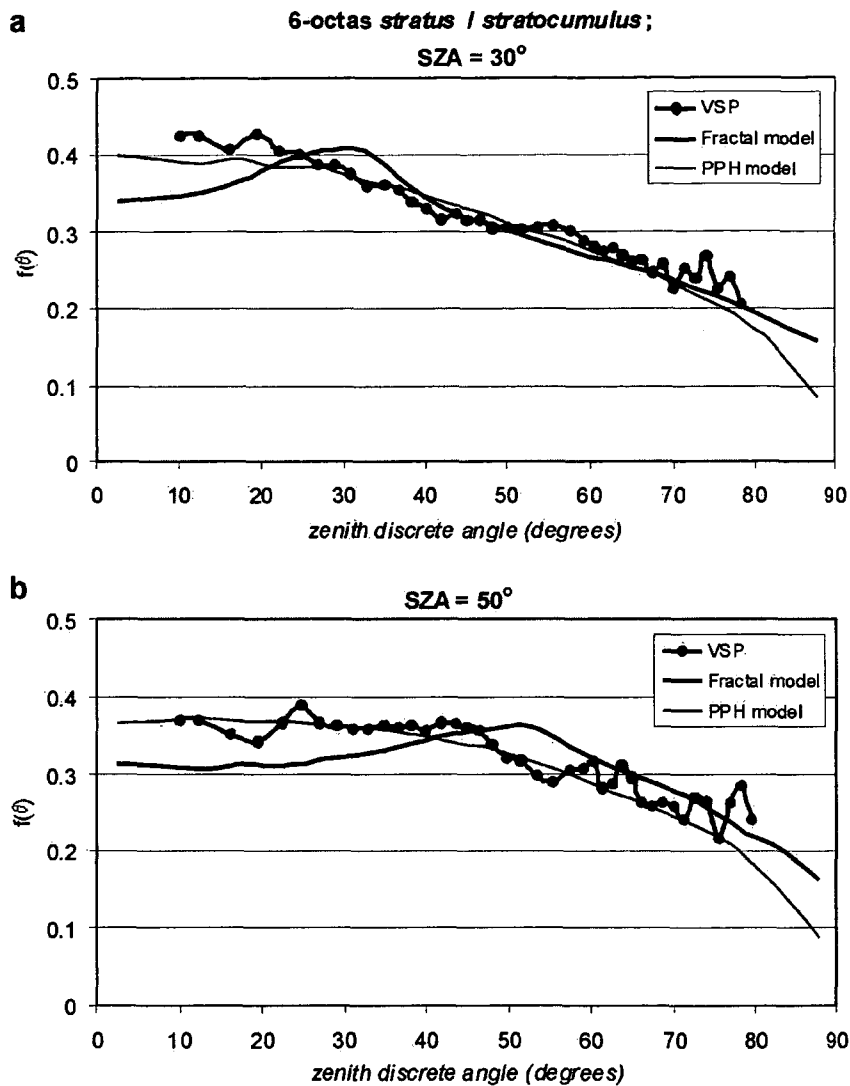
Figure 6.4: comparison of VSP measurements of the sky radiance distribution modeled results using Multifractal and PPH cloud models. For 6-octas stratiform cloud conditions and solar zenith angles of a) 30° and b) 50°. The function f, plotted as the ordinate, is the normalised and azimuthally averaged radiance.

177

smoothing of circumsolar irradiance is much less than for the PPH model. In some instances, the liquid water content approaches zero and is therefore much less than the aerosol optical depth. For these sky regions, the clear-sky circumsolar effect will be noticeable in the multifractal model, as evidenced by the hump around θ_0 in some of the multifractal curves in the same figures. Note that the effect in the multifractal curves is more pronounced under broken (lower mean optical depth) cloud conditions where the circumsolar forward scattering is less diffused, shown in Figures 6.4. The performance of the fractal and PPH models can be checked by comparison with the VSP measurements in each of the figures. For overcast stratus conditions, the agreement between multifractal and VSP data is exceptional, apart from the small scale variability in the measurements, as seen in Figures 6.3a and b. For broken stratus cloud conditions, Figure 6.4, the circumsolar hump is not evident in the measurements and hence the PPH model is in better agreement. The trend here is deemed to be a result of sampling bias in the VSP data at the lower cloud optical depth rather than under-performance in the fractal model. As described in section 6.1.2, 2-min VSP data were only accepted for analysis if the variability in measured global irradiance during the same time interval was low. As a result of this sampling method, measurement periods in which the direct beam is sometimes present and sometimes covered during the 2-min interval are rejected. Hence there is a bias towards periods where the direct beam is either completely obscured or continuously uncovered. However, the latter are very rare during the 6-octas cloud conditions. The result is an excess of cases where the cloud cover is concentrated around the sun position, and any gaps in the cloud cover are well away from the sun (since the cloud cover is constant). This leads not only to a diffusion of the circumsolar radiance but also an artificial raising of the radiance away from the sun through the gaps in the cloud. Thus the final effect of this sampling bias is that

178

the 6-octas measurements show an even smoother radiance distribution than the overcast conditions, as the circumsolar hump is completely hidden. The sampling problem does not appear in the completely overcast conditions because the sun is always obscured and no sampling periods need to be rejected.

6.4 Parameterisation of multifractal-cloud radiance distribution

From the previous section it is clear that the multifractal and PPH cloud models produce significantly different transmitted radiance distributions even when the total transmittance is the same. In addition, at least for overcast conditions, the results when using the multifractal cloud model are much closer to measured values than when using the PPH cloud model. Therefore a parameterisation of the diffuse radiance distribution under multifractal cloud is sought. This would extend the utility of the effective optical properties approximation, since it could be used to determine the probable sky radiance distribution after the effective PPH calculations have been used to determine the total transmittance.

The incoming radiance distributions at the ground under multifractal cloud fields were found using all of the Monte Carlo simulations described in section 6.2. At each cloud optical depth a Levenberg-Marquardt least-squares procedure was performed, fitting the calculated radiance distribution for multifractal clouds to the function:

$$I(\theta, \phi) = I_{mean}\{p_0 - p_1\theta^2 + p_2 \exp(-p_3\Psi)\} \qquad (6.5)$$

where $I(\theta, \phi)$ is the radiance at (viewing) zenith angle θ and azimuth angle ϕ; I_{mean} is the mean radiance over the sky distribution; p_i $(i = 0, .., 3)$ are the parameters

179

of the fit; and Ψ is the scattering angle defined by

$$\cos\Psi = \cos\theta\cos\theta_0 + \sin\theta\sin\theta_0\cos\phi \qquad (6.6)$$

Note that this formula assumes that the azimuth angle is defined such that the sun is at $\phi = 0$. The function (6.5) is similar in form to that used by *Grant et al.* [1997]. The first term in equation (6.5) represents a constant background skylight, the 2nd term describes the horizon darkening under cloud, and the third term represents any circumsolar component. The four parameters in equation (6.5) that were found by the least squares fit at each cloud optical depth are shown in Figure 6.5. Here, parameters p_2 and p_3 decrease and increase respectively with
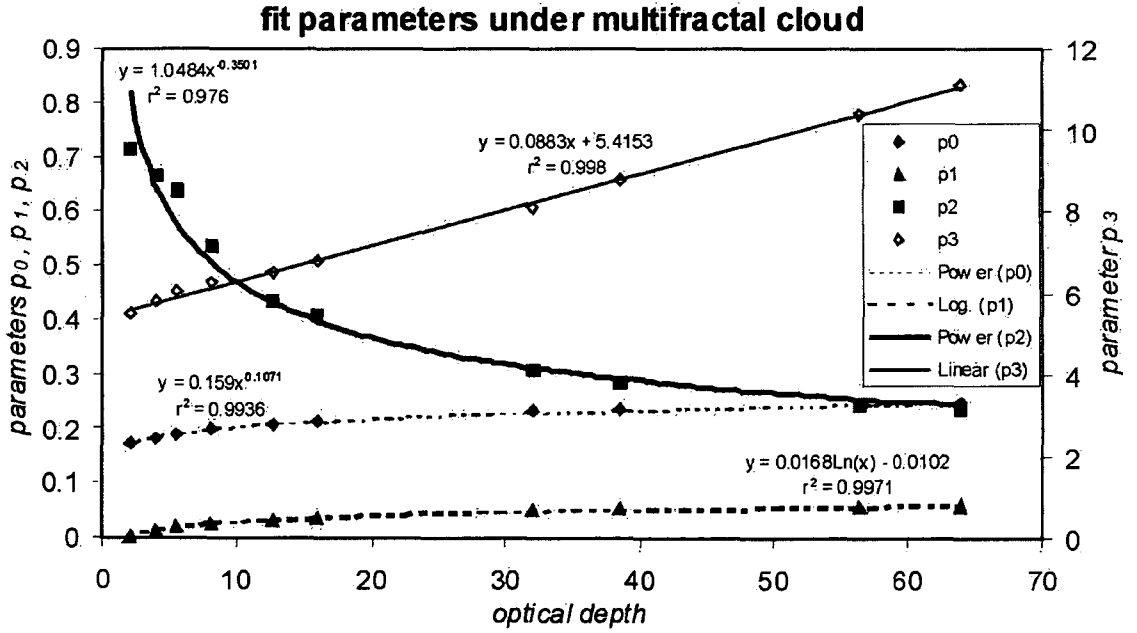
Figure 6.5: The fit parameters p_i ($i = 0, .., 3$) as a function of cloud optical depth for an empirical radiance distribution function under a multifractal cloud field.

180

increasing cloud optical depth. This indicates that the circumsolar term becomes less important as the cloud becomes thicker, as would be expected. In order to find values of the parameters at other optical depths, the curves shown in Figure 6.5 were fit to the p_i values. Resultant radiance curves based on the given empirical parameterization are given below.

Figures 6.6 and 6.7 compare (multifractal cloud) Monte Carlo model output with output from the empirical radiance distribution function (6.5). The results are grouped as in the previous section: Figures 6.6 is for overcast conditions, Figure 6.7 is for the 6 octas cloud and both have values for two different solar zenith angles (a and b). The mean optical depths used for each case are those found in Table 6.1. For additional comparison, Figures 6.6a and b also include output based on parameterizations from previous works for both translucent overcast skies [*Grant et al.*, 1997] and obscured overcast skies [*Grant and Heisler,* 1997] for a range of WMO low and middle cloud types. Recall that in the overcast case the multifractal model was in very good agreement with the VSP measurements. Results show that for both solar zenith angles, the Grant translucent-overcast parameterization is in better agreement with multifractal model at low zenith viewing angles. The Grant obscure-overcast parameterization represents optically thicker cloud increasing the likelihood of circumsolar smoothing. In contrast, the obscured-overcast parameterization is in better agreement with the multifractal model as it approaches the horizon. This difference is increased at high solar zenith angles. These parameterisations of *Grant et al.* [1997] and *Grant and Heisler* [1997] were developed from sets of observations and have no explicit optical depth dependence, and it would appear from the comparison that the overcast day observed here has optical depths that lie somewhere between the translucent and obscured cases as they have defined them. The advantage of the parameterisation developed here is that the optical thickness

181
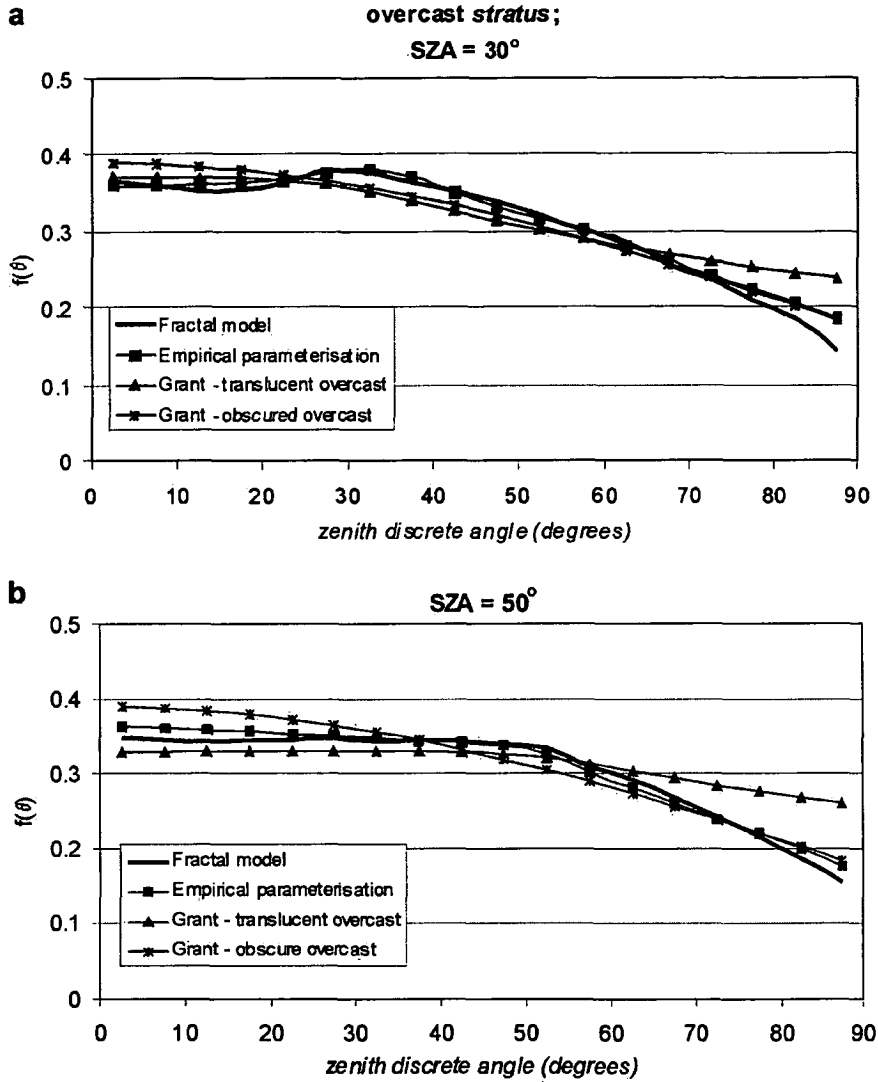
Figure 6.6: The sky radiance distributions for overcast stratus cloud conditions, with a) $\theta_0 = 30°$ and b) $\theta_0 = 50°$. Both show the Monte Carlo results with multifractal cloud, the parameterised values for multifractal cloud and the two Grant parameterisations (translucent and overcast).

a

6-octas *stratus* / *stratocumulus*;
SZA = 30°

b

SZA = 50°
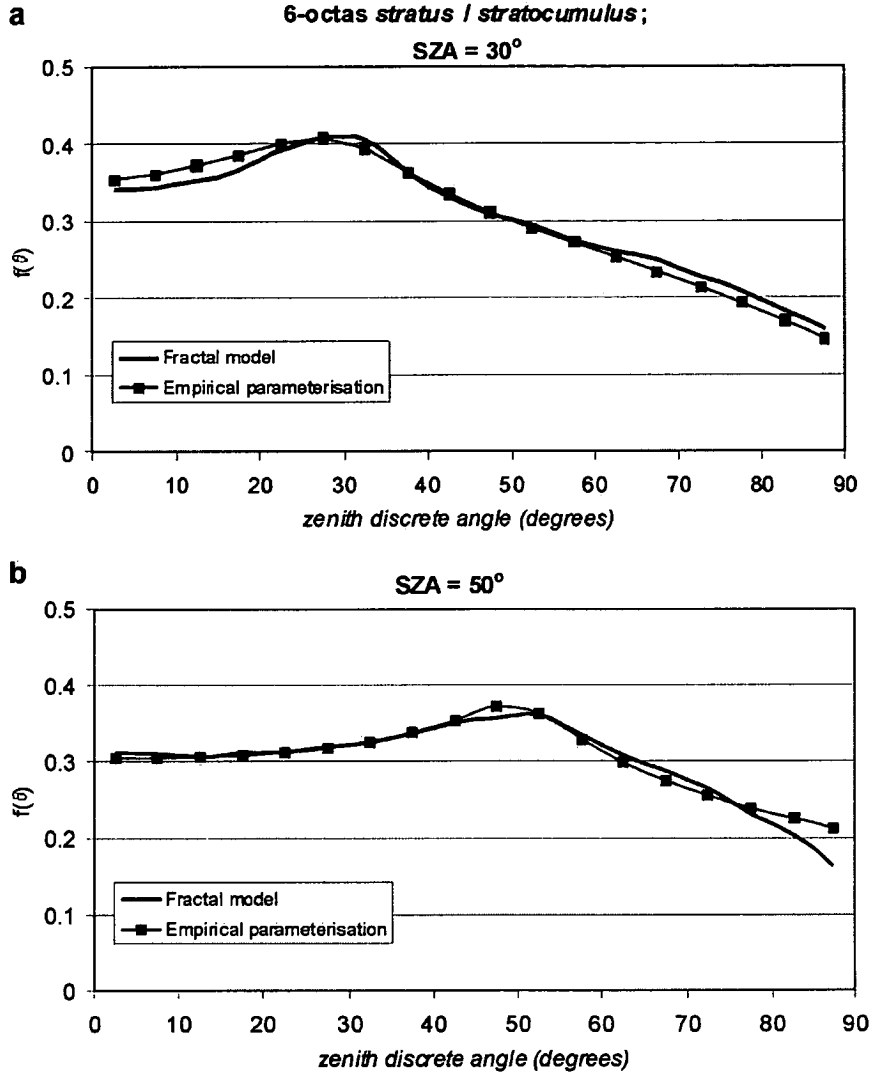
Figure 6.7: The sky radiance distributions for 6 octas stratiform cloud conditions, with a) $\theta_0 = 30°$ and b) $\theta_0 = 50°$. Shows the Monte Carlo results with multifratal cloud and the results of the parameterisation of multifractal cloud.

of the cloud can be taken into account when it is known. Finally, results in all four graphs show that the multifractal model and output from the fractal parameterization are similar. Of course, this is to be expected since the incoming radiance distributions used in the parameterization were derived from the same Monte Carlo simulation used in the fractal model. This attaches a degree of confidence to use of this parameterization (equation (6.5)) as a surrogate for the multifractal model in other radiative transfer applications.

6.5   Summary of Chapter 6

Azimuthally-integrated measurements of UV-B sky radiance distribution were compared with modelled radiances under a multifractal cloud field using a relatively new instrument. Data were also compared with model output for a plane parallel homogenous cloud layer and several empirical parameterisations. Sources of error in the comparison can be found in both the measurements and modelling. The SLC sensor in the VSP is relatively insensitive to near-horizon radiation due to the low amount of flux available to the erythemal filter and the cosine error of the filter/dome assembly. In addition, VSP two-minute measurement sampling was biased towards incidents of direct beam obscurity by clouds. This smoothed the broken cloud fields measurements so that they appeared even more isotropic then the overcast conditions.

Errors in the modelling scheme are primarily attributable to the input parameters. For example, the average cloud transmittances in this study were derived by comparison of VSP-measured clear-sky and cloudy data at the given solar zenith angle intervals. This allowed for derivation of relevant cloud optical depths for model input. Care was taken to ensure a constant ozone data set. However, some

error may be introduced here should atmospheric aerosol vary across both clear and cloudy measurement days. Although inter-day visibility agreement was factored into the data selection, diurnal variation in aerosol optical depth becomes significant if the aerosol single scattering albedo is low during any of the measurement times. This may result in UV radiance (and thus transmission) differences as intense cloud scattering events increase the likelihood of aerosol absorption. Another possible input error may also be attributable to the cloud fractal parameters themselves. The values used were mean values for low cloud and hence may not exactly represent the cloud structure on the given days.

Results show that for overcast conditions, the multifractal model is superior to the PPH model for producing realistic radiance distributions at the ground. For broken cloud conditions, the radiance measurements are biased towards higher instances of circumsolar smoothing by cloud as discussed. Under these conditions the multifractal model continues to exhibit the circumsolar effect, indicating that its performance may be still valid for radiation modelling. An empirical parameterization of the multifractal model produced similar sky radiance profiles for the given sky conditions in this study. Analysis for a more comprehensive range of sky conditions may confirm its suitability for further use as a tool in radiative transfer models. Overall, the study shows that inhomogeneities within the real cloud field have a significant effect on the radiation distribution at the ground even on an overcast day.

Chapter 7

Comparison of satellite cloud property retrieval with in situ measurements

7.1 Overview

Observations of cloud properties such as liquid water path is an important step in many endeavors, including: studying atmospheric processes, testing and providing input for global circulation models, and estimating radiation levels or rain rates at the surface. In making these observations, satellite remote sensing has the advantage of being able to cover a wider range of spatial scales than ground based or aircraft measurements. However, this raises the question of the accuracy of such satellite-derived estimations, and a straightforward way of evaluating this is by comparison with in situ measurements.

Some of the earliest comparisons of remote sensing with in situ measurements

186

of cloud properties demonstrated great discrepancies between the two data sets [*Twomey and Cocks*, 1982; *Rawlins and Foot*, 1990]. As new remote sensing techniques were developed [e.g. *Nakajima and King*, 1990; *Minnis et al.*, 1992; *Rosenfield and Gutman*, 1994; *Evans and Haigh*, 1995], the agreement between remotely retrieved cloud properties and aircraft measurements improved [e.g. *Nakajima et al.*, 1991; *Kuji et al.*, 2000], but these studies used aircraft mounted radiometry in the comparisons rather than satellite platforms. The problem in comparing satellite data directly with in situ measurements is generally the mismatch of scales involved, with satellite pixels representing an average over an area while aircraft measurements are generally a time series taken at very high spatial resolution but covering only a small fraction of each pixels area. In some cases this problem has been overcome - for example *Young et al.*[1998] examined orographic wave clouds because they are quite spatially and temporally homogeneous, while *Fouilloux and Iaquinta* [1997] used a mesoscale numerical model to link aircraft and satellite measurements. In this chapter another method of comparison is examined that is applicable to more cloud types and does not rely on a numerical model, but rather uses the spatial statistics and scaling behaviour of cloud liquid water fields found in chapter 3. These statistics are used in this study to "upscale" aircraft liquid water measurements, i.e. to estimate the average liquid water path in a satellite pixel from the small scale measurements inside the pixel. This is done using multifractal objective analysis based on the method developed by *Salvadori et al.*[2001]. Due to the lack of measurements for the vertical variations in the cloud field, in this chapter the cloud model again assumes vertical homogeneity so that the statistics of the liquid water path are assumed to be the same as for the liquid water content measured in chapter 3.

As well as investigating the effects of cloud spatial structure on the comparison

187

of data at different scales, the satellite and aircraft measurements are also used to show the effects of the PPH albedo bias and to test the effective optical properties approximation in the retrieval of cloud properties. Although the radiances reflected off cloud tops are used here, instead of total reflectance, section 4.5.3 shows that this introduced minimal errors into the calculations.

Therefore the structure of this chapter is as follows. The method of upscaling, or objective analysis, of aircraft measurements is described in section 7.2. Section 7.3 details the remote sensing technique and the data set used. The comparison between aircraft measurements and remote sensing results is then presented in section 7.4.

7.2 Objective Analysis of Multifractal Fields

The multifractal statistics of cloud fields found in chapter 3 can be used to extrapolate from sparse data points at a high resolution to a value at a lower resolution. In remote sensing validation this can be used to extrapolate any multifractal field from high resolution ground-truth data to the scale of the satellite pixels. It is useful whenever the high-resolution in situ data does not cover the whole of a satellite pixel. But not only is a method of upscaling measurements necessary to compare data taken at different scales, it is also important to understand the errors that result from the mismatch of scales.

The multifractal objective analysis developed by *Salavadori et al.* [2001] was used here for upscaling, and the full mathematical derivation can be found in that work. This method is used to first examine the possible errors when sampling a multifractal liquid water path field at random points, and then modified to take into account integration across a pixel rather than point sampling. A numerical version

188

of the analysis is used rather than the analytic formulae developed by *Salavadori et al.* [2001] because those only applied to lognormal multifractal fields.

First consider the differences between scales in the unconditional probability distributions. These are determined from the codimension function $c(\gamma)$ by equation (2.5), that is

$$\Pr(x_\lambda \geq \lambda^\gamma) \approx \lambda^{-c(\gamma)}, \tag{7.1}$$

for any multifractal field x_λ at resolution λ. The probability density $p(x_\lambda)$ can easily be found from the probability $\Pr(x_\lambda \geq \lambda^\gamma)$ by taking differences for finite bins (size Δx_λ), or the derivative for a continuous distribution:

$$p(x_\lambda) = \frac{\Pr(x'_\lambda \geq x_\lambda) - \Pr(x'_\lambda \geq x_\lambda + \Delta x_\lambda)}{\Delta x_\lambda}. \tag{7.2}$$

While the codimension $c(\gamma)$ is independent of resolution, the final probability density will vary with λ. Figure 7.1 shows the probability densities $p(x_\lambda)$ for $\lambda = 128$ and $\lambda = 2560$, calculated using the codimension function of the FIF multifractal model with the mean parameters from the aircraft measurements described in chapter 3, and normalised so that the mean of x_λ is 1. In terms of the remote sensing of cloud fields, the former scale could represent a 1 km satellite pixel with the scaling invariance extending out to 128 km, while the latter scale could then be ground-truth data taken at a 50 m resolution. At the higher resolution the probability density has a peak at ~ 0.25, while the peak at the lower resolution is around 0.5. Thus the most probable single point sample at the higher resolution is lower than the most likely single point sample at the lower resolution. However, it can also be seen that above 2.2 the probability densities cross again, so that the higher resolution also has a greater chance of getting an extremely high value. The result of this is that the high resolution, $\lambda = 2560$, will have many low points and
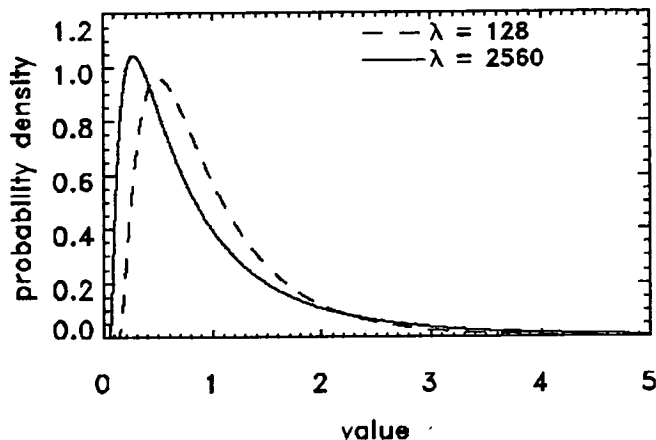
Figure 7.1: The probability density of a (normalised) multifractal field, shown for two spatial scales λ that are separated by a factor of 20.

a sparse few very high ones. The lower resolution follows the same pattern but in a less extreme manner with more values closer to the mean. The question now is how to move from one to the other.

7.2.1 Method description

The technique used to estimate values at a lower resolution from a sample at the higher resolution is known as Most Likely Parent (MLP) estimation [*Salavadori et al.*, 2001]. This name comes from the concept of fractals being formed by a cascade process, as described in Chapter 2. This assumes that the multifractal field is formed of a number of independent, stochastic cascade steps, and that the multifractal statistics described in section 2.1.3 apply to each step. That is, the values of the field at a higher resolution, $\lambda = \Lambda$ say, are the "offspring" formed by

190

the division in a cascade process of the "parent" structure at the lower resolution ($\lambda = \lambda_0$). This is shown schematically in Figure 7.2. In the validation of remote sensing the parent field would be at the resolution of the satellite images, so that each parent value is an average over a satellite pixel, and the offspring would be the points within each pixel at the resolution of the in situ data. Let the ratio between the parent and offspring resolution, $\tilde{\lambda}$, be given by

$$\tilde{\lambda} = \frac{\Lambda}{\lambda_0}. \tag{7.3}$$

Then the relationship between the parent field x and the offspring field X is

$$X = x\tilde{x}, \tag{7.4}$$

where $\tilde{x}$ is a multifractal field of scale $\tilde{\lambda}$, due to the scale independent and multiplicative nature of the cascade process [*Schertzer and Lovejoy*, 1995]. That is, at any point in the offspring field, for example X_2 shown in the Figure 7.2, is a product of the parent value at that point (x_i in the figure) and an independent factor ($\tilde{x}_2$ in the figure) that is also multifractal in nature with scale parameter $\tilde{\lambda}$. This means that the probability distribution of the field $\tilde{x}$ is given by equation (2.5), i.e. $\Pr(\tilde{x} \geq \tilde{\lambda}^{\tilde{\gamma}}) \approx \lambda^{-c(\tilde{\gamma})}$. Therefore if the codimension $c(\gamma)$ of the mutlifractal field is known, then the probability distributions of the three multifractal quantities, X, x, and $\tilde{x}$, are also known. In this work the $c(\gamma)$ is given by the FIF model value with the parameters determined from the aircraft measurements in chapter 3. Of the three quantities the parent x and the multiplicative ratio $\tilde{x}$ are independent.

The objective now is to use these known probability distributions to extrapolate from a set of N known offspring values, that do not cover all of the parent pixel, to the most likely value of the field in the parent pixel. To work with these fields

Parent Scale
$\lambda = \lambda_0$

common parent, x_i

Offspring
$\lambda = \Lambda$

| X_0 $= x_i . \tilde{X}_0$ | X_1 $= x_i . \tilde{X}_1$ | X_2 $= x_i . \tilde{X}_2$ | X_3 $= x_i . \tilde{X}_3$ | X_4 $= x_i . \tilde{X}_4$ | X_5 $= x_i . \tilde{X}_5$ |
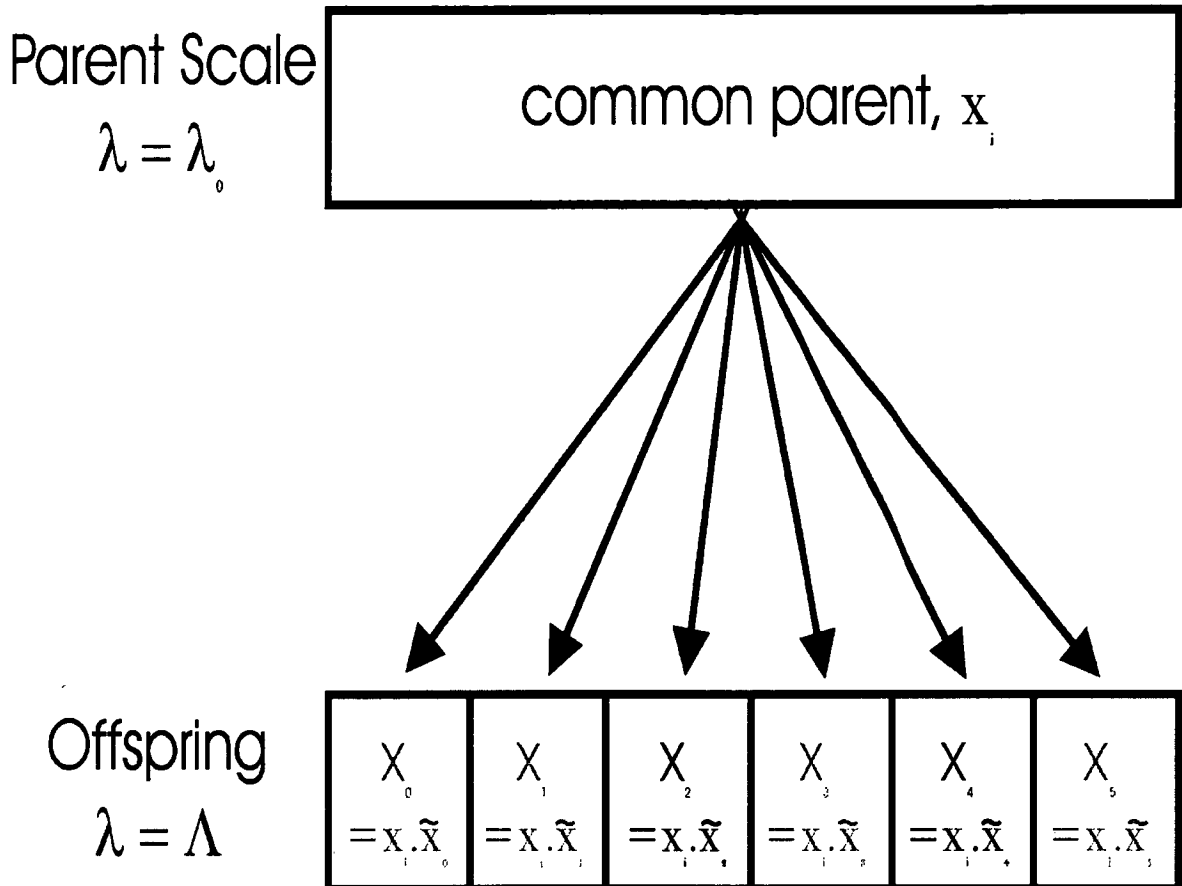
Figure 7.2: An example of the relationship between a parent structure at a low resolution ($\lambda = \lambda_0$) and an offspring at a high resolution ($\lambda = \Lambda$). The value of the field at low resolution is the parent value x_i, where the subscript i is used because it is just one pixel in a larger field (not shown here). The values at a higher resolution in the same area are the offspring values X_j ($j = 0, .., 5$), with each X_j being related to the parent x_i by the ratio field $\tilde{x}_j$ as shown. When using the MLP upscaling method only a subset of the offspring will be known - in this example this is represented by the known offspring values been shown in black and the remainder in grey.

that are at different resolutions, it is convenient to use exponential notation, where the values of the (normalised) multifractal field are given as powers of the scale. Therefore let the parent field be $x = \lambda_0^\gamma$, the offspring field be $X = \Lambda^\Gamma$, and the ratio field be $\tilde{x} = \tilde{\lambda}^{\tilde{\gamma}}$. If we have measurements of a particular set of N samples at the offspring scale (higher resolution) within the parent pixel, then let the offspring set be $\underline{\Gamma} = \{\Gamma_i$ s.t. $.X_i = \Lambda^{\Gamma_i}, i = 1, ..., N\}$, let the values of the ratio field at those points is described by the set $\underline{\tilde{\gamma}} = \{\tilde{\gamma}_i$ s.t. $\tilde{x}_i = \tilde{\lambda}^{\tilde{\gamma}_i}, i = 1, .., N\}$, and let γ be the exponent of the common parent of all the offspring (e.g. the total pixel value).

The equation (7.4) relating the offspring, parent, and ratio fields can then be rewritten in terms of the exponents:

$$\Lambda^{\Gamma_i} = \lambda_0^\gamma \tilde{\lambda}^{\tilde{\gamma}_i}, \qquad i = 1, .., N. \tag{7.5}$$

From (7.3), the scales are related by $\Lambda = \tilde{\lambda}\lambda_0$, so if we define $k = \ln \lambda_0 / \ln \tilde{\lambda}$, then the relation (7.5) becomes

$$\tilde{\lambda}^{(k+1)\Gamma_i} = \tilde{\lambda}^{k\gamma} \tilde{\lambda}^{\tilde{\gamma}_i} \tag{7.6}$$

and this can be manipulated to give the exponents of the ratio field in terms of the offspring and parent values:

$$\tilde{\gamma}_i = (1 + k)\Gamma_i - k\gamma, \qquad i = 1, .., N. \tag{7.7}$$

Of these fields only the offspring set $\underline{\Gamma}$ is initially known, but equation (7.7) gives the set $\underline{\tilde{\gamma}}$ in terms of the other two fields, leaving the single parent exponent γ as the only free variable. A probability density $p(\tilde{\gamma}_i)$ can then be found for each field using (7.2) and (2.5).

To determine the most likely parent exponent given the known set of offspring

exponents, we use the conditional probability distribution $p(\gamma \,|\, \underline{\Gamma})$ of obtaining γ given the particular offspring set $\underline{\Gamma}$. To obtain this we first need to consider the joint probability distributions $p(\gamma, \underline{\tilde{\gamma}})$ and $p(\gamma, \underline{\Gamma})$. The joint probability of having both the parent exponent γ and the ratio values $\underline{\tilde{\gamma}}$ is $p(\gamma, \underline{\tilde{\gamma}})$, and since the parent and ratio field are independent,

$$p(\gamma, \underline{\tilde{\gamma}}) = p(\gamma)p(\underline{\tilde{\gamma}}) = p(\gamma)\prod_{i=1}^{N} p(\tilde{\gamma}_i). \tag{7.8}$$

Therefore the joint probability $p(\gamma \,|\, \underline{\Gamma})$ can be found from the single point probabilities that are given by the FIF multifractal model. The joint probability of having both the parent and the offspring fields $p(\gamma, \underline{\Gamma})$ can then be written as

$$p(\gamma, \underline{\Gamma}) = (1 + k)^N \, p(\gamma, \underline{\tilde{\gamma}}), \tag{7.9}$$

where the factor of $(1 + k)^N$ is the Jacobian of the transform of $\underline{\Gamma}$ to $\underline{\tilde{\gamma}}$ (given by equation (7.7)). The MLP method then estimates the most likely parent, using the conditional probability distribution $p(\gamma \,|\, \underline{\Gamma})$ of γ given the particular offspring values $\underline{\Gamma}$, which is given by:

$$p(\gamma \,|\, \underline{\Gamma}) = \frac{p(\gamma, \underline{\Gamma})}{\int p(\gamma', \underline{\Gamma}) \, d\gamma'} \tag{7.10}$$

The estimate of the parent exponent is then the value of γ for which the conditional probability $p(\gamma \,|\, \underline{\Gamma})$ is a maximum. While *Salvadori et al.* [2001] found an analytical solution to this for the case of $\alpha = 2$, it is not clear that one is possible in the general case. In this work the maximum is numerically estimated from the probability distributions. If γ_{max} is the value of γ for which $p(\gamma \,|\, \underline{\Gamma})$ is a maximum, then the best estimate of the parent field is then $x = \lambda_0^{\gamma_{max}}$.

An example of the conditional probability density is shown in Figure 7.3, for seven offspring values, {0.5, 0.85, 0.95,1.0, 1.05,1.15,1.5}. This was again done
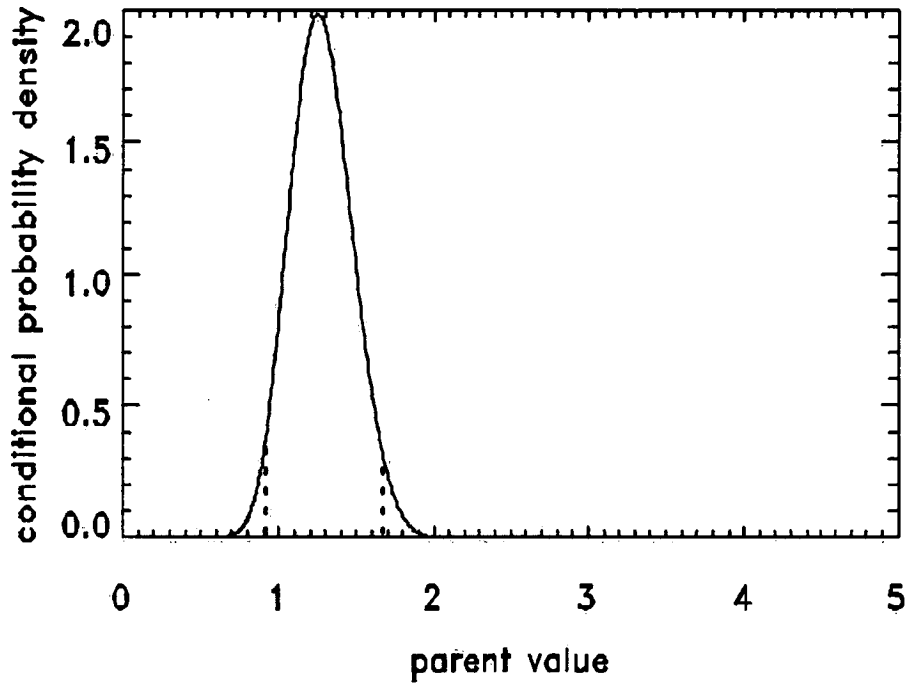
Figure 7.3: The conditional probability density of a parent-pixel value of the field occurring at scale $\lambda = 128$, given that seven samples were taken of the offspring field in the pixel at scale $\lambda = 2560$. The 7 samples are {0.5, 0.85, 0.95,1.0, 1.05,1.15,1.5}.

with a parent resolution of $\lambda_0 = 128$ and an offspring resolution of $\Lambda = 2560$ to simulate a typical case for moderate resolution remote sensing compared to ground truthing (1 km satellite pixels, ground based data at five points with 50m resolution, with scaling regime out to a scale of 128 km) . Note that the maximum point, or the MLP estimate, is 1.24, despite the fact that the mean of the offspring values is

195

1. The 95% confident values of 0.91-1.61 are plotted as dotted lines, and show the relatively wide range of possible values.

7.2.2 Numerical Simulation

To examine the results of the MLP method, multifractal fields were generated numerically using the discrete cascade algorithm given in Chapter 2 and the mean FIF model parameters derived for cloud fields from the flights in Chapter 3 ($\alpha = 1.48$, $C_1 = 0.106$, $H = 0.3$). Again the parent resolution was $\lambda_0 = 128$ and the offspring scale was $\Lambda = 2560$, for a scale ratio of $\bar{\lambda} = 20$. The values at λ_0 are considered to represent a perfectly accurate satellite measurement of moderate resolution pixels (1 km say), while the values at Λ are considered to be in-situ samples taken at much higher spatial resolution inside these pixels (point measurements at 50m resolution). The multifractals were two dimensional to simulate cloud liquid water path. Since the multifractal generation is stochastic, 30 fields were generated with different seed values.

Inside each of the 128×128 pixels at the low resolution in each field, a number of points at the high resolution were randomly selected. Several cases were investigated with different amounts of sampling - of the 400 high resolution points in each pixel we found the results when using 1,3,5,10, 20, 40,60, 80, 100, and 200 randomly selected points. From these points the MLP estimate was calculated, as was the mean of the sampled points, which would be the traditional estimate. Figure 7.4 contains a 1D cross-section of an example multifractal field, showing both the true pixel values and the MLP estimates with 10% of the pixels sampled. Although there is some error in the MLP estimate, it follows the general trend of the field quite well. To test the accuracy of this estimate we use the the relative error (RE)

196
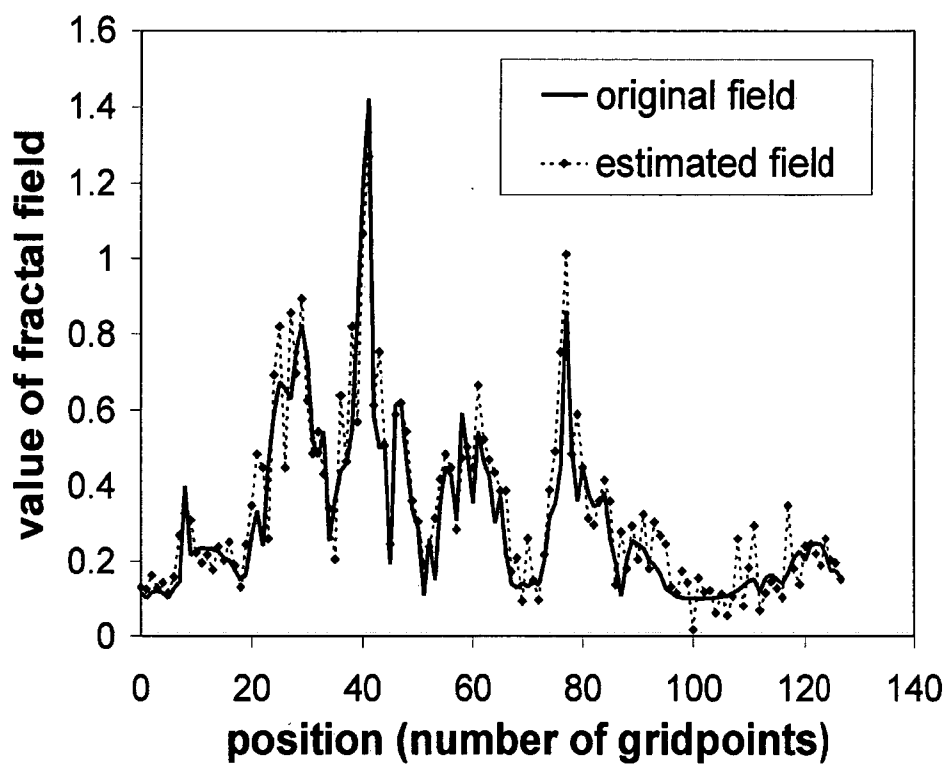
Figure 7.4: A 1-dimensional cut through a multifractal field, showing both the values of the field and the MLP estimate of this value given a random sample of 5% of the field.

197

in the estimation, given by

$$RE = \frac{E - x_\lambda}{x_\lambda},$$
(7.11)

where E is the estimation of the true parent value x_λ. Figure 7.5 shows the mean relative error and the root-mean-square relative error, i.e. $\sqrt{\frac{1}{n}\sum RE^2}$, for both the estimation made using the MLP method and the estimation made by simply taking the mean of the sampled points. This shows that the mean of RE is close to zero for both methods, but the root mean square relative error for the MLP method is slightly above half of that of the estimation by the mean value. This is true for all sampling numbers. Also note that even using the MLP method a significant proportion of the parent structure must be sampled to produce small root-mean-square errors - for example 20% of the area must be sampled to reduce the root mean square relative error to less than 10%.

7.2.3 Simulation of upscaling aircraft data

The MLP method described so far is useful for upscaling ground-truth data made at a small number of points inside a pixel, such as a radiosonde estimate, a lidar at a point, or a restricted aperture radiometer. But for in-situ data taken by aircraft-mounted instruments, the data is generally not recorded as randomly scattered points but rather as a line across the pixel at a very small scale. Therefore this situation was also simulated here using a numerical simulation of a multifractal field. The parent scale was again taken to be $\lambda_0 = 128$, while the offspring scale was now $\Lambda = 128,000$. This was done to simulate an aircraft run with resolution of 10 m, through parent pixels of 1 km, with a scaling regime assumed to extend from the 10 m scale to 128 km. The offspring values were chosen to form a line across the parent pixel, to simulate a single crossing of the satellite pixel by the aircraft. The

198
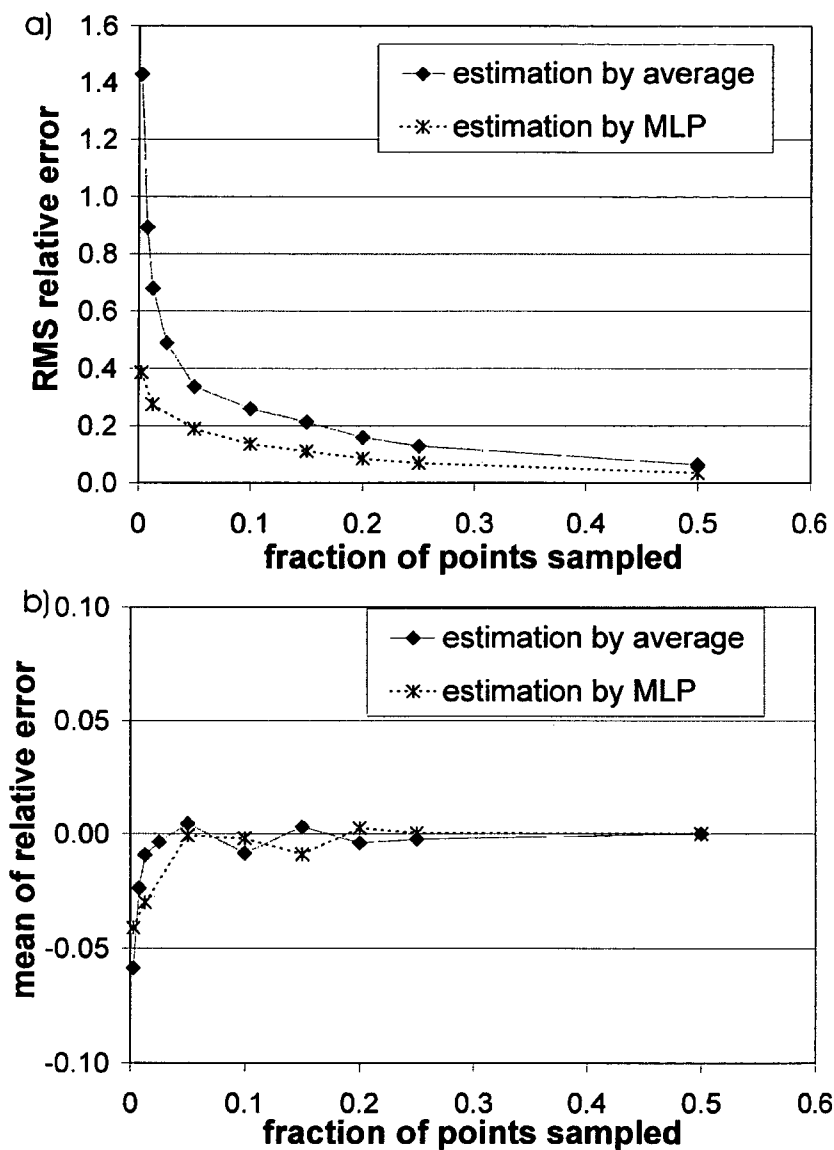
Figure 7.5: a)The mean of the relative error when estimating an area average from a number of point samples inside the area at a higher resolution, shown as a function of the fraction of the area that has been sampled. b) the standard deviation of the relative error. Both are shown for the MLP upscaling method and the traditional approach of taking the average of the points.

sampled line was placed at a random position but the orientation of the line was always parallel to one of the pixel edges, so that the sampled line across the parent pixel was always 1km in length. Twenty realisations of the field were generated, with the estimation of the parent values being made using the MLP method, and also by simply taking the mean of the measurements across the field. The relative errors were calculated for both methods and a frequency histogram of these relative errors are shown in Figure 7.6. The mean of the relative errors are close to zero in both cases, so there is no absolute bias but it is clear that the MLP errors shown in part b) of the figure are clustered much closer to zero than the errors in mean estimation method. This is reflected by the fact that the root mean square of the relative error is 0.27 in the case of the MLP method but 0.43 when only the mean is used to estimate the whole pixel value. Therefore the MLP method is a significant improvement in zooming out to the coarser resolution, but there still remains a significant error (27%) when comparing the data taken at different scales.

7.3   Data Acquisition Methods

The upscaling method is used to compare the cloud liquid water path derived from the satellite and aircraft data. This data was taken on the 3rd of April 2000 and the 23rd of May 2000 over northern Tasmania, designated flight A and flight B respectively. Cloud type on both days was predominantly stratocumulus. Care was taken to select overcast days with only a single layer of low cloud.
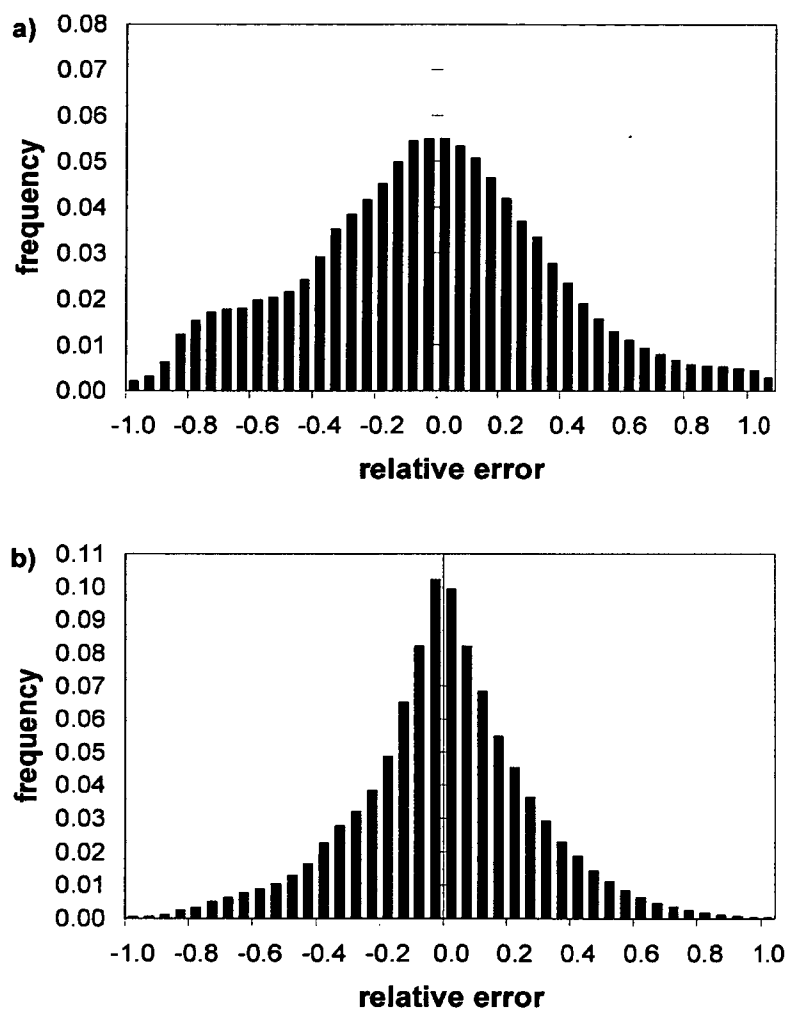
Figure 7.6: Frequency histogram of the relative error in the estimation of a 2-dimensional multifractal cloud field, given that each pixel is sampled by flight through it at a spatial scale 1/1000-th the pixel size. a) shows the relative error if the estimation of each pixel is simply the mean samples taken in the pixel, b) shows the relative errors if the MLP upscaling method is used.

7.3.1 Satellite Retrieval

The satellite retrieval of cloud liquid water path was done using the algorithm described in *Kuji et al.* [2000] with data from the Advanced Very High Resolution Radiometer (AVHRR) on the polar orbiter NOAA-14. This algorithm uses three channels of the AVHRR. The reflected solar radiation measured by channel 1 (0.58-0.68 μm) and channel 3 (3.55-3.93 μm) are the primary channels used to retrieve cloud properties, while channel 4 (10.5-11.5 μm) is used to correct the channel 3 for thermal emission. This algorithm retrieves cloud optical depth and effective droplet radius, as channel 1 is predominantly dependent on the former while solar radiation in the channel 3 band varies with the latter [*Nakajima and King*, 1990]. A multi-dimensional lookup table is used to derive the cloud properties from the satellite radiances, and this was created using the 16-stream discrete ordinate (DISORT) multiple scattering option of the MODTRAN 4 radiation code [*Berk et al.*, 1989; *Berk and Anderson*, 1995] with a typical mid-latitude winter atmospheric profile. This radiation code uses a PPH cloud model.

The use of the PPH cloud model in the calculations introduces a bias to the albedo in the visible channel as discussed in Chapter 4. However, since the reflectance in channel 3 is primarily dependent on the single-scattering albedo, the spatial structure in the optical depth (or liquid water path) considered in this work has comparatively little effect on the channel 3 reflectance. To demonstrate this the Monte Carlo model radiative transport code was used to find the reflectances in the middle infrared for 3-dimensionally multifractal cloud as described in Chapter 6. Figure 7.7 shows the ratio between reflectance found for 3D multifractal cloud (R_{mf}) and the reflectance found for PPH cloud (R_{PPH}) when the single-scattering albedo is 0.74 and the asymmetry factor is 0.84, which corresponds to $r_{eff} = 10\mu m$

202

and a wavelength of 3.69 μm (centre of channel 3). The pixel size considered is
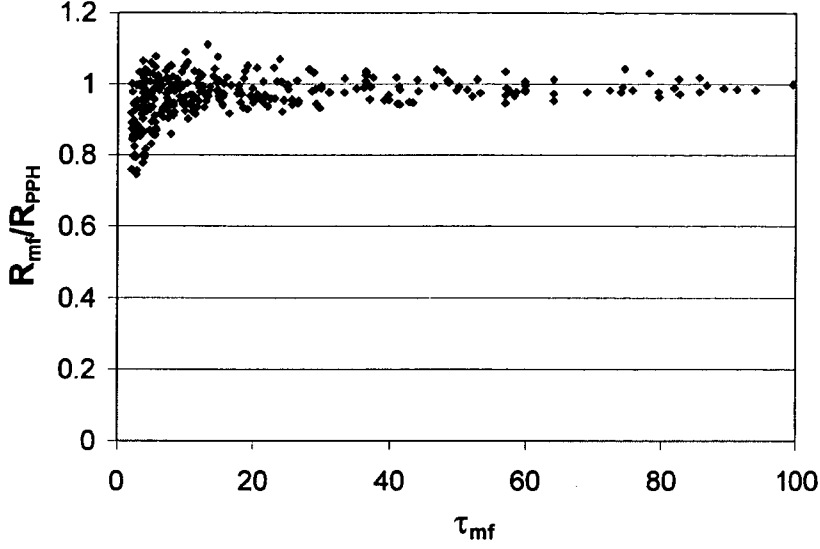
Figure 7.7: The ratio of the reflectance of a multifractal cloud to the that of a PPH cloud, for a wavelength of 3.69 μm and $r_{eff} = 10\mu m$. For a pixel size of 1.1 km.

1.1km, the nominal size of AVHRR pixels. This shows R_{mf}/R_{pph} to be very close to one, with the greatest scatter at low values of τ_{mean}. The mean value of the ratio is 0.984, which is a small bias in comparison with those seen in the visible portion of the spectrum in the previous chapter. Therefore no correction was made to the PPH calculations in channel 3.

For the visible optical depth (primarily dependent on channel 1 radiances) however, a correction to the PPH result was found using the parameterisation of the effective optical depth (4.2) found in section 4.3. The optical depth retrieved from the look-up table created using PPH cloud, labelled τ_{PPH}, is actually the effective optical depth of a multifractal cloud with the same reflectance. Therefore the parameterisation of the effective optical depth can be used to give the relationship

between the PPH estimate of the optical depth with the estimate made assuming multifractal cloud, τ_{mf}. A plot of the τ_{PPH} value given by equation (4.2) as a function of τ_{mf} is shown in Figure 7.8 for a pixel size of 1.1 km. This uses the
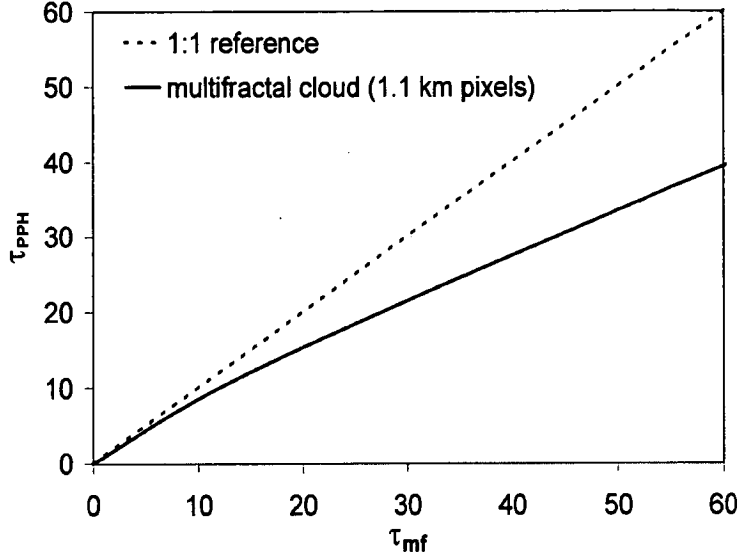
Figure 7.8: The PPH effective optical depth of a multifractal cloud, plotted as a function of the mean optical depth of the multifractal cloud. For a pixel size of 1.1 km.

parameters found for 2D multifractal cloud. Notice that at small optical depths the difference between τ_{PPH} and τ_{mf} is relatively small. Once the value of τ_{PPH} for a pixel was determined from the look-up table, the best estimate of the mean optical depth of a multifractal cloud in the pixel was therefore found by using cubic spline interpolation to find the value τ_{mf} that gives this τ_{PPH} in Figure 7.8.

Therefore the retrieval produces a droplet effective radius r_{eff} and mean cloud optical depth. These quantities can then be used to find the cloud liquid water

path, LWP, using the relationship [*Stephens*, 1978]:

$$LWP = \frac{2}{3}\tau\, r_{eff}\, D_w,\qquad\qquad (7.12)$$

where τ is the cloud optical depth and D_w is the density of water. Since we have two estimates of the optical depth, the PPH optical depth (τ_{PPH}) and the multifractal optical depth (τ_{mf}), there are similarly two estimates of the LWP that can be found with equation (7.12). Label these LWP_{PPH} and LWP_{mf} for the PPH and mean multifractal values respectively.

7.3.2   Aircraft Data

Cloud liquid water content was recorded on horizontal runs through cloud using an aircraft-mounted King hot-wire probe [*King et al.*, 1978]. A vertical flight was also carried out at the beginning and end of each horizontal run to measure the vertical profile of the of the liquid water content and hence by integration derive a LWP value. The values for the beginning and end runs were smoothed then averaged to produce a vertical profile to apply to the run. Following the procedure of *Kuji et al.* [2000], the "effective geometric height" was then taken to be the total cloud LWP for this profile divided by the liquid water content at the height of the horizontal run. This effective geometric height determined from the two vertical flights was then multiplied by the liquid water content at each point in the horizontal run to produce the LWP value. Note that this method assumes that the vertical structure and height of the cloud is relatively constant during the run.

The flight data used in the comparisons here was taken from the horizontal runs that were centered in time about the crossing time of the NOAA-14 satellite. The data used is restricted to 15 minutes either side of the image time, which was 5:39

UTC for flight A and 6:09 UTC for flight B, in order to reduce the effect of temporal changes in the cloud conditions. At an average speed of approximately 90 ms^{-1} this led to a data set covering a horizontal track of approximately 150 km in length. A sampling frequency of 10 Hz was used, meaning that the spatial resolution was ~9 m. GPS positioning was used to determine the aircraft position at any time. For each satellite pixel, the aircraft LWP was determined in two ways: firstly by taking the mean of the values of the aircraft LWP measured inside the pixel, and secondly by using the MLP upscaling analysis for integrated pixels described in section 7.2.3. Label these two estimates LWP_{mean} and LWP_{MLP} respectively. The multifractal objective analysis assumed that the scale invariant regime in the cloud fields extended to a scale of 150 km, and down to a scale of 10 m. That the scaling regime reached the top scale was shown in Chapter 3 but as this was the top scale measured it could extend further. That it extended down to 10 metres was shown by *Davis et al.*[1996] for stratocumulus cloud. The MLP upscaling procedure also requires that the field be normalised, and this was done by dividing the data by the mean of the entire horizontal run, as this is our best estimate of the ensemble average. After the procedure had been carried out, the MLP estimate for each pixel was re-multiplied by this ensemble mean in order to get the final LWP_{MLP} value.

7.4   Comparison of results

Table 7.1 shows the mean and standard deviations of the cloud liquid water path observed on the two days. Four versions of each statistic are shown: two for the two satellite estimates of liquid water path, LWP_{PPH} and LWP_{mf}, and two for the aircraft estimates LWP_{mean} and LWP_{MLP}. For both flights LWP_{mean} and LWP_{MLP} have very similar mean values, with the difference being that the MLP

Table 7.1: Mean and standard deviation of the four estimates of cloud liquid water path: the two in situ estimates for pixels, LWP_{mean} and LWP_{MLP}, and the two satellite values, LWP_{mf} and LWP_{PPH}.

Quantity	Flight A		Flight B	
	mean (gm^{-2})	std. dev.(gm^{-2})	mean (gm^{-2})	std. dev.(gm^{-2})
LWP_{mean}	99.6	73.3	61.2	45.4
LWP_{MLP}	100.4	52.4	61.8	33.2
LWP_{mf}	102.9	58.7	59.1	29.3
LWP_{PPH}	72.5	38.5	48.2	.22.32

estimate has a lower standard deviation - the general effect of the MLP upscaling procedure is to reduce the outliers and bring the distribution closer to the mean. The two methods of satellite retrieval, on the other hand, did produce significantly different mean values of the liquid water path. The mean PPH-model estimate of LWP is significantly lower than the mean multifractal value, because PPH clouds reflect more light than an inhomogeneous cloud with the same LWP. Note that on both days the mean of LWP_{PPH} is significantly lower than the mean of the aircraft estimates, while the mean of LWP_{mf} is quite close to the mean aircraft values of liquid water path.

The PPH results agree with the results of a comparison between satellite-based AVHRR data with aircraft-mounted microwave radiometer data by *Kuji et al.*[2000], which found on three separate flights that the (PPH based) satellite retrieval produced a lower mean LWP than the aircraft observations. Note that the aircraft mounted radiometer does not suffer a mean albedo bias caused by inhomogeneities because its spatial resolution is no bigger than the photon mean-free path length in the cloud, although it may have errors in individual point readings due to horizontal transport[*Cahalan et al.*, 1994b]. Our data not only confirm this result, but also indicates that the agreement in the mean satellite and in situ data can be improved if the satellite retrieval uses a correction for multifractal cloud

207

structure. This is graphically illustrated for flight A in Figure 7.9, where LWP_{PPH} and LWP_{mf} are both compared to the aircraft estimate LWP_{MLP} as function of flight distance. Part a compares the multifractal estimate with the aircraft data, part b compares the PPH estimate with the aircraft data. It can be seen in this figure that the PPH and multifractal retrieved values are practically identical at small liquid water path values, but that the larger the liquid water path the greater the difference between the two. The same plots for flight B are shown in Figure 7.10. Here the difference between LWP_{PPH} (Figure 7.10a) and the multifractal estimate LWP_{mf} (part b) is lower because the optical depths are lower on average and hence the correction predicted by Figure 7.8 is smaller.

The mean of LWP_{mf} is very close to the mean of both the aircraft estimates, but what about the correlation between individual points? There are two comparisons made now: between the remotely sensed value LWP_{mf} and the two aircraft estimates $(LWP_{MLP}$ and $LWP_{mean})$. It is LWP_{MLP} that is considered the best estimate of the liquid water path in the pixel, as was shown by the numerical simulation in section 7.2. The traditional estimate of LWP_{mean} on the other hand is used to demonstrate the results that would have been seen without the MLP upscaling method.

To quantify the agreement between the satellite and aircraft estimates we again consider the relative error, RE, as defined by equation (7.11). The root-mean-square relative error $(\sqrt{\frac{1}{n}\sum RE^2})$ for the comparison of LWP_{mf} and LWP_{MLP} is given in Table 7.2. Also shown in the this table is the error in the satellite estimation that would have been found if MLP estimation had not been used, i.e. the error in LWP_{mf} vs LWP_{mean}. The root-mean-square errors in both flights of around 30% between LWP_{mf} and LWP_{MLP} is quite large, but it is only slightly above the error of 27% found for the MLP estimate of the true value in the pixel by the numerical
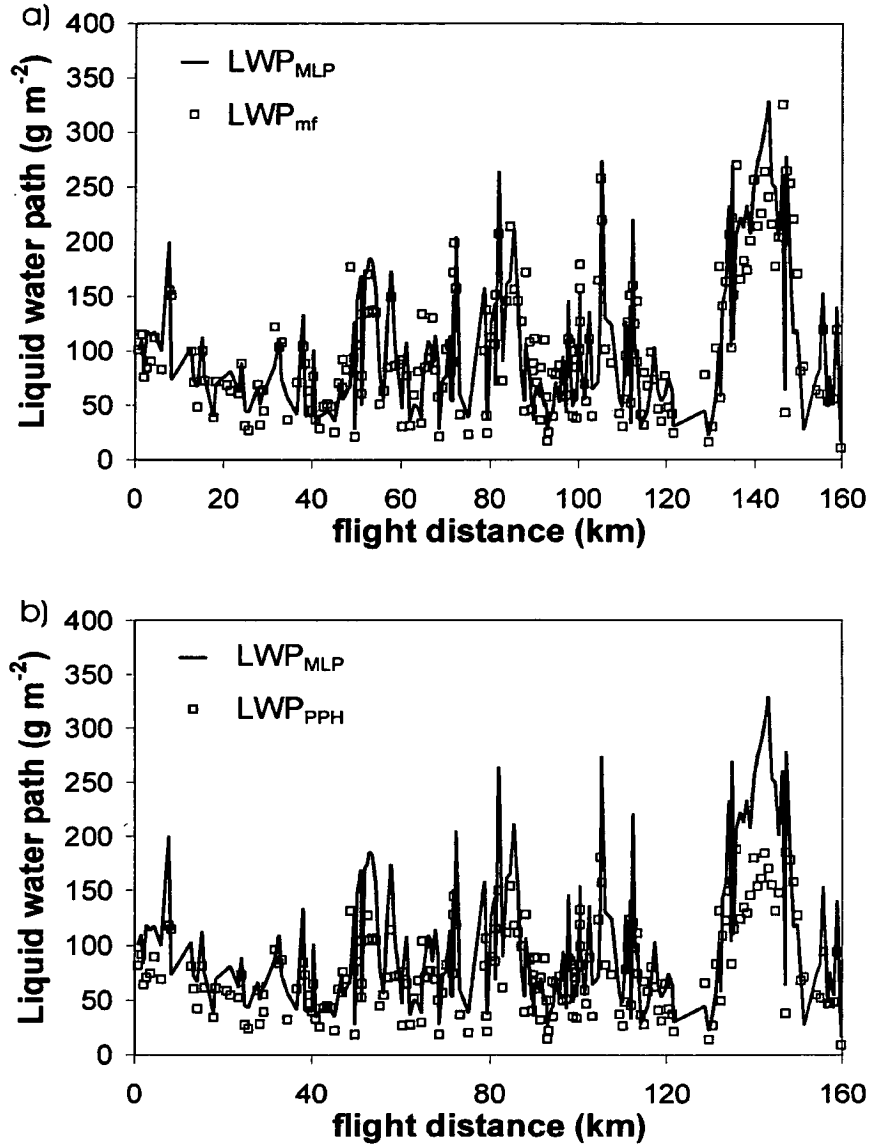
Figure 7.9: A comparison of retrieved liquid water path with the aircraft estimated value for flight A (3 April 2000) . a) shows the retrieval when a multifractal cloud is assumed, while b) shows the PPH cloud retrieval with no correction for inhomogeneity. The aircraft value is the same in both - the MLP estimate of the whole pixel value for each pixel the plane went through.
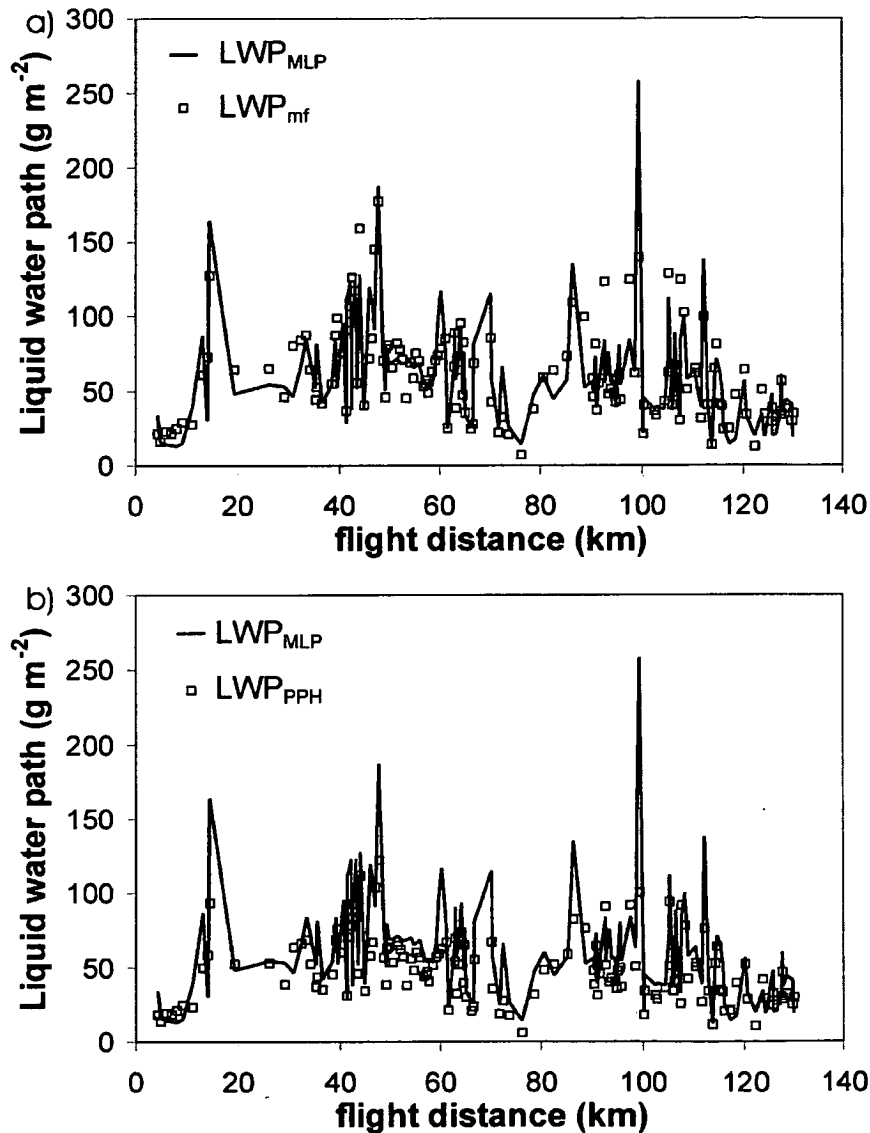
Figure 7.10: A comparison of retrieved liquid water path with the aircraft estimated value for flight B (23 May 2000) . a) shows the retrieval when a multifractal cloud is assumed, while b) shows the PPH cloud retrieval with no correction for inhomogeneity. The aircraft value is the same in both - the MLP estimate of the whole pixel value for each pixel the plane went through.

210

Table 7.2: The root-mean-square relative error, $(\sqrt{\frac{1}{n}\sum RE^2})$, for the comparisons of the satellite retrieved liquid water path (LWP_{mf}) with the two versions of the aircraft data, the MLP estimate (LWP_{MLP}) and the estimate made by simply taking the mean of all points in the satellite pixel (LWP_{mean}). For comparison the errors with respect to the PPH retrieval (LWP_{PPH}) are also shown.

	Flight A	Flight B
LWP_{mf} vs. LWP_{MLP}	0.308	0.291
LWP_{mf} vs. LWP_{mean}	0.472	0.442
LWP_{PPH} vs. LWP_{MLP}	0.491	0.487
LWP_{PPH} vs. LWP_{mean}	0.586	0.563

simulations in section 7.2.3. Similarly the root-mean-square errors between LWP_{mf} vs LWP_{mean} of around 45% is close to the value of the error found for the estimation of the pixel value using the mean of a thin line flown across it. Finally, Figure 7.11 shows the frequency histogram of the relative error, RE, between LWP_{mf} and LWP_{MLP}. This is similar to the frequency histogram of the errors in the numerical simulation shown in Figure 7.6b, and a two-sample Kolmogorov-Smirnov test [e.g. *Rhogati*, 1976] produced a significance level of $p = 0.69$, indicating a 69% probability that the two error distributions are the same.

The implication of this error analysis is not that the satellite estimation of the liquid water path is perfectly accurate, but rather that any errors in LWP_{mf} are small enough to be masked by the significant errors in the upscaling from the aircraft-instrument scale to the scale of the AVHRR pixel. Although the MLP method has allowed us to reduce this root-mean-square relative error, the comparison of satellite to aircraft data still did not show much more discrepancy than would be caused simply by upscaling error alone.
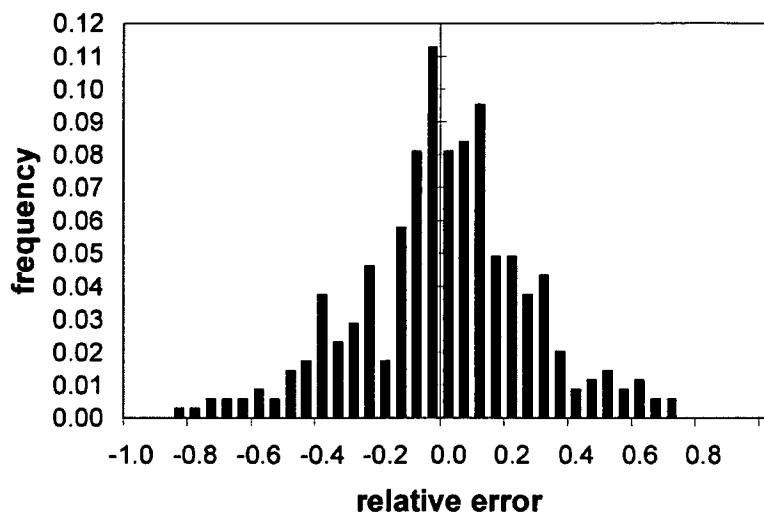
Figure 7.11: Frequency histogram of the relative error between the MLP estimate from the aircraft data, LWP_{MLP}, and the satellite estimate LWP_{mf}. Mean of distribution is 0.011, std. dev. is 0.298.

7.5   Summary of Chapter 7

In this chapter the implications of a multifractal cloud structure for moderate-resolution remote sensing have been examined, with a focus on the comparison between satellite data and in situ measurements. The numerical simulations have shown the high levels of error that result from comparing measurements at different resolutions in a multifractal field. The MLP method was summarised and shown to reduce these discrepancies by slightly less than half, for both spot measurements in a multifractal field and a line integrated across the field. This upscaling method was then used in the comparison of aircraft measurements with AVHRR data. This comparison showed that the traditional PPH cloud model led to a mean bias in liquid water path retrieval, as has been predicted by previous theoretical studies, but that this mean bias was almost totally eliminated by using an empirical correction to the retrieved optical depth that takes into account the multifractal structure of the cloud. Although the retrieval contained little or no mean bias after this correction had been made, there were still significant differences between the satellite retrieval of the LWP and the aircraft estimate in any particular pixel. However, these discrepancies were only slightly greater than those predicted for the MLP upscaling procedure i.e. they were not much greater than would have been seen even if the satellite estimation were perfect.

One of the key implications from these results is that ground-truthing of moderate-resolution cloud LWP retrieval cannot be made significantly more precise with single aircraft passes, because of the inherent errors involved in the comparison of data at very different spatial scales even when the MLP method is used. This is even ignoring any errors due to vertical inhomogeneity which was not considered in the simulations here. If a cloud remote sensing technique is to be compared with in

situ data with greater precision than the ~30% errors seen here, then it would seem that a greater degree of sampling in each pixel is required. This may require more than one aircraft or alternate instrumentation which covers a greater area. Even with greater sampling, the statistical upscaling like that used here will still be needed for the extrapolation between scales.

Chapter 8

Conclusion

8.1 Summary of Results

In this section the major results of the thesis are outlined, with special emphasis on those that are new or differ from the findings of others.

8.1.1 Cloud Spatial Structure

The FIF multifractal model was developed by *Schertzer and Lovejoy* [1987] for clouds using the theory of turbulence and the passive scalar advection of liquid water content. Since then the model has been shown to fit experimental observations of rain radar reflectivities [*Tessier et al.*, 1993; *Lovejoy and Schertzer*, 1995b], satellite-observed radiance reflected from cloud fields [*Lovejoy et al.*, 1993; *Tessier et al.*, 1993; *Lovejoy et al.*, 2001a] and rainfall measured at the ground [*Lovejoy and Schertzer*, 1995], and the parameters of the model have been found experimentally for these quantities. However, to the best of the author's knowledge the model has

215

not been compared or fitted to direct in-situ measurements of cloud liquid water content before this study. Since the relationship between cloud liquid water content and the radiation field - and the total liquid water content and precipitation - is complex and non-linear, the earlier observations do not translate directly to the spatial structure of cloud fields, and there is no reason at this stage to assume that the FIF model parameters found for those quantities can be used for liquid water content. Therefore the aircraft-based observations from flights presented in Chapter 3 add a significant degree of certainty to the use of the universal FIF multifractals to model cloud fields. Those observations were used to show that the horizontal spatial statistics of stratocumulus, altostratus and low-level cumulus clouds are scale invariant over a wide range of scales, and that their statistics behave as predicted by the universality classes of the FIF model. The FIF model parameters (α, C_1, H) for liquid water content modelling were obtained from these measurements.

The scale invariance of cloud fields has long been known, but an interesting result here is the lack of evidence of a scale break in the power spectrum at the low spatial frequencies (large scale) for stratocumulus and cumulus cloud, despite the fact that the scale extends out to ~160 km. The power spectrum of some individual flights in these cloud types did appear to flatten out at low frequencies, but this was not reflected when the ensemble averages for each cloud type were examined. The only cloud type that did show signs of flattening of the ensemble-averaged spectrum at low frequencies was altostratus. These results differ from those of *Davis et al.* [1996a] who found such a break in the scaling regime of stratocumulus cloud in the range of 20 - 60 km. This difference in the stratocumulus statistics is probably due to different climatological conditions - a generally thicker boundary layer and more vigorous dynamics over the Tasmania than seen over the ocean for the two

216

experiments analysed in *Davis et al.* [1996a]. Despite the difference in scaling range, the spectral exponent β of 1.42 found here for stratocumulus is effectively the same, given the error ranges in the estimations.

Although the FIF model has not been previously fitted to in situ cloud data, aircraft measurements of marine stratocumulus have also been used by *Marshak et al.* [1997] to find the mean intermittency and non-stationarity parameters (C_1 and H respectively) directly from the structure functions and singular measures of the liquid water content. The ensemble mean values found in that study of $C_1 = 0.1$ and $H = 0.29$ are similar to those found here for stratocumulus cloud, $C_1 = 0.108 \pm 0.002$ and $H = 0.30 \pm 0.02$. However, no equivalent of the multifracticality parameter α of the FIF model was found, so this is the first time a full set of the parameters required to use the universal multifractal classes of the FIF model to simulate cloud fields have been determined from in situ data. It is interesting to note that the two experiments in *Marshak et al.* [1997] of five flights each over the Pacific and Atlantic, and the 48 flights over Tasmania studied here, all produced approximately equal parameters (C_1, H) for stratocumulus cloud despite the widely different geographical locations. This implies some degree of commonality in the processes that shape the horizontal spatial structure of stratocumulus cloud, even under apparently different climatological conditions.

Another contribution from this project is the extension of the fractal analysis of liquid-water cloud structure, from marine stratocumulus that have been the primary focus of previous studies, to other cloud categories. The horizontal structure of altostratus and low-level cumulus were both confirmed as scale invariant over a wide range of scales, with the cumulus scaling over all ranges observed and altostratus scaling up until flattening of the power spectrum above 20-40 km as noted earlier. The spectral exponents β were found not to differ from that of the

217

stratocumulus by more than the error in the parameter estimation. Similarly the multifracticality parameter α and the non-stationarity parameter H could not be seen to vary between the three cloud types given the errors in estimation. Again this is an argument for some universality in the processes that create the horizontal structure of the three categories of cloud. However, the mean degree of inhomogeneity in the fields did vary, as measured by the parameter C_1. Altostratus were found to be the most homogeneous with $C_1 = 0.082 \pm 0.001$, altostratus was the middle case $C_1 = 0.108 \pm 0.002$, and low-level cumulus had the most intermittent result of $C_1 = 0.126 \pm 0.003$.

Anther interesting result from the analysis of the spatial structure in Chapter 3 was the diurnal cycle in the fractal parameters of stratocumulus cloud. *Cahalan et al.* [1994a] found a similar diurnal cycle in the fractal parameter of the bounded cascade model in ground-based microwave -radiometer measurements of the liquid water path of stratocumulus clouds. Although there is no simple relation between the parameters of the different models, the f parameter of the bounded cascade cloud measures the mean inhomogeneity, as the FIF parameter C_1 does. A cycle was found here in C_1 which was qualitatively similar to that found for the bounded cascade, with the mean inhomogeneity being lowest in the afternoon and highest in the early morning. There was also a cycle in the α parameter, roughly the opposite of the other. This means that although the mean inhomogeneity decreases during the day, there are still some extreme points that get further from the mean as the day progresses.

In addition to the daily cycle, a steady change in the multifractal parameters with the seasons was also observed here. Although there was no measurements in the summer months, so a complete annual cycle could not be investigated, the monthly averaged data showed the mean-intermittency parameter C_1 increasing

through the months of autumn, reaching a maximum in winter and then increasing in spring. This suggests a yearly cycle. As in the case of the diurnal cycle, the multifracticality parameter α was seen to be approximately the opposite of C_1, with a decrease in autumn, minimum in winter and increase in spring. These two cycles, daily and yearly, indicate a climatology of cloud spatial structure that is based on the similar cycles in the atmospheric boundary layer, but determining the exact link between boundary layer properties and cloud spatial statistics requires further investigation.

8.1.2 Radiation modelling

The mean parameters for all three cloud types considered as a single ensemble, $\alpha = 1.48$, $C_1 = 0.106$, and $H = 0.3$, where then used to numerically generate FIF multifractal cloud fields for use in radiation studies. One of the key goals was to find an effective optical properties approximation so that widely used PPH radiative transfer algorithms could easily be corrected for multifractal clouds. This has already been done for bounded cascade clouds with marine stratocumulus parameters in the effective homogenous cloud approximation [*Szczap et al.*, 2000a;b;c] and a very similar methodology was used here in Chapter 4 for the FIF cloud model with constant vertical profiles. The parameterisation of *Szczap et al.*[2000a] was found to overestimate the effective optical depth of the multifractal clouds considered in this thesis, due to the fact that our clouds were more inhomogeneous than the marine stratocumulus model used in *Szczap et al.*[2000a]. But it was found to be possible to fully define an effective optical properties approximation for the FIF clouds when the pixel size is ≥ 1.6 km and the solar zenith angle is not too high - i.e. it is possible to replace the multifractal cloud with a PPH cloud and still calculate all 3 of reflectance, transmittance and absorptance with a minimum

of error. This is in contrast to the case of the bounded cascade model of cloud when the parameters were set to inhomogeneity levels higher than marine stratocumulus, which a previous study found to not admit an effective optical properties approximation [*Szczap et al.*, 2000c]. The reason for this difference requires further investigation.

The FIF model, with the mean fractal parameters used here, was found to produce reflectance further from the PPH cloud value than was determined for typical overcast marine stratocumulus by *Cahalan et al.* [1994a]. This difference in the PPH bias was seen to increase with the spatial averaging size under consideration. Thus the effective single scattering albedo also depended on pixel size. A new parameterisation for the effective optical properties was developed that took this pixel size dependence into account explicitly. The effect of varying the asymmetry factor was also considered, and it was found to only change the effective optical properties by a small amount for the typical range of values. The result of changing the fractal parameters of the multifractal cloud was also investigated: increasing C_1 and α were found to increase the difference from the PPH case results, while increasing H was found to lead to results closer to the homogeneous case. One consequence of this relationship is that the radiative effects of the diurnal cycles observed in the α and C_1 (for stratocumulus cloud) will oppose one another - for example, the diurnal cycle sees C_1 increasing at the same time as α is decreasing, the former causing lower reflectance and the latter higher. The difference between the radiative properties of the three cloud types due to horizontal spatial structure was also found, with altostratus having a reflectance 3% higher than stratocumulus which in turn was 3% higher than low level cumulus. The reflected radiance distribution from multifractal cloud was found to be relatively similar to that of PPH cloud, except at very high viewing and solar zenith angles - meaning that

the effective optical depth approximation can be used in application like satellite remote sensing where reflected radiance distribution is important.

In the fifth Chapter of this thesis the radiative properties of clouds with a multifractal structure in all three dimensions was investigated. Until now, the effective optical properties concept has only been applied to vertically homogeneous clouds or 2-dimensional clouds, and studies of the radiative properties of 3-dimensionally fractal clouds have been rare [e.g. *Davis et al.*, 1991; *Liou et al.*, 2001]. For the case non-absorbing clouds the results were found to follow the same trends as the vertically homogeneous clouds, simply having reflectance and transmittance slightly further from the PPH results. The differences between 2-dimensionally and 3-dimensionally multifractal clouds increased with cloud optical depth, as previous studies have also shown [*Romanova*, 1998; *Stephens et al.*, 1991; *Marshak et al.*, 1998]. The other difference discovered here was the higher solar zenith angle dependency of the effective optical depth in 3D multifractal clouds, presumably due to the increase in horizontal transport of photons. In the case of absorbing clouds on the other hand the behaviour of the 3D multifractal clouds was seen to be qualitatively different from the vertically constant case at larger optical depth, with transmittance and absorptance actually moving closer to the PPH values as the mean optical depth increased. It was also found that an effective optical properties approximation could not be applied because of the differences between ω_{eff}^{RT} and ω_{eff}^{RA}. Only once the values of the mean optical depth were restricted to less than 20 were reasonable results produced by the parameterisation for the effective optical properties found in Chapter 4.

Although most studies on the radiative properties of inhomogeneous cloud concentrate on the reflected radiance field or the radiation budget, in Chapter 6 of this work the transmitted radiance distribution was investigated. This topic is also per-

tinent to the effective optical properties approximation, because the fact that a PPH cloud has the same total transmittance as the multifractal cloud does not mean the radiation field is necessarily identical. The modelled transmitted radiance distribution for a PPH and a multifractal cloud were compared to azimuthally-averaged measurements of the diffuse radiation field made by the Variable Sky Platform instrument. In overcast conditions the multifractal model produced a radiance field in good agreement with the observations - in both cases an increase around the solar zenith angle could be seen despite the complete coverage by cloud. However, the PPH cloud with the same transmittance as the multifractal cloud (and the measured conditions) produced radiance distributions noticeably smoother than the overcast observations, showing no sign of a circumsolar hump. Under the 6 octas cover however, the observations were actually smoother than the overcast measurements and closer to the PPH results than the multifractal. This is thought to be due to a bias in the VSP methodology under broken cloud fields, because of the need to discard 2-minute runs during which the sun is alternatively obscured and visible. An empirical parameterisation was found for the radiance under multifractal fields. Note that these results for transmitted radiance are in contrast to those for reflected radiance in chapter 4, where the PPH and multifractal radiance distributions were relatively similar.

8.1.3   Remote sensing

The comparison of the remote sensing data with in situ measurements in Chapter 7 uses both the radiation modelling results and the spatial statistics of the cloud field. The spatial statistics are used to upscale the aircraft measurements using the Most Likely Parent method. This method was developed, and tested using lognormal fractals, by *Salvadori et al.* [2001], but is applied to the comparison of

in situ and satellite-based comparisons for the first time here. It was first tested for FIF multifractal fields with the parameters measured here and was found to give a significant improvement in estimating the whole-pixel mean when compared to simply taking the mean value of point measurements inside the pixel. Values of the expected error were found that could be used in the experimental planning to determine the number of point measurements necessary to sample a multifractal field. Even using the MLP method the errors were still large until a significant percentage of the pixel was sampled, such is the nature of non-stationary fields. The original method was then modified here to represent taking an integrated path across a pixel rather than point measurements. Numerical simulation of this process on cloud fields showed that although it reduced the error of estimation, the root-mean-square relative error in the predicted pixel-scale value was still 27%. Just taking the mean value gives errors greater than 40%. These would be the minimum expected RMS errors when comparing moderate resolution remote sensing to single-aircraft measurements.

Despite these errors, it was seen that the use of the effective optical properties approximation to correct the satellite-retrieved liquid water path increased the agreement of the two data sets, as judged by their mean values. That is, the use of the effective optical depth approximation rather than the PPH assumption alone eliminated the mean bias, but significant scatter remained. This scatter was consistent with what was expected when comparing moderate resolution remote sensing to single aircraft measurements.

8.2 Outlook

The effective optical depth approximation that was the focus of this study was found to have many limitations. These include: a limit on the zenith angles and pixel sizes to which it can be applied when calculating all radiative quantities (T,R and A); that it is not applicable to absorbing 3-dimensionally multifractal clouds; that the transmitted diffuse radiance distribution of the PPH cloud is not the same as the multifractal cloud even when the total transmittance is equal. Thus while it is suitable to some applications, it does not seem a good choice for models that are required to calculate the radiation budget for all conditions. On the other hand, it does seem most applicable to satellite remote sensing applications such as the one used here, where only the reflectance is important and it can easily be used to correct current algorithms. It could also be used for estimating radiation at the ground if only irradiance is important, or if the parameterisation of transmitted radiance found in Chapter 5 was considered sufficient.

One area in which further work is required is the testing of the transmitted radiance distribution modelled by multifractal cloud under broken cloud conditions. This could be achieved using the Variable Sky Platform if the methodology of its use is altered. This could possibly be done by using a sky camera to assess the sampling bias by analysing cloud position and hence attempting to correct for it. Alternatively if the direct beam were measured with a separate shadowband instrument then this could be subtracted from the VSP distribution where necessary, negating the need to find the direct beam from the VSP output itself and thus the need to reject the 2-minute runs where the sun is alternatively visible and obscured.

The most obvious improvement that could be made to the cloud model and hence the radiation results that stem from it involves the measurement of the ver-

tical structure of clouds, and subsequent inclusion of these measurements into the cloud model. While in the 3-dimensionally multifractal cloud used here the scaling was assumed to be isotropic, so that the spatial statistics were the same in the vertical as the horizontal, in reality the force of gravity leads to different structures in the vertical direction. The natural theoretical framework for the inclusion of a more realistic vertical structure in the cloud model is the Generalised Scale Invariance of *Schertzer and Lovejoy* [1987, 1991], which is the generalisation of the fractal model used here to cases of "anisotropic scaling" where the spatial statistics can be different in different dimensions. To implement this extension of the cloud model would require sufficient vertical measurements of cloud liquid water content to determine the vertical parameters.

One final thing to note for future work in remote sensing is the implications of the errors found when simulating comparisons of multifractal data at different scales in Chapter 7. Although the MLP method shown here significantly decreased the errors in these simulations, they are still quite large for both point samples and integrated paths, unless a significant proportion of each pixel is sampled. The ways to reduce these errors is to increase the number of sampled points, or reduce the difference in resolutions compared. Similar results would apply to other multifractal fields. This needs to be considered in the planning of measurement campaigns that compare multifractal data at different scales.

Bibliography

Bak, P., C. Tang, and K. Weissenfield, Self-Organised critical phenomena, *Phys. Rev. Lett.*, *59*, 381-385, 1987.

Bellon, A., S. Lovejoy, and G. L. Austin, A short term precipitation forecasting procedure using combined radar and satellite data, *Mon. Wea. Rev.*, *108*, 1554-1566, 1980.

Berk, A. , L. S. Bernstein, and D. C. Robertson, MODTRAN: A moderate resolution model for Lowtran 7, GL-TR-89-0122, [available from Geophysics Directorate, Phillips Laboratory, Hanscom AFB, MA 01731],1989.

Berk, A. and G. P. Anderson, Upgrades to Modtran Layer Cloud/Rain Models, SSI-SR-69 [available from Spectral Sciences, Inc, 99 S. Bedford Street, Burlington, MA 01803],1995.

Boers, R., A. van Lammeren, and A. Fejit, Accuracy of cloud optical depth retrievals from ground-based radiometers, *J. Atmos. Ocean. Tech.*, *17*, 916-927, 2000.

R. Borde and H. Isaka, Radiative transfer in multifractal clouds, *J. Geophys. Res.*, *101*, 29,461-29,478, 1996.

Cahalan, R. F., Overview of fractal clouds, in *Advances in Remote Sensing Retrieval Methods*, edited by A. Deepak, H. Fleming and J. Theon, pp. 371-380, 1989.

Cahalan, R., and J. H. Joseph, Fractal statistics of cloud fields, *Mon. Wea. Rev.*, *117*, 261-272, 1989.

Cahalan, R.F., W. Ridgeway, W.J. Wiscombe, T.L. Bell, and J. B. Snider, The albedo of fractal stratocumulus clouds, *J. Atmos. Sci.*, *51*, 2434-2455, 1994a.

Cahalan, R.F., W. Ridgeway, W.J. Wiscombe, S. Gollmer, and Harshvardan, Independent pixel and Monte Carlo estimates of stratocumulus albedo, *J. Atmos. Sci.*, *51*, 3776-3790, 1994b.

Cairns, B., A.A. Lacis, and B.E. Carlson, Absorption within inhomogeneous clouds and its parameterization in general circulation models. *J. Atmos. Sci.*, *57*, 700-714, 2000.

Chambers, J.M., C. L. Mallows and B.W. Stuck, *Journal of the American Statistica Association*, *71*, p. 340, 1976.

Chandrasekhar, S., *Radiative transfer*, Oxford University Press, UK, 1950.

Chigirinskaya, Y., D. Schertzer, S. Lovejoy, A. Lazarev, A. Ordanovich, Unified multifractal atmospheric dynamics tested in the tropics: part I, horizontal scaling and self criticality, *Non-linear Processes in Geophysics,1,*105-114, 1994.

Coombes, C.A., and A.W. Harrison, Angular distribution of overcast sky short wavelength radiance, *Sol. Energy, 40,* 161-166, 1988.

Cullen, J.J., and M.P. Lesser, Inhibition of photosynthesis by ultraviolet radiation as a function of dose and dosage rate: results for a marine diatom, *Marine Biol.*, 111, 183-190, 1991.

Davis, A., S. Lovejoy, and D. Schertzer, Discrete Angle radiative transfer Part III: Numerical and results on homogeneous and fractal clouds, *J. Geophys. Res., 95,* 1990.

Davis, A., A. Marshak, W. Wiscombe and R. Cahalan, Multifractal characterizations of nonstationarity and intermittency in geophysical fields: Observed, retrieved, or simulated, *J. Geophys. Res., 99,* 8055-8072, 1994.

Davis, A., A. Marshak, W. Wiscombe and R. Cahalan, Scale invariance of liquid water distributions in marine stratocumulus. Part I: Spectral properties and stationarity issues, *J. Atmos. Sci., 53,* 1538-1557, 1996a.

Davis, A., A. Marshak, W. Wiscombe and R. Cahalan, Multifractal characterizations of intermitency in non-stationary geophysical signals and fields, in *Currrent Topics in Non-stationary Analysis*, edited by G. Treviño, World-Scientific, 97-158, 1996b.

Evans, K. F., The spherical harmonics discrete ordinate method for three-dimensional atmospheric radiative transfer, *J. Atmos. Sci.*, 55, 429446, 1998.

Evans, S. J., and J. D. Haigh, The retrieval of total optical depth and effective droplet radius of clouds from solar reflection measurements using the along track scanning radiometer-2 (ATSR-2), *Geophys. Res. Let.*, *22*, 695-698, 1995.

Feller, W., *An introduction to probability theory and its applications*, John Wiley and Sons, New York, 1971.

Fouilloux, A., and J. Iaquinta, Comparison of stratocumulus cloud modeling with satellite observations and in situ measurements, *J. Geophys. Res.*, *102D*, 13,595-13,602, 1997.

Gerber, H., B. G. Arends, and A. S. Ackerman, New microphysics sensor for aircraft use, *Atmos. Res.*, *31*, 235-252, 1994.

Goody, R. M., and Y. L. Yung, *Atmopsheric Radiation - A theoretical basis*, Oxford University Press, New York, 1989.

Grant, R.H., and G.M. Heisler, Obscured overcast sky radiance distributions for ultraviolet and photosynthetically active radiation, *J. Appl. Meteorol.*, *36*, 1336-1345, 1997.

Grant, R.H., G.M. Heisler, and W. Gao, Ultraviolet sky radiance distributions of translucent overcast skies, *Theor. Appl. Climatol.*, *58*, 129-139, 1997.

Gregory, D., J. J. Morcrette, C. Jakob, C. M. Beljaars, and T. Stockdale, Revisions to the convection, radiation and cloud schemes in ECMWF integrated forecasting system, *Q. J. R. Meteorol. Soc.*, *126*, 1685-1710, 2000.

Gu, Y., and K. N. Liou, Radiation parameterisation for three dimensional inhomogeneous cirrus clouds: Application to climate models, *J. Climate, 14*, 2443-2457, 2001.

Han, Q., W. B. Rossow, and A. A. Lacis, Near global survey of effective droplet radii in liquid water clouds using ISCCP data, *J. Climate, 7*, 465-497, 1994.

Harrison, A.W., and C.A. Coombes, An opaque cloud cover model of sky short wavelength radiance, *Sol. Energy, 41*, 387-392, 1998.

Harrison, E. F., P. Minnis, B. R. Barkstrom, V. Ramathan, R. D. Cess, and G.G. Gibson, Seasonal variation in cloud radiative forcing derived from the Earth Radiation Budget Experiment, *J. Geophys Res.*, *95*, 18 687 - 18703, 1990.

Hartmann, D. L., M.E. Ockert-Bell, and M. L. Michelson, The effect of cloud type on the on earths energy budget: Global analysis, *J. Climate*, *5*, 1281-1304, 1992.

Hu, Y. X., and K. Stamnes, An accurate parameterization of the radiative properties of liquid water clouds suitable for use in climate models, *J. Climate*, *6*, 728-743, 1993.

Kawamoto, K., T. Nakajima, T. Y. Nakajima, A Global determination of cloud microphysics with AVHRR remote sensing, *J. Climate*, *14*, 2054-2068, 2001.

King, W. D., D. A. Parkin, and R. J. Handsworth, A hot-wire liquid water device having fully calculable response characteristics, *J. Appl. Met. 17*, 1809-1813, 1978.

Kolmogorov, A. N., Local structure of turbulence in an incompressible liquid for very large Reynolds numbers, *Proc. Acad. Sci. USSR., Geochem. Sect.*, *30*, 299-303, 1941.

Kolmogorov, A. N., A refinement of previous hypothesis concerning the local structure of turbulence in viscous incompressible fluid at high Reynolds numbers, *J. Fluid Mech.*, *13*, 82-85, 1962.

Kuchinke, C., *Improved techniques for the spatial and temporal measurement of ultraviolet radiation*, Ph.D. thesis, University of Tasmania, 352 pp., 2002.

Kuchinke, C., and M. Nunez, Spectral dependence in the cosine response of broadband UV instruments, *J. Geophys. Res.*, *106*, D13, 14 287-14 300, 2001.

Kuchinke, C., and M. Nunez, A variable-sky platform for the measurement of ultraviolet radiation, IN PRESS, *J. Atmos. Ocean. Tech.*, 2003.

Kuji, M., T. Hayasaka, N. Kikuchi, T. Nakajima, and M. Tanaka, The retrieval of effective particle radius and liquid water path of low-level marine clouds from NOAA AVHRR data, *J. of Appl. Met.*, *39*, 999-1016, 2000.

D. Lavallée, D. Schertzer and S. Lovejoy, On the determination of the codimension function, in *Non-linear Variability in Geophysics: Scaling and Fractals*, edited by D. Schertzer and S. Lovejoy, Kluwer, pp. 41-82, 1991.

Lavallée, D., S. Lovejoy, D. Schertzer, and P. Ladoy, Nonlinear variability and landscape topography: analysis and simulation, in *Fractals in Geography*, edited by L. De Cola and N. Lam, New York: Prentice-Hall, 171-205, 1993:.

Lazarev, A., D. Schertzer, S. Lovejoy, Y. Chigirinskaya, Unified multifractal atmospheric dynamics tested in the tropics: part II, vertical scaling and generalized scale invariance, *Non-linear Processes in Geophysics,1,*115-123, 1994.

Lenoble, J., *Radiative Transfer in Scattering and Absorbing Atmospheres*, Deepak, Virginia USA, 1985.

Lensky, I. M., and D. Rosenfield, Estimation of precipitation area and rain intensity based on the microphysical properties retrieved from NOAA AVHRR data, *J. Appl. Meteorol., 36,* 234-242, 1997.

Lesser, M.P., J.J. Cullen, and P.J. Neale, Carbon uptake in a marine diatom during acute exposure to ultraviolet B radiation: relative importance of damage and repair, *J. Phycol., 30,* 183-192, 1994.

Lin, C.-C., C. Tinel, K. Caillault, J. Testud and E. Caubet : Spaceborne cloud profiling radar - Instrument parameter optimisation for resolving highly-layered cloud structures, SPIE Remote Sensing proceedings 4882, 23-27 September, Agia Pelagia, Crete, 2002

Liou, K. N, *An Introduction to Atmospheric Radiation*, Acacdemic Press, New York, 1990.

Liou, K.N., S.C. Ou, Y. Takano, F.P.J. Valero, and T.P. Ackerman, Remote sensing of the tropical cirrus cloud temperature and optical depth using 6.5 and 10.5 μm radiometers during STEP, *J. Appl. Meteorol., 29,* 716-726, 1990.

Los, A., and P. G. Duynkerke, Parameterization of solar radiation in inhomogeneous stratocumulus: Albedo bias, *Q. J. R. Meteorol. Soc., 127,* 1593-1614, 2001.

Lovejoy, S., Area-perimeter relationship for rain and cloud areas, *Science, 216,* 185-187, 1982.

230

Lovejoy, S., and D. Schertzer, Generalized scale invariance and fractal models of rain, *Water Resour. Res.*, *21*, 1233-1250, 1995a.

Lovejoy, S., and D. Schertzer, Multifractals and rain, in *New Uncertainty Concepts in Hydrology and Water Resources*, edited by Z. W. Kunzewicz, Cambridge Univ. Press, New York, pp. 62-103, 1995b.

Lovejoy, S., D. Schertzer, P. Silas, Y. Tessier, and D. Lavallée, The unified scaling model of atmospheric dynamics and systematic analysis of scale invariance in cloud radiances, *Ann. Geophysicae*, *11*, 119-127, 1993.

Lovejoy, S., D. Schertzer, and J.D. Stanway, Direct evidence of multifractal atmospheric cascades from planetary scales down to 1km, *Phys. Rev. Let.*, *86*, 5200-5203, 2001a.

Lovejoy, S., D. Schertzer, Y. Tessier and H. Gaonach, Multifractals and resolution-independent remote sensing algorithms: an example of ocean colour, *Int. J. Remote Sensing*, *22*, 1191-1234, 2001b.

Macke, A., D.L. Mitchell, and L.V. Bremen, Monte Carlo radiative transfer calculations for inhomogenous mixed phase clouds, *Phys. Chem. Earth B*, *24(3)*, 237-241, 1999.

Malinowski, S.P., and I. Zawadzki, On the surface of clouds, *J. Atmos. Sci.*, 50, 5-13, 1993.

Mandelbrot, B., *The fractal Geometry of Nature*, Freeman Press, San Francisco, 1983.

Mandelbrot, B., Fractal geometry: what is it and what does it do?, in *Fractals in the Natural Sciences*, edited by M. Fleischmann, D.J. Tildsley and R.C. Ball, Princeton University Press, pp. 3-16, 1989.

Mandelbrot, B., Random multifractals: negative dimensions and the resulting limitations of the thermodynamic formalism, *Proc. Royal Soc.*, *484*, 119-127, 1991.

Marchuk,G., G. Mikhailov, M. Nazaraliev, R. Darbinjan, B. Kargin and B. Elepov, *The Monte Carlo Method in Atmospheric Optics*, Springer-Verlag, New York, 1980.

Marshak, A., A. Davis, R. Cahalan, and W. Wiscombe, Radiative smoothing in fractal clouds, *J. Geophys. Res.*, *100*, 26,247-26,261, 1995.

Marshak, A., A. Davis, R. Cahalan, and W. Wiscombe, The Non-local Independent Pixel Approximation for computing radiation fields of inhomogeneous clouds, in *IRS '96: Current Problems in Atmospheric Radiation*, edited by Smith and Stamnes, Deepak Publishing, New York, 1996.

Marshak, A., A. Davis., W. Wiscombe and R. Cahalan, Scale invariance of liquid water distributions in marine stratocumulus. Part II: Multifractal properties and intermittency issues, *J. Atmos. Sci.*, *54*, 1423-1444, 1997.

Marshak, A., A. Davis, W. Wiscombe, and R. Cahalan, Radiative effects of sub-mean free path liquid water variability observed in stratiform clouds, *J. Geophys. Res.*, *103D*, 19 557-19 567, 1998.

McGuffie, K. and A. Henderson-Sellers, *A Climate Modelling Primer*, John Wiley and sons, 253pp, 1997.

Minnis, P., W. H. Heck, D. F. Young, C.W. Fairfall, and J. B. Snider, Stratocumulus cloud properties derived from simultaneous satellite and island-based instrumentation during FIRE, *J. Appl. Meteorol.*, *31*, 317-339, 1992.

Mitchell, J.F., The 'greenhouse' effect and climate change, *Rev. Geophys.*, *27*, 115-139, 1989

Morris, C.W., and J.H. Lawrence, The anisotropy of clear sky diffuse solar radiation, *ASHRAE Transactions, Part 11*, 136-141, 1971.

Nakajima, T., and M. D. King, Determination of optical thickness and effective particle radius of clouds from reflected radiation measurements. Part I: Theory, *J. Atmos. Sci.*, *47*, 1878-1893, 1990.

Nakajima, T., M. D. King, J.D. Spinhirne, and L. F. Radke, Determination of optical thickness and effective particle radius of clouds from reflected radiation measurements. Part II: Marine stratocumulus observations, *J. Atmos. Sci.*, *48*, 728-750, 1991.

Obukhov, A.M., Structure of the temperature field in a turbulent flow, *Izv. Akad. Nauk. SSSR., Ser. Geogr. i Geofiz.*, *13(1)*, 58-59, 1949.

G.W. Paltridge and C.M.R. Platt, *Radiative Processes in Meteorology and Climatology*, Elsevier, New York, 1976.

Parisi, G. and U. Frisch, A multifractal model of intermittency, in *Turbulence and predictability in geophysical fluid dynamics and climate dynamics*, edited by M. Ghil, R. Benzi and G. Parisi, North Holland, 84-88, 1985.

Pecknold, S., D. Schertzer, S. Lovejoy, C. Hooge and J.F. Malouin, "The simulation of universal multifractals", in *Cellular Automata: Prospects in Astronomy and Astrophysics*, eds. J. M. Perdang and A. Lejeune, World Scientific, pp. 228-267, 1993.

Pinker, R.T., R. Frouin, and Z. Li, A review of satellite methods to derive surface shortwave irradiance, *Remote Sens. Env.*, *51*, 108-124, 1995.

Ramanathan, V., R. D. Cess, E. F. Harrison, P. Minnis, B. R. Barstrom, E. Ahmad, D. Hartmann, Cloud radiative forcing and climate: results from the Earth Radiation Budget Experiment, *Science, 243*, 57-63, 1989.

Rawlins, F., and J. S. Foot, Remotely sensed measurements of stratocumulus properties during FIRE using the C130 aircraft multi-channel radiometer, *J. Atmos. Sci., 47*, 2488-2503, 1990.

Rhogati, V. K., *An Introduction to Probability and Mathematical Statistics*, J Wiley and Sons, New York, 1976.

Rogers, R. R., and M. K. Yau, *A short course in cloud physics*, Pergamon Press, Oxford UK, 1989.

Romanova, L. M., Solar Radiation transfer in inhomogeneous stratiform clouds, *Izvestiya - Atmospheric and Oceanic Physics, 34*, 726-733, 1998.

Romanova, L. M., Relationship between horizontal variations in the albedo and transmittance of a stratified cloud and its structure, *Izvestiya - Atmospheric and Oceanic Physics, 35*, 1999.

Rosen, M.A., and F.C. Hooper, A comparison of two models for the angular distribution of diffuse sky radiance for overcast skies, *Sol. Energy, 42*, 477-482, 1989.

Rosenfield, D., and G. Gutman, Retrieving microphysical properties near the tops of potential rain clouds by multispectral analysis of AVHRR data, *Atmospheric Research, 34*, 259-283, 1994.

Rossow, W. B., and A. A. Lacis, Global, seasonal cloud variations from satellite radiance measurements Part II: Cloud properties and radiative effects, *J. Climate, 3*, 1204-1253, 1990.

Rossow, W. B., and Y. C. Zhang, Calculation of surface and top of the atmosphere radiative fluxes from physical quantities based on ISCCP datasets 2: Validation and first results, *J. Geophys. Res.*, 100, 1167-1197, 1995.

Salvadori, G., D. Schertzer, and S. Lovejoy, Multifractal objective analysis: conditioning and interpolation, *Stochastic Environmental Research and Risk Assessment, 15,* 261-283, 2001.

Sassen, K., and H. Zhao, Supercooled liquid water clouds in Utah winter mountain storms: Cloud-seeding implications in a remote sensing dataset, *J. Appl. Meteorol., 32,* 1548-1557, 1993.

Schertzer, D., and S. Lovejoy, Generalised scale invariance in turbulent phenomena, *Physico-Chem. Hydrodynamics Journal,* 6, 623-635, 1985.

Schertzer, D., and S. Lovejoy, Physical modeling and analysis of rain and clouds by anisotropic scaling multiplicative processes, *J. Geophys. Res., 92,* 9693-9714, 1987.

Schertzer, D., and S. Lovejoy, Non-linear geodynamical variability: multiple singularities, universality, and observables, in *Non-linear variability in geophysics: scaling and fractals,* edited by D. Schertzer and S. Lovejoy, Kluwer, The Netherlands, 1991.

Schertzer, D., and S. Lovejoy, Hard and soft multifractal processes, *Physica A, 185,* 187-194, 1992.

Schertzer, D., S. Lovejoy, and D. Lavalleé, Generic multifractal phase transitions and self-organised criticality, in *Cellular Automata: Prospects in Astronomy and Astrophysics,* eds. J. M. Perdang and A. Lejeune, World Scientific, pp. 216-227, 1993.

Schertzer, D., and S. Lovejoy, From scalar cascades to lie cascades: joint multifractal analysis of rain and cloud processes, in *Space and Time Variability and Interdependence in hydrological processes,* Cambridge University Press, p. 153-173, 1995.

Schertzer, D., and S. Lovejoy, Universal fractals do exist!, *J. Appl. Meteorol., 36,* 1296-1303, 1997.

Simmer, C., U. Hargens, and E. Ruprecht, Influence of cloud water distribution on the passive microwave retrieval of humidity, *Adv. Space Res., 9,* (7)149-(7)152, 1989.

Stephens, G. L., The transfer of radiations through verticcally non-uniform stratocumulus clouds, *Contrib. Phys. Atmos., 49,* 237-253, 1976.

Stephens, G. L., Radiation profiles in extended water clouds II: Parameterization schemes, *J. Atmos. Sci., 35*, 2123-2132, 1978.

Stephens, G. L., P. M. Gabriel, and S.C. Tsay, Statistical radiative transport in one dimensional media and its application to the terrestrial atmosphere, *Trans. Theory Stat. Phys., 20*, 139-175, 1991.

Stull, R. B., *An introduction to Boundary layer meteorology*, Kluwer, The Netherlands, 1988.

Szczap, F., H. Isaka, M. Saute, B. Guillermet and A. Ioltukhovski, Effective radiative properties of bounded cascade non-absorbing clouds: Definition of the equivalent homogeneous cloud approximation, *J. Geophys. Res., 105*, 20,617-20,633, 2000a.

Szczap, F., H. Isaka, M. Saute, B. Guillermet and A. Ioltukhovski, Effective radiative properties of bounded cascade clouds: Definition of an effective single scattering albedo, *J. Geophys. Res., 105*, 20,635-20,648, 2000b.

Szczap, F., H. Isaka, M. Saute, B. Guillermet and Y. Gour, Inhomogeneity effects of 1D and 2D bounded cascade models on their effective radiative properties, *Phys. Chem. Earth B, 25*, 83-89, 2000c.

Szczodrak, M., P.H. Austin, P.B. Krummel, Variability of optical depth and effective radius in marine stratocumulus clouds, *J. Atmos. Sci., 58*, 2912-2926, 2001.

Tessier, Y., S. Lovejoy, and D. Schertzer, Univeral multifractals: Theory and observation for rain and clouds, *J. Appl. Meteorol., 32*, 223-250, 1993

Tiedke, M., Representing clouds in large scale models, *Mon. Weather Rev., 121*, 3040-3061, 1993.

Twomey, S., and T. Cocks, Spectral Reflectance of clouds of clouds in the near infrared: Comparison of measurements and calculations, *J. Meteor. Soc. Japan, 60*, 583-592, 1982.

Weihs, P., A.R. Webb, S.J. Hutchison, and G.W. Middleton, Measurements of the diffuse UV sky radiance during broken cloud conditions, *J. Geophys. Res., 105, D4*, 4937-4944, 2000.

Wielicki, B.A., R.D. Cess, M.D. King, D.A. Randall, and E.F. Harrison, Mission to Earth: Role of clouds and radiation in climate, *Bull. Amer. Meteorol. Soc., 76*, 2125-2153, 1995.

Wilson, J., D. Schertzer, and S. Lovejoy, Continuous multiplicative cascade models of rain and clouds,in *Non-linear variability in geophysics: scaling and fractals,* edited by D. Schertzer and S. Lovejoy, Kluwer, The Netherlands, 1991.

Young, D. F., P. Minnis, D. Baumgardner, and H. Gerber, Comaprison of in situ and satellite-derived properties during success, *Geophys. Res. Lett., 25,* 1125-1128, 1998.

List of Figures

238

240

241

244

246

247

List of Tables